



## **OPTIMIZED DUAL EXPANDER AEROSPIKE ROCKET**

### **THESIS**

**Joshua N. Hall, Captain, USAF**

**AFIT/GAE/ENY/11-M10**

**DEPARTMENT OF THE AIR FORCE  
AIR UNIVERSITY**

**AIR FORCE INSTITUTE OF TECHNOLOGY**

**Wright-Patterson Air Force Base, Ohio**

**APPROVED FOR PUBLIC RELEASE; DISTRIBUTION UNLIMITED**

The views expressed in this thesis are those of the author and do not reflect the official policy or position of the United States Air Force, Department of Defense, or the United States Government. This material is declared a work of the U.S. Government and is not subject to copyright protection in the United States.

**OPTIMIZED DUAL EXPANDER AEROSPIKE ROCKET**

**THESIS**

Presented to the Faculty

Department of Aeronautics and Astronautics

Graduate School of Engineering and Management

Air Force Institute of Technology

Air University

Air Education and Training Command

In Partial Fulfillment of the Requirements for the  
Degree of Master of Science in Aeronautical Engineering

Joshua N. Hall, B.S.

Captain, USAF

March 2011

APPROVED FOR PUBLIC RELEASE; DISTRIBUTION UNLIMITED.

**OPTIMIZED DUAL EXPANDER AEROSPIKE ROCKET**

Joshua N. Hall

Captain, USAF

March 2011

Approved:

  
LtCol Carl R. Hartsfield, USAF (Chairman)

11 Mar 11  
date

  
LtCol Richard D. Branam, USAF (Member)

3 Mar 2011  
date

  
Richard K. Cohn, USAF (Member)

3 March 2011  
date

  
LtCol Richard E. Huffman, USAF (Member)

11 Mar 11  
date

## Abstract

Research at the Air Force Institute of Technology (AFIT) focused on designing a cryogenic dual-expander aerospike nozzle (DEAN) upper stage rocket engine to produce 50,000 pounds-force (222.4 kilo-Newtons) vacuum thrust, 464 seconds of vacuum specific impulse and a thrust-to-weight ratio of 106.5. The use of dual expander cycles improves engine reliability, maximizes efficiency, and eliminates some catastrophic failure modes. An upper stage engine with an aerospike nozzle is shorter and lighter than an equivalent performing conventional bell nozzle upper stage engine. Previous research focused on first developing a feasible closed DEAN design model and secondly expanding the model to support parametric trade and optimization studies. The current research effort used previous research as a foundation to create a reliable system level modeling tool to estimate performance, engine weight, and geometry for the DEAN concept. The model incorporated the Numerical Propulsion System Simulation (NPSS<sup>TM</sup>) software by NASA, Two-Dimensional Kinetics '04 (TDK'04<sup>TM</sup>) by Software and Engineering Associates, Inc, and ModelCenter<sup>TM</sup> by Phoenix Integration. Research obtained a new DEAN design point meeting physical and reusability design constraints from model trade and optimization studies. The new design has a vacuum thrust and a thrust-to-weight ratio of 50,161 lb<sub>f</sub> (223.1 kN) and 142.2, respectively. Furthermore, the new design has a vacuum specific impulse of 430.6 seconds, failing to meet the vacuum specific impulse design goal by 33.4 seconds or 7.3%. The model used common metals, alloys, and ceramics to improve near-term manufacturability of the DEAN. Current research laid a pathway for further research to find the optimum DEAN design point meeting all the design goals including vacuum specific impulse.

## **Acknowledgements**

First, I would like to thank my Savior, Jesus Christ, for giving me the ability and wisdom to finish this research. Many thanks to LtCol Hartsfield, my thesis advisor, who provided an open ear to toss ideas, let me borrow his textbooks, and provided guidance and support throughout the entire research effort. My sincere thanks to LtCol Branam; he provided me with the thesis idea and provided guidance when I could not figure certain things out. Without his involvement, this research would have never unfolded, especially with his historical background with previous DEAN related research. My sincere thanks also to J. Simmons who was instrumental in the research effort. He graciously provided countless hours assisting me with coding and ModelCenter questions and helping me organize my many thoughts. Thanks to LtCol Huffman for being on my thesis committee and for providing me with a method of characteristics code. The code was instrumental in understanding radial engine geometry defines the design altitude of an aerospike nozzle. Many thanks to Dr. Cohn from the Air Force Research Laboratory at Edwards, AFB for being a part of the research effort and for being on my committee. Thanks also to Doug Coats of Software and Engineering Associates, Inc., for providing his time to answer questions regarding TDK'04 and aerospike nozzle design, and for information regarding the Angelino approximation method, which proved to be a vital component of the research. Lastly, to my wife, family and friends, thank you for your love, continued support and sacrifice throughout the entire project.

## Table of Contents

	Page
Abstract .....	iv
Acknowledgements .....	v
Table of Contents .....	vi
List of Figures .....	ix
List of Tables .....	xii
List of Symbols .....	xiv
List of Abbreviations .....	xviii
I. Introduction .....	1
I.1 DEAN Model Background and Basic Concept .....	3
I.2 Research Objectives .....	5
II. Theory and Previous Research .....	7
II.1 Orbit Transfer Engines and Previous Aerospike Engines .....	7
II.1.a. Orbit Transfer Engines .....	7
II.1.b. Previous Aerospike Engines .....	9
II.2 Mission Requirements .....	11
II.3 Rocket Engine Theory .....	16
II.3.a. Rocket Engine Design Process .....	16
II.3.b. Rocket Engine Cycles .....	17
II.3.c. Combustion Chamber Theory .....	20
II.3.d. Rocket Nozzle and Rocket Engine Performance Theory .....	26
II.3.e. Cooling Jacket Theory .....	38
II.3.f. Turbopump (Turbine and Pump) Theory .....	49
II.3.g. Basic Injector and Plumbing Theory .....	55
II.3.h. Material Choice .....	58
II.4 Past DEAN Research Efforts .....	59
III. Methodology .....	66
III.1 ModelCenter Overview .....	66
III.2 NPSS .....	68
III.2.a. NPSS Overview .....	68
III.2.b. NPSS Elements .....	70
III.2.c. DEAN NPSS Model .....	74
III.3 TDK and Aerospike Nozzle Design Altitude .....	76

	Page
III.3.a. Method of Characteristics Overview.....	76
III.3.b. TDK Overview.....	78
III.3.c. TDK with CEA and Angelino Nozzle Geometry Approximation .....	80
III.3.d. TDK Model with Boundary Layer Approximation .....	83
III.3.e. Correction to TDK Outputs.....	84
III.3.f. Aerospike Design Altitude .....	87
III.4 Description of DEAN ModelCenter Model Elements .....	92
III.4.a. DEAN Model Overview .....	92
III.4.b. Design Variables Assembly .....	94
III.4.c. Linear DEAN Model Assembly .....	97
III.4.d. Nonlinear DEAN Model Assembly .....	100
III.4.e. DEAN Post-Processing Overview .....	106
III.4.f. Fluid Mach Number Calculation .....	107
III.4.g. Cooling Jacket Design .....	108
III.4.h. Material Properties.....	117
III.4.i. Determination of Fluid Phase in Engine.....	123
III.4.j. Structural Jacket Design .....	125
III.4.k. Performance Calculation.....	134
III.4.l. Thrust-to-Weight Calculation .....	141
III.4.m. Rendering Geometry .....	144
III.5 Verification and Validation of the DEAN Model.....	145
III.5.a. Verification and Validation of DEAN Model from Previous Research....	146
III.5.b. Verification and Validation of DEAN Model.....	153
III.6 DEAN Engine Total Mass and Thrust-to-Weight Optimization Process .....	160
IV. Results and Analysis .....	164
IV.1 DEAN Model Variables.....	164
IV.2 DEAN Engine Mass and Thrust-to-Weight Optimization Results .....	165
IV.2.a. Design Variable Limits .....	165
IV.2.b. New DEAN Design Point .....	167
IV.2.c. Influence of Material Selection on Thrust-to-Weight Ratio .....	184
IV.2.d. DEAN Reusability .....	191
IV.2.e. Best Manufacturing DEAN Design .....	193
IV.2.f. Aerospike Nozzle Truncation Study .....	195
IV.3 Final DEAN Design.....	203

	Page
V. Conclusions and Recommendations .....	212
V.1 Research Conclusions .....	212
V.2 Research Significance.....	215
V.3 Recommendations for Future Research.....	215
V.3.a. Recommended Changes to DEAN Model.....	215
V.3.b. Recommended Research Objectives .....	221
V.4 Research Summary .....	222
Appendix A: Lessons Learned.....	223
Appendix B: Material Properties .....	224
B.1. Material Selection .....	224
B.2. Material Density.....	224
B.3. Material Melting Point.....	225
B.4. Material Thermal Conductivity.....	225
B.5. Material Ultimate Tensile and Yield Strength.....	229
Appendix C: NPSS Model .....	233
C.1. NPSS DEAN Model Enhancements .....	233
C.2. NPSS Linear and Nonlinear Model .....	237
C.3. NPSS Variable Sensitivity Analyses .....	240
C.4. Troubleshooting NPSS.....	251
C.5. Simplification to the Execution of the NPSS DEAN Models.....	255
Appendix D: TDK Model .....	257
D.1. TDK Model Comparison .....	257
D.2. TDK Perfect Gas (PFG) Model Sensitivity Analyses.....	265
Appendix E: DEAN Model Code .....	277
References.....	278
VI. Vita.....	282

## List of Figures

	Page
Figure 1. Schematic of DEAN Engine.....	4
Figure 2. Preliminary engine design flowchart.....	16
Figure 3. Common Engine Cycle Schematics .....	18
Figure 4. Combustion Chamber Processes .....	21
Figure 5. Truncated Aerospike Flow Regions .....	31
Figure 6. Solid Model of the Current Aerospike Engine Design.....	31
Figure 7. Exhaust Flow from a Full and Truncated Spike.....	32
Figure 8. Hot Fire Photo of a. SSME and b. J-2T-250K .....	34
Figure 9. Exhaust Flow Along a Truncated Aerospike Nozzle .....	36
Figure 10. Regenerative Cooling Heat Transfer Schematic .....	42
Figure 11. Channel Aspect Ratio .....	47
Figure 12. Cooling Channel Cross-Sectional Design .....	48
Figure 13. Schematic & Solid Model of the DEAN Hydrogen Turbopump Assembly ..	50
Figure 14. Schematic & Solid Model of the DEAN Oxygen Turbopump Assembly.....	51
Figure 15. Reversed Fluid Flow Diagram for Pressure Budget Analysis.....	52
Figure 16. Pintle Injector Design .....	56
Figure 17. DEAN Geometry with Station Numbers.....	60
Figure 18. NPSS Model Schematic .....	74
Figure 19. NPSS Elements at DEAN Stations.....	74
Figure 20. Aerospike Nozzle Geometry Comparison.....	83
Figure 21. Vacuum Performance as a function of <i>O/F</i> .....	91
Figure 22. System Level ModelCenter DEAN Model.....	93
Figure 23. Axial Geometry for Chamber and Aerospike.....	94
Figure 24. “Linear_DEAN_Model” Assembly Components .....	98
Figure 25. “NonLinear_DEAN_Model” Assembly Components .....	100
Figure 26. Nonlinear DEAN Model Subassembly Components .....	101
Figure 27. Nonlinear NPSS Subassembly Components .....	104
Figure 28. “Post_Processing” Assembly Components .....	107
Figure 29. Cooling Jacket and Structural Jacket Cross-Sectional Geometry .....	110
Figure 30. Curved Beam Analysis Diagram.....	111

	Page
Figure 31. Simple Beam Analysis Diagram .....	113
Figure 32. Chamber and Aerospike Pressure Vessel .....	127
Figure 33. Aerospike Bored Hole Geometry .....	132
Figure 34. DEAN Upper Stage Free Body Diagram .....	135
Figure 35. Rendered DEAN Geometry.....	145
Figure 36. Maximum Vacuum Specific Impulse for Varying Expansion Ratios and Chamber Pressures.....	151
Figure 37. Four-Dimensional Parametric Study .....	152
Figure 38. Performance as a function of <i>O/F</i> .....	154
Figure 39. Vacuum Performance Parameters as a Function of Engine Mass Flow .....	155
Figure 40. Engine Throat Area as a Function of Engine Mass Flow.....	157
Figure 41. Vacuum Performance Parameters as a Function of Chamber Length.....	158
Figure 42. Engine Throat Area as a Function of Chamber Length.....	159
Figure 43. Various Plots for Aerospike Radius Trade Study.....	169
Figure 44. Various Plots for Chamber Length Trade Study .....	171
Figure 45. Various Plots for Engine Mass Flow Trade Study .....	172
Figure 46. Influence of Chamber Radius on Vacuum Specific Impulse .....	176
Figure 47. Influence of Design Variables on Vacuum Specific Impulse .....	178
Figure 48. <i>T/W</i> and Vacuum Specific Impulse of Potential DEAN Designs.....	179
Figure 49. Maximum Hydrogen and Oxygen Fluid Temperatures of Potential DEAN Designs.....	180
Figure 50. Truncated DEAN Design Meeting Performance Design Goals .....	182
Figure 51. Influence of Material Selection on <i>T/W</i> for DEAN Engine Components ....	185
Figure 52. Engine Component Most Influencing <i>T/W</i> .....	188
Figure 53. Influence of Material Selection on Cooling Jacket Wall Temperature .....	189
Figure 54. Influence of Structural Jacket Material on <i>T/W</i> Using Material Ultimate Tensile Strength .....	190
Figure 55. Influence of Structural Jacket Material on <i>T/W</i> Using Material Yield Strength.....	192
Figure 56. Influence of Aerospike Nozzle Truncation on Chamber Pressure .....	196
Figure 57. Influence of Aerospike Nozzle Truncation on Throat Area .....	196
Figure 58. Influence of Aerospike Nozzle Truncation on Vacuum Thrust .....	197
Figure 59. Influence of Aerospike Nozzle Truncation on Vacuum Specific Impulse... 197	197
Figure 60. Influence of Aerospike Nozzle Truncation on Aerospike Mass .....	199

	Page
Figure 61. Influence of Aerospike Nozzle Truncation on Total Engine Weight.....	199
Figure 62. Influence of Nozzle Truncation on Aerospike Components' Mass .....	200
Figure 63. Influence of Aerospike Nozzle Truncation on <i>T/W</i> .....	202
Figure 64. Final DEAN Design Fluid Profiles.....	206
Figure 65. Chamber and Aerospike Hot and Cold Wall Temperature Profile.....	207
Figure 66. Cooling Jacket Fluid Mach Number.....	208
Figure 67. Rendered Final DEAN Geometry .....	211
Figure 68. NPSS Chamber Temperature Input Sensitivity.....	243
Figure 69. TDK Model Comparison of Nozzle Geometry .....	259
Figure 70. Aerospike Nozzle Geometry for a) PFG and b) Kinetic TDK Models .....	260
Figure 71. Magnified Aerospike Nozzle Geometry Comparison at Spike Tip.....	261
Figure 72. Aerospike Nozzle Pressure Profile Comparison Run #1.....	261
Figure 73. Aerospike Nozzle Pressure Profile Comparison Run #2.....	262
Figure 74. Aerospike Nozzle Pressure Profile Comparison Run #3.....	263
Figure 75. Influence of <i>THETA</i> on Aerospike Nozzle Geometry.....	267
Figure 76. Influence of <i>THETA</i> on the Nozzle Pressure Profile.....	268
Figure 77. Influence of <i>THETA</i> on Nozzle Pressure Thrust .....	268
Figure 78. Influence of <i>THETA</i> on Nozzle Performance.....	269
Figure 79. Influence of TDK VSJ Input on Nozzle Geometry .....	271
Figure 80. Influence of TDK VSJ Input on the Nozzle Pressure Profile .....	271
Figure 81. Influence of TDK VSJ Input on Nozzle Pressure Thrust .....	272
Figure 82. Influence of TDK VSJ Input on Engine Mass Flow Rate .....	272
Figure 83. Influence of Chamber Pressure TDK Input on Nozzle Geometry .....	274
Figure 84. Influence of Chamber Pressure TDK Input on Engine Mass Flow Rate .....	275
Figure 85. Influence of Chamber Pressure TDK Input on Nozzle Pressure Profile.....	275

## List of Tables

	Page
Table 1. Existing Liquid Oxygen/Liquid Hydrogen Upper Stage Engines .....	7
Table 2. Liquid Oxygen/Liquid Hydrogen Upper Stage Engines Under Development.....	9
Table 3. Liquid Hydrogen and Liquid Oxygen Propellant Characteristics .....	25
Table 4. DEAN Design Parameters from Martin.....	61
Table 5. Turbopump Parameters.....	63
Table 6. DEAN Design Parameters from Simmons .....	65
Table 7. Angelino Nozzle Geometry .....	88
Table 8. Comparison of Performance Parameters due to Expansion Ratio .....	89
Table 9. Materials Compatible with Engine Components .....	120
Table 10. Engine Components Where Fluid Phase Evaluated .....	124
Table 11. Propellant Critical Points .....	124
Table 12. Pressure Thrust Comparison.....	140
Table 13. Default Design Variables.....	141
Table 14. Design Variables from Martin .....	147
Table 15. Vacuum Specific Impulse Comparison .....	148
Table 16. Vacuum Thrust Comparison.....	149
Table 17. DEAN Model Set Variables .....	164
Table 18. DEAN Variable Ranges.....	167
Table 19. Engine Components and Material Selection.....	168
Table 20. DEAN Design Meeting Performance Design Goals.....	182
Table 21. Final DEAN Design Variables .....	184
Table 22. Material Selection for Maximum and Minimum <i>T/W</i> .....	186
Table 23. Component Weight and Percent Component Weight to Total Engine Weight for Different Material Selections .....	187
Table 24. Impact of Material Strength on <i>T/W</i> .....	192
Table 25. Impact of Material Strength on <i>T/W</i> .....	194
Table 26. DEAN Turbopump Parameters.....	204
Table 27. Engine Component Mass .....	204
Table 28. Individual Thrust Components .....	209
Table 29. Aerospike and Bell Nozzle Comparison.....	210

	Page
Table 30. <i>O/F</i> Study Evaluating NPSS Chamber Pressure Input Sensitivity .....	241
Table 31. Engine Mass Flow Rate Study Evaluating NPSS Chamber Pressure Input Influence .....	241
Table 32. NPSS Output Comparison of Maximum Wall Temperature Inputs .....	245
Table 33. NPSS Output Comparison of Range of Maximum Wall Temperature Inputs	246
Table 34. NPSS Output Comparison of Various Maximum Wall Temperature Inputs .	248
Table 35. Influence of Percent Oxygen Bypassing Turbine on Specific NPSS Outputs	250
Table 36. Comparison of Linear and Nonlinear NPSS Model Outputs.....	256
Table 37. VSJ Sensitivity Analysis Design Variables .....	265
Table 38. Chamber Pressure Sensitivity Analysis Design Variables. ....	273

## List of Symbols

### Symbol

$A$	Cross-Sectional Area
$a$	Half-Spacing between Coolant Channels or Throat Speed of Sound
$A_{base}$	Truncated Aerospike Base Cross-Sectional Area
$A_e$	Nozzle Exit Area
AR	Cooling Channel Aspect Ratio
$A_s$	Surface Area
$A_t$ or $A^*$	Throat Cross-Sectional Area
$a_{tx}$	Semi-major Axis of the Orbit Ellipse
$a_w$	Coolant Channel Width
$b$	Coolant Channel Length
$c^*$	Characteristic Velocity
$c_F$	Thrust Coefficient
$c_i, c_o$	Distance from Neutral Axis to Inner and Outer Fibers
$c_p$	Constant Pressure Specific Heat
$D$	Diameter of Combustion Chamber or Cooling Channel
$D_{ch}$	Coolant Channel Hydraulic Diameter
$d_i$	Pipe Inner Diameter
$d_o$	Pipe Outer Diameter
$dr$	Differential Aerospike Radius
$dx$	Differential Aerospike Length
$e$	Distance from Centroidal Axis to Neutral Axis
$F$	Total Thrust
$F_{corr}$	Corrected Pressure Thrust Acting on Aerospike Nozzle or Cowl
$F_{cowl}$	Thrust acting on Chamber Exit Lip
$F_{nondesign}$	Thrust Component Due to Operation in Other than Design Conditions
$F_{TDK}$	TDK Pressure or Cowl Thrust
$f(x)$ or $r$	Aerospike Radius
$f'(x)$ or $r'$	Slope of Aerospike Wall at Location x
$G$	Average Mass Flow Rate through Channel per Unit Area
$g_o$	Gravity Constant
$h$	Height of cooling channel or Convection Heat Transfer Coefficient
$h_A$	Altitude of Orbit A
$h_B$	Altitude of Orbit B
$H_p$	Pump Head Pressure Rise
$I$	Second Moment of Inertia
$i$	Orbit $i$ or Identified to Point Located on Aerospike Nozzle
$I_{sp}$	Specific Impulse
$k$	Thermal Conductivity
K	Pressure Loss Coefficient or K-Factor
$L$	Aerospike Length
$L^*$	Characteristic Length
$l$	Total Piping Length

$M$	Mach Number or Bending Moment
$M^*$	Fluid Mach Number at the Throat
$m$	Mass or Nozzle Slope
$\dot{m}$	Engine Mass Flow Rate or Mass Flow Rate through the Rocket
$M_e$	Exit Mach Number
$m_f$	Final Stage Mass
$m_i$	Initial Stage Mass
$\dot{m}_{TDK}$	TDK Output Engine Mass Flow Rate
$m_{tp}$	Mass of the Turbopump
$N_r$	Pump Rotational Speed.
$p^*$	Throat Pressure
$p_a, P_{amb}, P_{inf}$	Ambient or Atmospheric Pressure
$P_{available}$	Turbine Power Available
$p_{base}$	Truncated Aerospike Base Pressure
$P_c$ or $p_c$	Chamber Pressure
$P_{chan}$	Cooling Channel Pressure
$p_{dA}$	Pressure acting on Nozzle at Differential Cross-Sectional Area
$p_e$	Nozzle Exit Pressure
$p_o, p_i$	Outer and Inner Pressure Vessel Pressure
$P_{req}$	Pump Power Required
$p_{trat}$	Turbine Pressure Ratio
$P_x$	Static Pressure at x-coordinate on Aerospike
$q$	Heat Flux
$\dot{q}$	Heat Transfer per Unit Area
$\dot{Q}$	Heat Transfer Rate
$\dot{Q}_{in}$	Heat Flow In to System
$\dot{Q}_{out}$	Heat Flow Out of System
$R$	Exhaust Gas Constant
$r^*$	Aerospike Radius at the Throat
$Ratio$	TDK Correction Ratio
$r_{base}$	Radius of Truncated Base
$r_c^*$	Radius of Chamber Exit Lip at Throat
$R_{cent}$	Radius of Centroidal Axis
$r_i$	Orbit $i$ Radius from Center of Earth
$r_i, r_o$	Radius of Inner and Outer Wall Fibers
$r_n$	Radius of Neutral Axis
$SA$	Surface Area of Heat Exchange
$t$ or $h$	Cooling Channel Wall Thickness
$T_c$	Combustion Chamber or Flame Temperature
$T_{cl\_in}$	Incoming Coolant Temperature
$T_{cl\_out}$	Outgoing Coolant Temperature
$T_{cw}$	Cooling Channel Inner “Cold” Wall Temperature
$T_{hg}$	Hot Gas Mixture Temperature
$T_{hw}$	Cooling Channel Outer “Hot” Wall Temperature
$t_{SJ}$	Structural Jacket Thickness

$u_e$	Nozzle Equivalent Exit Velocity
$V$	Pipe Volume
$v$	Flow Velocity
$v^*$	Throat Velocity
$v_i$	Spacecraft Velocity at $r_i$
$v_{txi}$	Orbit $i$ Transfer Velocity
$W$	Weight
$w$	Cooling Channel Half-Width or Weight Flow Rate
$x$	Aerospike Axial Length

### Greek Symbols

$\gamma$	Exhaust Ratio of Specific Heats
$\Delta h$	Change in Enthalpy
$\Delta l$	Wall Thickness
$\Delta P$	Pressure Drop
$\Delta p_{dynamic}$	Dynamic Pressure Loss
$\Delta p_p$	Pump Pressure Rise
$\Delta v$	Change in Velocity
$\Delta v_i$	Change in Velocity at Orbit $i$
$\varepsilon$	Nozzle Expansion or Area Ratio
$\varepsilon_s$	Surface Emissivity
$\eta_{c*}$	$c^*$ Combustion Efficiency
$\eta_p$	Pump Efficiency
$\eta_T$	Turbine Efficiency
$\theta$	Throat Flow Angle or Flow Angle with respect to Symmetrical Axis
$\lambda$	Nozzle Efficiency
$\mu$	Dynamic Viscosity or Mach Angle
$\mu_s$ or GM	Earth's Gravitational Constant
$\nu$	Prandtl-Meyer Function
$\pi$	Pi
$\rho$	Density
$\sigma_b$	Bending Stress
$\sigma_i, \sigma_o$	Inner and Outer Surface Bending Stresses
$\sigma_r$	Radial Pressure Vessel Stress
$\sigma_s$	Stefan-Boltzmann Constant
$\sigma_t$	Tangential Pressure Vessel Stress
$\tau$	Pump Shaft Torque
$\tau_{max}$	Maximum Shear Stress

### Units of Measure

BTU	British Thermal Unit
cm	centimeter
ft	foot or feet
hp or HP	Horsepower

hr	Hour
Hz	Hertz
in	Inch
J	Joule
K	Kelvin
kg	kilogram
km	kilometers
kN	kilo-Newton
lb	Pound
lb <sub>f</sub>	Pound-Force
lb <sub>m</sub>	Pound-Mass
lb-mol	Pound-Mole
m	Meter
Mol	Mole
Pa or MPa	Pascal or Mega-Pascal
psi	Pounds per Square Inch
psia	Pounds per Square Inch Absolute
R	Rankine
RPM or rpm	Revolutions per Minute
sec or s	Seconds
W, kW, MW	Watt, kilo-Watt, Mega-Watt

## List of Abbreviations

### Abbreviation

AFIT	Air Force Institute of Technology
AFRL	Air Force Research Laboratory
AIAA	American Institute of Aeronautics and Astronautics
CALVEIN	California Launch Vehicle Education Initiative
CEA	Chemical Equilibrium with Applications
CSULB	California State University, Long Beach
DEAN	Dual-Expander Aerospike Nozzle
DoD	Department of Defense
DOE	Design of Experiments
GEO	Geosynchronous Orbit
GSC	Garvey Spacecraft Corporation
H <sub>2</sub>	Hydrogen
HEE	Hydrogen Environment Embrittlement
IHPRPT	Integrated High Payoff Rocket Propulsion Technology Program
JANNAF	Joint Army-Navy-NASA-Air Force
LEO	Low-Earth Orbit
LH <sub>2</sub> or LH <sub>2</sub>	Liquid Hydrogen
LOX	Liquid Oxygen
MABL	Mass Addition Boundary Layer
MINF	Freestream Mach Number
MOC	Method of Characteristics
MP	Number of Points on the Initial Line
MSJ	Throat Fluid Mach Number
NASA	National Aeronautics and Space Administration
NLV	Nanosat Launch Vehicle
NPSS	Numerical Propulsion System Simulation
O/F	Propellant Mixture Ratio (Oxidizer-to-Fuel Ratio)
O <sub>2</sub>	Oxygen
ODE	One-Dimensional Equilibrium
ODK	One-Dimensional Kinetic
PFG	TDK Perfect Gas Model
PINF	Freestream or Ambient Pressure
RMAX	Normalized Radius at the Nozzle Exit Plane
RWTD	Normalized Wall Throat Radius of Curvature Ratio
SCAP	Spray Combustion Analysis
SCC	Stress Corrosion Cracking
SEA	Software and Engineering Associates, Inc.
SI	International System of Units
SLV	Small Launch Vehicle
SSME	Space Shuttle Main Engine
SSTO	Single-stage-to-orbit
T/W	Thrust-to-Weight Ratio
TDE	Two-Dimensional Equilibrium

TDF	Two-Dimensional Frozen
TDK	Two-Dimensional Kinetic
TDK'04 or TDK	Two-Dimensional Kinetics '04
<i>THALW</i>	Axial Cowl Length Normalized by the Throat Radius
<i>THE</i>	Nozzle Exit Angle
<i>THETA</i>	Nozzle Attachment Angle
TRANS	Transonic
V&V	Verification and Validation
VSJ	Throat Fluid Velocity

# OPTIMIZED DUAL EXPANDER AEROSPIKE ROCKET

## I. Introduction

For decades, the United States Air Force has made use of space assets to assist in achieving its mission “to fly, fight, and win in air, space and cyberspace” [1]. The Air Force currently utilizes space for multiple purposes such as, but not limited to, space surveillance, global positioning, communications, and meteorology applications. In order to achieve the mission of the Air Force, scientists and engineers must figure out how to get a spacecraft designed for a specific purpose into the required orbit. A launch vehicle designed with a powerful engine is the answer.

During the 20<sup>th</sup> century, scientists and engineers designed multiple propulsion concepts for various missions from first stage boost to upper stage orbit transfer. Encompassing multiple missions, the bell nozzle combustion rocket engine design quickly became the engine of choice and the engine continues to dominate today. Reasons for the dominance of the bell nozzle include simplicity, manufacturability, and mission effectiveness. Despite the advantages, the bell nozzle does not optimally operate at all altitudes of flight. Furthermore, for high altitude and orbit transfer missions, the bell nozzle performs best with a high exit-to-throat area ratio, resulting in a long, heavy nozzle. An aerospike nozzle design is the answer to the disadvantages of the bell nozzle. The aerospike nozzle has better performance over the entire flight compared to the bell nozzle design. In addition, the design can decrease engine size and weight using a truncated aerospike nozzle with minimal performance losses.

The Department of Defense (DoD), the National Aeronautics and Space Administration (NASA) and rocket propulsion industry began execution of an initiative

in 1996 known as the Integrated High-Payoff Rocket Propulsion Technology program (IHPPT) [2]. The initiative focused on doubling the rocket propulsion capability of the United States by 2010 using a baseline of 1993 technology. Boost, orbit transfer, and spacecraft propulsion systems were each assigned specific goals.

The Phase III goals for liquid propellant orbit transfer propulsion systems are:

- Improve specific impulse ( $I_{sp}$ )
- Improve thrust-to-weight ( $T/W$ )
- Reduce support costs and hardware costs
- Reduce the stage failure rate

The first two goals are the focus of the current research effort. Meeting the first two performance goals result in a 22% increase in payload mass and a 33% reduction in launch cost for an expendable launch vehicle [2].

IHPPT was scheduled for completion in 2010; however, the desired goals were not met. The government has decided to extend the program to 2012 [3].

The current research effort will focus on the optimization of an upper stage aerospike nozzle engine design to meet the IHPPT Phase III goals. The best feature of the aerospike nozzle is its altitude compensation capability when operating in the atmosphere. In vacuum conditions, the aerospike nozzle behaves much like a conventional bell nozzle losing its altitude compensation capability. Consequently, the benefit of an upper stage aerospike nozzle is a shorter and lighter engine compared to a conventional bell nozzle with equivalent performance.

## I.1 DEAN Model Background and Basic Concept

A dual-expander aerospike nozzle (DEAN) computational model was completed by 2Lt David F. Martin in 2008 to demonstrate the feasibility of the DEAN design [4]. Martin chose to design an upper stage engine to meet the IHPRT Phase III orbit transfer vehicle goals at a single design point. J. Simmons enhanced the research performed by Martin by creating a system level model for evaluation of the solution space. Simmons modified the DEAN model by defining geometry as a variable for optimization studies. Furthermore, Simmons ran parametric trade studies of the solution space identifying a better starting design point for future optimization studies [5, 6]. The current research effort will further evaluate the solution space in an attempt to complete system-level optimization of the DEAN design.

The DEAN utilizes liquid hydrogen (LH<sub>2</sub>) and liquid oxygen (LOX) as the fuel and oxidizer, respectively. The engine design differs from other cryogenic upper stage engines in two ways. First, the engine utilizes separate expander cycles for the oxidizer and fuel. Second, the engine utilizes an aerospike nozzle.

In a traditional expander cycle, the fuel alone regeneratively cools the combustion chamber and nozzle. The heat transferred to the fuel from cooling provides enough power to the turbine to power both the fuel and oxidizer pumps prior to the injection of the fuel into the combustion chamber. The DEAN employs an oxidizer expander cycle to drive the oxidizer pump and similarly a fuel expander cycle to drive the fuel pump. The fuel and oxidizer remain physically separated until injection into the combustion chamber, eliminating the need of interpropellant seals; failure of these seals is the critical catastrophic failure mode in traditional expander cycle engines [4].

Inspired by Simmons [5], Figure 1 is a sketch of the two expander cycles with the red dotted loop representing fuel flow and the blue loop representing oxidizer flow. The propellant first travels from the propellant tank through the pump. The pump then delivers the propellant to the cooling jacket where the propellant gains energy from regenerative cooling of the combustion chamber (oxygen) or aerospike (hydrogen). The cooling jacket also keeps the combustion chamber and aerospike temperatures below structural thermal limits. The additional energy in the propellant from regenerative cooling drives the turbine/expander cycle. From the turbine, the propellant travels to the injectors and into the combustion chamber for combustion. Lastly, the combusted products (exhaust) expand against the aerospike to produce the desired thrust. Currently, a small percentage of the warm oxygen (~10%) bypasses the turbine to the injectors to control and balance the engine cycle.

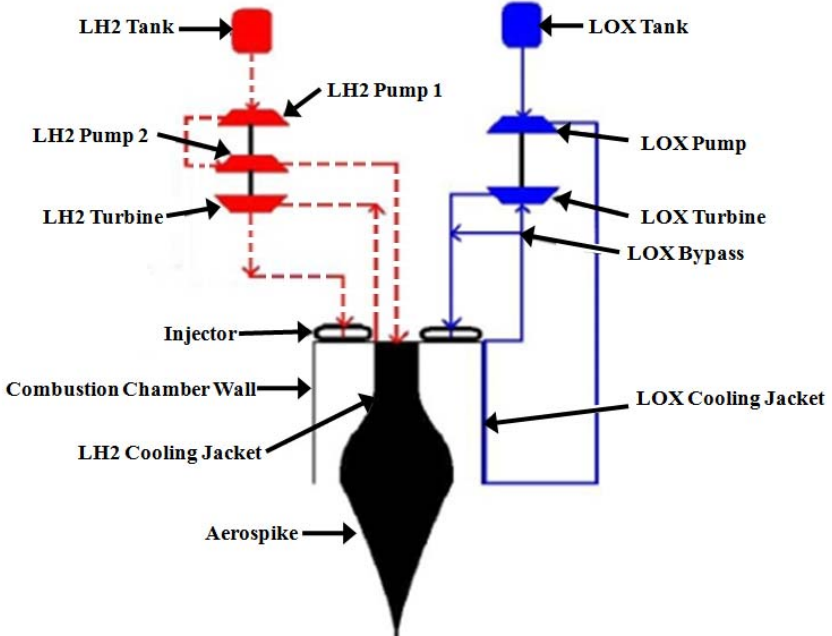


**Figure 1. Schematic of DEAN Engine; inspired by Simmons [5]**

The DEAN nozzle is an annular aerospike nozzle, also known as a radial in-flow plug nozzle. An annular aerospike nozzle contains a longitudinally elongated annulus forming a cylinder (the combustion chamber) with a specially designed spike in the center of it. The aerospike nozzle can operate near optimally at all altitudes below or at its design altitude. More specifically, the aerospike can compensate for changes in altitude and ambient conditions, meaning the aerospike nozzle will not suffer from the same overexpansion losses a bell nozzle suffers [8]. Above its design altitude, the aerospike nozzle behaves more like a conventional bell nozzle. For orbit transfer missions, rocket engines require a high expansion ratio increasing the length and mass of a traditional bell nozzle. The aerospike nozzle will be shorter and lighter than a bell nozzle with equivalent performance, especially if the aerospike nozzle is truncated. Previous research utilized the full aerospike nozzle length to explore highest achievable specific impulse performance; however, Martin did show performance degradation is limited with a truncated spike [4].

## I.2 Research Objectives

The current research effort will focus on system-level design optimization of the upper stage DEAN design by pursuing the following objectives to meet the IHPRT Phase III orbit transfer vehicle goals:

1. Design a tool to optimize weight of the DEAN engine and its components, including capability to evaluate nozzle truncation.
2. Design a tool to allow exploration of the solution space.
3. Identify critical technologies/limits relevant to the optimized DEAN model.

The final DEAN design should achieve, at a minimum, the following design goals:

1. 50,000 lb<sub>f</sub> (222.4 kN) of vacuum thrust
2. 464 sec of vacuum specific impulse ( $I_{sp}$ )
3. Thrust-to-weight ratio of 106.5
4. Reusable

Designing the engine to be reusable allows the engine to be robust against testing. The current research effort defines wall temperature and material strength as reusability constraints.

Computational tools are required to meet the objectives. The current research effort will utilize ModelCenter<sup>TM</sup> by Phoenix Integration, Numerical Propulsion System Simulation (NPSS<sup>TM</sup>) by NASA, Two-Dimensional Kinetics '04 (TDK'04<sup>TM</sup>) by Software and Engineering Associates, Inc. (SEA), and Chemical Equilibrium with Applications (CEA<sup>TM</sup>) by NASA. ModelCenter, containing an integrated computer model of multiple software programs and coding scripts, automates DEAN parametric trade and optimization studies. NPSS calculates the performance of individual DEAN components (i.e. turbopumps, cooling channels, and combustion chamber) and converges the two expander cycles to a valid design point. TDK'04 performs axisymmetric method of characteristics (MOC) calculations for aerospike nozzle geometry and CEA is required to perform chemistry calculations as an input into TDK'04.

## II. Theory and Previous Research

Chapter II serves to present the basic scientific theory involved in rocket engine design, the latest aerospike nozzle developments, and past DEAN research.

### II.1 Orbit Transfer Engines and Previous Aerospike Engines

#### II.1.a. Orbit Transfer Engines

There are varieties of liquid oxygen (LOX) and liquid hydrogen (LH<sub>2</sub>) upper stage engines currently in use around the world; Table 1 tabulates these engines with comparable performance specifications.

**Table 1. Existing Liquid Oxygen/Liquid Hydrogen Upper Stage Engines; based on Baker [9]**

Engine	RL10B-2	RL10A-4-2	CE-20	LE-5B	HM-7B	YF-75
Launch Vehicle	Delta IV	Atlas V - Centaur	GSLV	H-IIA	Ariane 5	Long March 3A (CZ-3A)
Country	USA	USA	India/ Russia	Japan	France	China
Vacuum Thrust	24,729 lb <sub>f</sub> (110 kN)	22,301 lb <sub>f</sub> (99.2 kN)	17,086 lb <sub>f</sub> (76 kN)	30,866 lb <sub>f</sub> (137.3 kN)	14,006 lb <sub>f</sub> (62.3 kN)	17,625 lb <sub>f</sub> (78.4 kN)
Vacuum Specific Impulse (sec)	465.5	450.5	450	447	446.1	442
Weight	583.12 lb (264.5 kg)	370.38 lb (168 kg)	--	628.32 lb (285 kg)	341.72 lb (155 kg)	--
Thrust-to-Weight Ratio	42.41	60.21	--	49.12	40.99	--

The thrust-to-weight ratio for each engine was calculated by dividing the thrust by the engine weight. The average vacuum thrust is 21,102 lb<sub>f</sub> (93.87 kN), the average vacuum  $I_{sp}$  is 450.2 sec, and the average vacuum thrust-to-weight (T/W) ratio is 48.18 for

operational LH<sub>2</sub>/LOX upper stage engines. *T/W* data for the CE-20 and YF-75 could not be verified.

In order to satisfy research goals, the DEAN needs to achieve a vacuum thrust of 50,000 lb<sub>f</sub>, a vacuum *I<sub>sp</sub>* of 464 sec, and a *T/W* of 106.5. Compared to current operational engines, the result is a 3.1% increase in *I<sub>sp</sub>* and a 121.2% increase in *T/W* for the DEAN design. Equation 1 calculates the percent increase.

$$\% \text{ Increase} = \frac{\text{DEAN Value} - \text{Current Average Value}}{\text{Current Average Value}} \times 100 \quad (1)$$

Table 2 tabulates other engines currently under development and their specifications. The RL-60 and MB-60 are currently under development for use on the Evolved Expendable Launch Vehicle (EELV) family, including both the Delta IV and the Atlas V. The upper stage engines in Table 2 provide an average vacuum *I<sub>sp</sub>* and *T/W* of 463.5 sec and 58.97, respectively. These values are extremely close to the goals of the DEAN, except the *T/W* goal for the DEAN represents approximately an 81% increase. The purpose of Table 2 is to show the DEAN is competitive with similar LOX/LH<sub>2</sub> upper stage engines currently under development. However, the primary focus of the DEAN design is to meet the IHPRT Phase III goals.

**Table 2. Liquid Oxygen/Liquid Hydrogen Upper Stage Engines Under Development**

Engine	Vinci [10, 11]	RD-0146 [10]	RL-60 [12]	MB-60 [12]
<b>Launch Vehicle</b>	Ariane 5	Onega/Proton/ Angara	EELV	EELV
<b>Country</b>	France/Germany	Russia	USA	USA
<b>Vacuum Thrust</b>	40,466 lb <sub>f</sub> (180 kN)	22,054 lb <sub>f</sub> (98.1 kN)	60,000 lb <sub>f</sub> (266.9 kN)	60,000 lb <sub>f</sub> (266.9 kN)
<b>Vacuum Specific Impulse (sec)</b>	464	463	460	467
<b>Weight</b>	617.29 lb (280 kg)	573.2 lb (260 kg)	700 lb (317.5 kg)	1300 lb (589.7 kg)
<b>Thrust-to-Weight Ratio</b>	65.54	38.48	85.71	46.15

### *II.1.b. Previous Aerospike Engines*

Four major aerospike engines have been built and tested on a test stand, with two of the four flight tested; the J-2T, the XRS-2200 (Linear Aerospike), the solid propellant Optimal 168 rocket with an aerospike nozzle, and the California Launch Vehicle Education Initiative (CALVEIN) Prospector liquid rocket engine. The Prospector rocket engine and the Optimal 168 rocket with an aerospike nozzle are the only flight tested aerospike engines. This section serves to provide a brief synopsis of each engine to reveal past and current use of aerospike engines.

In the 1960's, Pratt and Whitney Rocketdyne designed two liquid oxygen/liquid hydrogen toroidal aerospike plug nozzle versions of the J-2 Saturn V second and third stage engine; the J-2T-200K and J-2T-250K [13, 14]. The goal was to test the aerospike design and compare the results to the operational J-2 engine. The J-2T-250K is the larger of the two engines with a design performance of 249,898 lb<sub>f</sub> (1,111.6 kN) vacuum thrust and a vacuum  $I_{sp}$  of 435 sec [13]. Neither of the two J-2T designs entered production.

During the 1990's, revived work from the J-2T aided in the development of the XRS-2200, the propulsion system for NASA's X-33 single-stage-to-orbit (SSTO) launch vehicle and Lockheed Martin's proposed VentureStar. The liquid hydrogen/liquid oxygen linear aerospike operated at a sea-level thrust of 206,800 lbf (919.9 kN) and a sea-level specific impulse of 332 seconds [12]. Acceptance testing of two flight engines was about to begin when NASA and Lockheed Martin decided to cancel the program. However, prior to program cancelation, ground tests were able to prove the linear aerospike design was feasible.

The solid propellant Optimal 168 rocket with aerospike nozzle was designed, ground tested, and flight tested by a joint effort between NASA, Air Force, blacksky Corporation, and Cesaroni Technology/Cesaroni Aerospace. The research resulted in the first known set of transonic flight performance data for solid rocket engines with aerospike nozzles. Two aerospike engines and a conventional bell nozzle engine were tested and compared. Even though the solid propellant mixture was the same, data from the flight tests showed the chamber pressures and thrusts were lower for the aerospike engines than for the conventional engine. Furthermore, the test data led to computed nozzle efficiencies for the aerospike engines greater than one. Bui *et al.* believe the high nozzle efficiencies occurred due to a larger actual aerospike nozzle throat area than originally designed [15]. The increase in actual throat area may have occurred due to bad manufacturing and/or assembly tolerances, increased nozzle erosion rates, and/or possible "expansion of the aerospike external cowl structure under loads during motor firing" [15]. The research effort also documented the aerospike engines were significantly louder than the conventional engine at launch; the engine noise is probably inherent to all

aerospike nozzle designs. Bui *et al.* concluded their research with recommendations for future work in first pinpointing the lower aerospike chamber pressure and thrust cause and then conducting more complex flight tests [15]. Solid motor aerospike engines have also been ground tested and documented by Johnson and Leary [16].

CALVEIN is a partnership between California State University, Long Beach (CSULB) and Garvey Spacecraft Corporation (GSC) initiated in 2001. In September 2003, CALVEIN launched the P-2B launch vehicle with a 1000 lb<sub>f</sub> (4.4 kN) thrust LOX/ethanol aerospike engine, known as Prospector, historically marking the first flight test of a liquid propellant aerospike engine. CALVEIN has since advanced the aerospike engine to include ten thrust cells, each operating at a higher expansion ratio and producing 1,000 lb<sub>f</sub> thrust. CALVEIN is continuing to improve its aerospike engine for use on their Nanosat Launch Vehicles (NLV) and Small Launch Vehicles (SLV), all the while giving learning opportunities to CSULB engineering students [17].

## **II.2 Mission Requirements**

Clear and obtainable goals are required prior to launching a rocket with a payload into space. What is the purpose of the payload? What orbit does the payload need to be in to accomplish its purpose? These questions relate to the mission of the payload.

The mission of the DEAN engine is to propel a specific payload from low-earth orbit (LEO) to geosynchronous orbit (GEO), known as orbit transfer. Another name for an orbit transfer vehicle is an upper stage engine. To get to LEO, a multi-stage booster propels the upper stage and payload together from the surface of the earth. Once in LEO, the booster separates allowing the upper stage to place the payload into GEO. It typically

takes two burns to place a spacecraft in GEO from LEO; one burn to enter a transfer orbit and a second burn to circulize and, if required, change the orbit plane to the required GEO orbit. The second burn typically takes place at the apogee of the transfer orbit to save fuel mass. It is possible for a launch vehicle to place the upper stage and payload directly into a transfer orbit; however, doing so will lead to an extremely small launch window minimizing launch opportunities.

GEO is approximately 22,280 miles (35,856 kilometers) above the surface of the earth. A spacecraft in GEO has an orbit period equal to the rotation period of the earth (approximately 24 hours), allowing the spacecraft to remain approximately fixed above a location on the surface of the earth. When the orbit of the spacecraft is fixed directly above the equator (zero degree inclination), the orbit is referred to as geostationary. GEO and geostationary orbits are important for spacecraft missions such as communications, early warning, nuclear event detection, and weather [18, 19].

Part of the mission is to calculate the required change in velocity ( $\Delta v$ ) to place a specific payload mass into a desired orbit; the ideal rocket equation as stated in equation 2 does this [20]:

$$\Delta v = I_{sp} g_o \ln\left(\frac{m_i}{m_f}\right) \quad (2)$$

where

- $\Delta v$  = Change in Velocity (ft/s)
- $I_{sp}$  = Specific Impulse (seconds)
- $g_o$  = Gravity Constant (32.2 ft/s<sup>2</sup> or 9.81 m/s<sup>2</sup>)
- $m_i$  = Initial Stage Mass (lb<sub>m</sub>)
- $m_f$  = Final Stage Mass (lb<sub>m</sub>)

The ideal rocket equation can calculate a total vehicle change in velocity or a change in velocity for a single stage. The initial mass is the sum of the stage structural mass, propellant mass and payload mass. The final mass is the stage structural mass and payload mass. Payload mass is considered any mass above the stage in question. The ideal rocket equation shows improvement in specific impulse will equate to a higher change in velocity. Also, if the stage structural mass is decreased, then there will also be an improvement in  $\Delta v$ .

An estimated  $\Delta v$  can be calculated for the DEAN's orbit transfer mission using equations from Humble *et al.* [20]. Metric units will be used for the calculation and then converted back to imperial units at the end. To begin, assume a boost rocket placed the upper stage and payload in a circular LEO orbit at an altitude ( $h_A$ ) of 185 km (114.95 miles). The upper stage will transfer the payload to a circular GEO orbit ( $h_B$ ) at an altitude of 35,856 km (22,279.89 miles), assuming no inclination change is required. The following relationship can calculate the velocity of a spacecraft at a certain orbit ( $i$ ):

$$v_i = \sqrt{\frac{\mu_s}{r_i}} \quad (3)$$

where

$$\begin{aligned} v_i &= \text{Spacecraft Velocity at } r_i \text{ (miles/s or km/s)} \\ \mu_s &= \text{Earth's Gravitational Constant (GM)} = 398,600.5 \text{ km}^3/\text{s}^2 \\ r_i &= \text{Orbit } i \text{ Radius from Center of Earth (km)} \end{aligned}$$

The orbit radius is equal to the orbit altitude plus the radius of the earth (6,378.14 km). Using equation 3, the velocity a spacecraft travels at  $h_A$  and  $h_B$  equals 7.793 km/s and 3.072 km/s, respectively.

To calculate the velocity required by the upper stage to transfer the payload to GEO, a transfer method has to be assumed. For this scenario, assume a Hohmann transfer, the most efficient transfer method between two circular, coplanar orbits [20]. There are two transfer velocities: one to initiate the transfer and one to circulize the payload at GEO. Equation 4 calculates the transfer velocity:

$$v_{txi} = \sqrt{\frac{2GM}{r_i} - \frac{GM}{a_{tx}}} \quad (4)$$

where

$$\begin{aligned} v_{txi} &= \text{Orbit } i \text{ Transfer Velocity (miles/s or km/s)} \\ a_{tx} &= \text{Semi-major Axis of the Orbit Ellipse } (= \frac{r_A+r_B}{2}) \text{ (km)} \end{aligned}$$

From equation 4, the transfer velocities  $v_{txA}$  and  $v_{txB}$  for a spacecraft are equal to 10.253 km/s and 1.593 km/s respectively.

The following relationship calculates the change in velocity at each orbit:

$$\Delta v_i = |v_{txi} - v_i| \quad (5)$$

where

$$\Delta v_i = \text{Change in Velocity at Orbit } i \text{ (km/s)}$$

From equation 5,  $\Delta v_A$  and  $\Delta v_B$  are equal to 2.460 km/s and 1.479 km/s, respectively. Therefore, the total  $\Delta v$  to be used in the rocket equation for the DEAN is equal to the sum of  $\Delta v_A$  and  $\Delta v_B$ . The total  $\Delta v$  equals 3.939 km/s (2.448 miles/s) not accounting for any losses occurring during orbit transfer or any orbit inclination changes.

If the launch vehicle placed the spacecraft at an orbit inclination of  $28^\circ$  and the mission orbit required a  $0^\circ$  inclination (geostationary orbit), the upper stage would need an additional  $\Delta v$  to perform the inclination change. The  $28^\circ$  orbit inclination references a

launch from Cape Canaveral, Florida and the  $0^{\circ}$  orbit inclination references an equatorial orbit. The most efficient method for an orbit inclination change is to combine it with the “tangential burn at apogee of the transfer orbit” leading to an increased  $\Delta v_B$  [20]. Using the law of cosines, the new  $\Delta v_B$  equals 1.826 km/s. The total  $\Delta v$  assuming no losses with an orbit inclination change equals 4.286 km/s (2.663 miles/s)

The DEAN upper stage needs to provide at least a  $\Delta v$  equivalent to 2.448 miles/s to deliver a payload from LEO to GEO without an orbit inclination change or 2.663 miles/s from LEO to geostationary orbit. Knowing the specific impulse for the engine and using the calculated  $\Delta v$  in equation 2, a stage mass fraction ( $m_i/m_f$ ) is calculated. The stage mass fraction can be used to determine maximum payload mass based on known structural and propellant masses. Also, from equation 2, if  $\Delta v$  is known and constant and specific impulse increases, then the mass ratio would decrease closer to one allowing for the payload mass to increase while the propellant mass decreases. The purpose of the rocket equation analysis is to optimize payload mass within mission and engine performance constraints. Complete upper stage initial and final masses will not be determined during the current research effort. A complete DEAN upper stage design is a project for a future student. The current DEAN design focus is not to a specific  $\Delta v$  requirement; rather, the DEAN design focus is to meet the IHPPT Phase III goals.

## II.3 Rocket Engine Theory

### II.3.a. Rocket Engine Design Process

Rocket engine design is complicated. A closely followed design process is required to avoid schedule delays and cost overruns. Huzel and Huang provide a flowchart for preliminary engine design, redrawn in Figure 2 [8]. The design has many feedbacks with a variety of blocks affecting another block. The interdependency of the blocks requires the designer to analyze how any changes made to one portion of the design affects another portion, while maintaining an overall global design perspective.

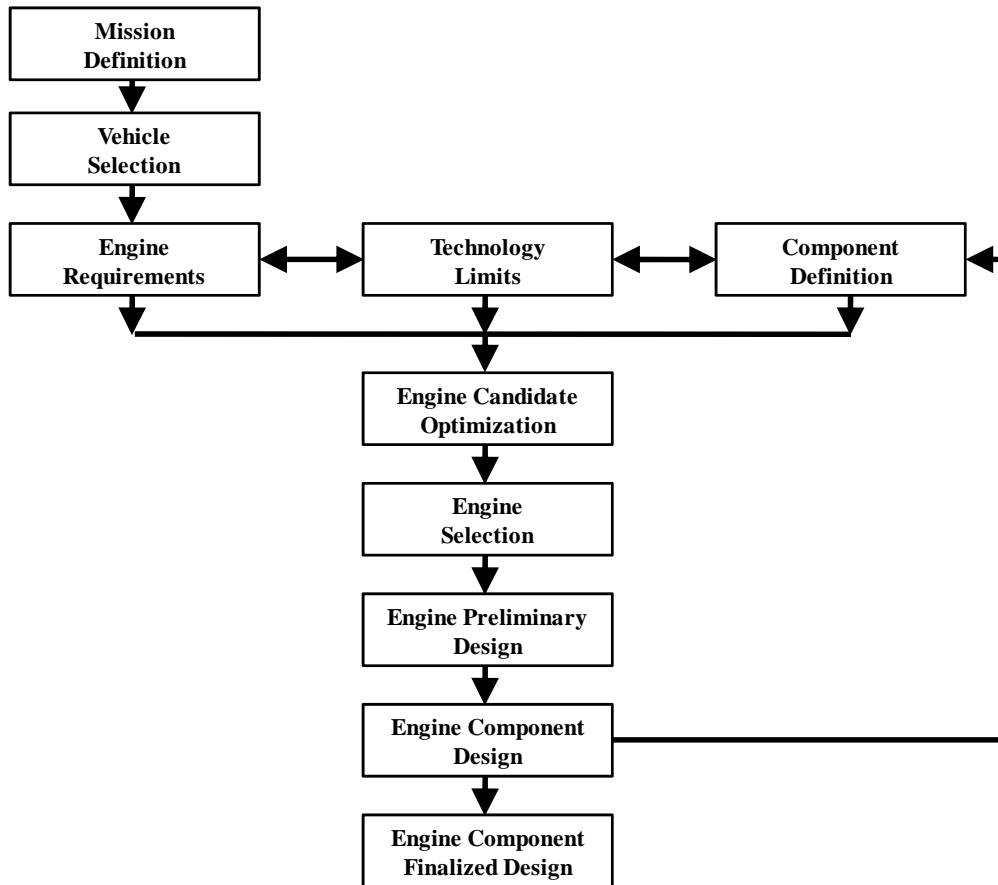


Figure 2. Preliminary engine design flowchart; redrawn from Huzel and Huang [8]

All of the blocks except for the final block have been touched upon in past work completed by Martin and Simmons. The mission is known and the engine requirements are known as defined by IHPPT. The current launch vehicle is unknown; however, DEAN engine dimensions will be kept within the envelope of the RL10B-2, the current Delta IV upper stage engine. During the current research effort, completion of the engine preliminary design or system level design optimization will occur, leaving the individual component design and optimization as follow-on work.

In each step of the design process, major rocket parameters need to be evaluated to ensure they are being met. According to Huzel and Huang, the major rocket engine design parameters are “thrust level, performance (specific impulse), run duration, propellant mixture ratio, weight of engine system at burnout, envelope (size), reliability, cost, and availability (schedule)” [8]. For the current research effort, evaluation of the thrust level, performance, propellant mixture ratio, engine mass, and envelope is completed. Since this research effort is not looking at a complete upper stage design with evaluation of propellant tank requirements, the run duration parameter is neglected. Furthermore, reliability, cost, and availability are not evaluated due to a lack of adequate resources to properly evaluate these parameters.

### ***II.3.b. Rocket Engine Cycles***

The most commonly used engine system configurations or engine cycles are the gas-generator cycle, the expander cycle, and the staged combustion cycle. Figure 3 shows basic schematics of these cycles derived from Huzel and Huang [8]. Various modifications to each cycle are possible with unique advantages and disadvantages.

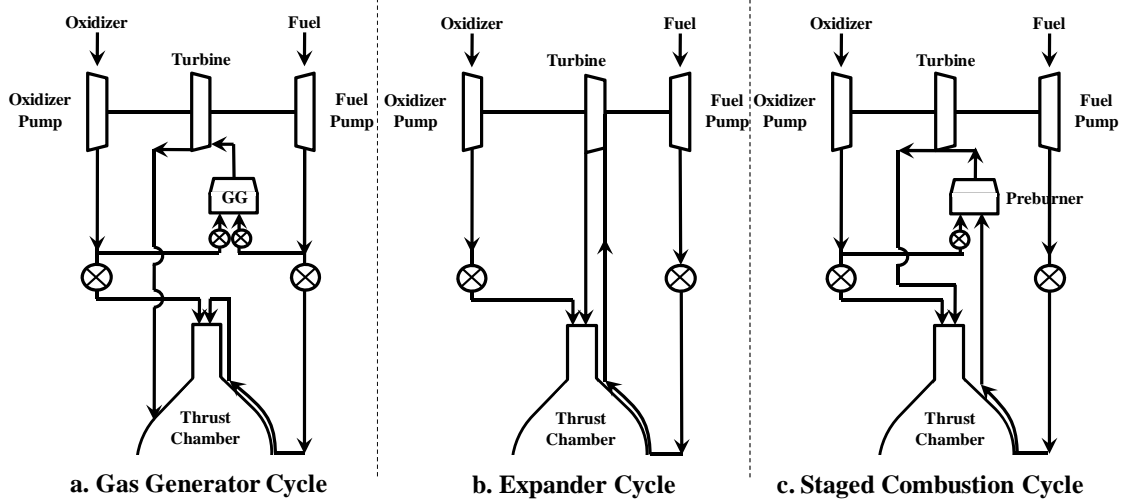


**Figure 3. Common Engine Cycle Schematics; redrawn from Huzel and Huang [8]**

The gas-generator cycle (Figure 3a) is an open cycle, defined as having a secondary flow from the propellant tanks that burn in a gas generator to drive the turbo machinery of the engine [21]. Figure 3a shows injection of the secondary flow into the thrust chamber. Injecting the secondary exhaust into the thrust chamber can have adverse effects, especially since the secondary exhaust is not fully expanded nor is the flow fully combusted to the same mixture ratio as the exhaust gases [8]. Therefore, the secondary flow can be discharged out a separate exhaust nozzle, as is the case for the Delta II first stage engine, the RS-27A. The disadvantage to the gas-generator cycle is the secondary exhaust is unusable decreasing the specific impulse and efficiency of the engine as compared to the staged combustion cycle. For aerospike nozzles, Manski *et al.* state the gas generator cycle is preferred since the gas generator exhaust can be released through the base of the truncated spike reducing base drag and increasing nozzle efficiency [21].

In a conventional expander cycle (Figure 3b), the fuel alone regeneratively cools the combustion chamber and nozzle. Prior to injection into the combustion chamber, the heat transferred to the fuel from cooling drives the turbopumps. The power available for

the pumps is limited by the heat transfer of the cooling cycle, meaning expander cycles typically have lower chamber pressures. The RL-10, used as the EELV upper stage, utilizes an expander cycle. The advantages to the expander cycle are its simplicity, lightweight turbopumps, and smooth ignition and startup [21]. Krach and Sutton state an absolute theoretical limit for a single expander cycle is difficult since the designer can increase the cooling jacket surface area to increase heat transfer to the propellant [22]. The practical limiting factors for an expander cycle are not necessarily related to heat transfer but rather to chamber weight and material properties. Krach and Sutton demonstrated a chamber pressure range of 1375 and 2300 psia (9.5 and 15.9 MPa) for a single expander cycle LOX/LH<sub>2</sub> engine at a thrust level of 65,000 lb<sub>f</sub> (289 kN) [22].

The staged combustion cycle (Figure 3c) has the highest performance of all the classic engine cycles due to the fact the turbine-inlet temperature is higher allowing for increased chamber pressure [8]. The increase in chamber pressure allows for a higher expansion ratio, delivering high specific impulse. The staged combustion cycle is typically preferred for boost engines; for example, the Space Shuttle Main Engine (SSME) utilizes this cycle. The disadvantages to the staged combustion cycle are complexity and high weight. A modification to the staged combustion cycle is the full flow cycle.

Although the DEAN utilizes the expander cycle, the DEAN is unique since both the oxidizer and fuel run separate expander cycles. The oxidizer expander cycle drives the oxidizer turbopumps and the fuel expander cycle drives the fuel turbopumps. The advantage is the fuel and oxidizer remain physically separated until injection into the

combustion chamber. Therefore, there is no need for interpropellant seals, the critical catastrophic failure mode in traditional expander cycle engines [4].

### ***II.3.c. Combustion Chamber Theory***

Chemical combustion is the most useful energy source in rocket engines: the propellants react or combust in a combustion chamber producing a light gas mixture with high internal energy. The hot, high pressure products in the chamber are accelerated and expelled through a nozzle to convert the internal energy of the gas to kinetic energy, producing thrust. To design a combustion chamber properly, the gaseous high temperatures and high pressures must be contained to allow for chemical reactions and to maximize the internal energy of the molecules. Combustion chamber material, geometry, and propellant choice are major design considerations in combustion chambers.

The combustion chamber material must be able to withstand the high temperatures and high pressures of the propellant combustion process. The geometry of the combustion chamber must be designed in such a way there is a large enough volume to allow for adequate propellant mixing and combustion while keeping the mass at a minimum; the design trade in combustion chamber design. Figure 4, inspired by Sutton and Biblarz, shows the multiple processes occurring in the combustion chamber [23].

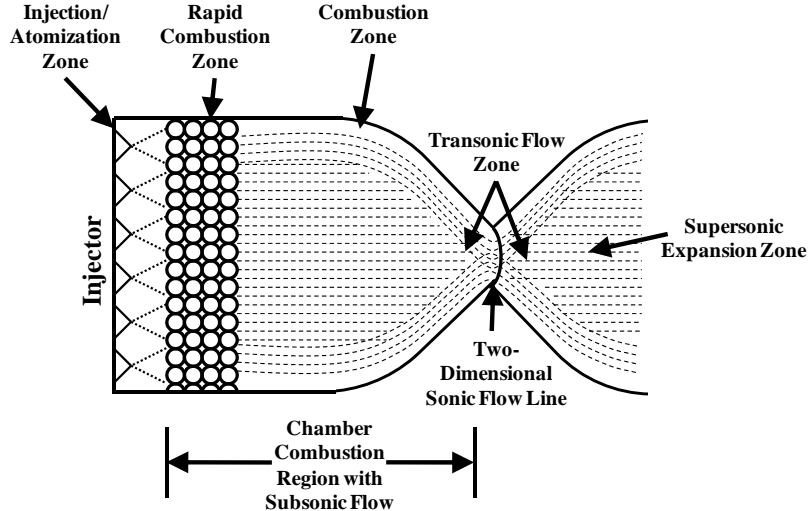


**Figure 4. Combustion Chamber Processes, inspired by Sutton and Biblarz [23]**

The amount of time in the combustion chamber for mixing and chemical reactions to occur is known as residence time. Residence time varies for different injectors, igniters, propellants, chamber pressure, chamber temperature, mixture ratios and chamber geometry. To maximize combustion, so all of the fuel and oxidizer react, the propellant velocity or Mach number in the chamber must be nearly zero. Therefore, the combustion chamber pressure and temperature are practically equivalent to the stagnation or total values, simplifying rocket performance calculations. The design trade in combustion chamber geometry can lead to incomplete combustion. Incomplete combustion leaves a small percentage of the propellants unburned causing a decrease in combustion efficiency; complete combustion means 100% combustion efficiency. According to Sutton and Biblarz, the designer initially chooses chamber geometry for new engine designs by utilizing successful historical data and gas dynamics for engines with comparable size, performance, and propellant type [23]. The designer can utilize other methods for chamber design as long as the goal is to minimize size and mass, while meeting adequate combustion efficiency.

If sonic flow velocity at the nozzle throat exists, a simpler method in designing the combustion chamber is the use of a characteristic length,  $L^*$ .  $L^*$  is defined as the ratio of chamber volume to throat area and has a specific value for a specific fuel/oxidizer mixture [8]. Knowing the nozzle throat area,  $L^*$  can be utilized to approximate the chamber volume required to maximize combustion; especially useful for system level rocket engine designs. In essence, the variable links combustion chamber volume to the residence time for the fuel/oxidizer mixture. The  $L^*$  value serves only as a starting point for combustion chamber design. The final  $L^*$  value for a specific combustion chamber depends on many variables such as propellant choice, mixture ratio, chamber pressure, injector design, and mass flow rate. Experimental studies should be performed to ensure combustion efficiency is acceptable with the  $L^*$  designed chamber. For hydrogen and oxygen propellants, typical  $L^*$  values are 30-40 inches (76.2-101.6 cm) for liquid hydrogen injection or 22-28 inches (55.9-71.1 cm) for gaseous hydrogen injection [8].

Different propellants mix and combust at different rates. A characteristic velocity ( $c^*$ ) is defined to compare combustion performance of different propellants. Huzel and Huang define the characteristic velocity as representing the effective energy level of the propellants and quality of the chamber design [8]. Shown in equation 6 from Sutton and Biblarz [23],  $c^*$  can be calculated from chamber and throat properties or from the thermo chemistry alone in the combustion chamber.

$$c^* = \frac{A_t P_c}{\dot{m}} = \frac{\eta_{c*} \sqrt{\gamma R T_c}}{\gamma \left( \frac{2}{\gamma + 1} \right)^{\frac{\gamma + 1}{2(\gamma - 1)}}} \quad (6)$$

where

$A_t$	=	Throat Cross-Sectional Area (in <sup>2</sup> )
$P_c$	=	Chamber Pressure (psia)
$\dot{m}$	=	Mass Flow Rate through the Rocket (slug/s)
$\eta_{c*}$	=	$c^*$ Combustion Efficiency
$\gamma$	=	Ratio of Specific Heats for Exhaust
$R$	=	Exhaust Gas Constant (ft <sup>3</sup> psi/(R-lb-mol))
$T_c$	=	Combustion Chamber or Flame Temperature (R)

The  $c^*$  combustion efficiency ( $\eta_{c*}$ ) is used to “express the degree of completion of the energy release and the creation of high temperature, high pressure gas in the chamber” [23]; values near one are typical.

The oxidizer-to-fuel ratio, or mixture ratio ( $O/F$ ), is the mass of oxidizer to the mass of fuel. The value of  $O/F$  will affect how the propellants react in the combustion chamber and, more importantly, rocket engine performance. A stoichiometric quantity of oxidizer is the perfect amount of oxidizer to burn a quantity of fuel [24]. Stoichiometric  $O/F$  is the mixture ratio where theoretical maximum temperature and heat release occurs [8]. For liquid hydrogen and liquid oxygen engines, the stoichiometric  $O/F$  value is 8:1 or simply 8.0 [23]. Interestingly, the optimum mixture ratio for rocket engines is not the stoichiometric value; rather, it is typically at a mixture ratio slightly fuel rich from stoichiometric. The reason is the exhaust tends to have lower exhaust molecular weight improving the engine performance parameters such as thrust and specific impulse. For hydrogen/oxygen engines, the optimum  $O/F$  is between 4.5 and 6.0 [23]. Chamber pressure, nozzle area ratio (exit area to throat area), and chamber temperature can all influence the optimum mixture ratio value.

Although a combustion chamber is specially designed for stable combustion, combustion instabilities can occur and, if not controlled, can cause catastrophic failure to the engine and launch vehicle through pressure spikes and/or increased temperature (heat transfer) spikes. Combustion instability is simply undesirable pressure, temperature, and velocity fluctuation interactions with the natural frequency of the propellant feed system or chamber acoustics. A combustion process is never smooth; therefore, combustion instabilities are always present and can only be damped through proper combustion chamber design. There are three instability categories: low frequency (known as chugging at 10-400 Hz), intermediate frequency (known as buzzing at 400-1000 Hz), and high frequency (known as screaming at greater than 1000 Hz). Chugging is typically due to pressure interactions between the propellant feed system and the combustion chamber or due to disturbances in propellant flow rate. Buzzing occurs due to structural vibrations, mixture ratio fluctuations, and flow eddies. The high frequency instability is the most devastating and most hard to correct; it can occur in two modes, longitudinal and traverse. The traverse mode is broken into tangential and radial modes. The tangential mode is the most dangerous since heat transfer rates can exponentially increase with high pressure leading to failure of the combustion chamber structure. Screaming occurs due to combustion forces, such as pressure waves and chamber acoustic resonances [23]. Since the current research effort is focusing on system level design optimization, analysis of combustion instabilities will not occur; however, it is important to understand instabilities are real problems and need to be evaluated during component level design.

The DEAN engine utilizes liquid oxygen (O<sub>2</sub>) and liquid hydrogen (H<sub>2</sub>) as the oxidizer and fuel, respectively. Hydrogen is the lightest and coldest of all known fuels. The main advantages of hydrogen are high specific impulse for rocket applications and hydrogen will form nontoxic exhaust gases when burned with oxygen. Disadvantages include low density and low liquid temperature. The low density necessitates large tanks for storage and the low temperature necessitates the need for first-class insulation. The low temperature of hydrogen is advantageous as a regenerative coolant [23]. The same advantage and disadvantage of the low temperature of hydrogen applies to liquid oxygen as well. Liquid oxygen is an excellent oxidizer in facilitating combustion. According to Huzel and Huang [8], liquid hydrogen and oxygen have the following characteristics as shown in Table 3.

**Table 3. Liquid Hydrogen and Liquid Oxygen Propellant Characteristics; based on Huzel and Huang [8]**

Propellant	Molecular Weight	Freezing Point	Boiling Point	Critical Pressure	Critical Temperature
<b>Liquid Hydrogen</b>	2.016	25.07 R (13.9 K)	36.77 R (20.4 K)	187.8 psia (1.3 MPa)	59.37 R (33.0 K)
<b>Liquid Oxygen</b>	32.00	97.67 R (54.3 K)	162.27 R (90.2 K)	735 psia (5.1 MPa)	277.67 R (154.3 K)

The standard equation for a hydrogen/oxygen reaction is H<sub>2</sub> + ½O<sub>2</sub> → H<sub>2</sub>O; however, this is not the only reaction occurring during combustion. According to Turns, assuming an eight species model for an H<sub>2</sub> and O<sub>2</sub> reaction, as many as 40 reactions will take place [24]. The eight species, or chemical reaction products, are H<sub>2</sub>, O<sub>2</sub>, H<sub>2</sub>O, OH, O, H, HO<sub>2</sub>, and H<sub>2</sub>O<sub>2</sub>.

#### ***II.3.d. Rocket Nozzle and Rocket Engine Performance Theory***

The rocket nozzle is responsible for engine performance through acceleration and ejection of the combustion products from the combustion chamber by means of converting the enthalpy of the hot, high pressure exhaust into kinetic energy [4]. Typical nozzle and rocket engine performance parameters are thrust, specific impulse, and thrust-to-weight. Design considerations aim to minimize the length of the nozzle while maximizing performance.

Two sources of thrust exist in conventional bell nozzle engine designs. First, the momentum of the combusted gases exiting the engine at high velocities produces thrust, known as momentum thrust; a combination of Newton's Second and Third Laws. Total system momentum must remain constant through the Conservation of Momentum governing equation. Since mass is accelerated out a rocket nozzle, the rocket itself must increase its forward momentum equally [20]. Second, the pressure acting along the nozzle wall produces thrust, known as pressure thrust. In axisymmetric nozzles, the integration of the horizontal component of the pressure acting along the nozzle wall multiplied by the differential nozzle cross-sectional area is equal to zero. The integral of the vertical component; however, does not equal zero and provides the magnitude of the pressure thrust. For bell nozzles, the integral of the pressure times a differential area can be simplified to equal to the imbalance between the pressure at the nozzle exit and the ambient pressure multiplied by the nozzle exit area. Ideal expansion is when the nozzle exit pressure is equivalent to the ambient pressure allowing for maximum thrust efficiency. The drawback is ideal expansion requires large heavy nozzles especially for space missions or will occur only at the design altitude of the engine. Since different

engines have different missions, thrust is typically presented in terms of vacuum thrust for comparison reasons. Vacuum thrust is the maximum thrust an engine can produce. In order for the exhaust to accelerate in the nozzle, the engine throat must be choked. The flow will be subsonic in the combustion chamber, become sonic at the throat, and accelerate through expansion of the nozzle to supersonic velocities. Another way to define thrust is by the nondimensional thrust coefficient ( $c_F$ ); it is equivalent to the thrust divided by the nozzle throat area and the chamber pressure.

Total impulse is simply “the total energy released by all the propellants in a propulsion system” [23]. It is equal to the integration of the thrust over the entire burn time of the engine. The total impulse value is only useful to a specific rocket stage and is unusable for engine comparisons. On the other hand, specific impulse is an important average performance parameter used to measure thrust versus propellant weight flow useful in engine comparison. Many different formulations of specific impulse exist; however, specific impulse relates to total impulse by equaling the total impulse divided by the weight of the propellant. In simplistic terms, specific impulse is the rocket parameter similar to the miles per gallon parameter in automobiles.

Thrust-to-weight ( $T/W$ ) is an important performance ratio. An engineer can design an engine offering incredible thrust magnitudes; however, if the engine weighs just as much as the thrust, the engine is not useable for boost applications. Sutton and Biblarz state the thrust-to-weight ratio is a “dimensionless parameter that is identical to the acceleration of the rocket propulsion system if the engine could fly by itself in a gravity-free vacuum” excluding tankage, payload, and rocket structure [23]. In order for an engine to be effective, the  $T/W$  must be greater than one for boost and could be any

value for space application engines. The engine designer should maximize engine  $T/W$  for a single stage (much greater than one for boost stages) to maximize the  $T/W$  of the entire vehicle; the goal is to successfully get a payload off the earth and into orbit.

Thrust, specific impulse, and thrust-to-weight are the primary performance parameters for a rocket nozzle and the rocket engine as a whole. The following equations summarize how the parameters are calculated [20]. The equations apply to bell nozzles; aerospike specific equations will be discussed in the next chapter. The thrust coefficient was added since it is another way to present the thrust in nondimensionalized form.

$$F = \dot{m}u_e + (p_e - p_a)A_e = I_{sp}\dot{m}g_o = A_t p_c \gamma \sqrt{\left(\frac{2}{\gamma-1}\right)\left(\frac{2}{\gamma+1}\right)^{\frac{\gamma+1}{\gamma-1}} \left[1 - \left(\frac{p_e}{p_c}\right)^{\frac{\gamma-1}{\gamma}}\right]} + (P_e - P_a)A_e \quad (7)$$

$$I_{sp} = \frac{F}{\dot{m}g_o} = \lambda \left\{ \frac{c^* \gamma}{g_0} \sqrt{\left(\frac{2}{\gamma-1}\right)\left(\frac{2}{\gamma+1}\right)^{\frac{\gamma+1}{\gamma-1}} \left[1 - \left(\frac{p_e}{p_c}\right)^{\frac{\gamma-1}{\gamma}}\right]} + \frac{c^* \varepsilon}{g_0 p_c} (p_e - p_a) \right\} \quad (8)$$

$$\frac{T}{W} = \frac{F}{mg_o} \quad (9)$$

$$c_F = \frac{F}{A_t p_c} \quad (10)$$

where

$F$	= Total Thrust (lb <sub>f</sub> )
$\dot{m}$	= Mass Flow Rate through the Rocket (slug/s)
$u_e$	= Nozzle Equivalent Exit Velocity (ft/s)
$p_e$	= Nozzle Exit Pressure (psia)
$p_a$	= Ambient or Atmospheric Pressure (psia)
$A_e$	= Nozzle Exit Area (ft <sup>2</sup> )
$I_{sp}$	= Specific Impulse (sec)

$\lambda$	=	Nozzle Efficiency
$\varepsilon$	=	Nozzle Expansion Ratio
$W$	=	Total Engine Weight (lb <sub>f</sub> )
$m$	=	Total Engine Mass (lb <sub>m</sub> )

Sutton and Biblarz present several methods for analyzing flow in a rocket nozzle based on certain assumptions [23]. Preliminary estimates utilize a one-dimensional nozzle flow analysis and assume all velocities and temperatures or pressures are equal at any cross-section of an axisymmetric nozzle. A two-dimensional nozzle flow analysis assumes the velocity, temperature, density, and Mach number may vary over the cross-sectional area of the nozzle. A three-dimensional nozzle flow analysis is not always performed for axisymmetric nozzles but can be beneficial for rectangular or elliptic shaped nozzles. Bell nozzles typically utilize a one-dimensional flow analysis. The aerospike is truly two-dimensional in nature; therefore, a two-dimensional flow analysis is required.

Rocket performance analyses also assume either frozen flow or equilibrium flow. Frozen flow assumes the product composition in the combustion chamber is equal to the composition at the nozzle exit; there are no chemical reactions. Frozen flow tends to underestimate the performance by approximately 1 to 4%. Equilibrium flow assumes simultaneous forward and reverse chemical reactions occur at the same rate under varying pressure and temperature as the flow expands along the nozzle. Therefore, the chemical composition of the exhaust will change and will be different from the composition in the combustion chamber. Equilibrium flow typically overestimates the performance by 1 to 4%. Realistically for rocket engines, the composition of combustion

products is between frozen and equilibrium flow assumptions. Realistic calculations are rarely used due to inadequate data on reaction rates of simultaneous reactions [23].

Engine designs begin with the ideal rocket due to simplicity and the fact historical rocket performance has actually been between 1 and 6% below the calculated ideal value.

Assumptions for the one-dimensional flow analysis of the ideal rocket are:

- The combusted products or exhaust are homogeneous, gaseous, and obey the perfect gas law.
- The flow is isentropic and steady; adiabatic flow, friction and boundary layer effects are negligible, and no shock waves occur in the nozzle.
- Chemical equilibrium occurs in the combustion chamber and the flow remains frozen in the nozzle.

Realistically, the one-dimensional ideal rocket assumptions are not true. The flow through nozzles will not be isentropic and reversible. Losses can be accounted for by boundary layer/wall friction effects, unsteady combustion, transient pressure distributions in the combustion chamber and nozzle, solid particles or liquid droplets in the gas, heat transfer to the nozzle walls and non-uniform gas composition [23].

The DEAN nozzle is not a typical bell nozzle; rather it is an annular aerospike nozzle. An annular aerospike nozzle is simply a longitudinally elongated annulus forming a cylinder with a truncated spike in the center of it. A radial in-flow plug nozzle contains an ideally long isentropic spike to expand the flow; the spike tends to be extremely long and heavy. In contrast, an aerospike is a radial in-flow plug nozzle with the spike truncated or cut-off at a specific point allowing the engine to operate close to the performance of the plug nozzle minus the disadvantage of length and weight. With

the truncated spike, some of the primary flow will begin to circulate subsonically at the flat truncated portion of the nozzle. When the subsonic flow interacts with the primary exhaust flow, the subsonic flow will form an aerodynamic spike that mimics an ideal isentropic spike; hence the name aerospike nozzle [8]. In recent years, the term aerospike has been used to refer to either a truncated or a full-length spike. Figure 5 shows the flow regions for a truncated aerospike nozzle and Figure 6 shows a solid model of the current DEAN aerospike and combustion chamber design taken from Martin [4] (government work with no copyright).

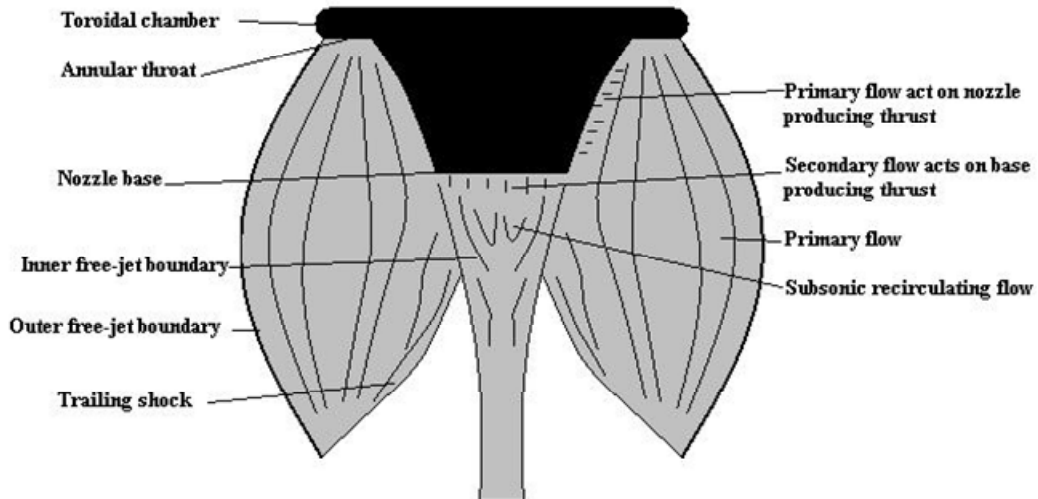


**Figure 5. Truncated Aerospike Flow Regions; taken from Martin [4]**

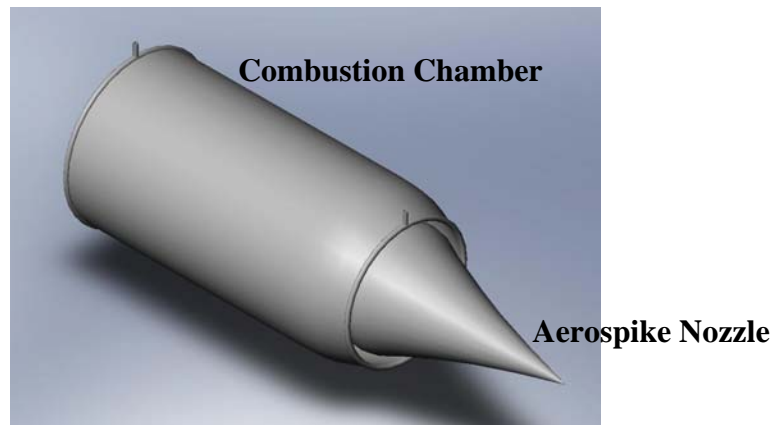


**Figure 6. Solid Model of the Current Aerospike Engine Design; taken from Martin [4]**

The main advantage to the annular aerospike nozzle design (both full length and truncated spike) is its altitude compensation ability below or at its design altitude. More specifically, the aerospike will not suffer from the same overexpansion losses a bell nozzle suffers and can operate near optimally, giving the highest possible performance at every altitude up to its design altitude [8, 23]. Above the design altitude, the aerospike behaves much like a conventional bell nozzle (reference Figure 7c) [26-28]. Figure 7 (reprinted with permission of the American Institute of Aeronautics and Astronautics) shows the exhaust flow along an aerospike at low altitudes, design altitude, and high altitudes for a full spike and a truncated spike [26].

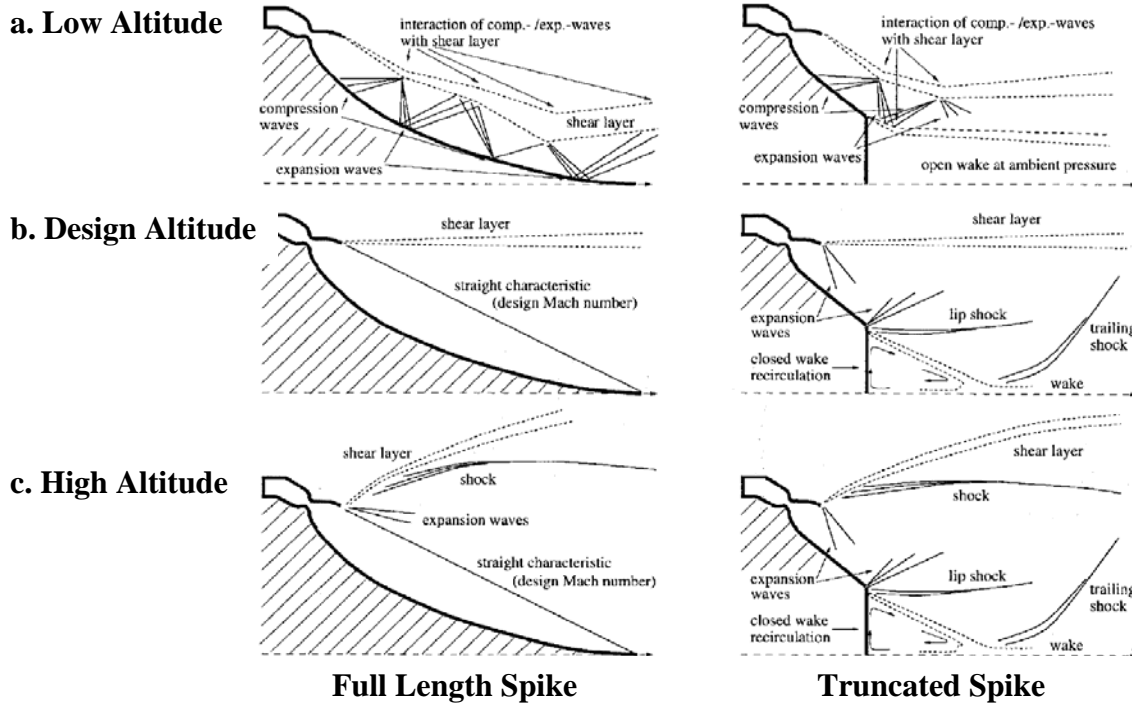


**Figure 7. Exhaust Flow from a Full and Truncated Spike; reprinted with permission from AIAA [26]**

Multiple expansion and compression, or shock, waves are evident in the flow in Figure 7; these waves lead to losses in thrust. The outer flow boundary of the aerospike

is the atmosphere itself. Unique to aerospike engines operating at their design altitude, engine geometry at the throat determines the expansion ratio of the aerospike nozzle and thus the corresponding engine performance. At the design altitude of the nozzle, the exhaust flow at the chamber exit lip will follow a parallel path to the centerline to the exit plane [26]. Therefore, the expansion ratio for a full-length spike at design altitude is equivalent to the chamber exit lip area divided by the throat area. As the ambient pressure decreases, the hot gas/ambient air boundary expands outward changing the pressure distribution along the spike; as a result, the expansion ratio increases. As the ambient pressure increases (low altitudes), the higher ambient pressure compresses the hot gas/ambient air boundary closer to the spike resulting in an expansion ratio decrease. The pressure distribution change along the spike and the location of the hot gas/ambient air boundary is automatic thus permitting altitude compensation up to the design altitude of the nozzle. Above the design altitude of the nozzle, the pressure distribution along the nozzle wall is constant [26]. The expansion of the flow exiting the combustion chamber is governed by the Prandtl-Meyer turning angle at the throat [8].

According to the aerospike nozzle numerical analyses by Hagemann *et al.*, the results of the altitude compensation capabilities of an aerospike up to the design altitude are undeniable [28]. Furthermore, Hagemann *et al.* state the aerospike performs worse at high altitudes compared to bell nozzles with equal expansion ratios (exit area divided by throat area); therefore, to get the benefit of the aerospike, the design pressure ratio and the expansion ratio should be chosen as high as possible [28]. The design pressure ratio is the ratio of the chamber pressure to the ambient pressure; ambient pressure is based on the chosen design altitude. If the spike is truncated, the aerospike advantage at higher

altitudes (orbit transfer missions) includes shortened nozzle length and lower mass as compared to an equivalent performance bell nozzle design for orbit transfer missions. The disadvantages of the aerospike include high cooling requirements of the spike, manufacturing difficulties, and lack of historical data and flight experience [23]. Since a boost-stage of a rocket experiences the greatest change in ambient pressure, it would benefit the most from the aerospike design.

Figure 8 shows a hot fire test photo of the Space Shuttle Main Engine (SSME) (left) and the J-2T-250K (right) reprinted with permission of PWRengineering.com; the hot fire test in both images is occurring at sea level [14].

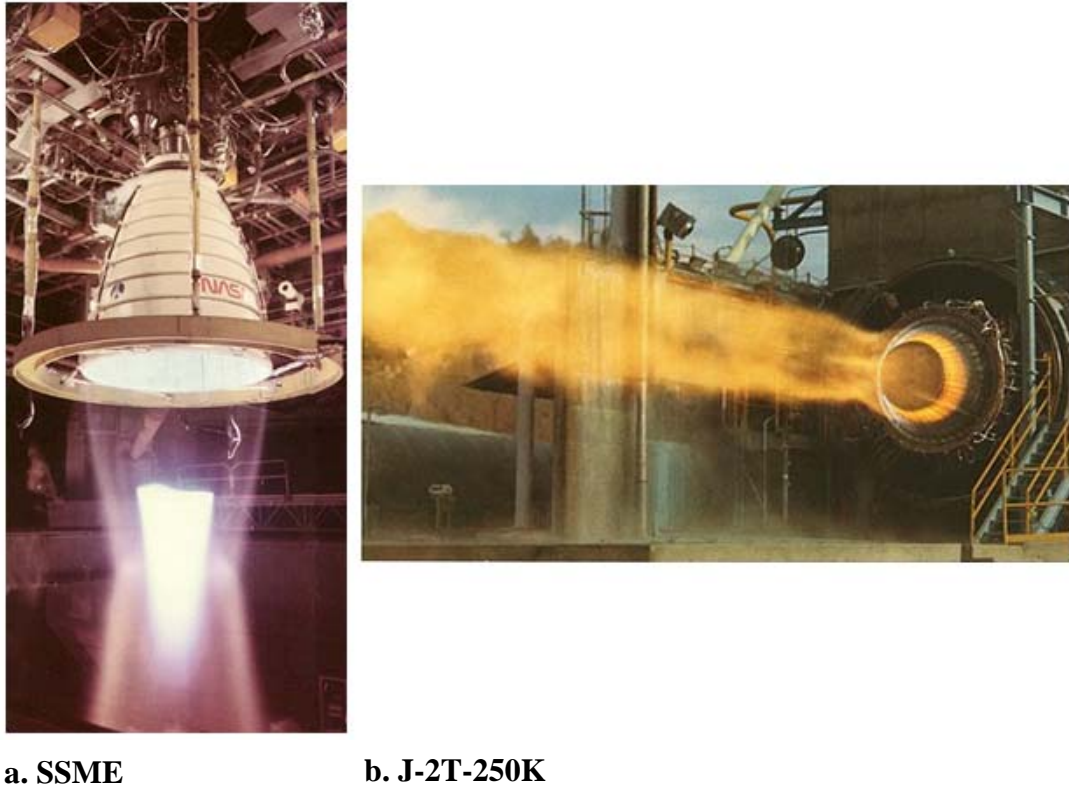


**Figure 8. Hot Fire Photo of a. SSME and b. J-2T-250K; reprinted with permission from PWRengineering.com [14]**

As shown in Figure 8a, the SSME is overexpanded. The higher ambient pressure is pushing the exhaust flow with lower pressure inward (compression) leading to a loss in thrust magnitude. The plume in the SSME photo shows a shock and an expansion wave but it does not show the location where the exhaust eventually flows parallel to the freestream. When the exhaust flows parallel to the freestream, the launch vehicle experiences maximum thrust (thrust vector is parallel to freestream velocity vector). Typically for bell nozzles operating at sea level, there are multiple shock/expansion waves occurring until the flow is parallel to the freestream or the flow pressure equals the ambient pressure. By the time the pressure equalizes, the thrust magnitude has decreased from its initial magnitude at the nozzle exit. Conversely, the flow exiting the throat of the J-2T-250K follows closely to the centerbody (Figure 8b). The high ambient pressure, acting as the outer boundary of the exhaust (the altitude compensation capability of the aerospike), attributes to the shape of the flow field along the nozzle. Observed in the J-2T-250K photo, the exhaust experiences a shock leaving the truncated nozzle but quickly reaches ambient pressure, where the exhaust is flowing parallel to the freestream; this is the significant advantage to the aerospike nozzle design.

Nozzle truncation, although it decreases the size and mass of the engine, has more performance losses than the ideal, full-length nozzle. The truncated spike flow in Figure 7 results in more shocks decreasing the thrust and efficiency of the engine. Figure 9 shows a more detailed truncated aerospike sketch, courtesy of SEA, Inc. [29].

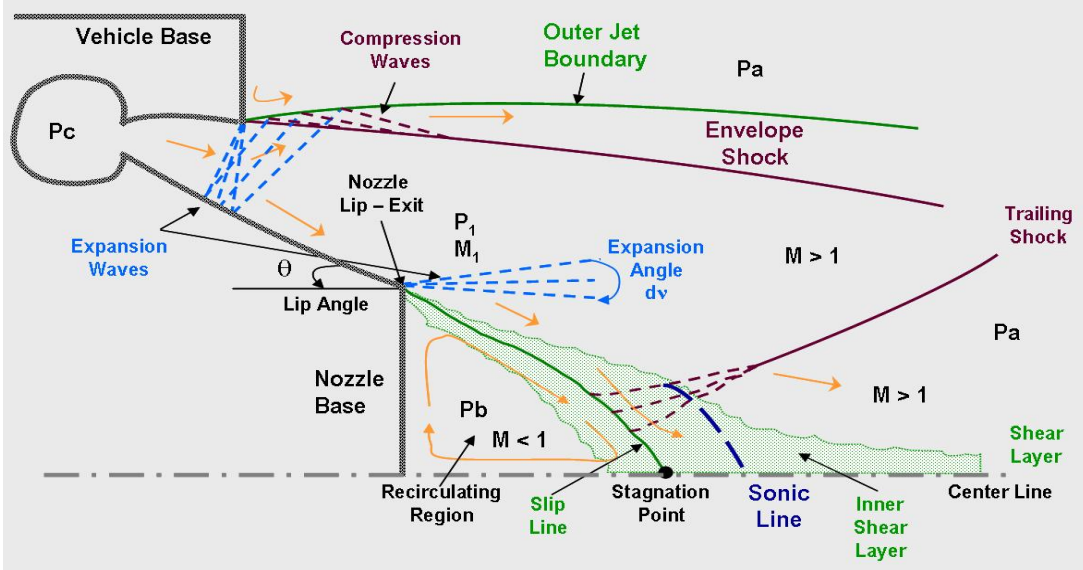


**Figure 9. Exhaust Flow Along a Truncated Aerospike Nozzle; reprinted with permission from SEA, Inc. [29]**

Ito, Fujii and Hayashi state performance losses on truncated nozzles are negligible because the “base pressure compensates the loss of the thrust force” [30]. Base pressure thrust is an added thrust component acting at the base for truncated aerospike nozzles. At low altitudes, the base pressure thrust produced is small; on the other hand, at high altitudes, the base pressure thrust is large. As altitude increases, the ambient pressure decreases and the difference between base pressure and ambient pressure increases accounting for increased base pressure thrust. Hagemann *et al.* state an open wake is present along the truncated aerospike base for nozzle operation below its design altitude [26]. Therefore, the base pressure thrust is minimal, even with a truncated aerospike, since the base pressure is approximately equal to the ambient pressure. Near the design altitude of the aerospike nozzle, the wake transitions to enclose the entire base area causing the base pressure to be greater than the ambient pressure. The closed wake remains at and above the design altitude of the nozzle, creating a positive base pressure thrust [26]. Ito, Fujii and Hayashi were able to prove thrust performance is “almost

insensitive to truncation of the nozzle length” [30]. A main concern in spike truncation is recirculating stagnant exhaust. The stagnant exhaust will have a higher temperature and it is vital in the design the temperature of the base remain below structural thermal limits.

As previously stated in section II.3.b, Manski *et al.* state the gas generator exhaust can be released through the base of the truncated spike, reducing the nozzle base drag and increasing nozzle efficiency [21]. A study by Ito and Fujii in 2001 showed the basic characteristics of the flow field at the base region do not change whether there is solely external flow or if base bleed is introduced [31]. Ito and Fujii term base bleed as the gas generator exhaust exiting through the truncated spike base [31]. A study by Ito and Fujii a year later in 2002 showed the base bleed interacts with the main exhaust flow allowing the thrust performance to be greater for base bleed than without, for all ranges of altitude [32]. Maximum pressure thrust at the base occurs when the base bleed is released in such a way as to cause recirculation. However, maximum overall performance came from the base bleed orientation directed at the outer region of the base and parallel to the nozzle axis [32]. Base bleed allows for increased nozzle efficiency when the engine utilizes a gas generator cycle.

The nozzle is a vital component to the rocket engine and, specifically, the aerospike nozzle in the current research effort. The thrust chamber collectively includes the injectors, combustion chamber, nozzle, and mounting hardware.

### ***II.3.e. Cooling Jacket Theory***

Combustion of the propellants in the combustion chamber creates extremely hot temperatures and high heat transfer rates to the chamber wall. To avoid catastrophic structural failure, cooling of the combustion chamber and nozzle is required.

There are multiple cooling methods used in rocket engines such as dump cooling, film cooling, transpiration cooling, ablative cooling, radiation cooling, and regenerative cooling [8, 20]:

- Dump cooling flows and dumps cold propellant through the thrust chamber walls and out openings at the bottom of the nozzle; this type of cooling can significantly influence performance.
- In film cooling, typically known as fuel boundary layer cooling, cold propellant(s) or coolant is/are injected close to the thrust-chamber wall. This type of cooling lowers the flame temperature and heat transferred to the wall. Normally the coolant does not react in the chamber. Film cooling will have a slight impact on specific impulse.
- Transpiration cooling is a special type of film cooling; coolant enters the chamber through pores in the wall at a tailored rate to maintain the temperature of the chamber wall at or near a desired value.
- In ablative cooling, the combustion chamber wall material in the combustion chamber is designed to melt, vaporize, or chemically change to dissipate heat resulting in lower wall temperatures. Solid propellant engines mainly use ablative cooling.

- In radiation cooling, the combustion chamber or nozzle become red or white hot and radiate into the environment [20]. Space applications most use this type of cooling, especially for upper stage nozzle extensions.
- Regenerative cooling is the most widely used cooling method; cold propellants run through a heat exchanger integral to the combustion chamber and nozzle wall absorbing heat before injection into the chamber. There are negligible thermal energy/performance losses since the heat absorbed by the cold propellants returns to the injector.

Each cooling technique has advantages and disadvantages. It is important the cooling method chosen absorb heat consistently to prevent hot spots or burn-through on any of the engine components.

Since the DEAN engine utilizes regenerative cooling, a cooling jacket is required around the interior of the combustion chamber and the exterior of the aerospike. The cooling jacket design needs to keep the walls cool enough to maintain structural integrity while providing adequate heat to the propellants to power the expander cycle. The cooling jacket itself integrates into the chamber and nozzle with small channels allowing cold propellant to pass through; a structural jacket surrounds the cooling jacket channels as added support for the high pressures the combustion chamber and nozzle will experience. The DEAN aerospike design adds complexity to cooling since hot exhaust flow surrounds the nozzle; the aerospike exhaust flow is different from the bell nozzle where cooler ambient air surrounds the nozzle exterior. Material choice is crucial in guaranteeing the spike will not structurally fail.

In the DEAN design, liquid hydrogen cools the aerospike and liquid oxygen cools the combustion chamber. An advantage to hydrogen cooled nozzles is temperature rise in the propellant during regenerative cooling will be high resulting in a specific impulse increase of more than 1%. The propellant passing through the cooling channels of the DEAN will be supercritical increasing heat transfer and preventing nucleate boiling and all other forms of boiling. Supercritical means the fluid is above its critical temperature and pressure point and continuously transforms from liquid to gaseous states. Nucleate boiling occurs when the wall temperature exceeds the boiling point of the liquid causing small vapor bubbles to form at the wall surface. The bubbles increase the local heat transfer rate leading to increased bubble formation. The increased bubble formation will then act as an insulator on the surface resulting in a decrease in the heat transfer rate. Therefore, supercritical fluid is preferred for a more predictable and controllable steady heat transfer rate. The nucleate boiling concern applies for coolants in both regenerative and film cooling methods [23].

The three major forms of heat transfer are conduction, convection, and radiation. According to Incropera and DeWitt, conduction is the transfer of energy in a medium due to a temperature gradient, convection refers to “heat transfer that will occur between a surface and a moving fluid when they are at different temperatures,” and, regardless of the form of matter, radiation is the emission of thermal energy through empty space [33]. In rockets, conduction occurs through the chamber and nozzle walls and convection occurs by fluid (gas and liquid) flow on both sides of the chamber and nozzle walls.

Hill and Peterson state convection is a boundary layer problem where the velocity and temperature boundary layers thicknesses are of the same order of magnitude [34].

Boundary layer thickness is minimum near the nozzle throat and increases to a maximum thickness at the nozzle exit. The maximum convective heat transfer rate occurs at the nozzle throat due to the smaller boundary layer. The convective heat transfer rate will change downstream due to varying wall curvature, pressure gradients, and temperature gradients.

Radiation occurs through emission of thermal energy to the internal walls of the engine and to the surrounding hardware/ambient air. Radiation will also occur from the downstream exhaust plume. Sutton and Biblarz state gases with symmetrical molecules, such as hydrogen and oxygen, do not “absorb much radiation and do not contribute considerable radiative energy to the heat transfer” [23]. Depending on the volume, pressure and temperature of the combustion chamber and on the composition of the reacting gases, radiation may contribute anywhere from 3 to 40% of the heat transfer to the walls [23].

To estimate the heat transfer rate from the combustion gases to the coolant (propellants), the engine designer may assume a one-dimensional heat transfer model. The following heat transfer calculations are based on the equations and the process presented by Humble, Henry and Larson [20]. Equation 11 is the governing conservation of energy equation based on the first law of thermodynamics.

$$\dot{Q}_{in} = \dot{Q}_{out} + \Delta h \quad (11)$$

where

$\dot{Q}_{in}$	=	Heat Flow In to System (W or BTU/hr)
$\dot{Q}_{out}$	=	Heat Flow Out of System (W or BTU/hr)
$\Delta h$	=	Change in Enthalpy (W or BTU/hr)

The heat transfer in the engine can be divided into distinct segments, shown in Figure 10 (inspired by Humble *et al.* [20]); note in the figure the chamber inner wall can be replaced with the aerospike wall. The first law of thermodynamics relates the segments, where the heat flow of each segment must be equivalent.

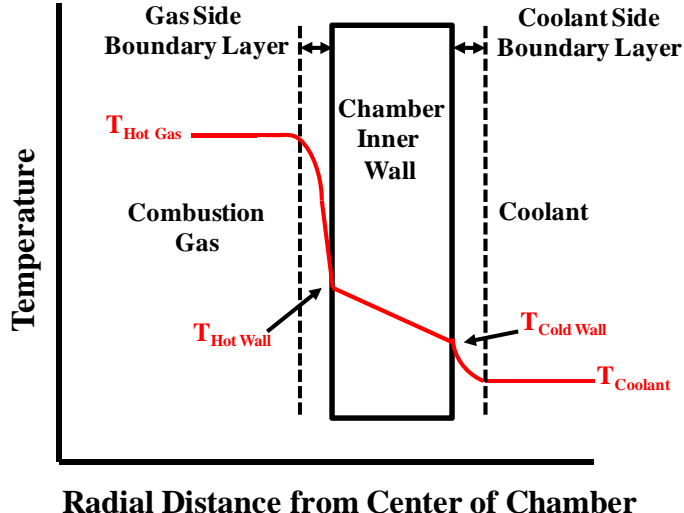


**Figure 10. Regenerative Cooling Heat Transfer Schematic; inspired by Humble *et al.* [20]**

The first segment is the convective heat transferred from the hot gas mixture in the combustion chamber to the wall of the coolant channel added with the associated radiative heat transfer. The following equations model the first segment utilizing the International System of Units (SI):

$$\dot{q}_1 = h_g (T_{hg} - T_{hw}) + (\varepsilon_{shg} \sigma_s T_{hg}^4 - \varepsilon_s \sigma_s T_{hw}^4) \quad (12)$$

$$h_g = 0.026k \left( \frac{\rho v}{\mu} \right)^{0.8} \left( \frac{1}{D} \right)^{0.2} \left( \frac{c_p \mu}{k} \right)^{0.4} \quad (13)$$

where

$\dot{q}_1$  = Heat Transfer per Unit Area (W/m<sup>2</sup>)

$h_g$  = Hot Gas Mixture Heat Transfer Coefficient (W/ m<sup>2</sup>-K)

$T_{hg}$  = Hot Gas Mixture Temperature (K)

$T_{hw}$	=	Cooling Channel Outer “Hot” Wall Temperature (K)
$\varepsilon_s$	=	Surface Emissivity
$\sigma_s$	=	Stefan-Boltzmann Constant ( $5.67051 \times 10^{-8} \text{ W/m}^2 \cdot \text{K}^4$ )
$k$	=	Thermal Conductivity of Hot Gas Mixture (W/m-K)
$\rho$	=	Hot Gas Mixture Density (kg/ m <sup>3</sup> )
$v$	=	Flow Velocity (m/s)
$\mu$	=	Hot Gas Mixture Dynamic Viscosity (kg/m-s)
$c_p$	=	Constant Pressure Specific Heat (J/kg-K)
$D$	=	Diameter of Combustion Chamber (m)

The combustion in the chamber is assumed a constant pressure process. The hot gas transfer coefficient, equation 13, is a form of the Bartz equation. At this point in the calculation, the diameter is the average diameter of the combustion chamber.

The second segment is the conductive heat transferred through the wall from the hot combustion side to the cooler coolant side wall. The following equation models the second segment:

$$\dot{q}_2 = \frac{-k}{\Delta l} (T_{cw} - T_{hw}) \quad (14)$$

where

$\dot{q}_2$	=	Heat Transfer per Unit Area (W/m <sup>2</sup> )
$T_{cw}$	=	Cooling Channel Inner “Cold” Wall Temperature (K)
$k$	=	Thermal Conductivity of Wall (W/m-K)
$\Delta l$	=	Coolant Channel Wall Thickness (m <sup>2</sup> )

The third segment is the convective heat transferred from the cool side wall to the coolant fluid in the channel assuming a rectangular cooling channel.

$$\dot{q}_3 = h_l(T_{cw} - T_{cl\_out}) \quad (15)$$

$$h_l = 0.023G C_p \left( \frac{\mu}{GD_{ch}} \right)^{0.2} \left( \frac{k}{C_p \mu} \right)^{\frac{3}{2}} \quad (16)$$

$$G = \frac{4\dot{m}_c}{\pi D_{ch}^2} \quad (17)$$

$$D_{ch} = \frac{4 b a_w}{2(b - 2\Delta l) + 2(a - 2\Delta l)} \quad (18)$$

where

$\dot{q}_3$	=	Heat Transfer per Unit Area (W/m <sup>2</sup> )
$h_l$	=	Heat Transfer Coefficient (W/ m <sup>2</sup> -K)
$T_{cl\_out}$	=	Outgoing Coolant Temperature (K)
$G$	=	Average Mass Flow Rate through Channel per Unit Area (kg/s-m <sup>2</sup> )
$k$	=	Thermal Conductivity of Coolant (W/m-K)
$\dot{m}_c$	=	Mass Flow through a Single Channel (kg/s)
$D_{ch}$	=	Coolant Channel Hydraulic Diameter (m)
$a_w$	=	Coolant Channel Width (m)
$b$	=	Coolant Channel Length (m)

The hydraulic diameter is equivalent to four times the channel flow area divided by the wet perimeter (interior channel perimeter).

The fourth segment explores the enthalpy change of the coolant. The heat added to the fluid is calculated using the initial temperature in the channel and the final temperature out of the channel. The following equation models the fourth segment:

$$\dot{Q}_4 = \dot{m} \cdot C_p (T_{cl\_out} - T_{cl\_in}) \quad (19)$$

where

$$\begin{aligned}\dot{Q}_4 &= \text{Rate of Heat Added to Coolant (W)} \\ T_{cl\_in} &= \text{Incoming Coolant Temperature (K)}\end{aligned}$$

The heat transfer equations (12, 14, 15, and 19) setup a system of four equations with four unknowns;  $T_{hw}$ ,  $T_{cw}$ ,  $T_{cl\_out}$ , and  $\dot{Q}$ .

$$\dot{Q} = (A_s \cdot \dot{q}_1) = (A_s \cdot \dot{q}_2) = (A_s \cdot \dot{q}_3) = \dot{Q}_4 \quad (20)$$

where

$$\begin{aligned}A_s &= \text{Surface area (m}^2\text{)} \\ \dot{Q} &= \text{Heat transfer rate (W)}\end{aligned}$$

The heat transfer process should be repeated for multiple locations in the combustion chamber and nozzle to accurately model the heat transfer occurring in the engine. The value of  $T_{cl\_out}$  at various locations verifies enough heat is transferred to the propellant to power the expander cycle. In addition, the value of  $T_{hw}$  is important in verifying the wall temperatures remain below structural thermal limits.

The Nusselt number is the ratio of convective to conductive heat transfer and is useful in determining the effectiveness of fluid convective heat transfer. Incropera and DeWitt present correlations to estimate the Nusselt number with a disclaimer that the results may be in error as large as 25% [33]. The use of more complex correlations with fewer assumptions made about the flow (i.e. turbulent versus laminar flow, uniform surface heat flux, and smooth surface) could reduce the Nusselt number error. Error in the Nusselt number calculation implies error in the conduction and convection heat transfer calculations. Therefore, reevaluation of the estimated heat transfer values within an acceptable factor of safety should occur to give the designer a conservative or “worst-

“case” temperature and heat transfer rate to guarantee the engine will not structurally fail [33].

The heat transfer from the combustion gases to the coolant must be large enough to power the turbopumps in an expander cycle. The amount of heat transfer from the combustion gases to the coolant is coupled to the surface area of heat exchange. Multiple methods exist to increase the surface area of heat exchange. One option is to increase the length of the combustion chamber [35]. However, extra length adds extra engine weight. Another option is to roughen the combustion chamber and/or coolant wall surfaces. Sutton and Biblarz state the results of surface roughening or turbulence-creating obstructions on the coolant wall surface are reduced coolant wall temperatures and an increase in the absorption of heat by the propellants [23]. On the other hand, surface roughness on the hot gas side of the combustion chamber will cause the exhaust flow to approach stagnation causing increased wall temperatures [23]. Schmidt, Popp and Frohlich found “doubling the coolant side heat transfer, by higher coolant velocity or coolant side surface roughening, would only increase the heat flux to the coolant by about 6-7%” [36]. They concluded the most straightforward design for increased heat transfer is increased surface roughness on the hot gas side [36]. A design trade in cooling jacket design presents itself as to whether there is increased heat transfer or higher wall temperatures.

Other ways to change the heat transfer performance is to change the cooling channel aspect ratio (AR). The cooling channels along the aerospike and combustion chamber walls provide an avenue for the cold propellants to collect heat from the hot exhaust gases all the while keeping the wall temperature below structural thermal limits.

A high aspect ratio channel is generally taller with less surface area along the wall; on the other hand, a low aspect ratio channel is wider with more surface area on the wall. Figure 11 shows the difference between a high and low aspect ratio cooling channel; taken from Martin [4].

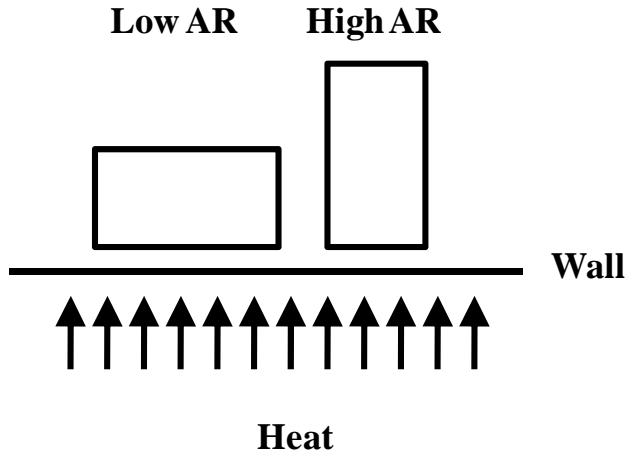


**Figure 11. Channel Aspect Ratio; taken from Martin [4]**

Carlile [37] conducted a high pressure, regeneratively cooled thrust chamber experimental investigation. The experiment included reducing the coolant pressure drop in increments to one-half the baseline chamber pressure. He found adequate heat transfer and reduced wall temperatures occurred in the high AR cooling channels even at lower channel pressures. With lower wall temperatures, Carlile concluded chamber life could be improved; also, reduced channel pressure would allow reduction in the turbopump power requirements [37]. Wadel and Meyer found increasing the surface area of a high AR channel resulted in more efficient heat transfer to the coolant [38]. Increasing channel height and/or changing surface roughness will increase the channel surface area. Wadel and Meyer also found it is possible to design a channel with greater total flow area, reducing the pressure drop, and still gain an increase in heat transfer [38]. Lastly, a

study by Schuff *et al.* found a small flow area, although it increases heat transfer, has a large pressure loss. Overall, higher aspect ratio cooling channels are “advantageous in balancing the pressure loss requirements with the heat transfer demands” [39].

The DEAN combustion chamber and aerospike cooling jackets utilize milled cooling channels with the cross-section design shown in Figure 12 inspired by Martin [4].

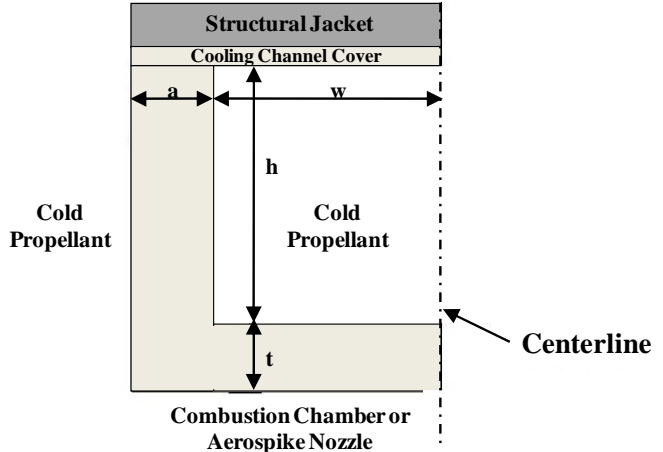


**Figure 12. Cooling Channel Cross-Sectional Design; inspired by Martin [4]**

The total number and size of the cooling channels is constrained by the radius of the combustion chamber and aerospike at each point. The channel in Figure 12 is symmetrical about the centerline. The shaded region is solid material, while the clear area is fluid flow. The parameter ‘a’ is the half spacing between channels, ‘w’ is the half width, ‘t’ is the wall thickness of the channel between hot combusted gases and coolant, and ‘h’ is the height of the channel. “To determine the number of channels, the circumference of the chamber is divided by twice the sum of ‘a’ and ‘w’, since one channel is represented by two times their lengths” [4]. Changing the thickness, height, width, or the aspect ratio of the channel will affect the wall and fluid temperatures and the heat transfer rate. Cooling channel design also influences the flow velocity through the channels; a Mach number constraint must be set for the fluid flow through the

channels to guarantee the flow will not go supersonic or past the physical limits of the propellant.

### ***II.3.f. Turbopump (Turbine and Pump) Theory***

Huzel and Huang state the use of turbopump-fed systems for high thrust, long duration engines can be beneficial over pressurized-gas fed systems by lowering overall engine weight while improving performance [8]. Turbopump-fed systems require low pump inlet pressures allowing the propellant tank pressures to be low. Furthermore, turbopump-fed systems allow for higher chamber pressures equating to higher thrust values. In pressurized-gas fed systems, higher propellant tank pressures lead to increased tank weight affecting total engine weight and performance, namely the *T/W* parameter.

In 2008, to meet Phase III IHPPT goals for upper stage engines, Arguello and Strain developed a detailed turbopump design process leading to complete component level designs for the hydrogen and oxygen turbopumps, respectively, at the DEAN design point found by Martin [4, 40, 41]. A turbopump is a turbine and pump assembly with a shaft connecting the two. Properly designed propellant turbopumps are crucial in powering the DEAN expander cycles; it is how the propellant gets from the propellant tanks to the combustion chamber. The overall design requirement is the turbine must fully provide the required power to the pump.

Arguello utilized a split flow design for the hydrogen pumps in the DEAN [40]. Due to low density of hydrogen, a second pump stage aids in providing enough pressure to force the hydrogen through the expander cycle. Arguello designed the DEAN hydrogen turbopump assuming the combustion chamber pressure is 1,740 psia (12 MPa).

“At the design condition, the turbine delivers 3,607 horsepower (2.7 MW) at a total pressure ratio of 1.84; the turbopump flow rates are 15.1 and 7.55 lb<sub>m</sub>/s (6.8 and 3.4 kg/s) into the first and second stage, respectively” [40]. The pump stage 1 and 2 and turbine efficiencies are 0.77, 0.80, and 0.977, respectively, with a turbopump shaft rotation speed of 110,000 rpm. The first and second stage pumps use unshrouded impellers and the turbine is a full admission reaction type. Figure 13 shows a schematic and a solid model of the DEAN hydrogen turbopump rotor assembly from Arguello [40] (government work with no copyright).

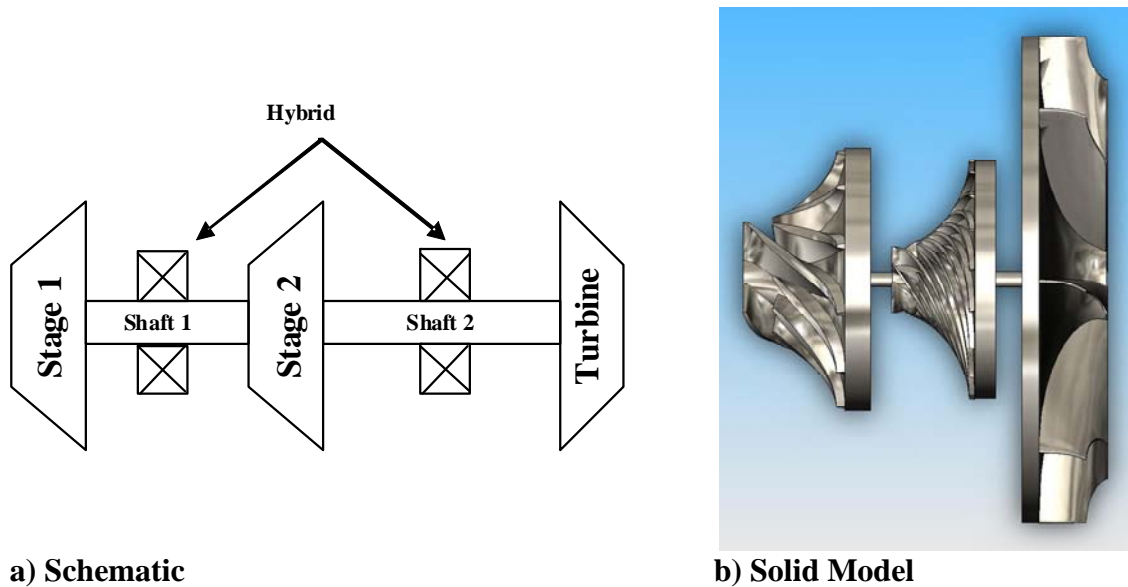
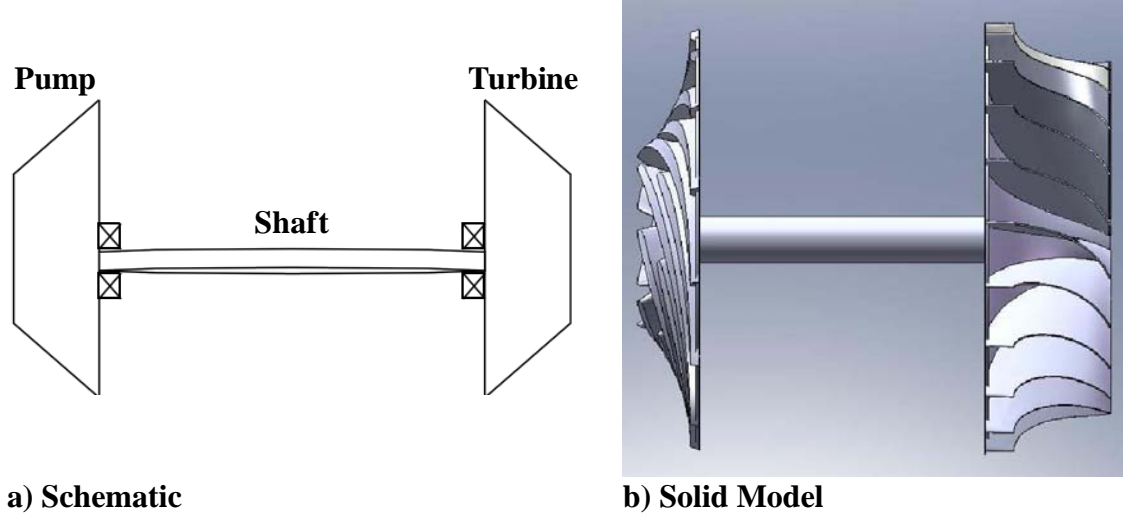


**Figure 13. Schematic and Solid Model of the DEAN Hydrogen Turbopump Rotor Assembly; taken from Arguello [40]**

Strain designed the DEAN liquid oxygen turbopump. To meet the needs of the DEAN engine, the turbopump had the following design requirements: “the pump needs to be capable of delivering 106 lbm/s (48.1 kg/s) at 4500 psi (31 MPa); this will necessitate a turbine capable of supplying at least 2215 hp (1652 kW)” [41]. The pump and turbine efficiencies are 0.773 and 0.941, respectively, with a turbopump shaft rotation speed of

32,000 rpm. Figure 14 shows a schematic and a solid model of the DEAN oxygen turbopump rotor assembly from Strain [41] (government work with no copyright).



a) Schematic

b) Solid Model

**Figure 14. Schematic and Solid Model of the DEAN Oxygen Turbopump Rotor Assembly; take from Strain [41]**

Each turbopump design requires a pressure budget to guarantee the turbine provides enough power to pump the propellants from the propellant tanks to the combustion chamber while accounting for pressure losses in the closed system. Humble *et al.* [20] outline a pressure budget process. To summarize the process, working backwards from the combustion chamber where the design chamber pressure is known, the pressure drop through the injectors is calculated, then through the turbine, then the cooling jacket, then viscous pipe losses and dynamic pressure losses can be calculated, and finally calculation of the required pump output pressure can be found. Knowing the pump input pressure is equal to the tank pressure, a required rise in pump pressure ( $\Delta p_p$ ) can be found; this value is vital in designing the turbopump. Figure 15 shows a flow chart of the fluid flow through the engine in reverse.

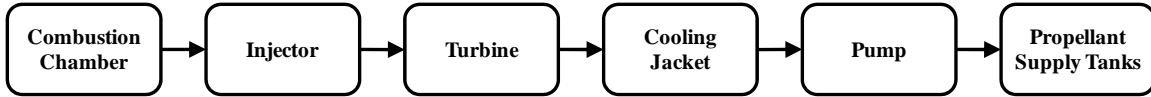


**Figure 15. Reversed Fluid Flow Diagram for Pressure Budget Analysis**

The pressure loss through the injectors is to “isolate chamber-pressure oscillations from the feed system, reducing pressure coupling between the combustion chamber and the feed system which could lead to instabilities or oscillations in the flow that are driven by variations in combustion” [20]. If needed, the injector pressure drop or loss is a useful throttling tool. The chamber pressure plus the pressure drop value of the chamber pressure equals the pressure prior to the flow entering the injectors. Humble *et al.* state a pressure drop equal to 30% for throttled engines and 20% for unthrottled engines [20].

Next, the pressure drop through the turbine can be found. A turbine pressure ratio needs to be assumed to complete the pressure budget initially; however, the turbine pressure ratio can later be tweaked during turbopump design to ensure the power available by the turbine is slightly greater than or equal to the power required by the pump. The output pressure of the turbine is equal to the pressure into the injectors while the input pressure to the turbine is equal to the turbine pressure ratio multiplied by the output pressure.

Following the turbine pressure drop calculation, the pressure drop through the cooling jacket can be found. For a regenerative cooling system, Humble *et al.* suggest a pressure drop of 15% of the chamber pressure; this value is based on historical data trends [20]. The pressure prior to entering the cooling jacket is equal to the input turbine pressure plus 15% of the chamber pressure.

The pressure drop due to viscous losses in the piping and the dynamic pressure losses can be calculated. Recognize the value of the viscous and dynamic pressure losses are the summation of these losses throughout the entire system. Viscous pipe losses are typically small compared to the combustion chamber pressure but should still be accounted for. The following relationship calculates the dynamic pressure loss:

$$\Delta p_{dynamic} = \frac{1}{2} \rho v^2 \quad (21)$$

where

$\Delta p_{dynamic}$	=	Dynamic Pressure Loss
$\rho$	=	Fluid Density (slug/ft <sup>3</sup> )
$v$	=	Flow Velocity in Piping

Lastly, the required rise in pump pressure can be found by taking the required pump output pressure and subtracting the tank pressure. A tank pressure is assumed to start the pressure budget process. The assumption is based on understanding the tank pressure is a function of propellant density and the tank pressure must be greater than the vapor pressure to avoid cavitation. The rise in pump pressure is vital in calculating the power required from the turbine.

When the pressure budget is complete, the initial tank pressure will be low. As the flow travels to the combustion chamber, the pressure will decrease incrementally from its maximum value at the pump to the chamber pressure value by multiple losses and designed pressure drops in the system.

Since the DEAN utilizes the expander cycle and regenerative cooling, the heat absorbed by the cold propellants is the energy used to drive the turbopump. Humble *et al.* lay out a detailed process to design a turbopump [20]. The main outputs from the

process are power required by the pump ( $P_{req}$ ) and power available from the turbine ( $P_{available}$ ). The following relationships by Humble *et al.* calculate the  $P_{req}$  and the  $P_{available}$  [20]:

$$P_{req} = \frac{g_o \dot{m} H_p}{\eta_p} = P_{available} = \eta_T \dot{m}_T c_p T_i \left[ 1 - \left( \frac{1}{p_{trat}} \right)^{\frac{\gamma-1}{\gamma}} \right] \quad (22)$$

where

$$\begin{aligned}
 P_{req} &= \text{Pump Power Required (horsepower)} \\
 H_p &= \text{Pump Head Pressure Rise (ft)} = \frac{\Delta p_p}{g_o \rho} \\
 \eta_p &= \text{Pump Efficiency} \\
 \dot{m} &= \text{Mass Flow Rate through the Pump (slugs/s)} \\
 P_{available} &= \text{Turbine Power Available (horsepower)} \\
 \eta_T &= \text{Turbine Efficiency} \\
 \dot{m}_T &= \text{Mass Flow Rate through the Turbine (slugs/s)} \\
 c_p &= \text{Constant Pressure Specific Heat of the Turbine Gases} \\
 p_{trat} &= \text{Turbine Pressure Ratio} \\
 \gamma &= \text{Turbine Gas Ratio of Specific Heats}
 \end{aligned}$$

The design process by Humble *et al.* is iterative until the power values are equal or close to equal within an acceptable tolerance [20]. With the turbine and pump designed, the final steps are to select a turbopump bearing, select a turbopump arrangement, and calculate the weight of the complete unit.

The turbopump design process by Arguello and Strain is more precise [40, 41], but for a single engine design point. The process by Humble *et al.* [20] gives a rough estimate of the turbopump size and properties useful for a system level model evaluating multiple design points.

### ***II.3.g. Basic Injector and Plumbing Theory***

The injector is an essential component to the combustion chamber and the engine as a whole. It injects, atomizes, mixes, and ignites the propellants in the combustion chamber while maintaining the required mixture ratio. The injector will also close off the top of the combustion chamber from the high temperatures and pressures it contains; the injector prevents the combustion flame from traveling into the propellant feed lines [8]. Furthermore, the injector determines excitation of combustion instability modes and, if required for the mission, throttles the engine. The performance of the injector directly influences the performance of the engine.

There are a variety of factors affecting the performance and operation of injectors such as injection orifice pattern and size, heat transfer, combustion instability, and structural design. The injection orifice pattern/size can affect mixture ratio, chemical reactivity of the propellants, and the speed of mixing/atomization of the propellants. The injector design needs to withstand the high temperatures in the combustion chamber without structurally failing; therefore, heat transfer is important in injector design. A low pressure drop across the injector is desired to minimize engine weight and pumping power; however, higher pressure drops are needed to damp combustion instabilities and enhance atomization of the propellants [23]. The structure of the injector must be able to withstand pressures from the combustion chamber and propellant feed system, withstand hot and cold temperatures from the combustion and incoming propellants, and prevent premature fuel and oxidizer interaction.

A variety of injector designs currently exist such as doublets, triplets, shear coaxial gas/liquid injectors and pintle injectors. The two broad injector categories are

impinging and nonimpinging. Impinging, the most popular approach, refers to two or more propellant streams striking one another to atomize the propellant [20]. The doublets and triplets inject either like or unlike propellants at an angle into each other. The shear coaxial gas/liquid injector flows gas propellant through a passage on either side of a liquid propellant passage. When the gas and liquid propellants meet at the end, they atomize and mix. Pintle injectors are an impressive, simple design delivering enhanced engine throttability and high combustion efficiencies [25]. Surprisingly “there has never been an instance of combustion instability in a Pintle engine during any ground or flight operations” [25]. Figure 16 shows the pintle injector design obtained from Martin [4] (government work with no copyright).

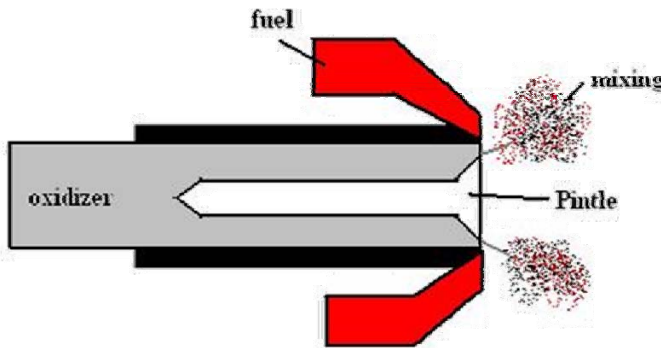


**Figure 16. Pintle Injector Design; taken from Martin [4]**

A properly designed injector is vital to a successful rocket engine. Detailed injector design will be performed during component level design of the DEAN engine in future work.

Plumbing connects all the engine components to each other. Huzel and Huang state “an optimum balance between low pressure-drop (by making the duct diameter as large as possible) and structural integrity” is the design trade in plumbing [8]. Plumbing is sometimes referred to as propellant supply ducts. It is imperative the plumbing

connections to the engine components not leak nor allow any movement of the pipe to cause excessive stress to another engine component, pipe or connector. In addition, fluid flow through the plumbing must maintain a Mach number below the physical limits of the propellant. Furthermore, a design concern is fluid heat transfer in the plumbing. Plumbing heat transfer accounts for a loss in overall engine efficiency; shorter ducts can minimize the amount of efficiency loss. The pipes will be subject to internal pressures, a range of temperatures, and vibrations during engine operation; it is important to account for all of these in the design. Due to the flow fluid changing through the different engine components, the size of the piping may change. For example, the cold propellant duct leading flow to the pump will differ from the hot propellant duct leading flow away from the turbine.

Assuming the piping calculated for the cold propellant entering the pump is equal to the piping required for the entire flow all the way to the combustion chamber, the following relationship calculates the pipe cross-sectional area:

$$\dot{m} = \rho A v \quad (23)$$

where

$\dot{m}$	=	Propellant Mass Flow Rate (slug/s)
$\rho$	=	Density of the cold propellant (slug/m <sup>3</sup> )
$A$	=	Pipe Cross-Sectional Area (ft <sup>2</sup> )
$v$	=	Velocity of the Fluid Flow in Piping (ft/s)

Knowing the pipe cross-sectional area, the inner pipe radius can be found using the formula for the area of a circle. The thickness and outer pipe diameter is found knowing the maximum pressure in the pipe and performing pressure vessel structural calculations. The calculated pressure vessel stress is compared to a chosen material

ultimate or yield strength and the pipe thickness is allowed to vary until the two stresses are equal within an acceptable factor of safety. Assuming a total pipe length and knowing the chosen material properties, the pipe weight can be calculated by multiplying the material density by the volume. Pipe volume is equal to:

$$V = \frac{\pi}{4} (d_o^2 - d_i^2) l \quad (24)$$

where

$$\begin{aligned} V &= \text{Pipe Volume (ft}^3\text{)} \\ d_o &= \text{Pipe Outer Diameter (ft)} \\ d_i &= \text{Pipe Inner Diameter (ft)} \\ l &= \text{Total Piping Length (ft)} \end{aligned}$$

### ***II.3.h. Material Choice***

Certain materials react negatively to certain propellants. It is vital the material chosen for the engine, especially the combustion chamber and nozzle, withstand the high combustion temperatures, the high chamber and cooling channel pressures, and any corrosive effects of the propellants. If the engine is to be reusable, then staying under the material thermal and structural limits is necessary within an acceptable factor of safety.

In the current DEAN design, the propellants are cryogenic requiring the engine material to be able to withstand a vast range of temperatures while keeping structural integrity. To make the DEAN reusable, Martin set the thermal limits of the material selected for the current model at a conservative 50% of the material melting point [4]. In addition, the material selected was chosen because it does not react negatively to the propellants; this is important so the material does not become brittle and crack. The cooling portion of the aerospike is made of copper while the non-cooling portion

(aerospike tip) is niobium; the cooling portion of the combustion chamber is made of silicon carbide with a structural jacket wrapping of aluminum [4].

#### **II.4 Past DEAN Research Efforts**

Martin and Simmons completed previous work at AFIT. Martin created an initial design model and validated the feasibility of the DEAN concept. Simmons enhanced previous research by parameterizing the design model created by Martin to allow exploration of the solution space; also, Simmons created a system level model for optimization studies. The results of past research demonstrated the DEAN is able to meet or exceed the design requirements.

David Martin utilized the Numerical Propulsion System Simulation (NPSS<sup>TM</sup>) software tool to design the initial DEAN computational model [4]. NPSS, designed by NASA and the aerospace propulsion industry, is a high fidelity computer simulation tool for modeling aircraft and rocket propulsion systems [43]. The DEAN model designed by Martin includes NPSS elements linked together to accurately represent DEAN engine components such as the combustion chamber, aerospike nozzle, tanks, plumbing, cooling jackets, and turbopumps [4].

Realistically the cooling jackets in the DEAN are continuous volumes; however, NPSS represents them as a series of discrete stations. Figure 17, inspired by Martin [4], shows the locations of the stations in the model using the original engine design with a 24 inch (60.96 cm) chamber and a 14 inch (35.56 cm) aerospike nozzle extending from the throat. The chamber is modeled using five equally spaced segments, with stations at the midpoint of each segment, and a sixth station located at the engine throat. The aerospike

contains eight total stations with five located in the chamber, one at the throat, and two additional stations in the first half of the nozzle. The oxidizer loop (the outer wall of the chamber) and the fuel loop (the aerospike) are represented by separate sets of stations and are represented as blue diamonds and red stars in Figure 17, respectively. The concept of the station locations is constant regardless of how parametric studies change the axial and radial geometry of the chamber and aerospike. The stations are used to both represent combusted gas flow and/or heat exchange in the combustion chamber and cold propellant flow through the chamber and aerospike cooling jackets.

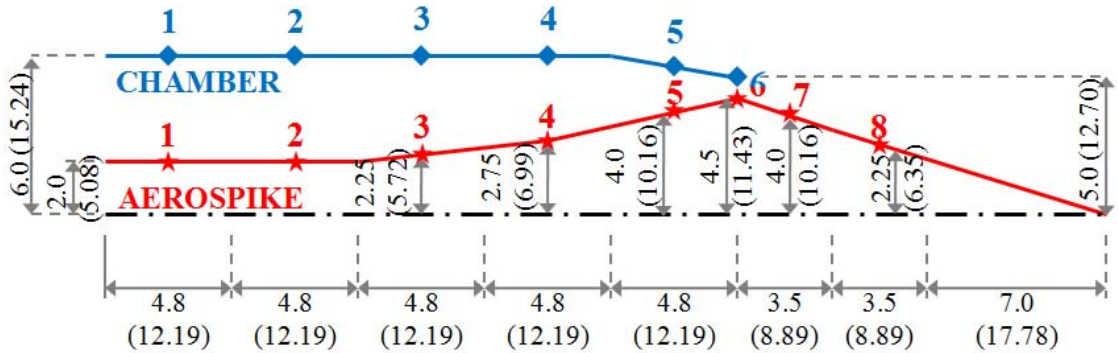


**Figure 17. DEAN Geometry with Station Numbers (dimensions in inches (centimeters)); inspired by Martin [4]**

The DEAN model by Martin not only met, but also exceeded the design objectives proving the feasibility of the engine. Table 4 tabulates the design and response variables at the DEAN design point found by Martin [4]. Martin approximated a thrust-to-weight ratio ( $T/W$ ) of 119 [4]. The ratio accounts for nozzle, combustion chamber, and propellant turbo machinery weight; it does not account for plumbing.

**Table 4. DEAN Design Parameters from Martin [4]**

Design Variables		Response Variables	
LOX Pump Pressure Ratio	103	Vacuum Thrust	57,000 lbf (254 kN)
LH <sub>2</sub> Pump 1 Pressure Ratio	45	Vacuum $I_{sp}$	472 s
LH <sub>2</sub> Pump 2 Pressure Ratio	2	Total Mass Flow	121 lb <sub>m</sub> /s (54.9 kg/s)
LH <sub>2</sub> Pump 2 Efficiency	0.83	$O/F$	7.03
Chamber Length	24 in (60.96 cm)	Chamber Pressure	1739 psia (11.9 MPa)
Chamber Radius at Injector Face	6 in (15.24 cm)	Chamber Temperature	6586 R (3658.9 K)
Aerospike Radius at Injector Face	2 in (5.08 cm)	LOX Pump Efficiency	0.66
Chamber Volume	2075 in <sup>3</sup> (0.034 m <sup>3</sup> )	LOX Pump Power	2587 HP (1.93 MW)
Throat Area	15.9 in <sup>2</sup> (102.6 cm <sup>2</sup> )	LH <sub>2</sub> Pump 1 Efficiency	0.67
Aerospike Nozzle Length	14 in (35.56 cm)	LH <sub>2</sub> Pump 1 Power	2527 HP (1.88 MW)
Expansion Ratio	125	LH <sub>2</sub> Pump 2 Power	1046 HP (0.78 MW)
		LOX Turbine Pressure Ratio	1.82
		LOX Turbine Efficiency	0.95
		LOX Turbine Power	2587 HP (1.93 MW)
		LH <sub>2</sub> Turbine Pressure Ratio	1.84
		LH <sub>2</sub> Turbine Efficiency	0.9
		LH <sub>2</sub> Turbine Power	3573 HP (2.66 MW)

Simmons enhanced the research performed by Martin by parameterizing the NPSS model to allow exploration of the solution space and created a system level model for optimization studies [5, 6].

Before modifying the DEAN model to support parametric trade studies to explore the solution space, Simmons performed two NPSS architecture changes to the fuel expander cycle. The first change removed the liquid hydrogen bypass, thus allowing the cooling jacket for the aerospike to utilize the full mass flow of the liquid hydrogen. The second change required the two fuel pumps run at the same pressure ratio. The change minimized the maximum pressure ratio required for the fuel pumps [6].

The parametric DEAN model uses two types of parameters: geometry parameters and rocket engine parameters. Simmons simplified the geometry of the aerospike nozzle and cooling volumes to linear approximations from higher order calculations (for example, Martin [4] calculated the aerospike nozzle radii using the method of characteristics in a separate effort) [5, 6]. With fixed DEAN thrust and  $I_{sp}$  requirements, Simmons altered the design variables to support optimization studies focusing on minimizing engine weight and maximizing engine  $T/W$ . Geometry and material selection drive chamber and aerospike weight, while the propellant mass flows drive the turbopump weight [20]. The new design variables became the chamber and aerospike geometries and the propellant mass flows to the turbopumps.

Under some configurations in the NPSS model by Martin, the independent pump efficiencies would be set to unattainable or unrealistic values by the NPSS solver. For example, due to the pump efficiencies being independent variables, the output NPSS turbopump efficiencies in Table 4 differ from the detailed component level design turbopump efficiencies from Strain and Arguello mentioned in section II.3.f [40, 41]. In addition, the two user specified fuel pump pressure ratios would define the  $O/F$  ratio indirectly leading to coupled effects in  $O/F$  trade studies. To correct these issues, the

pump efficiencies became NPSS component inputs and another NPSS dependent variable was added to set the two fuel pump pressure ratios equal to each other [5, 6]. Table 5 tabulates the NPSS input turbopump efficiencies; the values originated as “guess” inputs in the NPSS model by Martin [4-6]. The rocket engine parameters, such as *O/F* ratio and total engine mass flow, were made available as overall user design variables by changing the dependent variables in the model; note the propellant mass flows to the turbopumps are functions of the total engine mass flow and the *O/F* ratio. The new design variables cause the throat area and the pressure ratios for all three pumps to become responses in the NPSS model as opposed to hard-coded values [6].

**Table 5. Turbopump Parameters from Martin and Simmons [4-6]**

<b>OXIDIZER</b>	
Pump Efficiency	0.773
Pump Gear Ratio	1.0
Turbine Efficiency	0.949
Shaft Mechanical Speed (rpm)	32,000
<b>FUEL</b>	
Pump #1 Efficiency	0.8
Pump #1 Gear Ratio	1.0
Pump #2 Efficiency	0.83
Pump #2 Gear Ratio	1.0
Turbine Efficiency	0.9
Shaft Mechanical Speed (rpm)	110,000

Simmons made one final change to the NPSS model. In the model created by Martin, the mass flow through the oxidizer bypass was hard coded to a specific value. A specified bypass value would cause instabilities in the model when the system mass flow or the *O/F* ratio would change; both system mass flow and *O/F* affect the total oxidizer mass flow [6]. To address the instability, the *O/F* ratio and total system mass flow were

held constant as design variables and the oxidizer mass flow through the bypass was set to 10% of the total oxidizer mass flow. The percentage of oxidizer bypass and the design variables were made user configurable.

Simmons built a system level model of the DEAN using the ModelCenter<sup>TM</sup> software by Phoenix Integration. ModelCenter is a diverse modeling tool allowing designers to more quickly and efficiently examine design trade spaces and perform optimization studies while keeping design constraints in place. The DEAN system level model contained the parametric NPSS DEAN model, along with other required modeling elements such as capability to calculate fluid Mach numbers through the engine [6].

Simmons performed parametric trade studies with the updated NPSS/ModelCenter DEAN model over varying chamber lengths, *O/F* ratios, and total engine mass flow rates to determine design trade space boundaries [6]. The results of the trade studies were significant in finding a new starting point for optimization studies and discovering if the fluid Mach numbers are within reasonable subsonic limits. Through the trade studies, Simmons was able to reduce the size of the turbopumps by reducing the total engine mass flow. Simmons also found an improved *O/F* ratio increasing performance and found the overall engine length could be reduced by 25% compared to the original design by Martin, all the while meeting the thrust and  $I_{sp}$  design requirements. Table 6 summarizes the new DEAN design parameters utilizing results from the parametric trade studies [6].

**Table 6. DEAN Design Parameters from Simmons [6]**

Design Variables		Response Variables	
<i>O/F</i>	6.0	Vacuum Thrust	50,900 lb <sub>f</sub> (226 kN)
Total Engine Mass Flow	104 lb <sub>m</sub> /s (47.2 kg/s)	Vacuum $I_{sp}$	489 s
Chamber Length	14.25 in (36.19 cm)	Chamber Pressure	1310 psia (9.0 MPa)
Chamber Radius at Injector Face	6 in (15.24 cm)	Chamber Temperature	6413 R (3562.8 K)
Aerospike Radius at Injector Face	2 in (5.08 cm)	Throat Area	18.9 in <sup>2</sup> (121.9 cm <sup>2</sup> )
Expansion Ratio	125	Nozzle Length	13.6 in (34.5 cm)
		LOX Temperatures in Plumbing	160-435 R (88.9-241.7 K)
		LOX Pressure in Plumbing	2450-2600 psia (16.9-17.9 MPa)
		Max LOX Mach Number	0.37
		LH <sub>2</sub> Temperature in Plumbing	73-324 R (40.6-180.0 K)
		LH <sub>2</sub> Pressures in Plumbing	2960-3770 psia (20.4-26.0 MPa)
		Max LH <sub>2</sub> Mach Number	0.96

### III. Methodology

Chapter 3 discusses the methodology implemented to optimize the DEAN design while attempting to meet the design goals of 50,000 lb<sub>f</sub> (222.4 kN) of vacuum thrust, 464 sec of vacuum  $I_{sp}$ , and a thrust-to-weight ratio of 106.5. ModelCenter, NPSS, CEA, and TDK'04 are the main computational tools utilized for the research effort.

The chapter will begin with an overview of the ModelCenter software. Next, the chapter discusses the computer software utilized and an explanation of the final ModelCenter DEAN model and all its elements. The chapter concludes with verification and validation of the model followed by the process to meet the research objectives.

#### III.1 ModelCenter Overview

ModelCenter, by Phoenix Integration, is a powerful integration tool for engineering models with multiple components. ModelCenter has the ability to link multiple programs such as NPSS, CEA, TDK, Microsoft Excel, MATLAB, MathCad, and command line executables into a single model. Outputs from one program can be linked as inputs into another program allowing for automation of engineering design calculations. Furthermore, ModelCenter has a script component based on the VBScript programming language. The script component is useful for many applications such as performing intermediary calculations between different elements.

Built-in ModelCenter features include tools to perform optimization studies and parametric trade studies of the design space. The parametric trade study tool allows engineers to explore the solution space of the design and determine what variables are key design drivers. ModelCenter includes three unique optimization tools: a gradient

optimizer, a genetic optimizer called Darwin<sup>TM</sup>, and “an optimizer that utilizes surrogate models of the design space during optimization called DesignExplorer<sup>TM</sup>” [6, 42]. The designer also has the ability to render a visual representation of the engineering design in the user interface of ModelCenter.

This versatile program in building and executing a design model, allowing for exploration of the solution space, and enabling optimization studies makes ModelCenter the program of choice for continued DEAN research.

Designers have two model options in ModelCenter: data or process model. The data dependency model, or simply known as the data model, executes by how the individual model components are linked. More specifically, the ModelCenter scheduler will automatically execute one element to get specific outputs required by another element that requires those outputs as inputs. The data model is easy to build and execute as long as there are not many loops driving variable convergence. The process model is a “graphical flowchart-like model that explicitly tells ModelCenter what order (and under what conditions) to run each component” (a top-down system design and execution model) [42]. The benefit of the process model is the user can tell ModelCenter exactly how to execute the model. Furthermore, the process model has the ability to execute certain model components based on “if” commands and the ability to execute elements in parallel. Most importantly, the process model can better deal with variable convergence loops. The data model was selected as the model choice for the DEAN concept due to its simplicity to build [42].

Phoenix Integration verified and validated the ModelCenter program, along with its built-in tools, prior to the public release of the software. However, the model designer

must verify and validate their individual models built in ModelCenter. Phoenix certifies their components will function as stated in the user manual. It is up to the user to ensure their model, with all its links to different elements, functions as expected through multiple trade studies. The DEAN model will be validated and verified as part of the current research effort.

### **III.2 NPSS**

This section provides a quick overview of the Numerical Propulsion System Simulation (NPSS) program and an explanation of how NPSS models the DEAN concept.

#### ***III.2.a. NPSS Overview***

The Numerical Propulsion System Simulation (NPSS) program is a highly reliable computer simulation tool for modeling aircraft and rocket propulsion systems. The program was developed by the NASA Glenn Research Center in partnership with the DoD and the aerospace propulsion industry. NPSS serves to provide realistic fluid flow and physical interactions in an engine, “accelerate concept-to-production development time and reduce the need for expensive full-scale tests and experiments” [43].

Models constructed in NPSS contain a series of interconnected software objects, known as elements, representing the components of the engine under consideration. Each element has a coded set of inputs and outputs, independent and dependent variables, and equations to calculate the required outputs. NPSS has a variety of built-in elements along with capability for a user to edit existing elements or create a new element. Ports link the elements to each other. The ports perform multiple roles, such as modeling fluid flow

and/or heat transfer between the individual elements. NPSS includes multiple thermodynamic gas property packages for air breathing and rocket engine analysis. A built-in solver drives the design variables of the model to balance the fluid flows, mechanical connections, and thermal flows in the model to converge to a closed design point [43]. In essence, the solver will perform conservation equations such as conservation of mass and energy through the engine. The built-in solver is user configurable.

For rocket engine models, the NPSS *Rockets Supplement* recommends use of the CEA thermodynamic gas property package for modeling combustion and determining combustion product concentrations [44]. Chemical Equilibrium with Applications (CEA), a NASA computer program, calculates chemical equilibrium product concentrations from any set of reactants, determines thermodynamic and transport properties for the product mixture, and calculates theoretical rocket performance [46]. Utilizing CEA source code in NPSS is useful for rocket propellants other than hydrogen and oxygen. NPSS has a built-in compiled thermodynamic gas property package known as “Rocets” designed solely for hydrogen and oxygen combustion; “Rocets” is loosely based on CEA [44]. The DEAN model built by Martin utilizes the “Rocets” package [4]. NPSS assumes the combustion efficiency in the combustion chamber is 100%.

NASA verified and validated the NPSS software in conjunction with industry. Multiple operating engines, both air breathing and rocket engines, were designed in NPSS and the outputs from the engine models were validated with the parameters of the actual engines. For example, NASA performed successful NPSS analyses on the RL-10.

The elements in NPSS are valid as long as they are utilized in the same manner as stated in the user guide [43, 44].

### ***III.2.b. NPSS Elements***

NPSS power balances the dual expander cycles of the DEAN. The DEAN model utilizes multiple built-in NPSS elements. Some of the built-in elements were tailored due to the modeling approach. The NPSS elements utilized for DEAN engine components are as follows [4, 43, 44]:

- 1) *RocketComb1* to model the combustion chamber. Primarily, the element performs thermo chemistry calculations using the “Rocets” thermodynamic package. The element also calculates the hot side convection heat transfer coefficient for the chamber and aerospike walls separating the combusted gases from the coolant in the cooling jackets. Included are both the oxidizer cooling jacket (chamber) and the internal portion of the fuel cooling jacket (aerospike). The cooling jacket contains the propellant that absorbs heat to drive the propellant expander cycle. Element inputs include propellant choice, chamber radius, fluid flow volume, propellant mixture ratio (*O/F*), weight flow, and guesses for chamber temperature and chamber pressure. The element also includes *ThermalOutputPorts* to model heat transfer and requires the radius at the specific port location, the cross-sectional area of the combusting flow in the chamber, and the surface area of the portion of the chamber in contact with the combusting flow as inputs [5, 44].
- 2) *RocketNozzle* to model the aerospike nozzle in the Linear NPSS model. Element inputs include throat area, nozzle expansion ratio ( $\epsilon$ ) and ambient pressure. The

element also includes *ThermalOutputPorts* to model the heat exchange between the cooled portion of the aerospike and the fuel cooling jacket.

- 3) *RocketNozzleAerospike* models the aerospike nozzle in the nonlinear NPSS model. The element is a tailored version of the *RocketNozzle* element. All the same outputs of the original element are calculated, except the addition of code to calculate the momentum thrust out the throat. The variable  $\theta$  was added to the code as an input.  $\theta$  is the angle of the flow out the throat referenced to the axisymmetric centerline plane of the engine; the default value is zero degrees.
- 4) *Starter* elements to model the oxidizer and fuel propellant tanks. The element starts fluid flow. Element inputs include tank temperature and pressure.
- 5) *Valve04* and *CoolingVolume02* to model the plumbing. *Valve04* requires cross-sectional area and a pressure loss coefficient to model the pressure drop in the plumbing. *CoolingVolume02* requires cross-sectional area and fluid volume to model the heat loss. *CoolingVolume02* was edited to include a reference value of 100 BTU/lb<sub>m</sub> in the total enthalpy calculation of the element; the edited code was included in the thesis document written by Martin [4]. *CoolingVolume02* includes *UnReactedFluidOutputPorts* to allow mass flow from one element to the next.
- 6) Combination of *Valve04*, *CoolingVolume02* and *Wall2* to model the cooling jackets. *Valve04* was utilized in the same way as mentioned for plumbing. *CoolingVolume* was utilized to model the change in energy of the flow and *Wall2* was utilized to model the heat transfer from the combustion chamber to the coolant. *CoolingVolume02* inputs include cross-sectional area, fluid volume, and number of cooling channels. *Wall2* requires a guessed wall temperature at a

minimum. Other optional *Wall2* inputs include specific heat capacity at constant pressure, thermal coefficient and the density of the wall material. The combination of the *CoolingVolume02*, *RocketComb1* and *Wall2* elements will output a hot and cold side convective heat transfer coefficient that can be utilized outside NPSS to calculate the true wall temperature with user selected materials. *CoolingVolume02* elements in the cooling jacket use *ThermalOutputPorts* to exchange heat and *UnReactedFluidOutputPorts* to allow mass flow between elements.

- 7) Customized *Pump02* element to model the pumps. Required inputs include weight flow, gear ratio, efficiency, and a guessed pressure ratio.
- 8) Customized *Turb03* element to model the turbines. Required inputs include weight flow and efficiency. The tailored pump and turbine element source codes are included in Martin's thesis [4].
- 9) *Shaft* to model the link between the pump and turbine. The element performs the power balance and ensures the turbine provides enough power to the pump to drive the expander cycle. The only input required is a guessed mechanical rotational speed with units in revolutions per minute (RPM). NPSS will vary the mechanical rotational speed to balance the pump and turbine torques.

A complete list of required inputs, outputs, and a detailed description of the element and its potential uses are available in the NPSS user guide [43, 44]. The DEAN NPSS model contains 70 elements linked together. Figure 18 is a diagram of the NPSS components. Figure 19 is a diagram of the DEAN with corresponding stations and what NPSS element names used in the source code apply to the station.

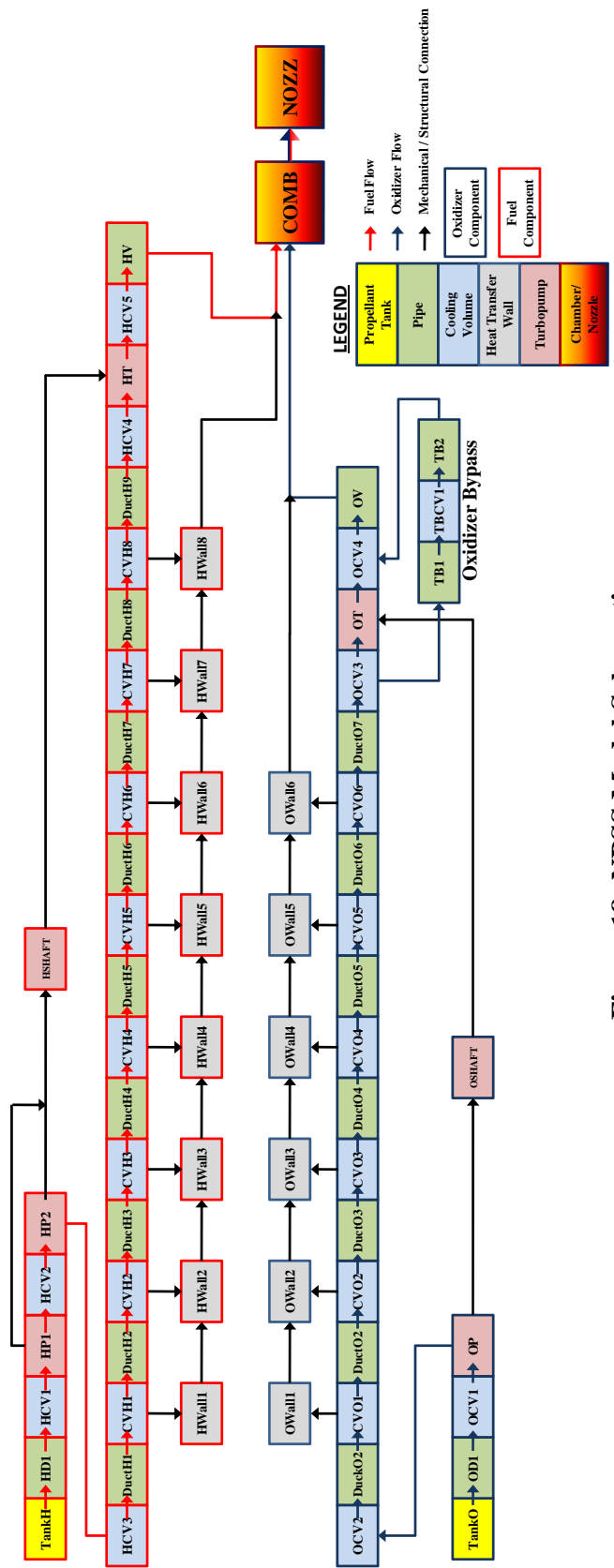
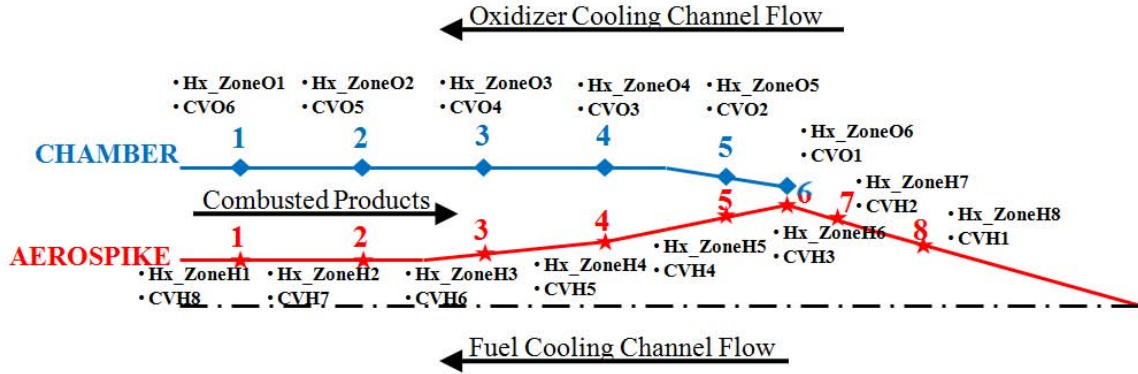


Figure 18: NPSS Model Schematic



**Figure 19. NPSS Elements at DEAN Stations**

### III.2.c. DEAN NPSS Model

The architecture of the NPSS model for the current research effort is similar to the architecture by Simmons [5]. The specific differences are discussed in Appendix C.1.

Two variations of the enhanced NPSS model were developed: a linear model and a nonlinear model. The linear and nonlinear models are very similar in that they both balance the engine expander cycles and both assume linear approximations for the aerospike geometry internal to the combustion chamber. However, the linear and nonlinear models differ in numerous ways. The linear model utilizes linear approximations developed by Simmons [5, 6] for the aerospike nozzle and uses bell nozzle performance calculations. The nonlinear model utilizes the nonlinear aerospike nozzle geometry and calculates the momentum thrust of the engine. The output momentum thrust from the nonlinear NPSS model is used in combination with other DEAN ModelCenter elements to calculate total engine performance independently. Both models run in the final ModelCenter DEAN model; section III.4 discusses their individual applications in the final model.

NPSS variable sensitivity analyses were performed on the linear and nonlinear NPSS models to determine how certain “guess” inputs influence the outputs. The sensitivity analyses led to simplifications in NPSS model execution without negatively influencing the outputs of interest. Appendix C.3 discusses the details of the sensitivity analyses.

Both the linear and nonlinear NPSS models are extremely brittle. An unknown coupled relationship between the design variables and the NPSS inputs exist in each NPSS model. Chamber length, chamber and aerospike radii at the injector face, engine mass flow rate, percentage oxidizer bypassing the turbine, and oxygen and hydrogen cooling channel geometry, such as aspect ratio and initial half-width, all need to be the right combination to prevent NPSS errors. Multiple attempts were made to find the relationship to open opportunities for optimization studies. Currently with the NPSS models as is, the user must change the design variables and NPSS inputs manually until a combination leads to successful NPSS execution, especially for changes in radial geometry.

Appendix C.4 documents the NPSS troubleshooting in an attempt to add flexibility to the model. One option did provide additional model flexibility to the aerospike radius at the injector face design variable. The option uses constant cooling channel cross-sectional areas instead of constant cooling channel aspect ratios used in previous research. Constant cooling channel cross-sectional areas allowed evaluation of multiple aerospike radii points with a constant chamber radius, whereas the constant cooling channel aspect ratios could only evaluate one or two aerospike radii with constant chamber radius. The increase in NPSS flexibility, although only on the aerospike side, is

an improvement. From the increased flexibility, new design solutions could be evaluated. For example, as the aerospike radius approaches the chamber radius, the chamber pressure increases leading to a smaller throat area and improved thrust and specific impulse. The final ModelCenter DEAN model utilizes constant cooling channel cross-sectional areas.

### **III.3 TDK and Aerospike Nozzle Design Altitude**

In previous research, Martin utilized Two-Dimensional Kinetics (TDK'04), a full method of characteristics (MOC) analysis, for calculating the aerospike nozzle geometry extending from the throat [4]. Simmons simplified the geometry of the aerospike to linear approximations [5, 6]. For the current research effort, TDK'04 will be utilized; however, in a different manner than Martin.

Besides just obtaining the MOC aerospike nozzle geometry, the pressure profile along the aerospike nozzle is desired. The pressure profile would allow for calculation of the individual pressure thrust component acting along the nozzle and thus a more accurate thrust estimate for the DEAN. Furthermore, pressure thrust losses due to viscous effects are also desired and can be calculated in TDK'04.

This section will present an overview of the method of characteristics, introduce TDK'04, discuss the use of TDK in the final DEAN ModelCenter model, and conclude with a discussion on the design altitude of the aerospike nozzle.

#### ***III.3.a. Method of Characteristics Overview***

Anderson [47] presents the basic procedure for performing an axisymmetric method of characteristics. The assumptions made to solve the problem are irrotational

and inviscid flow, no shocks along the nozzle wall, and a choked nozzle throat. Equations 25-27 are the four equations required to calculate the four unknowns ( $\theta$ ,  $r$ ,  $M$ ,  $x$ ), where  $v$  and  $\mu$  are functions of  $M$ . Anderson recommends utilizing the finite difference method in solving the problem [47].

$$\left(\frac{dr}{dx}\right)_{char} = \tan(\theta \mp \mu) \quad (25)$$

$$d(\theta + \nu) = \frac{1}{\sqrt{M^2 - 1} - \cot\theta} \frac{dr}{r} \quad (\text{along a C. Characteristic}) \quad (26)$$

$$d(\theta - \nu) = \frac{1}{\sqrt{M^2 - 1} + \cot\theta} \frac{dr}{r} \quad (\text{along a C}_+ \text{ Characteristic}) \quad (27)$$

where

$dr$	=	Differential Aerospike Radius (in)
$dx$	=	Differential Aerospike Length (in)
$\nu$	=	Prandtl-Meyer Function (deg)
$\theta$	=	Flow Angle with respect to Symmetrical Axis (deg)
$M$	=	Mach Number
$\mu$	=	Mach Angle (deg)

The values of  $r$ , aerospike radius, and  $x$ , nozzle axial distance, will give the geometry of the aerospike. The Mach number ( $M$ ) will give  $v$  and  $\mu$  by the following relationships (equations 28 and 29) [47]:

$$v = \sqrt{\frac{\gamma + 1}{\gamma - 1}} \tan^{-1} \sqrt{\frac{\gamma - 1}{\gamma + 1} (M^2 - 1)} - \tan^{-1} \sqrt{M^2 - 1} \quad (28)$$

$$\mu = \sin^{-1} \frac{1}{M} \quad (29)$$

where

$$\gamma = \text{Exhaust Ratio of Specific Heats}$$

Knowing  $M$ , the pressure ratio ( $P_c/P_x$ ) can be calculated using equation 30 [20]:

$$\frac{P_c}{P_x} = \left(1 + \frac{\gamma - 1}{2} M^2\right)^{\frac{\gamma}{\gamma-1}} \quad (30)$$

where

$$\begin{aligned} P_x &= \text{Static Pressure at x-coordinate on Aerospike (psi)} \\ P_c &= \text{Chamber Pressure (psi)} \end{aligned}$$

Since the chamber pressure is known from the combustion process, the value of  $P_x$  can be found. The pressure thrust acting on the aerospike nozzle uses the  $P_x$  value in its calculation.

### ***III.3.b. TDK Overview***

For over 40 years, TDK has provided reliable nozzle performance predictions for liquid rocket engines. The software, first developed in the 1960s, became a JANNAF Standard Code in 1967 [48]. The code is now the property of Software and Engineering Associates, Inc (SEA).

TDK'04 contains seven modules, each required to perform a “complete two dimensional non-equilibrium nozzle performance calculation with boundary layer” [48]. Depending on the needs of the user and how much accuracy they require, all or part of the modules may be used. The modules are ODE, SCAP, ODK, TRANS, MOC, BLM, and MABL. ODE and ODK perform one-dimensional equilibrium or kinetic rocket nozzle expansion calculations. SCAP (Spray Combustion Analysis) is used only for specific problems relating to incomplete propellant vaporization or non-equilibrium chamber conditions. The TRANS module supplements the MOC (method of characteristics) module by performing transonic calculations. The MOC module

performs the method of characteristic method and obtains nozzle geometry. Lastly, the BLM and MABL modules are very similar performing boundary layer analyses. The MABL module is an updated version of the BLM module. TDK can perform both axisymmetric and planar calculations. For the DEAN, only the axisymmetric ODE, ODK, TRANS, MOC, and MABL modules are of interest [48].

The user defines the problem type at the beginning of the code. Problem types include a one- or two-dimensional equilibrium problem (ODE, TDE), a one- or two-dimensional kinetic rocket nozzle expansion problem (ODK, TDK), a two-dimensional frozen (at chamber conditions) rocket nozzle expansion problem (TDF), a two-dimensional constant gas properties rocket nozzle expansion (PFG, known as the perfect gas option), and/or a combination of each [48]. If the kinetic, equilibrium, or frozen problem types are utilized, the user is required to input specific propellant properties and basic chemistry parameters (i.e. propellant species declaration, propellant reactions, and third body reaction rate ratios); these problem types will perform thermo chemistry calculations in the chamber and along the nozzle. If the perfect gas option is used, the user is required to input nozzle throat chemistry parameters (i.e. ratio of specific heats ( $\gamma$ ), molecular weight, and exhaust density). Each problem type has its advantages and disadvantages

A newer option in the TDK software is its ability to perform aerospike (or plug) nozzle calculations. The software models the aerospike as a scramjet [48]. The downside is only the aerospike nozzle from the throat to the exit plane can be evaluated and throat conditions must be input. If a bell nozzle calculation was being performed, chamber conditions could be input to evaluate both transonic flow to the nozzle throat

and supersonic flow expansion along the nozzle. Another downside is the throat Mach number must be supersonic ( $M^* > 1$ ) leading to inflated outputs; realistically, the throat flow is sonic. Even with these downsides, the TDK outputs using the scramjet option for an aerospike nozzle are correctable. The capability of TDK to produce reliable axisymmetric nozzle geometry with a corresponding pressure profile quickly makes the software desirable for continued DEAN research.

SEA has verified and validated TDK over the years by comparison to current operating engines. The TDK software comes with many sample codes representing actual engines. The TDK'04 user manual mentions a couple test cases used to validate the software [48]. Furthermore, Dunn and Coats published two papers discussing the capability of the TDK software with a comparison of software outputs to actual engine parameters with good results [49, 50].

### ***III.3.c. TDK with CEA and Angelino Nozzle Geometry Approximation***

Since TDK'04 utilizes the scramjet option to model an aerospike nozzle, the problem begins at the throat. In order to execute ODE, ODK, TDE, TDK, and TDF problems in TDK'04, the user must input specific chemistry parameters including propellant reaction equations. For the PFG problem, the user is required to input chemistry parameters at the throat; therefore, the chemistry parameters at the throat need to be independently calculated and then input into the TDK PFG code.

As previously stated, CEA by NASA is recommended for use with NPSS [44]. CEA can quickly and accurately perform hydrogen and oxygen reactions for an equilibrium and frozen flow rocket problem. CEA assumes “one-dimensional form of

the continuity, energy, and momentum equations; zero velocity at the combustion chamber inlet; complete combustion; adiabatic combustion; isentropic expansion in the nozzle; homogeneous mixing; ideal-gas law; and zero temperature and velocity lags between condensed and gaseous species" [46]. If the TDK PFG model is used, the following CEA outputs are required: ratio of specific heats ( $\gamma$ ), exhaust products' molecular weight in the chamber, throat pressure, throat temperature, and the speed of sound at the throat. Linking CEA to the TDK PFG model improves the accuracy of the required thermo chemical inputs.

Sutton and Biblarz state frozen and equilibrium flow underestimate and overestimate the performance of the nozzle by 1 to 4%, respectively [23]. In linking CEA to the TDK PFG model and attempting to improve the accuracy of the TDK inputs, a linear average of the frozen and equilibrium CEA outputs was performed.

Regardless of TDK problem type used (i.e. TDK, PFG, and ODE), the length of the aerospike is a required input. The MOC module in TDK creates a curved line from the throat to the input aerospike length avoiding shock formations on the nozzle. A guess on aerospike length is possible; however, it is not the best method. SEA, Inc. provided AFIT with a technique known as the Angelino approximation method.

Angelino developed an approximation method for two-dimensional and axisymmetric plug nozzle design in 1964 [51]. The method assumes linear characteristic lines with constant properties extending from the chamber exit lip, also known as the cowl, and sonic flow velocity at the throat (choked throat). Angelino showed the agreement between the linear approximation and actual method of characteristics is good for nozzles having a large base radius (truncated spike) and for nozzles with a high exit

Mach number regardless of base radius. In more general terms, the approximation is good when expansion characteristics are significantly straight lines with constant properties [51].

SEA, Inc. also provided AFIT with FORTRAN code that automates the Angelino approximation method. The FORTRAN code requires input of chamber chemistry and outputs aerospike radii at the throat, throat area, nozzle length, and the pressure profile along the spike. Due to different design approaches, the FORTRAN code could not be utilized directly. However, the FORTRAN code aided in rewriting the code into a ModelCenter script component. The output aerospike nozzle length from Angelino was vital in getting the TDK models to function properly. Assumptions for the Angelino code are isentropic and adiabatic nozzle, choked flow, and constant ratio of specific heats ( $\gamma$ ) and molecular weight along the nozzle.

Linking the Angelino approximation method to the TDK models and CEA to the TDK PFG model proved successful in finding good TDK inputs. Using CEA and Angelino provided more validity in TDK inputs instead of relying on user guesses. Figure 20 compares the aerospike nozzle geometry output from the TDK PFG model, the Angelino method, and a simple linear approximation. The throat radius normalizes the radial and axial lengths. Inputs for each method used a chamber pressure of 1740 psia (12 MPa), *O/F* of 6.0, a chamber radius at the injector face of 6.0 inches (15.2 cm), a mass flow rate of 104 lb<sub>m</sub>/s (47.2 kg/s), and a throat area of 18.899 in<sup>2</sup> (121.9 cm<sup>2</sup>). Since TDK models the aerospike as a scramjet, the temperature and pressure values of the flow at the throat are input instead of chamber conditions.

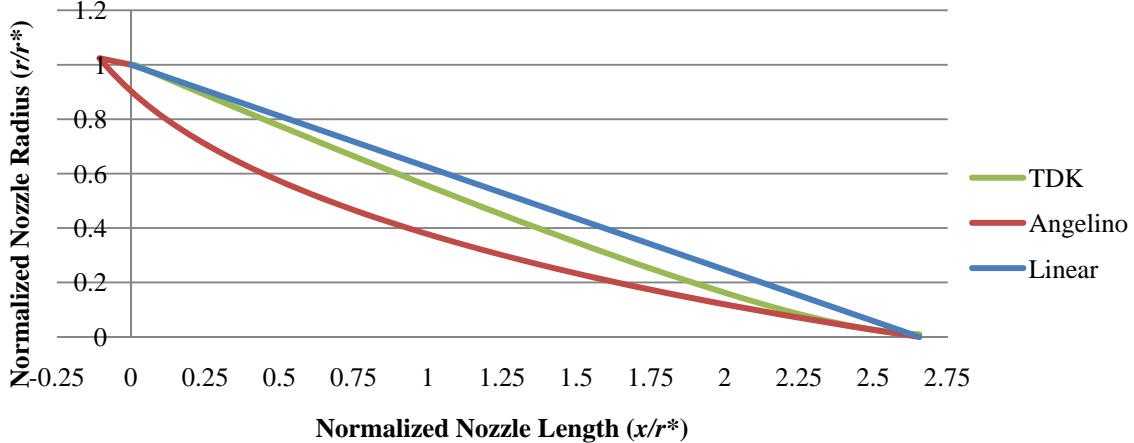


**Figure 20. Aerospike Nozzle Geometry Comparison**

Figure 20 illustrates the differences in geometry between the three methods. The Angelino method shows strange geometry at the throat. Due to the way Angelino approximates the wall surface, the surface near the throat requires a large geometric angle for the flow to keep in sync with the low Prandtl-Meyer function and high Mach angle accounting for the reversal in wall geometry. The Angelino surface produced is physically not possible and, therefore, not useable for the DEAN. However, the calculated nozzle length from Angelino is useable in TDK and the wall surface created by TDK is physically possible. Figure 20 also plots the linear surface to show the curvature of the TDK surface. The Angelino method used in conjunction with TDK provides reasonable aerospike nozzle geometry.

#### ***III.3.d. TDK Model with Boundary Layer Approximation***

TDK uses the mass addition boundary layer (MABL) module to calculate the boundary layer and associated performance losses on the aerospike nozzle. The MABL module can be used in conjunction with any of the problem types (i.e. PFG, TDK, and ODE).

The DEAN TDK model needs two MABL modules: one for the chamber and the other for the aerospike. The MABL module for the chamber will evaluate the boundary layer along the chamber wall extending from the throat to the end of the chamber exit lip or cowl. The associated performance loss for the chamber is the pressure thrust loss due to boundary layer effects acting on the chamber exit lip. For the aerospike, the MABL module will evaluate the boundary layer along the aerospike wall extending from the throat to the end of the cooled portion of the aerospike. The associated performance loss due to boundary layer effects for the aerospike is pressure thrust loss along the nozzle. There are no differences in percent boundary layer loss or TDK outputs if only the cooled portion of the aerospike or the full aerospike axial length is input. The TDK boundary layer problem is defined using the cooling jackets' start and ending axial points.

### ***III.3.e. Correction to TDK Outputs***

Various analyses presented in Appendix D.1 led to the conclusion to use the TDK PFG model for the final ModelCenter DEAN model. Furthermore, sensitivity analyses in Appendix D.2 revealed ways to simplify the number of parametric TDK PFG model inputs.

The final ModelCenter DEAN model requires the use of both NPSS and TDK. NPSS calculates performance assuming a mass flow rate and varying chamber pressure and throat area until throat area converges. TDK uses scramjet calculations to model an aerospike; it is not a direct comparison in terms of calculating engine performance. The issue is how to link the two programs together.

For NPSS, engine mass flow rate ( $\dot{m}$ ) is an input from the user design variables and chamber pressure and throat area are outputs. In contrast, TDK requires chamber pressure and throat area as inputs and  $\dot{m}$  is an output. Furthermore, for TDK to function, the throat Mach number must be greater than 1.0, while for NPSS, the throat Mach number must be less than or equal to 1.0. A simple solution is to edit the NPSS model so chamber pressure and throat area become inputs and  $\dot{m}$  becomes an output; however, editing the NPSS model will change the optimization problem. The current optimization problem is set to maximize engine  $T/W$ . The solution to the problem is to get the NPSS input  $\dot{m}$  and the TDK output  $\dot{m}$  equal.

The desired outputs from TDK are the nozzle geometry and the pressure profile along the nozzle. First, linking NPSS and TDK to each other so the input throat areas are equal improved the difference between the NPSS and TDK  $\dot{m}$ . Next, changing the velocity of the flow at the throat ( $VSJ$ ) from a user “guess” to a variable decreased the difference between the calculated TDK and the NPSS input  $\dot{m}$  from 20% to 10%, with the TDK value being greater.

The value for the nozzle throat pressure ( $PSJ$ ) input into TDK comes from CEA assuming the throat is choked (Mach number at throat equals 1.0). However, to get TDK to model an aerospike, TDK assumes the throat Mach number is 1.1 and uses that value to calculate  $VSJ$ . Using equation 30 and setting the Mach number to 1.1, a more accurate  $PSJ$  input value can be calculated. The resulting  $PSJ$  value will be less than the CEA calculated value; however, the output pressure profile from TDK will more closely align to the actual DEAN pressure profile. With both  $VSJ$  and  $PSJ$  corrections, the TDK output  $\dot{m}$  and the NPSS input  $\dot{m}$  percent difference decreased to approximately 5%, with

now the NPSS input  $\dot{m}$  being greater. As a result, the TDK calculated pressure profile slightly underestimates the actual pressure profile of the DEAN.

The DEAN model uses the TDK pressure profile to calculate the pressure thrust acting on the nozzle. In an attempt to get a pressure thrust more closely relating to the NPSS input  $\dot{m}$ , a linear correction factor to TDK thrust calculations is introduced. The correction factor is used for the calculated full-spike pressure thrust and for the calculated cowl (or chamber exit lip) thrust. The linear correction factor assumes the difference between the TDK and NPSS  $\dot{m}$  is minimal. Equations 31 and 32 show the correction factor equations used.

$$Ratio = F_{TDK}/\dot{m}_{TDK} \quad (31)$$

$$F_{corr} = Ratio * \dot{m} \quad (32)$$

where

$Ratio$	=	TDK Correction Ratio
$F_{TDK}$	=	TDK Pressure or Cowl Thrust (lb <sub>f</sub> )
$\dot{m}_{TDK}$	=	TDK Output Engine Mass Flow Rate (lb <sub>m</sub> /s)
$F_{corr}$	=	Corrected Pressure Thrust Acting on Aerospike Nozzle or Cowl (lb <sub>f</sub> )
$\dot{m}$	=	NPSS Input Engine Mass Flow Rate (lb <sub>m</sub> /s)

The result of the TDK correction factor is a corrected pressure and cowl thrust value relating to the NPSS input  $\dot{m}$ . However, the nozzle exit pressure remains uncorrected and, therefore, underestimates the thrust produced from nozzle operation above or below its design altitude ( $F_{nondesign}$ ); a detailed explanation of  $F_{nondesign}$  is in section III.4.k. The DEAN model assumes the amount of underestimation for  $F_{nondesign}$  is negligible.

### ***III.3.f. Aerospike Design Altitude***

Previous DEAN system level studies assumed an expansion ratio based on underexpanded flow (flow expands outward radially from chamber exit lip) due to operation in a vacuum, and noting that conventional bell nozzle upper stage engines physically require large expansion ratios to achieve desired performance. More research shows the nozzle expansion ratio is a function of outer chamber geometry and throat area defining the design altitude of the aerospike nozzle. The value of the expansion ratio is extremely important in the DEAN design since engine performance calculated in the linear NPSS model is strongly dependent on the expansion ratio. Furthermore, all of the method of characteristics software evaluated (i.e. TDK and Angelino) calculate aerospike nozzle geometry at the nozzle design altitude. At the nozzle design altitude, the exhaust flow at the chamber exit lip will follow a parallel path to the centerline to the exit plane [26].

Utilizing the Angelino approximation method for an axisymmetric plug nozzle, a quick analysis was performed to determine throat geometry for an aerospike engine designed to operate in near vacuum conditions (1 Pascal); the DEAN being an upper stage has a vacuum operational environment [51]. Table 7 tabulates the inputs and results utilizing chamber variables from Simmons' model (Table 6) [5, 6].

**Table 7. Angelino Nozzle Geometry**

Input Variable	Value	Result	Value
Mass Flow Rate (lb <sub>m</sub> /s)	104 lb <sub>m</sub> /s (47.2 kg/s)	Chamber Radius at Throat	472.7 in (12 m)
Molecular Weight	13.4	Aerospike Radius at Throat	472.69 in (12 m)
Ratio of Specific Heats ( $\gamma$ )	1.14	Throat Area	3.3 in <sup>2</sup> (21.3 cm <sup>2</sup> )
Chamber Pressure	1310 psia (9 MPa)	Aerospike Length	4436.9 in (112.7 m)
Chamber Temperature	6413 R (3562.8 K)		
Ambient Pressure	0.000145 psia (1 Pa)		

The results in Table 7 show an unmanufacturable throat with a fluid flow passage between the chamber and aerospike at the throat of 1/1000 inch (254/1000 cm). Furthermore, chamber and aerospike throat radii and aerospike length are unrealistically large proving a near vacuum equivalent design altitude is not practical. Therefore, a more realistic nozzle design for an upper stage aerospike engine would be a lower design altitude (higher ambient pressure). The aerospike nozzle exhaust flow will expand radially outward from the chamber exit lip and the nozzle overall will behave more like a conventional bell nozzle; the aerospike nozzle flow can be considered underexpanded.

The amount of radial outward expansion of the exhaust flow above the nozzle design altitude depends on the interaction of the flow with the ambient conditions. The interaction of the exhaust flow with ambient conditions is best suited for a complex computational model. The nozzle exit pressure defines the design altitude pressure for an aerospike fully expanding the flow; the nozzle exit pressure is also the same pressure acting on the chamber exit lip or cowl. Ambient pressures different from the design altitude pressure will produce another thrust component ( $F_{nondesign}$ ).

The linear NPSS model will be used to show the influence of epsilon at the nozzle design altitude. For the linear NPSS model, the chosen chamber exit lip radius and the calculated throat area from NPSS will determine the expansion ratio/performance of the engine. Utilizing Simmons' DEAN geometry [6] and assuming the engine operates at its design altitude, the calculated expansion ratio is much less than 125; therefore, the current performance calculations are less than previously published. Table 8 compares the performance parameters for an expansion ratio of 125 and the performance parameters for Simmons' DEAN geometry operating at its design altitude using the linear NPSS model and the same design variables.

**Table 8. Comparison of Performance Parameters due to Expansion Ratio**

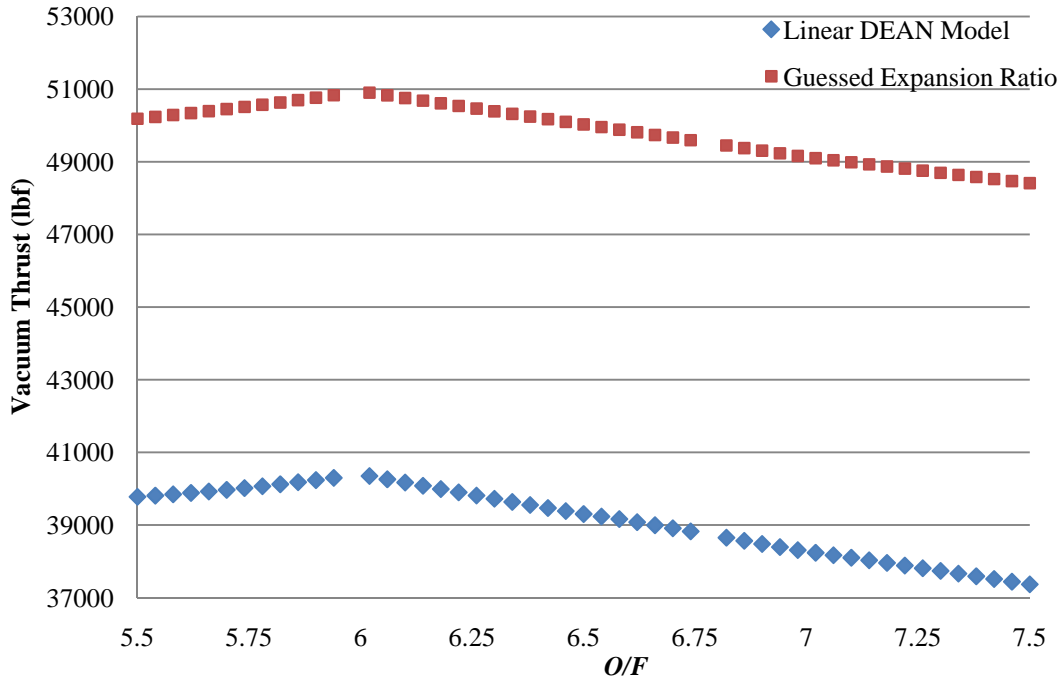
	Assumed Expansion Ratio DEAN Model [6]	Calculated Expansion Ratio DEAN Model
<b>Expansion Ratio</b>	125	4.16
<b>Vacuum Thrust</b>	50,900 lb <sub>f</sub> (226 kN)	40,396 lb <sub>f</sub> (179.7 kN)
<b>Vacuum Isp</b>	489 s	388 s

The results in Table 8 are intriguing, showing a much lower expansion ratio and decreased performance for the same nozzle geometry. The design altitude expansion ratio is a more accurate approach to engine performance estimation as opposed to assuming epsilon equal to 125. Assuming design altitude performance estimation, improved performance can be calculated by increasing the expansion ratio by geometrically increasing the chamber exit lip radius and/or decreasing the throat area.

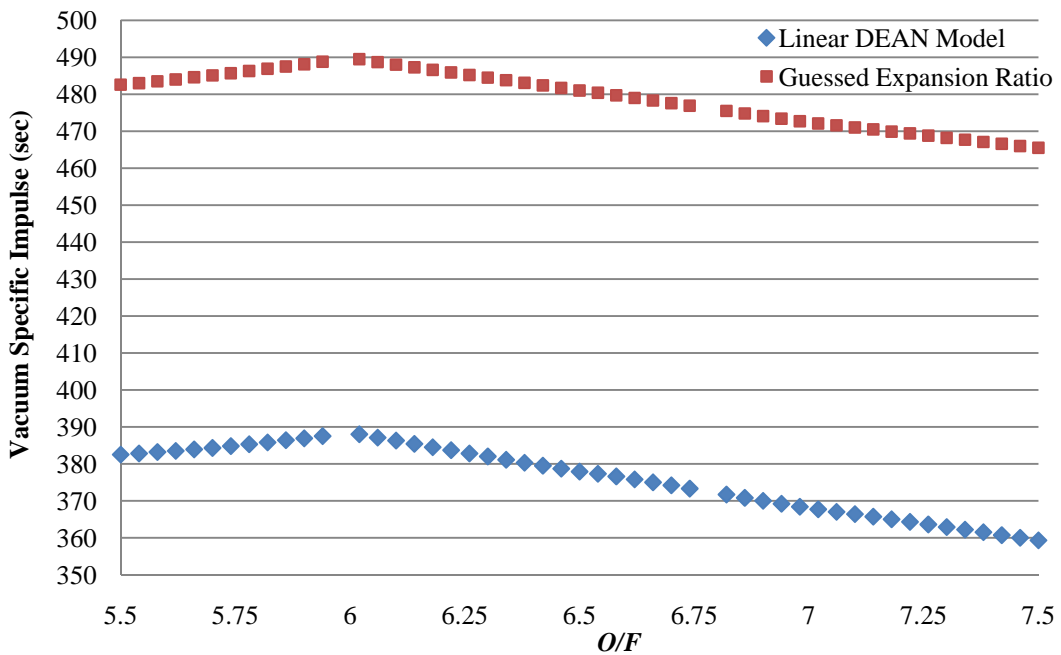
The change in expansion ratio does not influence the validity of the DEAN model. Simmons performed verification and validation of the DEAN ModelCenter and NPSS model as discussed in [5] and [6]. Figure 21 plots engine performance as a function of *O/F* comparing Simmons' DEAN Model to the NPSS linear model. The NPSS linear

model has the same plot shape to previous research with only the performance magnitude differing; the observation is consistent with a decreased epsilon. Although each point in Figure 21 represents a different engine (i.e. different chamber pressure, chamber temperature, throat area), the same conclusion from Simmons' previous research applies to current research where the maximum performance occurs at an *O/F* of 6.0. All trade studies performed by Simmons were re-accomplished with the linear NPSS model and the shapes of the plots were consistent with only magnitudes differing.

The purpose of this study was to show how aerospike geometry influences the nozzle expansion ratio and engine performance. The linear NPSS model was used for simplification. Section III.5 compares Simmons' trade studies to the same trade studies performed in the final ModelCenter DEAN model.



a) Vacuum Thrust as a function of  $O/F$



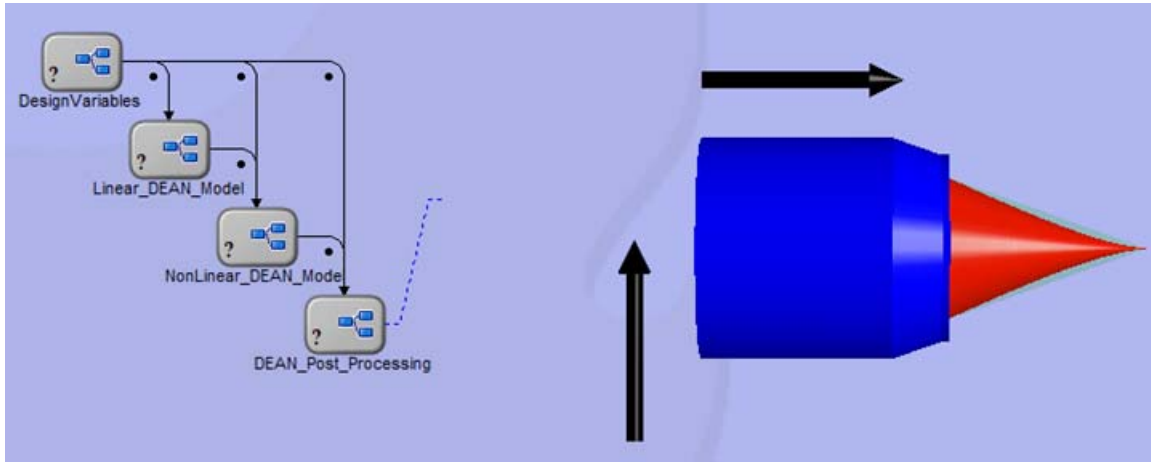
b) Vacuum Specific Impulse as a function of  $O/F$

Figure 21. Vacuum Performance as a function of  $O/F$

### **III.4 Description of DEAN ModelCenter Model Elements**

#### ***III.4.a. DEAN Model Overview***

With user input design variables, the final ModelCenter DEAN model will provide a system level estimate of performance with the inclusion of estimating engine component weight and an engine thrust-to-weight ratio, along with balancing the two propellant expander cycles. The model contains four main assemblies. The first main assembly is “DesignVariables” containing all the system level variables required to execute the model. The second assembly is “Linear\_DEAN\_Model”. The assembly executes the linear NPSS DEAN model to provide valid input estimates to the next assembly, “NonLinear\_DEAN\_Model”. The “NonLinear\_DEAN\_Model” assembly will execute TDK and the nonlinear NPSS model to calculate aerospike nozzle geometry and certify the fluid mechanics and thermo chemistry of the DEAN satisfy governing laws. The last assembly is “Post-Processing”. The assembly post-processes the TDK and NPSS data, such as calculating the cooling jacket wall temperatures, designing the chamber and aerospike structural jackets, and calculating overall performance. “Post\_Processing” also renders the geometry of the DEAN. Figure 22 shows the overall system level DEAN model with rendered geometry.



**Figure 22. System Level ModelCenter DEAN Model**

The DEAN design consists of twelve engine components: combustion chamber and aerospike cooling jackets, combustion chamber and aerospike structural jackets, aerospike nozzle tip, two turbopump assemblies (pump, turbine, and shaft combination), plumbing for each propellant, injectors, oxidizer dome, and hardware. Each component adds mass to the engine. The model assumes the mass of the injectors and oxidizer dome are part of the combustion chamber and aerospike masses. The cooling jackets serve to physically separate the hot combusted products from the coolant while maximizing heat transfer to the coolant to power the turbopumps. The structural jackets serve to restrain the cooling channel and combustion chamber pressures. The aerospike nozzle tip is the uncooled portion of the aerospike nozzle. Two turbopumps exist; one for the fuel and the other for the oxidizer to power the individual expander cycles. Plumbing exists for both the fuel and oxidizer and serves as a physical boundary to move propellant from one engine component to another. Hardware, such as nuts, bolts, wiring, and rivets, is an assumed percentage of the total engine weight. Figure 23 is an axial view of the DEAN design showing the aerospike and combustion chamber structural and cooling jackets. Fifty percent of the full-length aerospike nozzle is cooled.

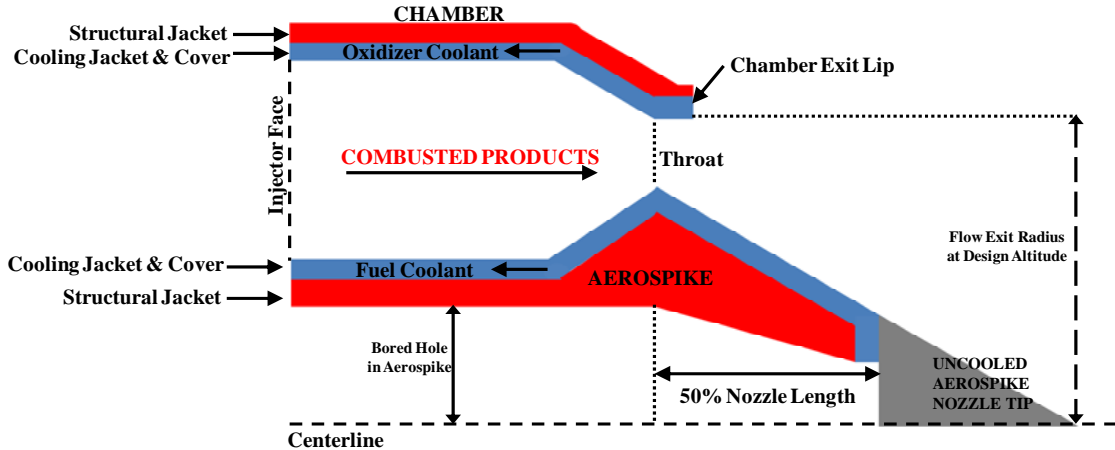


**Figure 23. Axial Geometry for Chamber and Aerospike**

Some ModelCenter DEAN script components calculate variables that may not be used elsewhere in the model nor are desired outputs. Certain script components, such as those calculating NPSS inputs and post-processing TDK information, are repeated elsewhere in the model. Instead of having a unique script for every component, a master script was created and the outputs of interest either are linked to other model components or are highlighted in the model.

#### *III.4.b. Design Variables Assembly*

As previously stated, the “DesignVariables” assembly stores all system level variables required to execute the model. With fixed performance design goals, Simmons edited the DEAN design variables driving engine weight for fixed performance [6]. The goal is to minimize engine weight or, said another way, maximize engine thrust-to-weight ratio, while meeting the design goals of thrust and specific impulse. Chamber, aerospike, and plumbing weight are a function of component geometry and material selection. Turbopump weight is a function of engine mass flow rate and  $O/F$ . Therefore, the main design variables are the oxidizer-to-fuel ratio ( $O/F$ ), the engine mass flow rate,

combustion chamber length, aerospike and chamber radius at the injector face, and material selection for the aerospike and chamber cooling jackets, aerospike and chamber structural jackets, aerospike nozzle tip, and oxygen and hydrogen plumbing. Also included in the design variables is the user specified “Percent\_Weight\_Hardware” and “Performance\_Loss”. “Percent\_Weight\_Hardware” has a default value of 5% and provides an estimate for hardware weight based on a percentage of the total engine weight. “Performance\_Loss” is a user input option to account for other than boundary layer performance losses; the variable is a percentage of total thrust and is currently set to zero percent. Section III.4.h discusses the materials available for selection.

Other user inputs are required in the “DesignVariables” assembly to execute the model. For NPSS, the user is required to enter cooling channel geometry inputs for the chamber and aerospike, a guessed aerospike and chamber maximum wall temperature, a percentage of oxygen bypassing the turbine and going straight to the injectors, and a plumbing area for pipes not associated with the cooling jackets. The NPSS cooling channel geometry inputs for both the chamber and aerospike are an initial channel half-width, a half-thickness between the cooling channels, and the channel aspect ratio.

The assembly contains three “decision” variables the user must select prior to executing the model. The first is “Material\_Strength\_Option”. The two options are ultimate tensile strength or yield strength. A related variable is  $fs$ , an assumed factor of safety for structural analyses. The user selected material strength option affects the thickness of the structural jacket and plumbing walls. If the model user selects the ultimate tensile strength option, the thickness of the structural jacket and plumbing will be calculated to a stress equal to the selected material ultimate tensile strength divided by

a user input factor of safety; a similar process is true for the yield strength option. The second “decision” variable is “Cooling\_Geom\_Option” containing two options; one, “SJ is Cover” and two, the default choice, “Channel Cover + SJ”. “SJ is cover” means the chamber or aerospike structural jacket covers the cooling channels. The option limits material selection for the structural jackets and only materials compatible with the propellants are useable. The second option, “Channel Cover + SJ”, means a channel cover of the same cooling jacket material covers the cooling channels allowing the structural jacket to be of any material. The option assumes galvanic corrosion is negligible. The last “decision” variable is “Pamb\_Decision” and has two options: “Design” and “Operational”. If the user selects “Design”, DEAN performance will be calculated at the nozzle design altitude or design ambient pressure. If the user selects “Operational”, DEAN performance will be calculated at an ambient pressure selected by the user through another variable called “Poperational”. The default model selection is “Operational” with a “Poperational” value of 0.000145 psia (1 Pa) to calculate DEAN performance in a vacuum.

Lastly, the assembly contains two variables for aerospike nozzle truncation studies. The user has the ability to perform aerospike nozzle truncation studies by changing the “PerTrunc” variable; default value is 0% for a full-length nozzle. The “PerTrunc” variable is a percentage of engine length. For example, “PerTrunc” equal to 5% means 5% of the nozzle is truncated from the full-length nozzle’s exit plane; therefore, 95% of the nozzle remains. In addition, part of truncation studies is the variable “Per\_Uncooled\_Spike”. The DEAN design cools 50% of the full-length aerospike nozzle. For truncation between 0 and 50%, there is no change in the location

of where the nozzle is cooled. However, evaluation of nozzle truncation greater than 50% results in changes to the nozzle cooling location. “Per\_Uncooled\_Spike” is a variable to ensure there is a cover at the end of the truncated spike creating a solid base and allowing the coolant to travel to the end of the cooled portion of the nozzle and through the aerospike cooling jacket. Although user configurable, the default value of “Per\_Uncooled\_Spike” is 10%. This means for nozzle truncation studies greater than 50%, 10% of the truncated spike length remains uncooled, while 90% of the truncated spike length is cooled.

The model is executable once the user defines the design problem through user input variables.

#### ***III.4.c. Linear DEAN Model Assembly***

The “Linear\_DEAN\_Model” assembly, shown in Figure 24, contains 3 main subcomponents with one unused subassembly. The basis of the “Linear\_DEAN\_Model” is to execute the linear NPSS model to obtain good guesses for chamber pressure, throat area, and pressure, enthalpy, and density profiles to be input into the nonlinear NPSS model. The linear NPSS model, based on research by Simmons [5, 6], is contained in the master NPSS model with the nonlinear NPSS code commented so it will not execute.

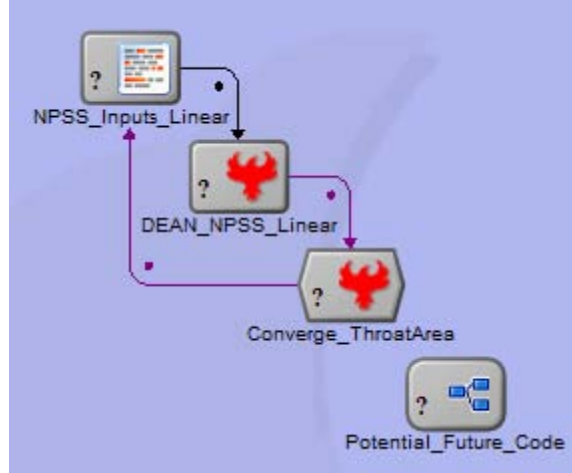


**Figure 24. “Linear\_DEAN\_Model” Assembly Components**

The assembly begins with the “NPSS\_Inputs\_Linear” component. “NPSS\_Inputs\_Linear” assumes linear approximations for the internal and external (to the combustion chamber) geometry of the aerospike. The component calculates the radius of the aerospike nozzle at the throat, chamber volume, and expansion ratio. The radius of the aerospike nozzle at the throat and the chamber volume are calculated using linear equations presented in Simmons’ research [5, 6]. Equation 33 calculates the nozzle expansion ratio based on the nozzle design altitude. The radius of the truncated base is equal to zero for full-length aerospike nozzle calculations.

$$\varepsilon = \frac{\pi(r_c^{*2} - r_{base}^2)}{A^*} \quad (33)$$

where

- $\varepsilon$  = Nozzle Expansion Ratio
- $r_c^*$  = Radius of Chamber Exit Lip at Throat (in)
- $r_{base}$  = Radius of Truncated Base (in)
- $A^*$  = Throat Area ( $\text{in}^2$ )

The next component “DEAN\_NPSS\_Linear” executes the linear NPSS model. The DEAN model uses inputs from the “NPSS\_Inputs\_Linear” component and uses pressure, enthalpy, and density inputs from the Simmons/Martin NPSS model output file [4-6]. The outputs from the Simmons/Martin NPSS model are more accurate than “guessing” a value as done in previous research. Furthermore, the NPSS linear model uses the turbopump and shaft parameters used in the original NPSS model by Martin [4] (Table 5); applies also to the nonlinear NPSS model. Utilizing outputs of successfully run NPSS code improves the convergence of the linear NPSS model.

The next component, “Converge\_Throat\_Area”, starts an initial throat area guess at 30 in<sup>2</sup> and inputs the value into the “NPSS\_Inputs\_Linear” component and the NPSS linear model. The NPSS linear model will output a new throat area where the converger replaces the output value as the input value and continues to do so until the input and output throat area values are equal to within a specified tolerance. The converger is a built-in ModelCenter component and its default convergence tolerance is 0.001 (absolute difference between the variables).

The next component, “Potential\_Future\_Code”, is not used in the execution of the final model. The “Potential\_Future\_Code” component is another assembly with subcomponents to calculate the oxidizer and fuel pressure profile and oxidizer and fuel turbopump parameters based on documentation by Humble *et al* [20]. The code was being used to create “good” input guesses for the pressure profile and also for turbopump parameters such as pump and turbine efficiency, guessed pump pressure ratio, and guessed shaft rotational speed. However, integration of the code into the NPSS model was unsuccessful. The code may be useful to future research.

### III.4.d. Nonlinear DEAN Model Assembly

Five subassemblies make up the “NonLinear\_DEAN\_Model” assembly as shown in Figure 25. Two of the assemblies execute the nonlinear NPSS code and three of the assemblies calculate aerospike nozzle geometry. The nonlinear NPSS code executes twice in an attempt to provide more exact chamber pressure, chamber temperature, pressure profile, enthalpy profile, and density profile inputs. It is impossible to converge every variable in NPSS; however, executing a linear model and two nonlinear models is an attempt to do so. Between each nonlinear NPSS run is an assembly to calculate the aerospike nozzle geometry. After the final nonlinear NPSS run, the DEAN model executes TDK one last time to calculate the final aerospike nozzle geometry and the pressure profile acting along the spike including viscous losses. The term nonlinear applies to the external geometry of the aerospike nozzle. The linear approximations from Simmons [5, 6] for aerospike geometry internal to the combustion chamber remain the same.

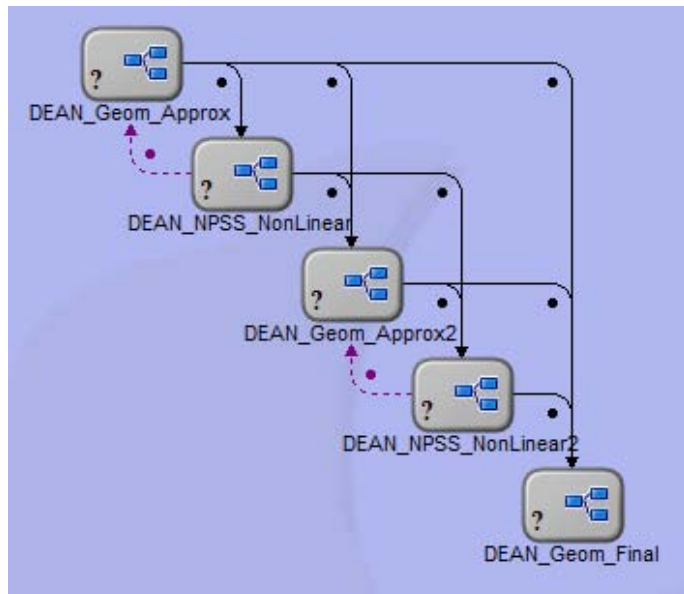
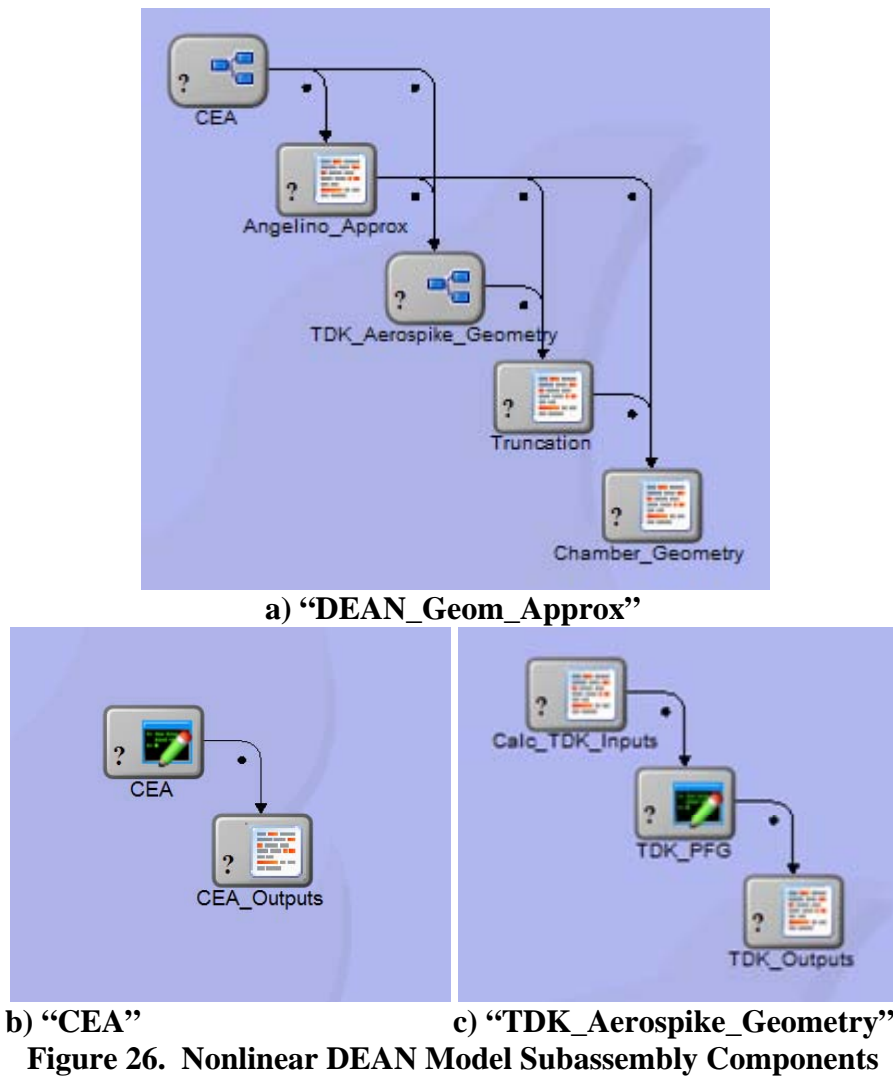


Figure 25. “NonLinear\_DEAN\_Model” Assembly Components

The “DEAN\_Geom\_Approx” subassembly uses the chamber pressure and throat area output from the linear NPSS model to create the nonlinear aerospike nozzle geometry. The subassembly contains three ModelCenter script components and two more subassemblies. Figure 26 shows the subcomponents of the “DEAN\_Geom\_Approx” subassembly, along with the “CEA” and “TDK\_Aerospike\_Geometry” sub-subassemblies. The “DEAN\_Geom\_Approx”, “DEAN\_Geom\_Approx2”, and “DEAN\_Geom\_Final” assemblies have nearly identical components with minor differences in each.



**Figure 26. Nonlinear DEAN Model Subassembly Components**

Section III.3.c discusses the execution details of CEA, Angelino, and the TDK PFG model. “CEA” calculates chemistry parameters used by the “Angelino\_Approx” script component and the TDK PFG model. The use of CEA allows utilization of the TDK PFG model. CEA computes both equilibrium and frozen flow parameters and the linear average of the two outputs are used as inputs into Angelino and TDK. “Angelino\_Approx” calculates the aerospike nozzle length and the aerospike radius at the throat. The Angelino outputs are inputs in the TDK PFG model.

The TDK subassembly contains three components. The first subcomponent takes CEA and Angelino outputs and edits them for use in TDK. For example, the output CEA pressure at the throat is in units of bars but TDK requires units of psia. In addition, TDK requires normalization of the Angelino aerospike nozzle length by division of the aerospike throat radius. The “TDK\_PFG” subcomponent is a ModelCenter Quick Wrap 2.0 component used to execute the TDK PFG model. The last subcomponent is an output script component. For the “DEAN\_Geom\_Approx” and DEAN\_Geom\_Approx2” assemblies, the output script component will set the ambient pressure to either the design altitude pressure (nozzle exit pressure) or operational pressure based on the user “Pamb\_Decision” from the design variables assembly. Only the aerospike nozzle geometry is of interest for the “DEAN\_Geom\_Approx” and “DEAN\_Geom\_Approx2” assemblies.

The two remaining script components in “DEAN\_Geom\_Approx” are “Truncation” and “Chamber\_Geometry”. “Truncation” first takes the normalized radial and axial aerospike nozzle arrays from TDK and dimensionalizes them by multiplying each array element by the aerospike throat radius. Next, if the user is performing

truncation studies, the script will create the axial, radial, and pressure arrays corresponding to the amount of nozzle truncation. For example, if the user truncates the nozzle by 10% (90% of nozzle remains), TDK will create a new axial, radial and pressure array extending from the nozzle to the truncated point on the nozzle. The last point in the arrays, corresponding to the truncated nozzle axial location, will be linearly interpolated between the previous and subsequent points in the original normalized output TDK arrays. The truncation script will also calculate the nozzle expansion ratio and create exclusive arrays for geometry rendering.

The “Chamber\_Geometry” script component calculates the internal chamber and aerospike geometry and station locations, fluid chamber volume, and the beginning, middle, and end locations of the two aerospike nozzle stations. The fluid chamber volume is calculated by taking the solid volume of the chamber and subtracting the solid volume of the aerospike portion internal to the combustion chamber. The aerospike remains a linear approximation based on research by Simmons [5, 6]. The volumes for the chamber and aerospike use cylinder and conical frustum volume equations. For truncation studies greater than 50%, the two aerospike nozzle stations (stations 7 and 8) are variable and are a function of the “Per\_Uncooled\_Spike” design variable. The chamber geometry script will also calculate the characteristic length ( $L^*$ ) of the combustion chamber;  $L^*$  serves as an output of interest to determine if the chamber length design variable can be shortened to lower weight without influencing combustion. Furthermore, the chamber geometry script will calculate the maximum fluid temperature for both propellants. The maximum fluid temperature is used later to calculate the thicknesses of the structural jackets and plumbing walls.

The “DEAN\_NPSS\_Nonlinear” assembly uses the calculated nozzle geometry from the “DEAN\_Geom\_Approx” assembly. The nonlinear NPSS model assembly contains three components as shown in Figure 27.

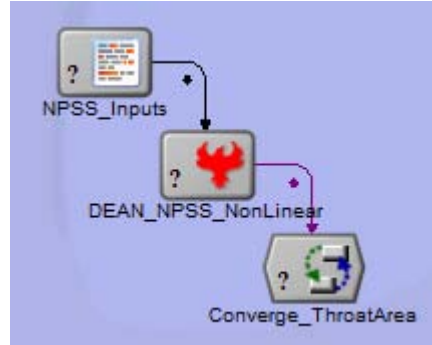


**Figure 27. Nonlinear NPSS Subassembly Components**

The “NPSS\_Inputs” script component takes axial and radial station locations from the “DEAN\_Geom\_Approx” code and renames them as NPSS input variables. In addition, the code calculates the surface area of heat exchange on the nozzle using equations 34 and 35. Equations 34 and 35 are the surface area integral and the trapezoidal approximation formulas, respectively [45].

$$SA = \int_0^L f(x) \sqrt{1 + (f'(x))^2} dx \quad (34)$$

$$\int_a^b f(x) dx = \frac{1}{2} \sum_2^N [x(i) - x(i-1)][f(x(i-1)) + f(x(i))] \quad (35)$$

where

$SA$	=	Surface Area of Heat Exchange (in <sup>2</sup> )
$f(x)$	=	Aerospike Radii Array (in)
$x$	=	Aerospike Axial Length Array (in)
$f'(x)$	=	Slope of Aerospike Wall at Location x
$L$	=	Aerospike Length (in)

The next component, “DEAN\_NPSS\_NonLinear” executes the nonlinear NPSS model. The last component, “Converge\_ThroatArea”, when run will perform the same function as the same component in the linear NPSS assembly except this converger connects to the throat area in the Angelino approximation code. Connecting the converger to Angelino approximation code allows for recalculation of the aerospike nozzle geometry for each iteration of NPSS throat area convergence and ensures the aerospike nozzle geometry calculated in TDK and used in NPSS are identical.

The next two subassemblies in the “NonLinear\_DEAN\_Model” main assembly are “DEAN\_Geom\_Approx2” and “DEAN\_NPSS\_NonLinear2”. These two subassemblies are identical to the previously mentioned subassemblies of similar name except with changes in component names. A second run of similar subassemblies is done for two reasons: first, to ensure “good” NPSS inputs (chamber pressure, pressure profile, enthalpy profile, etc.) are used; second, to ensure the TDK calculated nonlinear aerospike nozzle geometry causes the nonlinear NPSS model to execute successfully without errors. The nozzle station locations (stations 7 and 8) between the linear and nonlinear NPSS models are different. By executing the nonlinear NPSS model twice, better NPSS outputs are expected due to using better inputs.

The last subassembly under the “NonLinear\_DEAN\_Model” assembly is “DEAN\_Geom\_Final”. The assembly is identical to the “DEAN\_Geom\_Approx” subassembly shown in Figure 26a except the TDK model involves boundary layer calculations. The purpose of the assembly is to calculate the final aerospike nozzle geometry and resulting pressure profile acting along the nozzle accounting for viscous losses. The TDK PFG model with boundary layer calculates losses to the full-length

nozzle pressure thrust and losses to the chamber exit lip pressure thrust. The TDK output script component is different from the other TDK output components; this component calculates the percent boundary layer loss and the required TDK correction factor to link TDK and NPSS correctly.

If there are no failures after two nonlinear NPSS model and three nozzle geometry executions, the DEAN design is validated from a fluid mechanics and thermo chemistry standpoint with two fully functional expander cycles.

#### ***III.4.e. DEAN Post-Processing Overview***

The final main assembly in the DEAN ModelCenter model is “Post\_Processing,” containing nine subcomponents as shown in Figure 28. The components serve to calculate final DEAN performance parameters, check physical limits to ensure there are no violations, perform structural analyses, and render the chamber and aerospike for visualization.

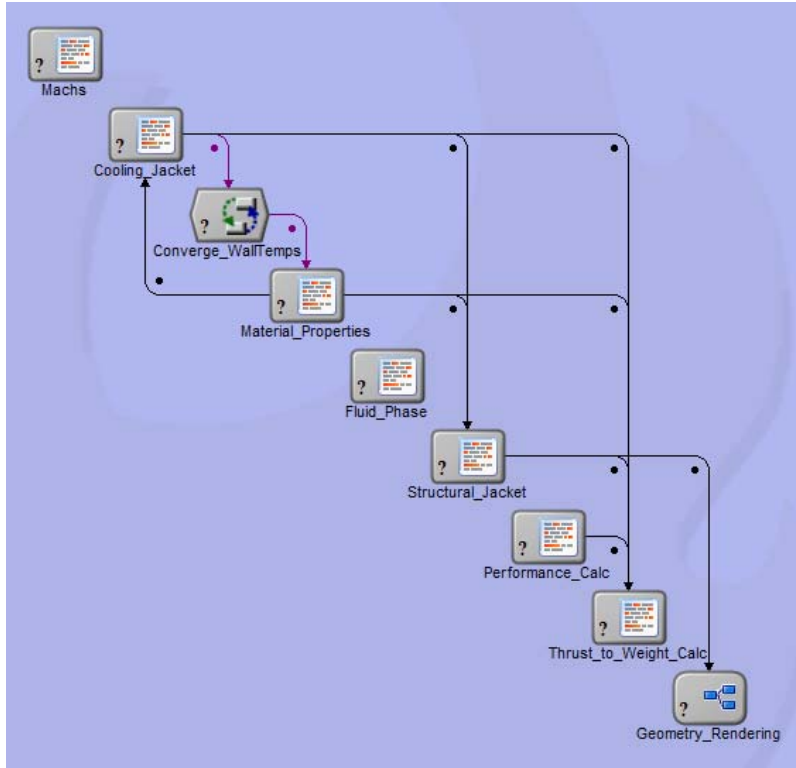


**Figure 28. “Post\_Processing” Assembly Components**

### *III.4.f. Fluid Mach Number Calculation*

The first post-processing subcomponent is “Machs.” The goal of “Machs” is to find the maximum flow Mach number in each propellant expander cycle and verify the magnitude does not violate physical constraints. The maximum oxygen and hydrogen Mach number is 0.6 and 0.9, respectively [4].

The expected maximum Mach number is in the propellant cooling jackets. In the cooling jackets, the flow gains energy through heat transfer with the combusted products. After leaving the cooling jacket, the flow will begin to cool and experience a drop in pressure as it enters and leaves the turbine; the flow will lose velocity from the decrease in fluid temperature. Therefore, the maximum Mach number in the propellant expander cycles is located at the last station in the cooling jackets.

Simmons [6] wrote the code to calculate the fluid Mach numbers. In short, the code Simmons wrote was able to automate the process of looking up the speed of sound for the fluids at a specific temperature and pressure from the “Thermophysical Properties of Fluid Systems” online handbook from the National Institute of Standards and Technology by creating a third order polynomial [52, 6]. The third order polynomial was created using ModelCenter tools over realistic pressure and temperature ranges [6].

Calculation of the fluid Mach number occurs at each propellant cooling jacket station. As expected, the last cooling jacket station has the maximum Mach number; therefore, the related variable was set as an output of interest. The maximum Mach number output is used in optimization studies to ensure designs evaluated by the optimizer meet physical fluid Mach number constraints.

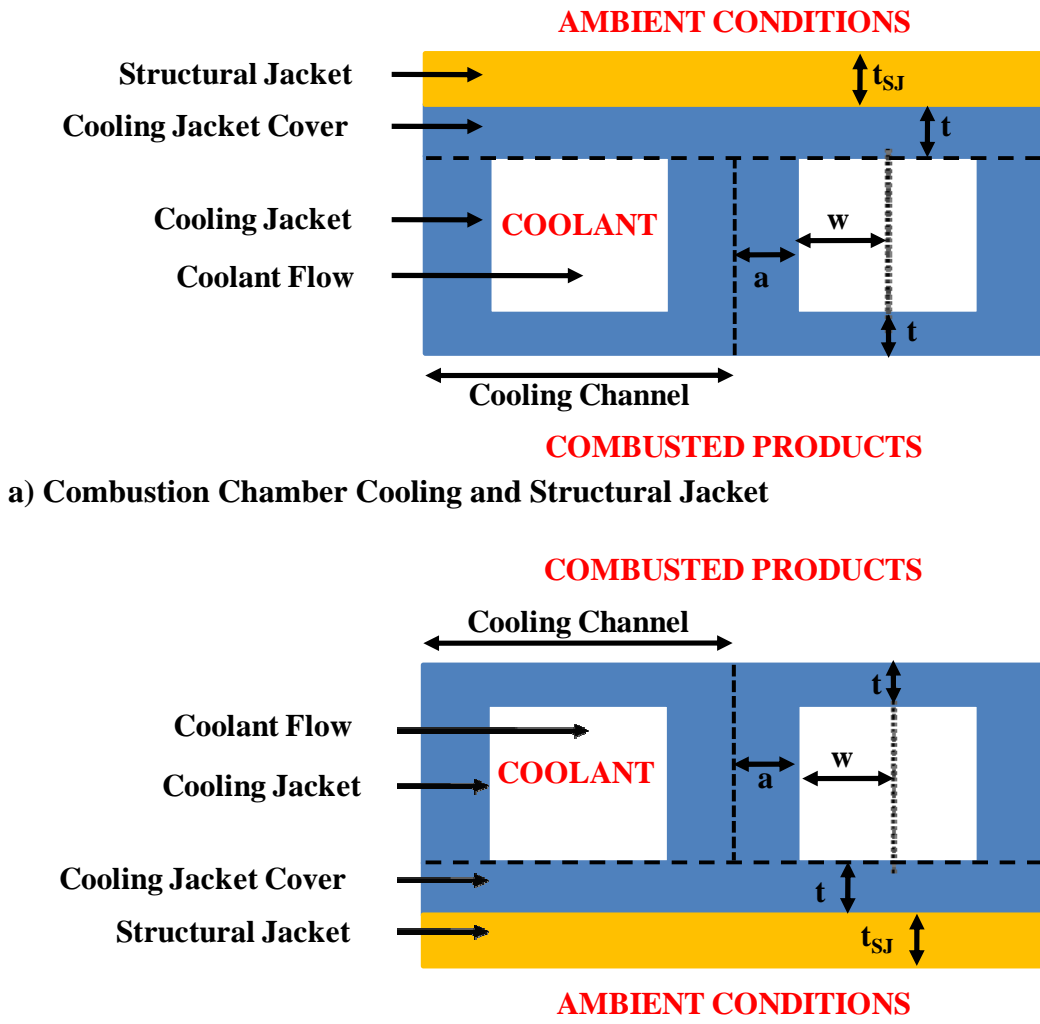
The maximum fluid Mach number is a function of cooling channel geometry. If the maximum Mach number calculated in the cooling channels is above physical limits, the user can change NPSS inputs in the design variables. More often than not, increasing the aspect ratio of the cooling jacket channels and/or increasing the initial width of the cooling channels fixes the problem.

### ***III.4.g. Cooling Jacket Design***

The “Cooling\_Jacket” subcomponent serves two main purposes: first, calculate a wall thickness between the combusted gases and coolant that can structurally survive; second, calculate the hot and cold wall temperature of the cooling jacket stations and compare the maximum temperature to the material melting point.

Cooling jacket geometry is vital in maximizing heat transfer from the combusted products in the combustion chamber to the coolant in the cooling jacket. The amount of heat transfer occurring directly influences whether the propellant expander cycle will function and determines whether the chamber or aerospike material will thermally survive. Figure 29 shows the cross-sectional geometry of the cooling jacket along with the location of the structural jacket for both the chamber and aerospike. The figure also shows two cooling channels; the cooling channels and structural jacket continue around the entire circumference of the chamber and aerospike. The number of cooling channels is a function of chamber and aerospike radial geometry and cooling channel geometry. The variable  $w$  is equal to the fluid half-width of the cooling channel,  $a$  is the half-thickness between the cooling channels,  $t$  is the wall thickness between the coolant and the combusted products, and  $t_{SJ}$  is the structural jacket thickness. NPSS models the cooling channels as rectangles; realistically, they are trapezoids due to the curvature of the chamber and aerospike.

Two structural analysis approaches are performed in calculating an aerospike and chamber wall thickness between the combusted products and coolant that will structurally survive the high combustion chamber and cooling channel pressures. One approach assumes simple beam theory and the other assumes simple curved beam theory in calculating wall bending stress using simple supports at each end. Shear stress is also calculated assuming simple beam theory. For both approaches, the model assumes a default factor of safety of 1.5; the value is user configurable.



b) Aerospike Cooling and Structural Jacket

**Figure 29. Cooling Jacket and Structural Jacket Cross-Sectional Geometry**

Both approaches neglect thermal stress due to expansion/compression of the material. Since the cooling jackets experience large variations in temperatures, the cooling jacket will expand and contract. Calculation of a compressive stress is possible, assuming there is no expansion of the material for increased temperatures. Due to the high wall temperatures, the compressive stress can become extremely large and unusable. Therefore, some sort of expansion/compression of the material at room temperature must be assumed in calculating thermal stress. Component level design of the cooling jackets

should evaluate thermal expansion/compression and associated stresses, especially from a manufacturing standpoint to ensure there are no openings for combustion products to enter the cooling channels.

Due to the curvature of the cooling jacket walls, curved beam theory was chosen to calculate the bending stresses acting on the walls more accurately. Figure 30 shows a diagram of the curved cooling channel wall and associated forces. The cooling channel pressure ( $P_{chan}$ ) is greater than the chamber pressure ( $P_c$ ). To simplify the analysis and maintain a conservative approach, the analysis will use the maximum cooling channel width and pressure, even if the maximum values do not correspond to the same cooling channel station. In addition, for a conservative approach, the minimum aerospike and chamber radii will be utilized. Minimum radius increases stress. The maximum stress value is desired to guarantee the entire cooling jacket wall will not fail.

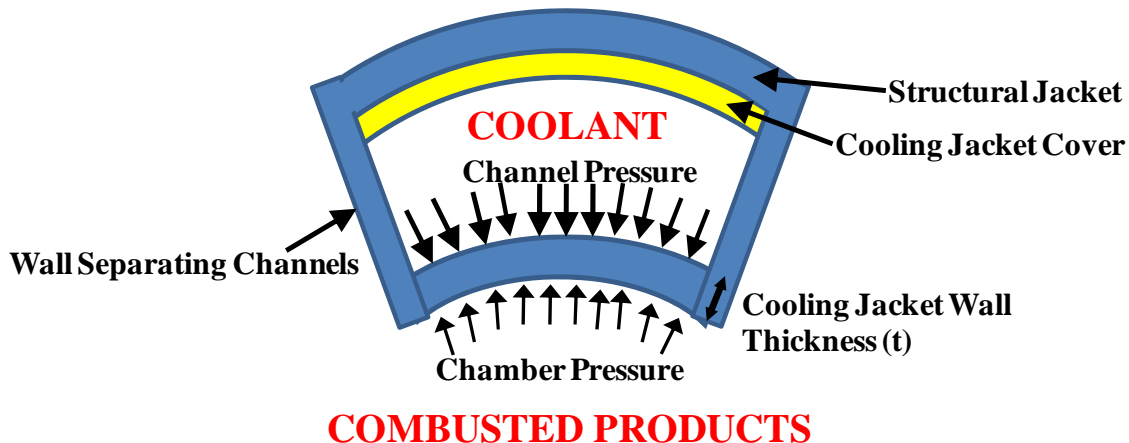


**Figure 30. Curved Beam Analysis Diagram**

Equations 36 – 44 calculate the bending stress using curved beam theory [62]. The equations assume a rectangular cooling jacket wall cross-section. Radii lengths extend from the axisymmetric centerline to the chamber or aerospike. Axial depth of the cooling channels ( $b$ ) is defined as the chamber length for the chamber and the length

from the injector face to the end of the cooling jacket station on the nozzle (end of aerospike station 8) for the aerospike.

$$r_n = \frac{A}{\int \frac{dA}{r}} = \frac{h}{\ln \frac{r_o}{r_i}} \quad (36)$$

$$\sigma_i = \frac{Mc_i}{Aer_i} \quad (37)$$

$$\sigma_o = - \frac{Mc_o}{Aer_o} \quad (38)$$

$$c_o = r_o - r_n \quad (39)$$

$$c_i = r_i - r_n \quad (40)$$

$$R_{cent} = r_i + \frac{h}{2} \quad (41)$$

$$e = R_{cent} - r_n \quad (42)$$

$$M = \frac{\Delta Pl^2}{8} \quad (43)$$

$$A = bh \quad (44)$$

where

$r_n$	=	Radius of Neutral Axis (in)
$h$	=	Cooling Jacket Wall Thickness (in)
$r_i, r_o$	=	Radius of Inner and Outer Wall Fibers (in)
$\sigma_i, \sigma_o$	=	Inner and Outer Surface Bending Stresses (psi)
$M$	=	Bending Moment (in-lb <sub>f</sub> )
$c_i, c_o$	=	Distance from Neutral Axis to Inner and Outer Fibers (in)
$A$	=	Cooling Jacket Wall Cross-Sectional Area (in <sup>2</sup> )
$e$	=	Distance from Centroidal Axis to Neutral Axis (in)
$R_{cent}$	=	Radius of Centroidal Axis (in)
$\Delta P$	=	Difference between Maximum Cooling Channel Pressure and Chamber Pressure (lb/in)
$l$	=	Twice the Maximum Cooling Channel Width (in)
$b$	=	Axial Depth of Cooling Channels (in)

The calculated bending stress at the inner and outer wall fibers are the critical stresses acting on the cooling jacket wall. The maximum magnitude of the inner or outer wall stresses is set as the maximum bending stress for comparison to yield or ultimate tensile strength. The units of  $\Delta P$  are lb/in but the units of pressure are lb/in<sup>2</sup>. The pressure difference multiplied by  $b$  corrects the  $\Delta P$  units.

Simple beam theory calculates the bending stress in a more straightforward way. Figure 31 shows a diagram of the simple beam analysis.

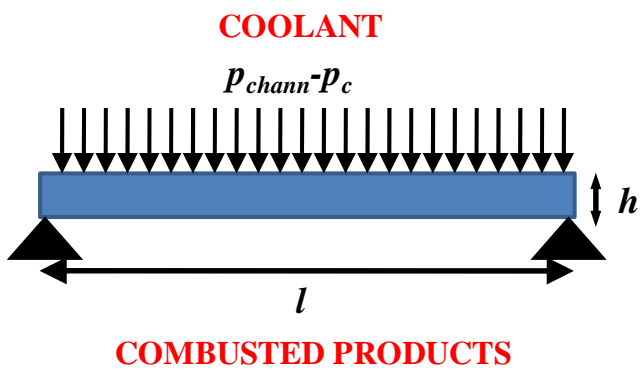


**Figure 31. Simple Beam Analysis Diagram**

Equations 45 - 47 calculate the bending stress using simple beam theory [62]. The moment (M) is calculated the same way as equation 44 and the equations assume a rectangular wall cross-section.

$$I = \frac{bh^3}{12} \quad (45)$$

$$c = \frac{h}{2} \quad (46)$$

$$\sigma_b = \frac{Mc}{I} \quad (47)$$

where

$I$  = Second Moment of Inertia (in<sup>4</sup>)

$c$  = Distance from Centroid to Outer Wall Fibers (in)

$\sigma_b$  = Bending Stress (psi)

Since the length of the beam being analyzed ( $l$ ) and the wall thickness are so small, the distance between the neutral axis and centroidal axis is negligible. Therefore, there is a slight difference between the bending stress calculated by curved beam theory and by linear beam theory. The percent difference between the two methods is 0.13% for the chamber and 0.38% for the aerospike. The conclusion is linear beam theory is acceptable to calculate the bending stress acting on the cooling jacket wall. Since both methods are in the DEAN model, the DEAN model uses curved beam theory bending stress multiplied by a factor of safety as the comparison to the material ultimate or yield strength.

As previously mentioned, the shear stress is calculated assuming simple beam theory using equation 48 [62].

$$\tau_{max} = \frac{3}{2} \frac{\Delta P}{hb} \frac{l}{2} \quad (48)$$

where

$$\tau_{max} = \text{Maximum Shear Stress (psi)}$$

The overall process for the cooling jacket structural analyses is as follows: to start, an initial wall thickness, set by manufacturing limits, is assumed to equal 0.02 inches. A bending and shear stress is calculated and multiplied by a factor of safety as a conservative approach. The bending and shear stresses are then compared to the user selected ultimate tensile or yield strength for bending stress and a function of ultimate tensile strength for shear stress. The shear strength equals one-third the material ultimate strength. If either the bending or shear stress is greater than the allowable strength, the

code will add  $10^{-6}$  inches ( $2.54 \times 10^{-6}$  cm) to the initial wall thickness until the wall stresses, multiplied by a factor of safety, either meet or are below the allowable strength.

Following the calculation of a structurally sound cooling jacket wall, calculation of the hot and cold wall temperatures is next. Research by Martin showed the wall temperature calculated by NPSS is only a balance of heat in and out of the wall and does not account for material properties. Therefore, Martin [4] utilized equation 49, a balance of three heat equations, to calculate the wall temperature for different material selections.

$$q = h_H A_H (T_H - T_{WH}) = k A_H \left( \frac{T_{WH} - T_{WC}}{t} \right) = h_C A_C (T_{WC} - T_C) \quad (49)$$

where

$q$	=	Heat Flux
$h_H$	=	Hot Side Convective Heat Transfer Coefficient
$A_H$	=	Hot Side Area
$T_H$	=	Combustion or Hot Side Temperature
$T_{WH}$	=	Wall Temperature on Hot Side
$k$	=	Thermal Conductivity
$t$	=	Wall Thickness
$T_{WC}$	=	Wall Temperature on Cold Side
$h_C$	=	Coolant Side Convective Heat Transfer Coefficient
$A_C$	=	Cold Side Area
$T_C$	=	Coolant or Cold Side Temperature

The values of  $q$ ,  $h_H$ ,  $h_C$ ,  $A_H$ ,  $A_C$ ,  $T_H$  and  $T_C$  are outputs from NPSS. The value of  $k$  is a property of material choice and the cooling jacket wall thickness,  $t$ , is from the aforementioned structural analysis. Hot and cold wall temperatures are calculated at each chamber and aerospike cooling jacket station.

The maximum wall temperature is found evaluating the magnitude of each wall temperature array element. The maximum wall temperature divided by the melting point of the selected material gives a percentage of the chamber and aerospike material melting point.

Material properties are functions of temperature. In order to match wall temperatures and material properties correctly, a converger called “Converge\_WallTemps” is required. A guessed maximum wall temperature in the material properties component links to the converger. Material properties at the guessed temperature are input into the cooling jacket code. The initial guessed maximum wall temperatures for the chamber and aerospike are 3000 and 2000 R, respectively. The cooling jacket code calculates a new maximum wall temperature using the material properties at the guessed temperature. The converger takes the calculated value and inputs it into the material properties component as a new guess. The process continues until the input and output maximum wall temperatures are approximately equal within a specified tolerance. The relative tolerance of the converger is 0.001 R (0.00056 K).

A physical design limitation, the maximum wall temperature must be less than the melting point of the selected material. One of the design requirements is to make the DEAN reusable and/or robust against testing. Taking a conservative approach, 60% of the material melting point is the maximum wall temperature for both the combustion chamber and aerospike to prevent material strength degradation; the constraint relates to the reusability design goal. Martin used 50% the melting point as the maximum wall temperature constraint; however, this seemed too conservative [4]. Limits, or constraints, can be placed on the ModelCenter variables; however, for optimization studies, the limits

are set to the material melting point instead of the 60% reusability goal. More research is required for reusability thermal limits since different materials have different physical limits related to thermal and structural cycles.

#### ***III.4.h. Material Properties***

The material properties subcomponent contains the properties of standard metals, alloys and ceramics compatible with the propellants. Seven DEAN components utilize material properties for structural analyses and weight estimation. Material selection is required for the combustion chamber and aerospike structural and cooling jackets, the aerospike nozzle tip (also known as the uncooled portion of the aerospike nozzle), and the oxygen and hydrogen plumbing. Inputs to the components are the maximum aerospike and chamber cooling jacket wall temperatures and the maximum oxygen and hydrogen fluid temperatures.

Both oxygen and hydrogen are compatible with specific materials. The designer must select the engine materials to withstand the vast range of temperatures and pressures from the propellant tanks to the nozzle. Huzel and Huang state material “compatibilities must be determined on an individual, case-by-case basis” [8]. Therefore, the designer should test the materials prior to prototype development to certify the final DEAN material decision. Arguello and Strain [40, 41] evaluated potential materials for the turbopumps.

Huzel and Huang list the following materials historically used as plumbing on a rocket engine: stainless steel, nickel alloys, iron-base superalloys (WASPALOY<sup>®</sup>),

titanium alloys, and cobalt alloys [8]. Nickel alloys, titanium alloys, and stainless steels can react negatively to hydrogen and oxygen.

There are material compatibility concerns with hydrogen. Due to the low molecular weight of hydrogen, a major concern is the ability of hydrogen to permeate engine walls. Metals exposed to gaseous hydrogen are susceptible to hydrogen environment embrittlement (HEE); typically metals are immune at temperatures less than 260 R (144.4 K) [8]. For example, copper alloys with high oxygen grades are susceptible to HEE [8]. In the DEAN, HEE is a concern as hydrogen gains heat passing through the aerospike cooling jacket. Huzel and Huang state liquid hydrogen is compatible with austenitic stainless steels, iron-base alloys, copper alloys, and cobalt alloys [8].

There are also material compatibility issues with oxygen. Spontaneous ignition can occur when oxygen contacts certain materials, such as titanium, magnesium, and aluminum at high pressures [8]. Huzel and Huang state liquid oxygen is compatible with austenitic stainless steels, iron-base alloys, nickel alloys, cobalt alloys, and copper alloys [8]. Schoenman states the engine designer should avoid aluminum alloys, titanium alloys and stainless steels with high iron and chrome compositions due to the ability of oxygen to ignite the materials [53].

In choosing material for the combustion chamber and aerospike, the material must be resistant to stress corrosion cracking (SCC). Materials resistant to SCC include “alloy steels heat-treated to high strength, precipitation-hardening stainless steels in high-strength conditions, and high-strength aluminum alloys in the T6 temper” [8]. Huzel and Huang present a detailed discussion of material types and applications to liquid propellant rocket engines [8].

During the initial DEAN model development, Martin chose chamber and aerospike cooling jacket materials with high thermal conductivity and elevated melting points to deal with the high wall temperatures. Martin also evaluated materials for the structural jacket to surround the cooling jacket [4]. The structural jacket is required to contain the high combustion chamber and cooling channel pressures; the material selected would need high tensile strength and low density. Lastly, Martin evaluated materials compatible with oxygen; he stated materials used with oxygen should have a low heat of combustion and a low burn factor [4].

Thirteen different materials were selected for the DEAN design based on their compatibility with the propellants. Table 9 summarizes the materials used in the DEAN model and summarizes what materials are useable for the individual engine components. Some materials are useable only if they are not exposed to the propellants (i.e. aluminum and titanium). In addition, different materials are useable for different engine components. The interaction of dissimilar metals is realistic; however, there are varieties of methods to minimize galvanic corrosion. The DEAN model assumes galvanic corrosion is not an influential design factor.

The material properties utilized in the DEAN model include material density, material melting point, thermal conductivity, ultimate tensile strength, and yield strength. The modulus of elasticity and the linear coefficient of thermal expansion properties are included in the code but are not currently utilized. The properties, where possible, are coded as functions of temperature. Material properties as a function of temperature provide more accuracy to the structural analyses for the walls separating the coolant and combusted gases since the wall experiences both hot chamber temperatures and cold

coolant temperatures. Appendix B tabulates the material properties as a function of temperature used in the final DEAN ModelCenter model. Material properties, collected from [33] and [54 – 61], are a function of how the engine components are manufactured and of the purity of the material. Component level design should further evaluate the material properties for more accurate heat transfer and mass estimation calculations. The tabulated properties used in the model give a rough estimate of engine component mass.

**Table 9. Materials Compatible with Engine Components**

Material	Propellant Compatibility / Selected
Pure Copper (Annealed)	Compatible with O <sub>2</sub> and H <sub>2</sub> / Useable for chamber and aerospike cooling jacket, structural jacket, and O <sub>2</sub> and H <sub>2</sub> plumbing
Silicon Carbide (Highly-Pure)	
INCOLOY® 909 (Age Hardened)	
HAYNES® 188 alloy (Bright Annealed)	
Beryllium Copper (C17000 TH04)	
Oxygen-Free Copper (C10100 1180 Temper)	
Cobalt (Forged Electrolytic)	Compatible with O <sub>2</sub> / Useable for chamber cooling jacket, structural jacket, and O <sub>2</sub> plumbing
INCONEL ® 718 (Annealed & Aged)	
INCONEL® 625 (Annealed)	
Aluminum 7075 T6	Not compatible with O <sub>2</sub> or H <sub>2</sub> / Useable for chamber and aerospike structural jacket as long as propellant contact does not occur
Aluminum 2024 T6	
Titanium (ASTM Grade 3, 99.1% Ti)	
Pure Niobium	Compatible with Exhaust / Useable for uncooled portion of aerospike nozzle

The DEAN model makes several assumptions concerning material properties. First, the model assumes constant density while neglecting thermal expansion of the materials. The mass of a material will not change for increased temperature; however, volume will increase causing an overall decrease in density. The DEAN model uses density to estimate engine component mass; therefore, room temperature density is

useable to estimate mass since the model neglects expansion effects. However, material expansion effects must be evaluated during component level design to model heat transfer and engine component manufacturability more accurately. Second, if a wall temperature falls between two tabulated values for a specific property, the DEAN model selects the property corresponding to the higher temperature value. For example, if thermal conductivity is tabulated between 800 and 1000 R and the wall temperature equals 845 R, the thermal conductivity value at 1000 R will be used. Using the property at the higher temperature value is a conservative approach, especially for structural analyses using yield and ultimate tensile strengths, where strength values decrease for increased temperatures. Material properties are typically not linear for increasing temperature, so linear interpolation of properties between tabulated temperatures may not be accurate. The third assumption is if a wall temperature is greater than a tabulated entry, the model will use the last table entry value. For example, if the final tabulated entry for yield strength is at 1200 R and the wall temperature equals 1400 R, the model uses the yield strength at 1200 R. This is a liberal assumption and was chosen as the best path since properties at higher temperatures could not be found and the decision to use a property value of zero would lead to certain material selections to be completely unusable. Fourth, the model neglects ambient temperatures. In the vacuum of space, materials exposed to ambient conditions can have large variations in temperature, especially if the material is exposed to direct sunlight and gains heat from radiation. Lastly, since most material properties decrease with increased temperature, the model selects material properties using the maximum wall temperature of the material as a conservative approach, instead of using the minimum or average wall temperature.

Each engine component has a hot and cold side due to heat transfer. For example, the outer chamber cooling jacket wall will be hot on one side due to direct interaction with the combustion gases and cold on the other side due to direct interaction with the coolant. How hot or cold the component walls are depends on the amount of heat transfer occurring due to convection and conduction. The DEAN model neglects radiation effects. The temperatures driving the DEAN design are the maximum hot wall temperatures for the two cooling jackets and the maximum fluid temperature in the cooling channels affecting the plumbing and structural jacket material properties. The model conservatively assumes the uncooled portion of the aerospike (nozzle tip) has a wall temperature equal to the maximum wall temperature for the aerospike cooling jacket; realistically, the assumption is not true. As the flow expands along the nozzle, the exhaust will lose temperature and the nozzle wall temperature will be less than the wall temperature of the aerospike internal to the combustion chamber.

Typically, material strength degrades as temperature increases necessitating the use of a maximum hot wall temperature as a conservative design approach, especially important in the structural jacket and plumbing designs. The DEAN model neglects heat transfer through the structural jackets and plumbing and assumes the maximum cooling jacket fluid temperature calculated in NPSS equals the structural jacket and plumbing wall temperatures. The material properties at the maximum fluid temperature are then utilized in the model as a conservative approach. Realistically, the structural jacket, when not in contact with the propellants, will have a different wall temperature than the maximum fluid temperature due to conduction and environmental conditions. The same is true for the propellant plumbing. In addition, for the plumbing, the DEAN model

assumes a maximum wall temperature for the entire plumbing of the engine. Realistically, the pipe from the tank to the pump will experience different wall temperatures than the pipe from the cooling jacket to the turbine; however, to simplify the problem, a maximum wall temperature equal to the maximum fluid temperature is assumed across all engine plumbing for a specific propellant. The plumbing and structural jacket material selections are required to calculate a pipe or structural jacket thickness. Using a higher temperature leads to a thicker wall and more weight; however, the result will be a conservative estimate.

The different materials compatible with specific engine components will be evaluated in an attempt to maximize  $T/W$  while meeting mechanical and thermal limitations.

#### *III.4.i. Determination of Fluid Phase in Engine*

For the DEAN design, the fluid phase at the injector face is preferred to be supercritical to improve injection, atomization, and mixing of the fuel and oxidizer. In addition, supercritical fluid in the cooling jacket is preferred for a more predictable and controlled steady heat transfer rate [23]. The propellant will begin in liquid form in the propellant tanks. In most cases, the propellant will gain enough heat in the cooling jacket to change to supercritical and will remain as such until injection in the combustion chamber.

The “Fluid\_Phase” model script component determines whether the fluid is supercritical or not at twelve engine stations for the oxidizer and fifteen engine stations

for the fuel. Table 10 tabulates the different engine components where the fluid phase was evaluated.

**Table 10. Engine Components Where Fluid Phase Evaluated**

<b>Chamber Engine Components</b>	<b>Aerospike Engine Components</b>
Tank	Tank
Pump Inlet	Pump 1 Inlet
Pump Outlet	Pump 1 Outlet / Pump 2 Inlet
Cooling Jacket Station 6 (Throat)	Pump 2 Outlet
Cooling Jacket Station 5	Cooling Jacket Station 8
Cooling Jacket Station 4	Cooling Jacket Station 7
Cooling Jacket Station 3	Cooling Jacket Station 6 (Throat)
Cooling Jacket Station 2	Cooling Jacket Station 5
Cooling Jacket Station 1	Cooling Jacket Station 4
Turbine Inlet	Cooling Jacket Station 3
Turbine Outlet	Cooling Jacket Station 2
Injector Inlet	Cooling Jacket Station 1
Chamber	Turbine Inlet
	Turbine Outlet
	Injector Inlet
	Chamber

The oxygen and hydrogen critical points were obtained from NIST [52] and are tabulated in Table 11.

**Table 11. Propellant Critical Points from NIST [52]**

	<b>Oxygen</b>	<b>Hydrogen</b>
<b>Critical Temperature</b>	278.246 R (154.6 K)	59.661 R (33.1 K)
<b>Critical Pressure</b>	731.43 psia (5.0 MPa)	188.03 psia (1.3 MPa)
<b>Critical Density</b>	27.23 lb <sub>m</sub> /ft <sup>3</sup> (436.2 kg/m <sup>3</sup> )	1.95 lb <sub>m</sub> /ft <sup>3</sup> (31.3 kg/m <sup>3</sup> )

For a fluid to be supercritical, the fluid pressure and temperature must both be greater than the critical point of the propellant regardless of fluid density. For both the oxidizer and fuel, the fluid pressure and temperature outputs at each station from the

second NPSS nonlinear model are compared to the critical point values of the propellant to determine if the fluid is supercritical or not. If the fluid is not supercritical and goes supercritical at a certain station, an individual variable will declare what station the fluid goes supercritical. Furthermore, another individual variable will state if the fluid phase in the injectors is supercritical or not. The “Fluid\_Phase” outputs are variables of interest and do not drive any other DEAN model components.

### ***III.4.j. Structural Jacket Design***

The “Structural\_Jacket” script component calculates the structural jacket geometry required for both the chamber and aerospike. The structural jackets serve to bring structural stability and rigidity to the chamber and aerospike by containing the cooling channel and combustion chamber pressures. The oxidizer structural jacket surrounds the outside of the combustion chamber experiencing tension while the fuel structural jacket surrounds the interior of the aerospike experiencing compression. The code also calculates the mass of each structural jacket along with the volume and mass of the uncooled nozzle aerospike tip, the volume of the aerospike and chamber cooling channel covers, and the material cross-sectional area of the fuel and oxidizer plumbing.

The script component utilizes the largest chamber or aerospike radius for calculating structural jacket thickness as a conservative approach; the larger the radius, the larger the required thickness. Next, the code utilizes the cooling channel pressure instead of the chamber pressure since the channel pressure is greater. Lastly, to calculate the structural jacket thickness and the plumbing wall thickness, the code utilizes a factor

of safety equivalent to the factor of safety utilized by the cooling jacket code; the default factor of safety value is 1.5.

As previously mentioned, the user has a decision design variable named “Cooling\_Geom\_Option”. The user can select to use the structural jacket as the cooling channel cover or select for an individual cooling channel cover plus the structural jacket. Both options have advantages and disadvantages. Using the structural jacket as the cooling channel cover limits what materials are available for selection due to propellant compatibility issues; for example, the aluminum and titanium materials will react negatively to the propellants and are not useable if the structural jacket serves as the cooling channel cover. Currently the cooling channel heights vary from station to station; they can be thought of as being stepped. When manufactured, the cooling channels will be sloped versus stepped. If a structural jacket serves as the cooling channel cover or if a cooling channel cover is used, the bottom portion of the cover will be stepped to avoid material gaps in the cooling channels. The benefit of the option is the subtraction of one more piece of hardware: the cooling channel cover. The second option to use a cooling channel cover and structural jacket allows the designer to evaluate all materials for the structural jacket since the structural jacket will not be exposed to the propellant. Having the cooling channel cover allows utilization of stronger and lighter materials for the structural jacket. The cooling channel cover as previously mentioned will be stepped on one side to mold to the cooling channel shape and flat on the other side; having a flat side allows for easier manufacturability of the structural jacket.

The user also has another decision design variable influencing the execution of the structural jacket code. The user has the option to use ultimate tensile or yield strength

to calculate structural jacket and plumbing thicknesses. The ultimate tensile strength choice will lead to thinner walls and less component weight, while yield strength will lead to thicker walls yet allow for reusability. The DEAN model assumes the structural jacket and pipe maximum wall temperature is equal to the maximum cooling channel fluid temperature. The assumption influences the ultimate tensile and yield strengths of the selected structural jacket and plumbing materials.

Thin-wall pressure vessel equations can be utilized when the wall thickness is approximately  $1/20^{\text{th}}$  or less of the inner radius of the vessel [62]. With the capability of the DEAN model to evaluate a range of chamber and aerospike radii, there is no way to guarantee thin-walled pressure vessel equations are useable at all times. Therefore, the code utilizes thick-wall pressure vessel equations (also known as cylinder stress calculations) to calculate the required thickness for the structural jacket and plumbing walls. The thick-wall pressure vessel equations assume “a right section of the cylinder remains plane after stressing” [62]. The code assumes negligible longitudinal stress at the ends of the aerospike and chamber pressure vessels. Figure 32 shows the chamber and aerospike pressure vessel problem.

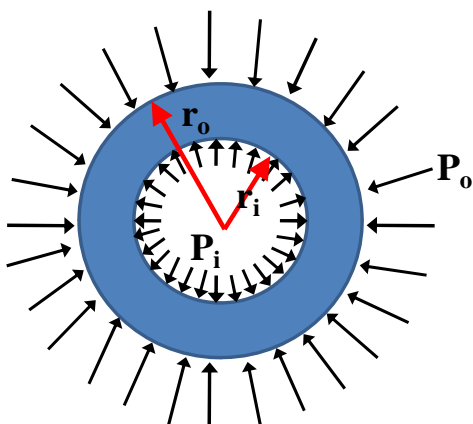


**Figure 32. Chamber and Aerospike Pressure Vessel**

The process for the chamber is as follows: to start, the inner and outer cooling channel surface radial dimensions are known from the output file of the NPSS model. The cooling channel cover surface closest to the combustion chamber (inner wall) has radial dimensions at each station equal to the chamber station radius plus the cooling jacket wall thickness plus the height of the cooling channels; the inner cooling channel cover surface is stepped with the varying channel heights. The cooling jacket wall refers to the wall separating the coolant and combusted products. The minimum thickness of the cooling channel cover is assumed to equal the cooling jacket wall thickness calculated in the “Cooling\_Jacket” script component. The minimum thickness is added to the minimum radius (occurs at station 6 at the throat) of the inner cooling channel cover. The outer cover wall at station 5 is equal to the outer cover wall radius at station 6 plus 0.5 inches (1.27 cm) and the remaining stations (1-4) have outer cover wall radii equal to station 6 plus one inch (2.54 cm). The process leads to a smooth outer cover wall improving structural jacket fabrication.

The user decision “Cooling\_Geom\_Option” now comes into play. If the user decides the structural jacket acts as the cooling channel cover, the structural jacket inner surface will be the inner cooling channel cover surface and will be stepped. If the user selects the option to use both a cooling channel cover and structural jacket, the structural jacket inner surface will mate to the outer cooling channel cover surface and the structural jacket inner wall will be smooth. With the inner structural jacket radii set at the different chamber stations, the pressure vessel calculation can occur to calculate structural jacket thickness. Figure 23 shows an axial sketch of the DEAN structural jacket and cooling jacket geometry, while Figure 29 shows a sketch of the cross-section.

The maximum oxidizer cooling channel pressure and maximum inner structural jacket wall radius are used for the chamber pressure vessel calculation. The maximum inner structural jacket wall radius for the chamber occurs at the injector face ( $r_i$ ). An initial structural jacket thickness of 0.1 inches (0.254 cm) is assumed; the outer structural jacket wall radius ( $r_o$ ) equals the inner structural jacket wall radius plus the assumed thickness. The tangential stress and radial stress are calculated with the assumed thickness using the relations in equations 50 and 51 multiplied by a factor of safety. For the chamber, the outer pressure is ambient pressure (previously calculated and based on the “Pamb\_Decimal” from the user) and the inner pressure is the maximum oxidizer cooling channel pressure.

$$\sigma_t = \frac{p_i r_i^2 - p_o r_o^2 - r_i^2 r_o^2 (p_o - p_i) / r^2}{r_o^2 - r_i^2} \quad (50)$$

$$\sigma_r = \frac{p_i r_i^2 - p_o r_o^2 + r_i^2 r_o^2 (p_o - p_i) / r^2}{r_o^2 - r_i^2} \quad (51)$$

where

$\sigma_t$	=	Tangential Stress (psi)
$p_i, p_o$	=	Internal and External Pressure (psi)
$r_i, r_o$	=	Internal and External Radius (in)
$r$	=	Radius between or equal to External or Internal Radii (in)
$\sigma_r$	=	Radial Stress (psi)

Typically, the tangential stress will be greater than the radial stress. However, the larger stress value will be compared to the allowable strength of the material (yield or ultimate tensile strength based on the choice of the user). For the chamber, the value of  $r$  is equal to the structural jacket inner radius. If the larger stress value is greater than the

allowable strength, the thickness of the structural jacket will increase by  $10^{-5}$  inches ( $2.54 \times 10^{-5}$  cm) until the larger stress value equals the allowable strength. The outer structural jacket surface radius is equal to the inner structural jacket surface plus the calculated thickness.

With known structural jacket and cooling channel cover geometry, the volume of each component can be calculated. For each structural jacket and cooling channel cover station, the volume of the component at the individual station is calculated using cylinder and conical frustum volume equations. An additional cylindrical volume calculation is performed on the chamber exit lip extending past the throat (required for TDK and NPSS; reference Appendix C.1 and D.1). The volumes of the components are calculated for the inner and outer surfaces. The total chamber component material volume is equal to the outer volume minus the inner volume. The cooling channel cover volume is an input into the thrust-to-weight script component. If the user decides the structural jacket performs the cooling channel cover function, the cooling channel cover volume equals zero. The last step with the structural jacket is to multiply the volume of the structural jacket by the user selected material density to obtain the mass of the structural jacket. The DEAN model uses the mass of the structural jacket in the thrust-to-weight model script component.

The DEAN model performs a similar process for the aerospike; however, since the aerospike structural jacket is under compression from the cooling channel pressures, the initial radius arrays are calculated in reverse from the chamber arrays. The same is true for the cooling channel cover. For example, instead of adding cooling channel height and cooling jacket wall thickness to the aerospike radius, those values are

subtracted. The same process is utilized to calculate the structural jacket thickness where the outer pressure is the maximum pressure in the hydrogen cooling channels and the inner pressure is assumed equal to ambient pressure (conservative approach). With known cooling channel cover and structural jacket geometry, the volume of both components is calculated. The aerospike cooling channel cover is calculated just like the chamber. The structural jacket outer wall geometry (wall closest to the combustion chamber) is also calculated similarly to the chamber; however, the inner wall geometry (wall closest to axisymmetric centerline) is calculated differently.

To improve fabrication of the aerospike, the geometry of the inner wall is simplified to a bored hole with a truncated cone at the end. The bored hole serves to lower aerospike mass. It also serves as an opening in the aerospike to run plumbing to the end of the cooled portion of the aerospike nozzle to allow flow through the hydrogen cooling channels back towards the injector face. The bored hole extends from the injector face to the throat at a radius equal to the minimum radius of the inner structural jacket wall array between the injector and throat. From the throat to the end of the cooled portion of the aerospike nozzle (end of station 8), the bored hole will slant towards the end of station 8 at a final radius of the minimum radius of the inner structural jacket wall array between the throat and end of station 8. The resulting structural jacket thickness between the throat and end of station 8 is at least the minimum structural jacket thickness. If the aerospike radius at the injector face is greater than the nozzle radius at the end of station 8, the bored hole slant will have a negative slope. However, in the off chance the aerospike radius at the injector face is less than the nozzle radius at the end of station 8, the bored hole will slant with a positive slope. Figure 33 depicts both slant slopes. In all

trade studies run, a slant with negative slope was observed; however, a slant with a positive slope is a possibility as a consequence of how the code was written.

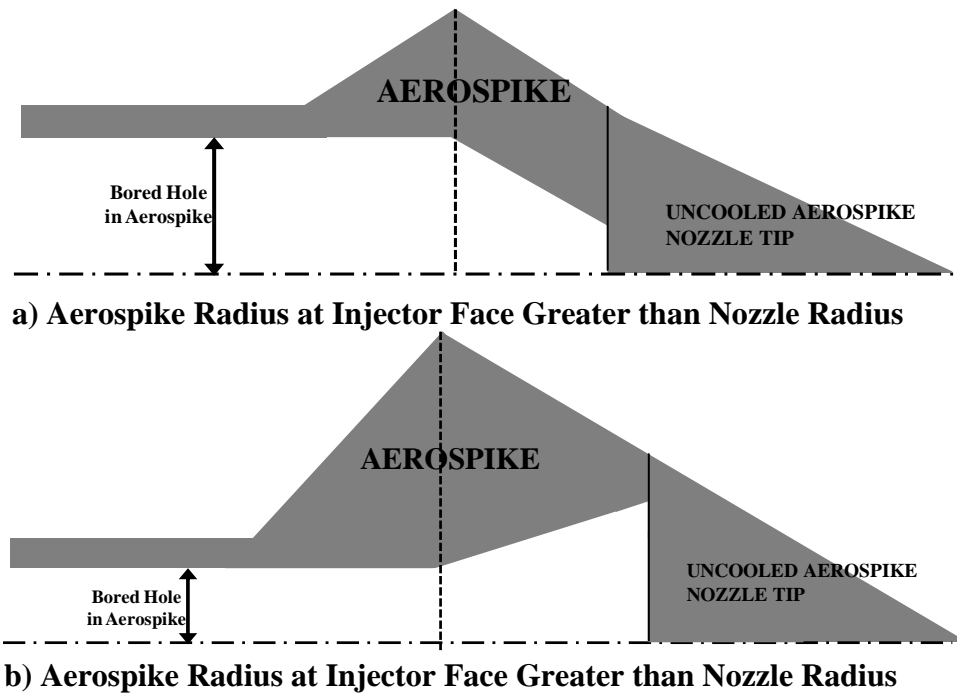


**Figure 33. Aerospike Bored Hole Geometry**

If the aerospike structural jacket thickness is greater than or equal to the aerospike structural jacket outer wall radius at any station (distance from axisymmetric centerline to the outer jacket wall), the code will set the outer structural jacket wall radius to zero. Therefore, the radius at the station will equal zero and the spike becomes solid (bored hole is nonexistent). The code calculates if the spike is solid at two locations: first, the bored hole extending from the injector face to the throat, and second, the slanted bored hole extending from the throat to the end of the cooled portion of the nozzle. A specific output variable will state whether the aerospike is solid, bored hole, or half-bored hole. Bored hole means entire bored hole and truncated cone exist; half-bored hole means only bored hole from injectors to throat exists, rest of nozzle is solid.

The aerospike can be manufactured in two independent pieces. The first piece, the aerospike component internal to the combustion chamber and the cooled portion of the aerospike, can be manufactured. The bored hole can easily be cut out at this point in fabrication. The second piece is the solid uncooled aerospike nozzle tip that can attach to the first piece. To decrease aerospike mass, future research can evaluate boring a hole in the uncooled aerospike nozzle tip.

The structural jacket script component also calculates the material area of the oxidizer and fuel plumbing. The external pressure of the plumbing is set to ambient pressure and the internal pressure of the plumbing equals the maximum pressure in all plumbing. The code assumes the pipe area is equal to the average plumbing area output from NPSS, from which the inner pipe radius can be calculated; the assumption is reasonable since it accounts for increased pump and turbine inlet and outlet areas. The thickness of the plumbing is calculated in the same way as the structural jackets including a factor of safety of 1.5. Pipe wall thickness is assumed constant for all plumbing. The material area of the plumbing is equal to  $\pi$  multiplied by the difference of the outer pipe radius squared and the inner pipe radius squared. The DEAN model uses the material area as an input into the thrust-to-weight script component to estimate engine plumbing.

Lastly, the structural jacket code will calculate the overall chamber and aerospike thickness for rendering the geometry in ModelCenter. The thickness accounts for the cooling jacket wall, cooling channel height, cooling channel cover, and the structural jacket.

### III.4.k. Performance Calculation

The “Performance\_Calc” script component serves to calculate the thrust and specific impulse of the DEAN engine.

The linear DEAN NPSS model relies on the NPSS ROCKETNOZZLE element code; the element calculates performance assuming a bell nozzle design. For the aerospike, the equation to calculate thrust is slightly different. According to Sutton and Biblarz, the thrust of an aerospike nozzle consists of three components [23]. First, there is the axial thrust component through the throat; momentum thrust. Second, the pressure distribution or integral of pressure acting on the length of the aerospike over the spike cross-sectional area; pressure thrust. Third, if the aerospike is truncated, the pressure acting over the base area; base pressure thrust. The sum of the three thrust components equal one total thrust value ( $F$ ), with units in  $\text{lb}_f$ , as represented in equation 52 [23]:

$$F = [\dot{m}v^* \cos \theta + (p^* - p_{amb})] + \int^A pdA + (p_{base} - p_{amb})A_{base} \quad (52)$$

where

$\theta$	= Angle of Flow to Centerline of Spike (deg)
$\dot{m}$	= Total Propellant Flow Rate ( $\text{lb}_m/\text{s}$ )
$v^*$	= Throat Velocity (ft/s)
$p^*$	= Throat Pressure (psia)
$pdA$	= Pressure acting on Nozzle at Differential Cross-Sectional Area
$p_{base}$	= Truncated Aerospike Base Pressure (psi)
$p_{amb}$	= Ambient Pressure (psi)
$A_{base}$	= Truncated Spike Base Cross-Sectional Area ( $\text{ft}^2$ )

Equation 52 does not account for the “negative effect of the slipstream of air around the engine (which causes a low-pressure region) and the friction on the aerospike”

[23]. The third thrust component only applies if the full-length aerospike nozzle is truncated.

When the aerospike nozzle operates above or below its design altitude, an additional thrust component exists due to the difference in the ambient and nozzle exit pressures. Figure 34 shows a free body diagram of the DEAN upper stage.

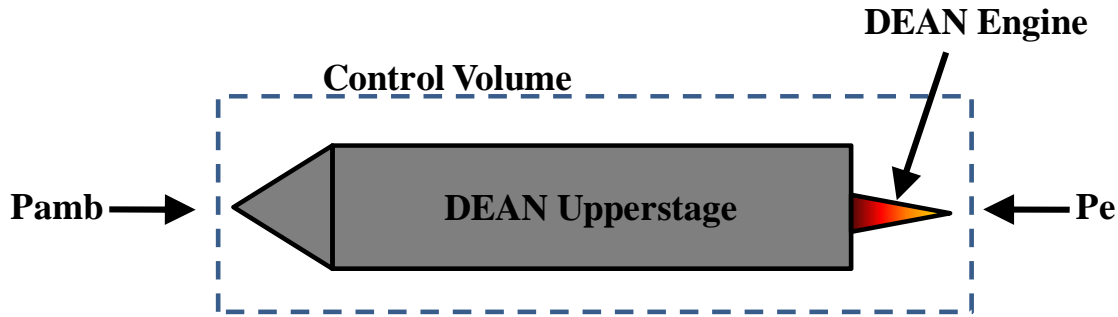


**Figure 34. DEAN Upper Stage Free Body Diagram**

From equation 7, the  $\dot{m}u_e$  term will account for the thrust produced in equation 52. The last portion of equation 7, the  $(p_e - p_a)A_e$  term, accounts for the additional thrust component for engine operation at an altitude other than the design altitude; the new thrust term will be referred to as  $F_{nondesign}$ , where  $p_a$  and  $p_e$  are the ambient and nozzle exit pressures (psia) and  $A_e$  is the exit area of the flow, respectively.  $F_{nondesign}$  will equal zero when the nozzle operates at its design altitude.

For a full-length aerospike nozzle, the exit pressure is equivalent to the pressure acting at the last point on the nozzle. The ambient pressure is equivalent to the pressure associated with the altitude the engine is operating in. For the DEAN, the operational environment is the vacuum of space. Mathematically for the DEAN model to function (NPSS and TDK), the operational ambient pressure is equivalent to 0.000145 psia or 1 Pa. As previously stated, for an aerospike operating above its design altitude, the flow

field will expand radially outward from an imaginary line parallel to the centerline extending from the chamber exit lip to the exit plane. How much the flow expands radially outward depends on the interaction of the flow with the ambient conditions; this flow interaction is best suited for a computational model. Therefore, with the current DEAN model as is, the exact flow exit area is unknown. However, the flow exit area will at least be equal to the chamber exit lip area (design flow exit area) and an underestimated  $F_{nondesign}$  thrust component can be calculated.

When the aerospike is truncated, the difference between  $F_{nondesign}$  and truncation thrust is hard to distinguish, especially since both equations are similar in nature. In addition, the base pressure thrust acting on the truncated nozzle base is hard to define. One could assume the base pressure thrust is equal to the wall pressure at the truncated position. However, the assumption leads to strange calculations where a 90% truncated body has better thrust than the full-length spike; this not the right answer. An improved answer is to return to the original definition of the term ‘aerospike’. Defined in section II.3.d, the term aerospike refers to when the subsonic recirculating flow, acting along the truncated base, interacts with the primary exhaust flow, the subsonic flow will form an aerodynamic spike mimicking an ideal isentropic spike [8]. Therefore, due to the truncated base, the exhaust flow will still expand against the subsonic recirculating flow. How much the exhaust flow expands along the aerodynamic spike may vary. For the current research effort, the DEAN model assumes the flow fully expands to the full-length aerospike exit pressure. With this assumption, there is no difference between the truncation thrust and  $F_{nondesign}$ ; consequently, truncation thrust in equation 52 must be neglected. The exit area for  $F_{nondesign}$  remains unchanged (not equal to the truncated base

area) because of the assumption of full flow expansion for truncation studies. Hence, the estimated total thrust for the DEAN, regardless if the nozzle is truncated or full-length, is equivalent to equation 53. As a reminder,  $F_{nondesign}$  underestimates the actual value; as a result, the total thrust calculated in equation 53 is a conservative estimate.  $F_{cowl}$  is the thrust acting on the chamber exit lip and is calculated in TDK.

$$F = [\dot{m}v^* \cos \theta + (p^* - p_{amb})] + \int^A p dA + (p_e - p_{amb})A_e + F_{cowl} \quad (53)$$

The thrust component represented in brackets in equation 53 is the momentum thrust out the throat of the nozzle. The nonlinear NPSS model uses the *RocketNozzleAerospike* element to calculate the momentum thrust out the throat and also calculate the bell nozzle performance for comparison. The element is a tailored version of the *RocketNozzle* NPSS element using equation 7 divided by throat area, to calculate the momentum thrust, where  $\varepsilon = 1$  and  $p_e$  is changed to the throat pressure ( $p^*$ ) assuming the throat is choked with a Mach number equal to 1.0.

For the full-length aerospike, the actual pressure thrust is calculated and output in TDK. However, for truncation studies, the integral ( $\int^A p dA$ ) in equation 53 must be solved. To remain consistent, the code estimates the pressure thrust using the integral in equation 53 for the full-length and truncated aerospike.

The pressure used in the integral is the normal component of the pressure to the axisymmetric centerline axis. The normal pressure component at a specific nozzle location is found taking the inverse tangent of the nozzle slope, taking the sine of the inverse tangent value, and multiplying the sine value by the corresponding TDK pressure

profile value. The absolute value of the normal pressure magnitude is used in the integral.

The differential area ( $dA$ ) relates to surface area of the aerospike nozzle; therefore, since the nozzle is axisymmetric, a surface of revolution integral can be used. Equation 54 shows the surface of revolution integral along with the corresponding trapezoidal approximation used to solve the integral computationally;  $f(x)$  is equal to the function in the integral where  $p$  and  $r$  are functions of  $x$  [45].

$$2\pi \int_0^L Pr\sqrt{1 + (r')^2} dx = \pi \sum_2^N [x(i) - x(i-1)][f(x(i-1)) + f(x(i))] \quad (54)$$

where

$$\begin{aligned} p &= \text{Aerospike Normal Pressure at Point i (psia)} \\ r &= \text{Aerospike Radius at Point i (in)} \\ r' &= \text{Slope of Aerospike at Point i} \\ L &= \text{Nozzle Axial Length (in)} \\ dx &= \text{Differential Axial Length (in)} \end{aligned}$$

The surface of revolution integral introduces a nozzle slope term ( $r'$ ). The nozzle slope at a specific location was found using two different methods. First, a Newton's backwards difference quotient was assumed for all points including end points; the method starts at the first nozzle point past the throat. The second method used Newton's backward difference for the end points and central difference (or three point estimate) for the internal points. Equation 55 and 56 show the backward difference and central difference slope equations, respectively. The first method underestimated the TDK calculated pressure thrust for a full-length spike by 0.5%. The second method

overestimated the pressure thrust by 0.5%. To remain conservative, the DEAN model uses the first method, equation 55, to calculate the nozzle pressure thrust.

$$m = \frac{r(i) - r(i-1)}{x(i) - x(i-1)} \quad (55)$$

$$m = \frac{r(i+1) - r(i-1)}{x(i+1) - x(i-1)} \quad (56)$$

where

$m$	=	Nozzle Slope at Point i
$r$	=	Nozzle Radius (in)
$x$	=	Nozzle Axial Distance from Throat (in)
$i$	=	Identifier to Point Located on Aerospike Nozzle

The calculated pressure thrust from equation 54 uses the pressure profile from TDK. The calculated mass flow rate in TDK is different from the user design variable mass flow rate; therefore, a correction factor is required to correct the calculated pressure thrust to the actual user design variable mass flow rate. Also, the calculated pressure thrust needs to be corrected to include boundary layers losses; note the TDK output pressure profile does not account for boundary layer losses. The first correction is the boundary layer correction. For the full spike, a percent boundary layer loss was calculated in the “TDK\_Outputs” code for the TDK PFG with boundary layer model by taking the difference between the boundary layer pressure thrust and no boundary layer pressure thrust and dividing by no boundary layer pressure thrust. Realistically, the percent boundary layer loss will vary along the length of the spike with most losses recognized at the beginning of the nozzle out the throat. However, to simplify the calculations and remain conservative, the percent boundary layer loss is assumed constant for all nozzle truncation studies. For example, if TDK calculated a full-length aerospike

nozzle boundary layer loss of 4.0%, then the boundary layer loss at 90% truncation is also equal to 4.0%. The corrected pressure thrust value will equal the calculated pressure thrust value multiplied by the percent boundary layer loss and then subtracted from the calculated value. The second correction uses a simple linear correction factor, equations 31 and 32, to correct the pressure thrust.

To validate the trapezoidal approximation function used to estimate the pressure thrust, the calculated value for the full-length spike is compared to the true calculate value in TDK using the same correction factors in Table 12. The default design variables in Table 13 (based on the design point used by Simmons [6]) were used as model inputs for the comparison. The percent difference is calculated by taking the difference between the TDK and estimated pressure thrust and dividing by the TDK value. The percent difference is less than 1% proving the accuracy of the trapezoidal approximation function.

**Table 12. Pressure Thrust Comparison**

	<b>TDK</b>	<b>Estimated</b>	<b>% Difference</b>
<b>Corrected Pressure Thrust</b>	7312.99 lb <sub>f</sub> (32.5 kN)	7265.4 lb <sub>f</sub> (32.3 kN)	0.65%

The total thrust is the sum of the momentum thrust, the pressure thrust, the  $F_{nondesign}$ , and the chamber exit lip or cowl thrust ( $F_{cowl}$ ) including aerospike nozzle viscous losses. Specific impulse is easily calculated by dividing the thrust by the weight flow rate.

The last portion of the “Performance\_Calc” script is a comparison of calculated DEAN performance to the bell nozzle performance calculated in the nonlinear NPSS model. A percent difference in thrust and specific impulse is calculated by taking the

DEAN value minus the NPSS value and dividing by the NPSS value. The percent difference can be positive or negative. A negative value means the DEAN performs worse than the bell nozzle and vice versa for a positive value. The NPSS performance values assume no losses, while the DEAN performance values include boundary layer losses.

**Table 13. Default Design Variables**

Design Variables	Default Value
Chamber Pressure Guess	1740 psia (12 MPa)
Chamber Temperature Guess	6550 R (3639 K)
<i>O/F</i>	6.0
Engine Mass Flow	104 lb <sub>m</sub> /s (47.2 kg/s)
Chamber Length	14.25 in (36.2 cm)
Chamber Radius at Injector Face	6.0 in (15.2 cm)
Aerospike Radius at Injector Face	3.3 in (8.4 cm)
Max Wall Temperature Guess (Chamber & Aerospike)	900 R (500 K)
Percent Aerospike Nozzle Truncation	0% (Full Spike)
Percent Oxygen Bypassing Turbine	10%
Cooling Channel Geometry	Constant Aspect Ratio
Aerospike Cooling Channel Aspect Ratio	0.67
Chamber Cooling Channel Aspect Ratio	1.5

### ***III.4.1. Thrust-to-Weight Calculation***

The “Thrust\_to\_Weight\_Calc” script component is the objective of the DEAN ModelCenter model. All the previous script components, TDK, and NPSS are executed to obtain a trustworthy *T/W* estimate for a working dual-expander aerospike nozzle engine meeting physical constraints. The *T/W* script component calculates the total chamber, aerospike, plumbing, turbopump, hardware, and total engine masses for the *T/W* estimate. The script also calculates the total engine length and a length-to-diameter ratio as outputs of interest.

The process to calculate the chamber and aerospike masses are very similar. First, the script component calculates the outer cooling channel material volume knowing the geometry of a single channel and multiplying the geometry by the number of cooling channels and the channel length. The inner cooling channel volume is equal to the fluid flow volume; an output from NPSS. Taking the difference between the outer and inner volumes provides the total material volume for the cooling jacket. Adding the cooling channel jacket volume to the cooling channel cover volume (calculated in the structural jacket code) and multiplying by the cooling channel material density leads to the cooling channel mass. The final chamber and/or aerospike mass is equal to the structural jacket mass plus the cooling jacket mass. The aerospike does differ in one aspect where the aerospike mass includes the uncooled nozzle tip (calculated in the structural jacket code).

The turbopump mass is a function of the oxidizer-to-fuel ratio and the engine mass flow rate. Relationships from Humble *et al.* are used to calculate the turbopump mass [20]:

$$\tau = \frac{P_{req}}{N_r} \quad (57)$$

$$m_{tp} = A\tau^B \quad (58)$$

where

$\tau$	=	Pump Shaft Torque (W)
$P_{req}$	=	Required Pump Power (W)
$N_r$	=	Pump Rotational Speed (rad/s)
$m_{tp}$	=	Mass of the Turbopump (kg)
$A$	=	Coefficient, 1.5
$B$	=	Coefficient, 0.6

To use the coefficients properly, the inputs had to be converted from imperial to metric units and the calculated mass converted from kg to  $\text{lb}_m$ . Humble *et al.* recommend the coefficient values for turbopump conceptual design [20]. An oxidizer and fuel turbopump mass is calculated and the total turbopump mass is the sum of the two.

The fuel and oxidizer plumbing mass estimate is conservative. The pipe material area was calculated in the structural jacket code. A pipe length is assumed equal to twice the total engine length (chamber length plus nozzle length). Ideally, the turbopumps will be close to the chamber injector face minimizing the length of the plumbing. However, since a detailed engine layout has not been completed, a conservative total plumbing length is assumed. The plumbing mass is calculated by multiplying the pipe material area by the assumed plumbing length and pipe material density. The total plumbing mass is equal to the combined mass of the fuel and oxidizer plumbing.

Hardware mass is assumed to equal a conservative estimate of 5% the sum of the aerospike, chamber, turbopumps, and plumbing masses. Raymer recommends a 5% hardware estimate for conceptual aircraft designs; the recommendation also seems valid for a conceptual rocket engine design [63]. Hardware accounts for rivets, nuts, bolts, wiring, etc.

The total engine mass is equal to the sum of the chamber, aerospike, turbopump, plumbing, and hardware masses, not including propellant weight.  $T/W$  is calculated by taking the total DEAN thrust and dividing it by the total engine weight. For imperial units  $1 \text{ lb}_m = 1 \text{ lb}_f$ ; therefore, total engine mass equals total engine weight.

### ***III.4.m. Rendering Geometry***

The final subassembly of the “Post\_Processing” assembly and of the DEAN ModelCenter model renders the geometry of the DEAN design. The subassembly contains eight components. Seven of the components are built-in ModelCenter geometry primitives; in use are five surface of revolution functions and two 12 inch (30.48 cm) long arrows. The arrows provide a horizontal and vertical scale for the DEAN geometry. The five surface of revolutions render the aerospike (both the component internal to the combustion chamber and the nozzle) in red, the chamber in blue, the bored hole of the aerospike in black, the location on the spike where the bored hole ends in yellow, and a linear aerospike in light green to visually show the curvature of the method of characteristics calculated nozzle. The eighth component is a script component taking the individual radial and axial coordinates of the DEAN NPSS stations and combines each array element into a string of “(axial, radial)” coordinates used by the surface of revolution components. The chamber and aerospike thicknesses represent the cooling jacket wall, cooling channel height, cooling channel cover, and the structural jacket. Figure 35 shows the individual rendered components as an example with two orthogonal views of the engine.

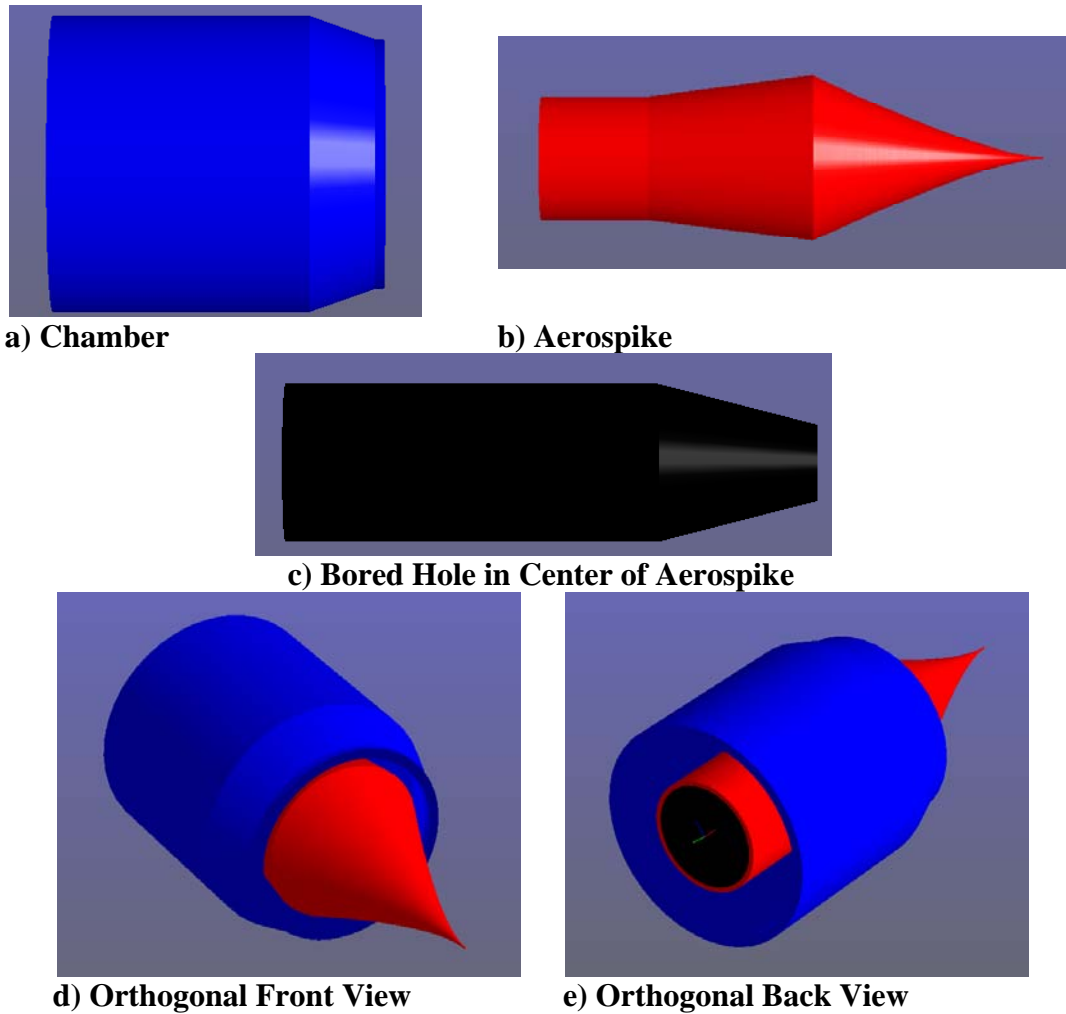


Figure 35. Rendered DEAN Geometry

### III.5 Verification and Validation of the DEAN Model

Although NPSS, TDK, CEA, and ModelCenter have been verified and validated separately, the completed DEAN ModelCenter model must be verified and validated. Verification of a model is the process of determining whether the model accurately fulfills specific requirements; the model does what it is suppose to do. Validation is the process of determining the degree a model accurately represents the real world. Together verification and validation combined, known as V&V, qualify the model for use. The DEAN model will be verified in two steps. First, the V&V procedure and results of

previous research from Simmons and Martin will be discussed. Second, V&V of the final DEAN ModelCenter model will be presented to prove the computed outputs are trustworthy and real.

### ***III.5.a. Verification and Validation of DEAN Model from Previous Research***

Two unique analyses were performed to prove the legitimacy of previous DEAN research. The first analysis verifies and validates the performance parameters (vacuum specific impulse and vacuum thrust) of the DEAN NPSS/ ModelCenter model by Martin and Simmons. The DEAN NPSS/ModelCenter model by Simmons was published in [5] and [6]. The second analysis discusses previously presented vacuum specific impulse results as a function of oxidizer-to-fuel ratio from Simmons [5, 6].

To verify and validate the accuracy of the previous DEAN model, vacuum thrust and vacuum specific impulse values from the DEAN model are compared with calculated values from basic ideal rocket performance equations and from CEA. A percent difference calculation similar to equation 1 was utilized as the comparison tool; percent difference was calculated where the numerator equals the absolute value of the calculated or CEA value minus the DEAN model value divided by the calculated or CEA value. A low percent difference (assumed less than 5%) verifies the DEAN model correctly calculates engine performance. Table 14 tabulates the design variables from Martin [4] used in this study.

**Table 14. Design Variables from Martin [4]**

Design Variables	Default Value
Chamber Pressure Guess	1740.5 psia (12 MPa)
Chamber Temperature Guess	6550 R (3639 K)
<i>O/F</i>	5.5
Engine Mass Flow	121.25 lb <sub>m</sub> /s (55.0 kg/s)
Chamber Length	24.0 in (60.96 cm)
Chamber Radius at Injector Face	6.0 in (15.2 cm)
Aerospike Radius at Injector Face	2.0 in (5.1 cm)
Percent Oxygen Bypasses Turbine	10%
Cooling Channel Geometry	Constant Aspect Ratio
Aerospike Cooling Channel Aspect Ratio	0.67
Chamber Cooling Channel Aspect Ratio	1.5
Expansion Ratio ( $\varepsilon$ )	125

Prior to calculating vacuum specific impulse and vacuum thrust, the following rocket performance equations are utilized to calculate the exit Mach number [20]:

$$\varepsilon = \frac{1}{M_e} \left[ \left( \frac{2}{\gamma + 1} \right) \left( 1 + \frac{\gamma - 1}{2} M_e^2 \right) \right]^{\frac{\gamma + 1}{2\gamma - 2}} \quad (59)$$

where

$$\begin{aligned} \varepsilon &= \text{Nozzle Expansion Ratio or Area Ratio} \\ M_e &= \text{Exit Mach Number} \\ \gamma &= \text{Exhaust Ratio of Specific Heats} \end{aligned}$$

The pressure ratio was calculated using equation 30. The variables  $M_e$ ,  $R$ ,  $T_c$ ,  $A_b$ ,  $P_c$ , and  $\gamma$  are outputs from the NPSS model. Using equations 59 with equations 6, 7, 8, and 30, the vacuum specific impulse and vacuum thrust of the DEAN are calculated (the ambient pressure ( $P_a$ ) was assumed to equal zero for the calculation).

Since certain variables from the DEAN model are used to calculate vacuum thrust and vacuum specific impulse, the verification of the DEAN model may be biased.

Therefore, the rocket application in CEA is used as a comparison to the performance parameters of the DEAN model.  $P_c$ ,  $O/F$ , and  $\varepsilon$  are utilized as inputs to CEA. It is assumed these inputs do not bias the data. The liquid hydrogen and liquid oxygen injector temperature is set to 500 K (900 R) as another CEA input. Outputs from CEA are vacuum specific impulse and thrust coefficient. The thrust coefficient is transformed into vacuum thrust utilizing equation 10 and using the  $P_c$  and  $A_t$  values from the DEAN NPSS model.

Tables 15 and 16 compare the results of the vacuum specific impulse and vacuum thrust comparison, respectively.

**Table 15. Vacuum Specific Impulse Comparison**

Inputs		Vacuum Specific Impulse (sec)			DEAN vs. Calc	DEAN vs. CEA
O/F	$P_c$	Calculated	DEAN	CEA	% Difference	% Difference
5.5	2,293 psia (15.8 MPa)	485	485	499	0.01	2.81
6	2,416 psia (16.7 MPa)	494	495	496	0.02	0.34
6.5	2,322 psia (16.0 MPa)	485	485	493	0.03	1.56
7	2,199 psia (15.2 MPa)	475	475	488	0.01	2.62
7.5	2,135 psia (14.7 MPa)	468	468	483	0.05	3.01

**Table 16. Vacuum Thrust Comparison**

Inputs		Vacuum Thrust (lb <sub>f</sub> )			DEAN vs. Calc	DEAN vs. CEA
O/F	P <sub>c</sub>	Calculated	DEAN	CEA	% Difference	% Difference
5.5	2,293 psia (15.8 MPa)	58,823 lb <sub>f</sub> (261.7 kN)	58,804 lb <sub>f</sub> (261.6 kN)	56,031 lb <sub>f</sub> (249.2 kN)	0.03	4.95
6	2,416 psia (16.7 MPa)	59,970 lb <sub>f</sub> (266.8 kN)	59,958 lb <sub>f</sub> (266.7 kN)	57,153 lb <sub>f</sub> (254.2 kN)	0.02	4.91
6.5	2,322 psia (16.0 MPa)	58,826 lb <sub>f</sub> (261.7 kN)	58,799 lb <sub>f</sub> (261.6 kN)	56,344 lb <sub>f</sub> (250.6 kN)	0.04	4.36
7	2,199 psia (15.2 MPa)	57,663 lb <sub>f</sub> (256.4 kN)	57,638 lb <sub>f</sub> (256.4 kN)	55,476 lb <sub>f</sub> (246.8 kN)	0.04	3.90
7.5	2,135 psia (14.7 MPa)	56,770 lb <sub>f</sub> (252.5 kN)	56,730 lb <sub>f</sub> (252.3 kN)	54,803 lb <sub>f</sub> (243.8 kN)	0.07	3.52

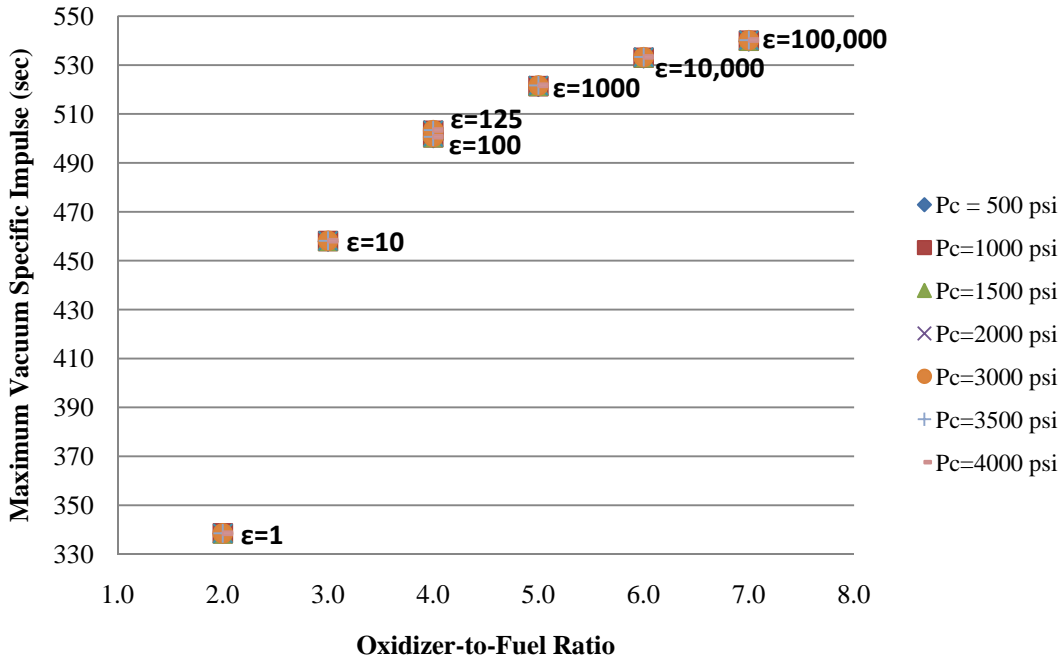
As shown in Table 15 and 16, the difference between the DEAN model and calculated values is trivial. This is likely due to the calculated values using similar DEAN model parameters such as  $M_e$ ,  $R$ ,  $T_c$ ,  $A_b$ ,  $P_c$ , and  $\gamma$ . The real comparison is between the DEAN model and the CEA performance values since CEA calculates rocket performance parameters differently than the DEAN model. The DEAN model calculates rocket performance parameters based on closing the engine design; more specifically, the DEAN model verifies regenerative cooling provides enough heat to the turbines to power the two propellant expander cycles. On the other hand, CEA is solely looking at ideal performance calculations similar to the equations used to find the calculated values. CEA does not include energy lost to power the turbopumps or any other loss mechanisms. There is a close relationship between CEA and DEAN model values with percent difference less than 5%.

With the close agreement between CEA and the calculated vacuum specific impulse and vacuum thrust with the values of the DEAN model, the conclusion is the

model designed by Simmons and Martin is validated and verified and the performance parameters are trustworthy. The DEAN model does what it is suppose to and the model accurately represents reality as long as meaningful inputs are used. When the more accurate expansion ratio based on aerospike engine geometry is entered into CEA, the results between CEA and the linear NPSS model are still within 5%.

The second analysis discusses previous research conclusions. Research by Simmons' found a peak in vacuum specific impulse at an  $O/F$  of 6.0 [5]. If an  $O/F$  of 6.0 truly leads to a vacuum  $I_{sp}$  peak, then the value should be utilized and kept constant for the remainder of the research effort. Since NPSS utilizes CEA for thermodynamic calculations, a standalone version of CEA was used to help discover why there is a performance peak at  $O/F$  equal to 6.0 [43].

Utilizing the rocket problem in CEA, maximum vacuum  $I_{sp}$  as a function of  $O/F$  was plotted in Figure 36 for multiple nozzle area ratios (exit area divided by throat area) and chamber pressures. The inlet propellants were gaseous hydrogen and oxygen at a temperature of 500 K (900 R). Equilibrium combustion was assumed. The chamber pressure varied from 500 to 4000 pounds per square inch (psi) in 500 psi (1 psi = 6894.8 Pa) increments. The nozzle expansion ratio or nozzle area ratio ( $\epsilon$ ) ranged from 1 to 100,000 in one order of magnitude increments and one data set with an  $\epsilon$  equal to 125 (value used by Martin [4]).



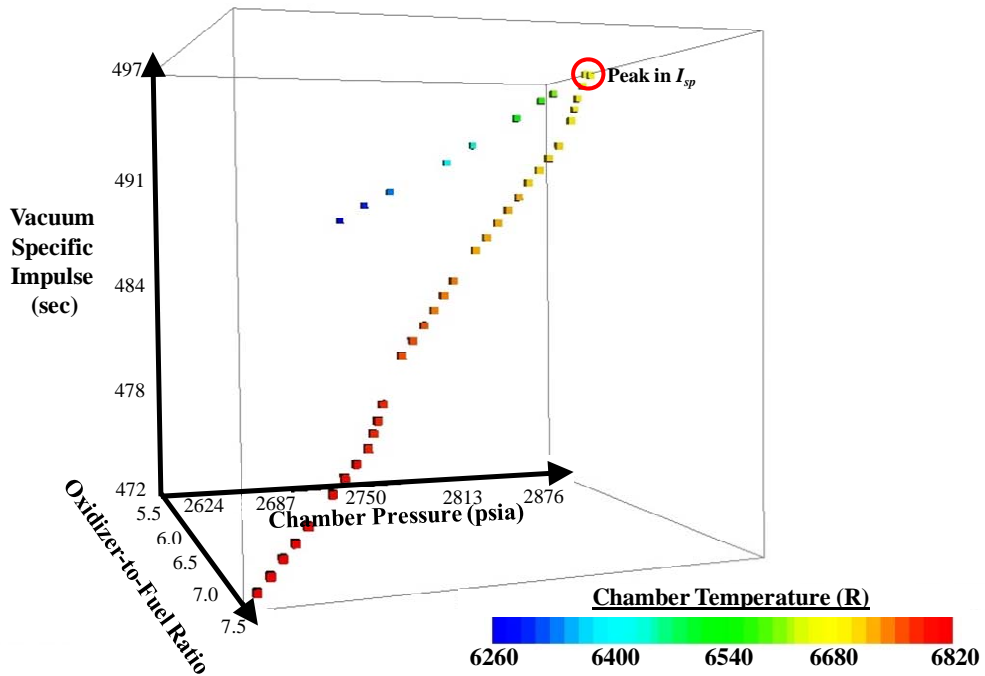
**Figure 36. Maximum Vacuum Specific Impulse for Varying Expansion Ratios and Chamber Pressures**

Figure 36 shows nozzle area ratio has a critical influence on the  $O/F$  value at maximum specific impulse. As expansion ratio increases by an order of magnitude, the  $O/F$  value giving maximum vacuum specific impulse increases by a value of 1.0 ( $\varepsilon = 10$ ,  $O/F = 3.0 \rightarrow \varepsilon = 100$ ,  $O/F = 4.0$ ). Chamber pressure has a negligible effect on the  $O/F$  value with maximum vacuum  $I_{sp}$ .

From Figure 36, the  $O/F$  value with maximum vacuum  $I_{sp}$  for an expansion ratio of 125 (value used by Martin) should be approximately 4.0; however, not the case as documented by Simmons [6]. The reason is NPSS calculates closed design parameter values meeting thermo chemistry and expander cycle/turbo machinery constraints. CEA is solely calculating values based on thermo chemistry.

Simmons performed a more detailed vacuum  $I_{sp}$  versus  $O/F$  parametric trade study to four-dimensions using the design variables in Table 14 [6]. Figure 37, taken

from Simmons [6], shows the solution space for the four dimensions; vacuum  $I_{sp}$  (y-axis),  $O/F$  (z-axis), chamber pressure (x-axis), and chamber temperature (varies by color). A peak in vacuum specific impulse is observed at  $O/F$  equal to 6.0 (indicated at the center of the red circle); however, recognize each point represents a different chamber pressure and chamber temperature. Therefore, the relationship between vacuum  $I_{sp}$  and  $O/F$  in Figure 37 does not show an optimum  $O/F$  but rather shows a possible set of design points for the DEAN. This conclusion applies for all trade studies run by Simmons.



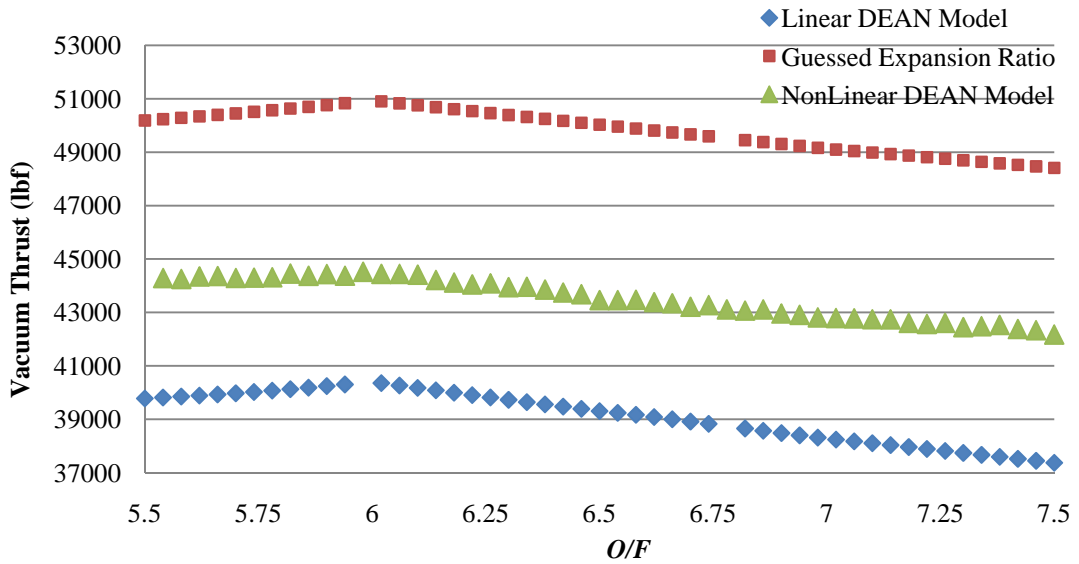
**Figure 37. Four-Dimensional Parametric Study, taken from Simmons [6]**

The  $O/F$  point at 6.0 in Figure 37 represents an engine design with the highest chamber pressure. Since the DEAN design problem focuses on maximizing thrust-to-weight,  $O/F$  equal to 6.0 is a good starting point for future optimization studies. Typically, higher chamber pressures lead to improved performance as long as the throat area is small.

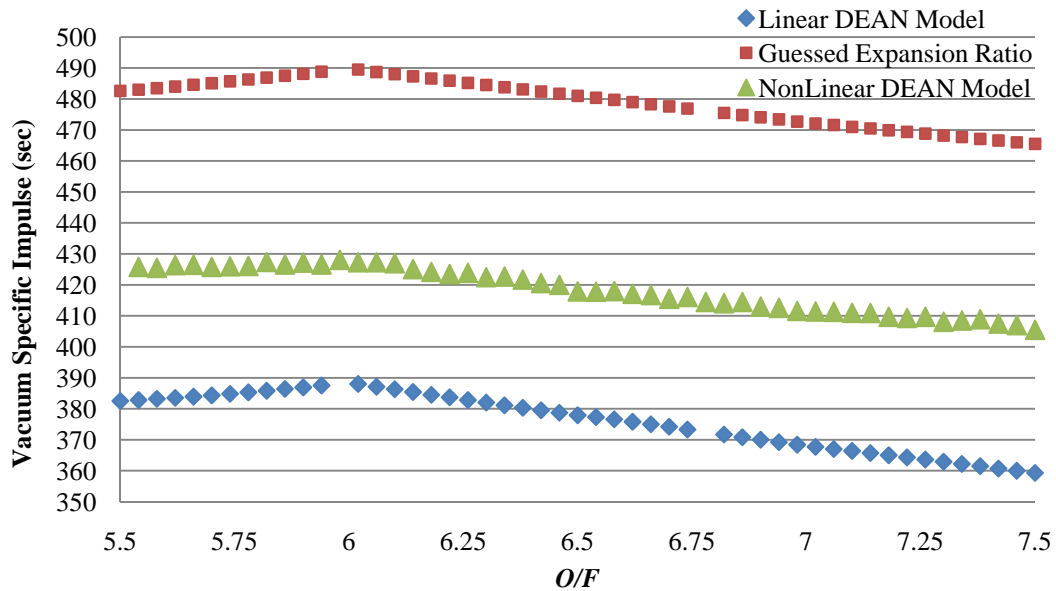
### ***III.5.b. Verification and Validation of DEAN Model***

The final DEAN ModelCenter model will be verified and validated by completing the trade studies performed by Simmons [5, 6] (represented as ‘Guessed Expansion Ratio’ in the plots) and comparing the results; discussed in the previous section, the performance numbers are within the realm of reality. The expectation is the plot shapes should match, thus validating conclusions from previous research. The design variables in Table 13 will be used. The following trade studies will be performed: *O/F*, engine mass flow rate, and chamber length. Furthermore, the computed results will be compared to research presented at the 2011 AIAA Aerospace Sciences Meeting [7] (represented as ‘Linear DEAN Model’ in the plots). The research presented at the AIAA conference included updates to the expansion ratio using the linear NPSS model. Simmons and the conference model utilize constant aspect ratio for cooling channel geometry; the final DEAN ModelCenter model utilizes constant cooling channel area geometry. Some test runs will work in one model and not the other due to this difference. The guessed expansion ratio is equal to 125 and the expansion ratio for the linear and nonlinear DEAN models are equal to 4.16 and 4.34, respectively.

A range of 5.5 to 7.5 in 0.04 increments was used for the *O/F* trade study. Figure 38 plots the vacuum thrust and vacuum specific impulse as a function of *O/F*.



a) Vacuum Thrust

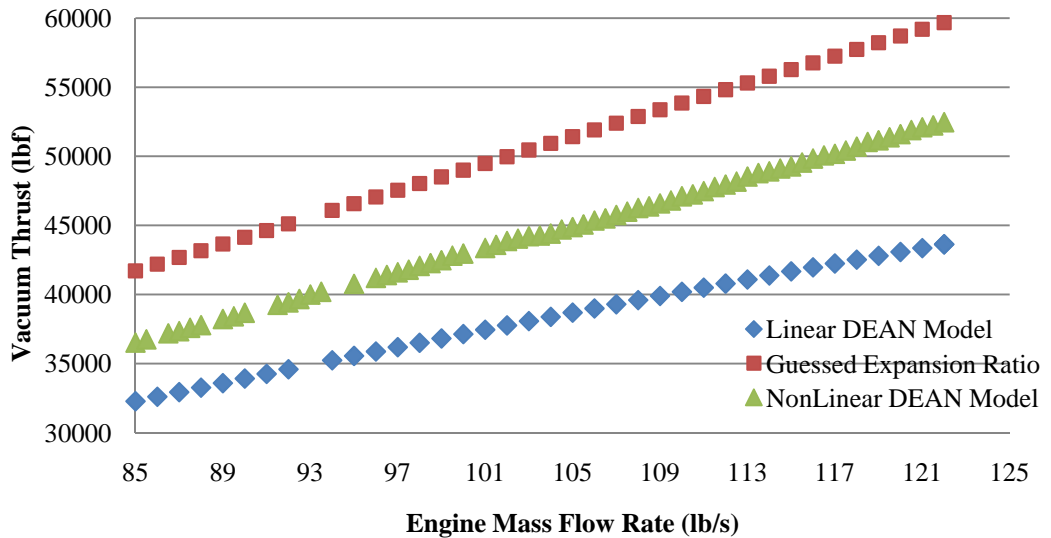


b) Vacuum Specific Impulse

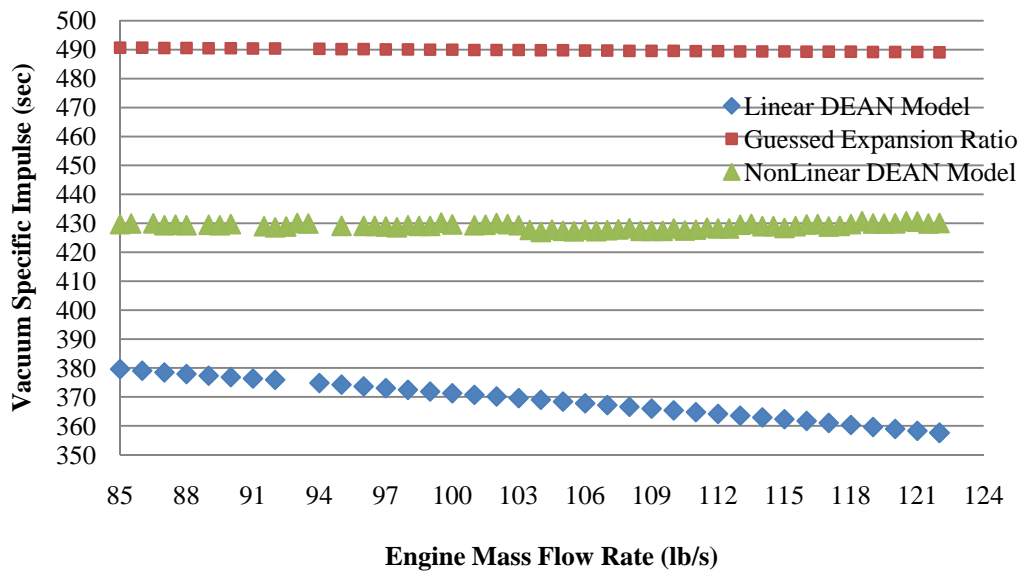
Figure 38. Performance as a function of  $O/F$

The nonlinear DEAN model compared to the linear models ('Linear DEAN Model' and 'Guessed Expansion Ratio') has approximately the same plot shape. There is more noise noted in the nonlinear DEAN model due to the addition of the  $F_{nondesign}$  thrust component. A performance peak is still observed for the nonlinear DEAN model at  $O/F$  equal to 6.0.

A range of 85 to 122 in 0.5 lb<sub>m</sub>/s (1 lb<sub>m</sub>/s = 0.45 kg/s) increments was used for the engine mass flow trade study. Figure 39 plots vacuum performance parameters (thrust and specific impulse) as a function of engine mass flow.



a) Vacuum Thrust



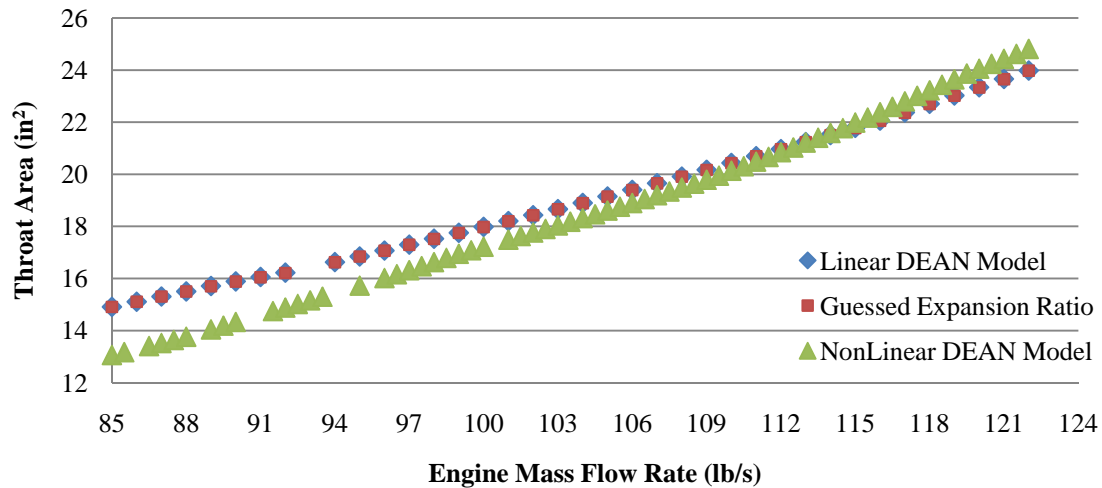
b) Vacuum Specific Impulse

Figure 39. Vacuum Performance Parameters as a Function of Engine Mass Flow

A similar general trend for each DEAN model is recognized in Figure 39. The slope of each data series in the vacuum thrust plot is slightly different; however, the trend, as expected, is vacuum thrust increases for increased engine mass flow.

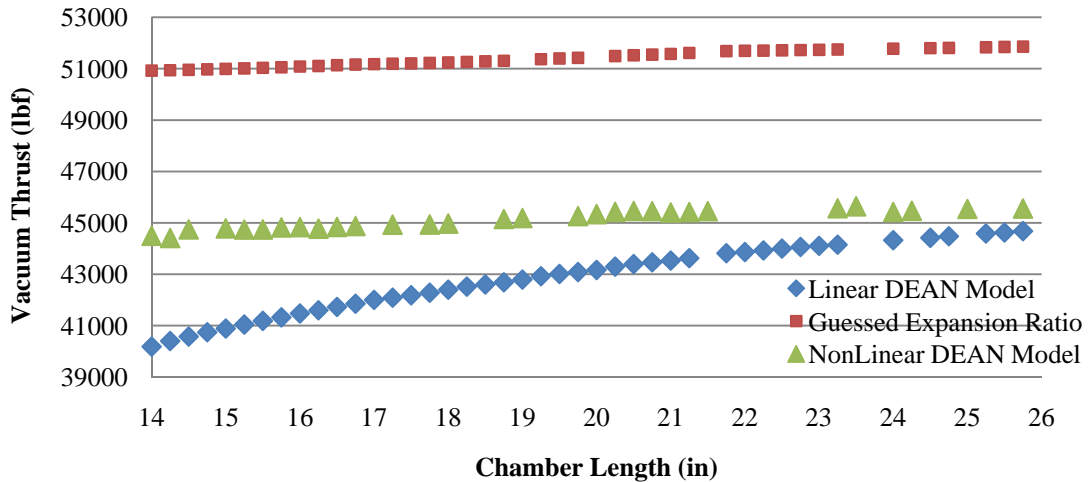
Both linear models show a slight decrease in vacuum specific impulse, while the nonlinear DEAN model is more noisy. The actual magnitude decrease in specific impulse is small showing a fairly linear plot, especially for the guessed expansion ratio data series. For the linear models, NPSS calculates vacuum specific impulse as a function of thrust and engine mass flow. Since NPSS holds mass flow constant in its calculations, the chamber pressure, chamber temperature, throat area, etc are all different for each point represented in the plot. The change in engine mass flow is greater than the change in vacuum thrust causing the decreasing trend in specific impulse in Figure 39b for the linear models.

Due to the noisy nature of the nonlinear model in the vacuum specific impulse plot, more analysis is required. Again, the nonlinear noise is from the  $F_{nondesign}$  thrust component. Looking at the throat area as a function of engine mass flow rate in Figure 40, the general trend is similar; increased engine mass flow leads to increased throat area. For increased engine mass flow, chamber pressure will decrease causing an increase in throat area. The slopes of the linear and nonlinear models are different more likely due to the difference in cooling channel design.

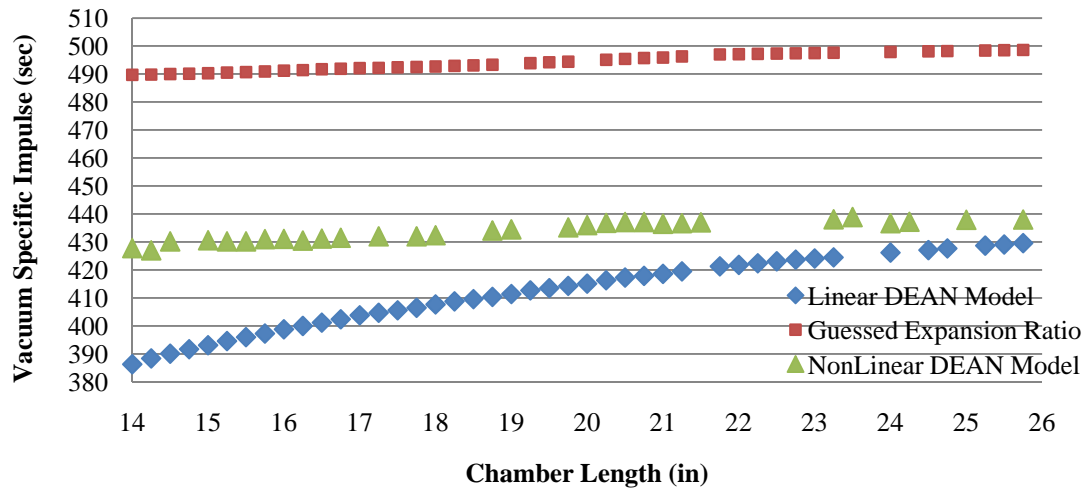


**Figure 40. Engine Throat Area as a Function of Engine Mass Flow**

A range of 10 to 26 in 0.25 inch (1 in = 2.54 cm) increments was used for the chamber length trade study. Figure 41 plots the vacuum performance as a function of chamber length. There is a noticeable difference between the two linear models. They both show increased performance for increased chamber length; however, the linear DEAN model shows a much larger change in magnitude compared to the guessed expansion ratio data series. Although noise is observed in the nonlinear DEAN model, a similar trend of increased performance exists, more closely following the guessed expansion ratio data series.



**a) Vacuum Thrust**



**b) Vacuum Specific Impulse**

**Figure 41. Vacuum Performance Parameters as a Function of Chamber Length**

Figure 42 plots throat area as a function of chamber length. With increased chamber length, there is more heat transfer to the coolant leading to higher chamber pressures. Since the DEAN model holds mass flow constant, the throat area decreases as a result of increased chamber pressure. The decreased throat area and increased chamber pressure lead to improved performance. Again, a difference in plot magnitude is detected

between the linear and nonlinear models most likely due to the different cooling channel geometry. The overall trend of the data series is very similar.

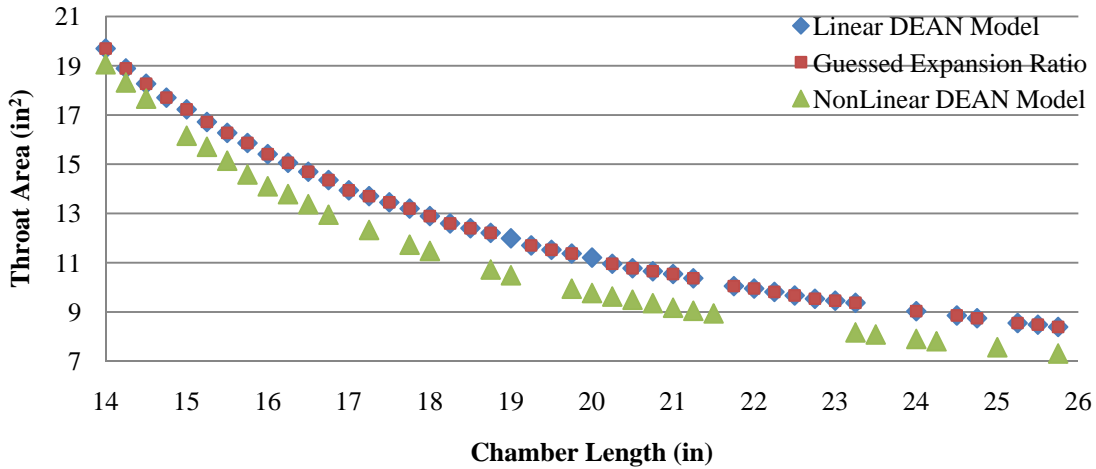


**Figure 42. Engine Throat Area as a Function of Chamber Length**

Although each linear model ('Linear DEAN Model' and 'Guessed Expansion Ratio') and nonlinear model differs in plot magnitude, the general trend in each model is comparable even with different cooling channel geometry. Knowing the performance calculations are within the realm of reality from previous V&V testing and since the plots show comparable trends, the conclusion is the nonlinear DEAN model accurately performs its calculations providing realistic, trustworthy outputs.

Another check on the validity of the nonlinear DEAN model performance values is a percent difference variable (*Per\_Diff\_Thrust* and *Per\_Diff\_Isp*) used to compare the performance of DEAN aerospike nozzle to the performance of a bell nozzle. As previously mentioned, an aerospike nozzle behaves and performs much like a conventional bell nozzle in vacuum conditions. Through numerous trade studies, the percent difference varied from -5% to +10%. The percent differences are reasonable in

validating the nonlinear DEAN model performance values along with the aforementioned trade study comparison conclusions.

The above verification and validation of the nonlinear DEAN model focused on engine performance. However, verification and validation of the engine weight estimation portion of the model was performed just on a smaller scale. The details of these V&V tests are included in the component explanations of section III.4. For example, each integral calculation using a trapezoidal approximation technique was compared to linear approximations to ensure the trapezoidal approximation code provided acceptable results. Also, for the cooling jacket wall thickness calculation, both linear and curved beam theory was used with similar results. Overall, the nonlinear DEAN model provides conservative performance and weight estimates with capability to measure physical constraints and ensure the constraints are not violated.

### **III.6 DEAN Engine Total Mass and Thrust-to-Weight Optimization Process**

The final ModelCenter DEAN model meets objectives one and two for the current research effort. With a working model, a specific engine or group of engines meeting the design goals can be found. Due to a more accurate estimate of expansion ratio and performance, the DEAN design in Table 13 does not meet the design goals. This section will discuss the methodology to find a new engine design and the process to optimize engine mass and  $T/W$ .

To find a new engine design, individual trade studies of the design variables (chamber length, engine mass flow rate, and aerospike and chamber radii) will be performed. The  $O/F$  value will be set to a constant 6.0. The data points showing promise

to meet the design goals from the individual trade studies will be combined to find a new engine design meeting both the design goals and physical constraints. Only the thrust and specific impulse design goals are of interest for this portion of the study. The physical constraints for the engine are the hydrogen and oxygen maximum Mach number through the expander cycle must be less than 0.9 and 0.6, respectively. The aerospike and chamber maximum cooling jacket wall temperature is a function of material selection and will be neglected for this portion of the study.

Once a new design meeting the performance design goals is found, a parametric trade study over the seven individual engine components (i.e. structural jackets, cooling jackets, plumbing) requiring material selection will be performed. The trade study will not include the turbopumps since turbopump mass is a function of mass flow and not related to material selection. To begin, all components will have pure copper as the material selection. The initial  $T/W$  will be recorded followed by individual trade studies by varying material selection alone. The maximum and minimum  $T/W$  for each individual component study will be recorded. The engine components with the highest range in  $T/W$  have the most influence over the  $T/W$  of the total engine. Engine components with low ranges have very little influence over the  $T/W$  of the total engine; therefore, a material can be selected for these components and kept constant. The goal is to find the engine components with the strongest influence over the mass and  $T/W$  of the total engine. The cooling jacket wall temperature physical constraint is neglected during this study.

A trade study varying material selection on just the influential engine components from the previous study will be performed next. The user strength option should be set to

ultimate tensile strength and the cooling geometry option should be set to cooling channel cover and structural jacket. Having a cooling channel cover allows for stronger, less dense materials to be utilized for the structural jacket. For this study, the aerospike and chamber cooling jacket maximum wall temperature must be less than the material melting point. The goal of the trade study is to find what material selections provide a  $T/W$  equal to or greater than the 106.5 design goal without melting the chamber.

Next, a study on DEAN reusability will be performed. First, the goal is to select materials to achieve the maximum wall temperature equal to 60% the material melting point. The user strength option should also be set to yield strength. The goal is to determine if a  $T/W$  design goal of 106.5 is achievable while meeting reusability constraints.

Designing the DEAN with the material selection giving the best  $T/W$  can be challenging, especially for the aerospike. To improve aerospike manufacturability, the same material will be utilized for the aerospike cooling jacket and structural jacket. Using the same material may influence the previously calculated  $T/W$ ; however, the resulting design will be more realistic from a manufacturing standpoint.

The last study is nozzle truncation. For a truncated nozzle, the engine will have less performance than the full-length spike; however, the engine will also have less mass. The goal is to determine if nozzle truncation can improve  $T/W$  with minimal performance losses and still meet physical constraints and design goals.

At the conclusion of the trade studies, a new DEAN design will emerge. The new design will be maximized for  $T/W$  while meeting the design goals and physical

constraints. Outputs such as the pressure profile, turbopump parameters, and performance values will be tabulated for this DEAN design.

## IV. Results and Analysis

Chapter IV discusses the results of trade and optimization studies using the final ModelCenter DEAN model to find an optimum engine design meeting the design goals and physical constraints.

### IV.1 DEAN Model Variables

Certain TDK, Angelino, and NPSS variables must be set and kept constant to perform trade and optimization studies. The set NPSS variables showed improved NPSS model flexibility (reference Appendix C). In addition, the set TDK and Angelino variables provided additional flexibility in model execution (reference Appendix D). The set TDK cowl angle (*THALW*) straightens the flow through the throat maximizing thrust; Appendix D.1 discusses other TDK inputs. Table 17 summarizes the set model variables for DEAN solution space exploration.

**Table 17. DEAN Model Set Variables**

VARIABLE	VALUE
<b>NPSS</b>	
Cooling Channel Half-Width ( <i>H2_w_init</i> , <i>O2_w_init</i> )	0.02 in (0.051 cm)
Half-Distance between Cooling Channels ( <i>H2_a</i> , <i>O2_a</i> )	0.01 in (0.025 cm)
<i>O<sub>2</sub></i> Aspect Ratio ( <i>O2_AR</i> )	2.5
<i>H<sub>2</sub></i> Aspect Ratio ( <i>H2_AR</i> )	3
Percent Oxidizer Bypass Turbine ( <i>Ox_Bypass</i> )	5%
Pipe Cross-Sectional Area ( <i>pipe_area</i> )	2 in <sup>2</sup> (12.9 cm <sup>2</sup> )
Fuel Maximum Cooling Jacket Wall Temperature Guess	900 R (500 K)
Oxidizer Maximum Cooling Jacket Wall Temperature Guess	900 R (500 K)
<b>Angelino Approximation Code</b>	
Number of Points on Initial Line ( <i>num_points</i> )	50
<b>TDK</b>	
Number of Points on Initial Line ( <i>MP</i> )	50
Flow Angle at Spike Exit Plane ( <i>THE</i> )	0 deg
Cowl Angle ( <i>THALW</i> )	0 deg
Nozzle Attachment Angle ( <i>THETA</i> )	25 deg

## IV.2 DEAN Engine Mass and Thrust-to-Weight Optimization Results

### IV.2.a. Design Variable Limits

The second objective for the current research effort was to create a tool to explore the solution space. By creating the DEAN model in ModelCenter, the user can take advantage of built-in parametric trade study and optimization tools in ModelCenter. All trade studies performed explored the solution space of the DEAN.

The third objective for the current research effort is to identify critical technologies and limits relevant to the optimized DEAN model.

Previous research by Martin found the maximum allowable Mach number for the propellants is 0.6 for oxygen and 0.9 for hydrogen [4]. Furthermore, the cooling jacket wall temperature must not exceed the material melting point, or the wall temperature equal to 60% the material melting point for reusability. These limits are physical design constraints.

Other limits include a fluid Mach number at the throat equal to 1.0 to allow supersonic flow expansion along the aerospike. The oxidizer-to-fuel ratio has limits of 4.0 to 7.0. An *O/F* value less than 4.0 would be less than thermo chemically optimum, while an *O/F* greater than 7.0 would run the risk of running lean and excess oxygen damaging the combustion chamber.

A simple analysis using equation 7 (the  $F = I_{sp} \dot{m} g_o$  portion) was completed to determine a valid engine mass flow range for the DEAN design. Keeping the  $I_{sp}$  at a constant 464 seconds and varying the thrust from 50,000 to 60,000 lb<sub>f</sub> (222.4 to 266.9 kN), the calculated engine mass flow range equaled 107 to 130 lb<sub>m</sub>/s (48.5 to 59.0 kg/s).

Now keeping the thrust at a constant 50,000 lb<sub>f</sub> (222.4 kN) and varying the  $I_{sp}$  from 464 to 500 seconds the engine mass flow range equaled 99 to 107 lb<sub>m</sub>/s (44.9 to 48.5 kg/s). Therefore, the potential range for evaluating the DEAN model is 99 to 130 lb<sub>m</sub>/s (44.9 to 59.0 kg/s). The mass flow range assumes at least 50,000 lb<sub>f</sub> (222.4 kN) vacuum thrust and 464 seconds vacuum  $I_{sp}$  (the DEAN design goals) is achievable. Previous trade studies, such as those performed for DEAN V&V, showed  $I_{sp}$  could be improved by lower engine mass flow rates. Therefore, the lower end of the engine mass flow range was changed from 99 lb<sub>m</sub>/s (44.9 kg/s) to 85 lb<sub>m</sub>/s (38.6 kg/s).

The range of chamber length is highly dependent on the range of chamber and aerospike radii at the injector face. Chamber length and chamber and aerospike radii have to create a large enough combustion chamber volume equal to or greater than the characteristic length of the propellant to maximize combustion. The chamber and aerospike radii have a set range of 5 to 20 inches (12.7 to 50.8 cm) with the constraint the aerospike radius must be less than the chamber radius. Chamber radii greater than 20 inches (50.8 cm) result in high wall temperatures above material melting points. Increased chamber radius leads to increased expansion ratios and better performance; however, the wall temperatures must remain below their melting points. Regardless of wall temperature, the true maximum radius for the chamber is the radius of the Delta IV four-meter diameter second stage; the maximum radius is approximately 78 inches (2 m) [64]. Another concern with large chamber and aerospike radii is an extremely long full-length aerospike. The longer the spike, the more heat transfer to the hydrogen leading to higher wall temperatures. Furthermore, the weight and size of the aerospike drastically increase; truncation studies, without a doubt, are required to meet *T/W* design goals if a

large radial DEAN design is pursued. The set range for chamber length is 14 to 26 inches (35.6 to 66.0 cm).

The range of DEAN design variables were set for evaluation of the solution space to find an optimum engine design. Table 18 tabulates the variable ranges.

**Table 18. DEAN Variable Ranges**

Design Variables	Range
O/F	5.5 – 7.5
Engine Mass Flow Rate	85 – 130 lb <sub>m</sub> /s (38.6 – 59.0 kg/s)
Chamber Length	14 – 26 in (35.6 – 66 cm)
Chamber Radius at Injector Face	5 – 20 in (12.7 – 50.8 cm)
Aerospike Radius at Injector Face	5 – 20 in (12.7 – 50.8 cm)
Material Strength Option	Ultimate Tensile, Yield
Percent Aerospike Nozzle Truncation	0 – 100%
Material List	Table 9

#### ***IV.2.b. New DEAN Design Point***

Multiple trade studies were performed in an attempt to find a new design point meeting all design goals within physical constraints. Due to the brittleness of the NPSS model with coupled design variables, it is challenging to utilize the optimizers to find a design point meeting the design goals with only varying chamber length, engine mass flow rate, and chamber and aerospike radii at the injector face. A working design point was found, referred to as the default design for this study, with a chamber radius, aerospike radius, chamber length and engine mass flow rate of 7.0 inches (17.8 cm), 5.5 inches (14.0 cm), 17.5 inches (44.5 cm), and 115 lb<sub>m</sub>/s (52.2 kg/s), respectively. Trade studies were performed on chamber length, aerospike radius, and engine mass flow rate to determine the individual influence of the variables; the default design is denoted as a red square on the trade study plots. Previous research found a best material selection for

the default design variables in Table 13 using the linear NPSS model [7]. Table 19 summarizes the best material selection used for the trade studies from Hall *et al.* [7]. As a reminder, the performance values include nozzle boundary layer losses.

**Table 19. Engine Components and Material Selection from Hall *et al.* [7]**

Engine Component	Best Material Selection
Aerospike Cooling Jacket	Silicon Carbide
Aerospike Structural Jacket	Aluminum 7075 T6
Uncooled Aerospike Tip	Silicon Carbide
LH <sub>2</sub> Plumbing	INCOLOY® 909
Chamber Cooling Jacket	Silicon Carbide
Chamber Structural Jacket	Aluminum 7075 T6
LOX Plumbing	INCONEL® 718

Setting the engine mass flow rate, chamber length and chamber radius at the injector face to a constant 115 lb<sub>m</sub>/s (52.2 kg/s), 17.5 inches (44.5 cm) and 7.0 inches (17.8 cm), respectively, the aerospike radius at the injector face was varied from 3 to 6.5 in 0.5 inch (1 in = 2.54 cm) increments. Figure 43 plots the various results. As the aerospike radius approaches the chamber radius, the chamber pressure increases while the throat area decreases; this variable reaction makes sense since the DEAN model is keeping the engine mass flow rate constant. Increased chamber pressure and decreased throat area improve vacuum performance (including vacuum thrust), as shown in Figure 43 with increasing vacuum specific impulse; a total 3.8% increase in performance. At the same time, the *T/W* is decreasing due to the increased aerospike radius and due to the increased aerospike and chamber structural jacket mass. The chamber and aerospike wall temperatures as a percentage of the material melting point (chamber and aerospike percent melt) show a drastic increase as the aerospike radius approaches the chamber radius. Increased wall temperature leads to increased heat transfer to the coolant. The

higher coolant temperature leads to lower structural strength, leading to increased structural jacket thickness and mass.

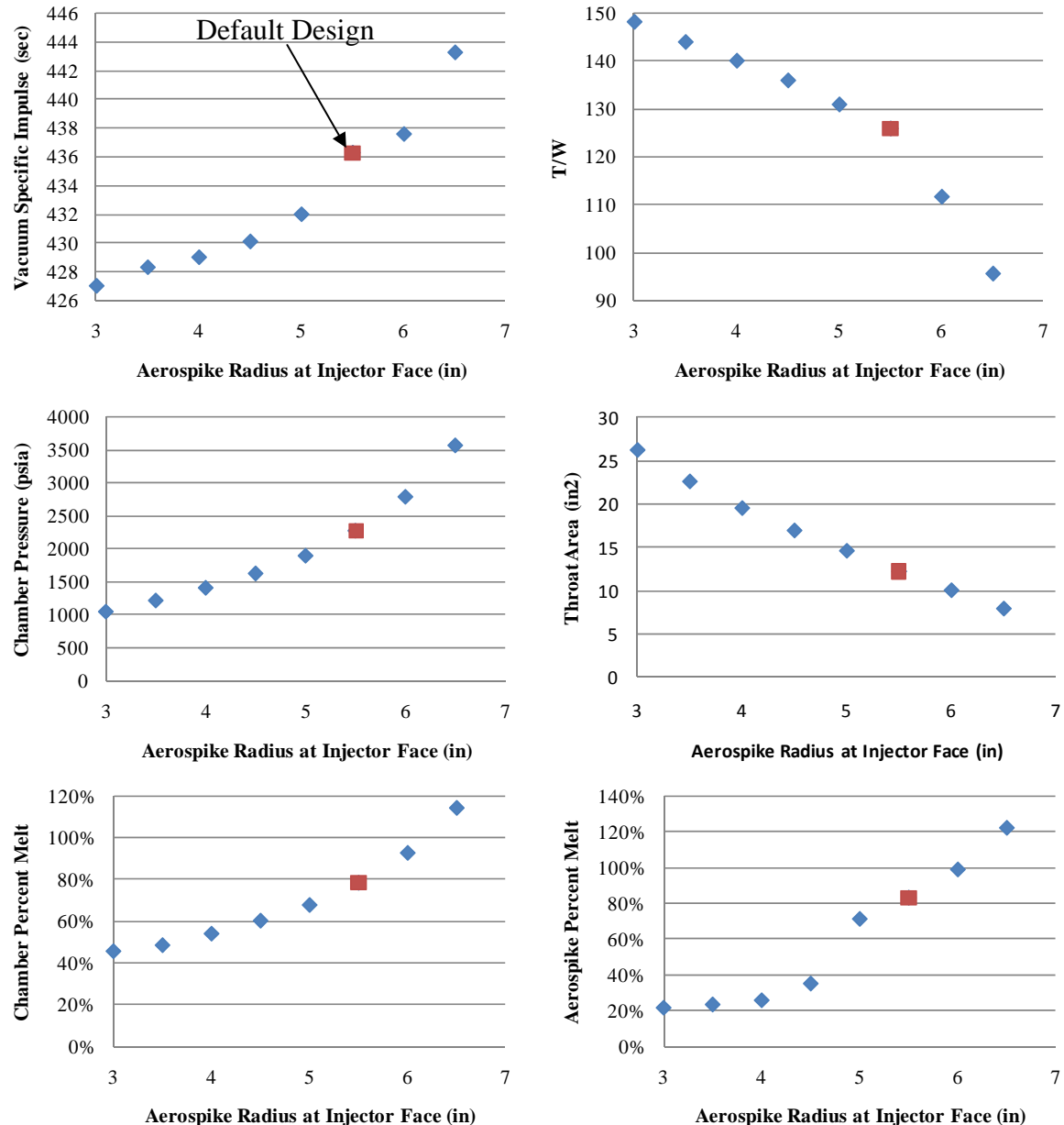


**Figure 43. Various Plots for Aerospike Radius Trade Study**

Setting the engine mass flow rate, aerospike radius and chamber radius to a constant  $115 \text{ lb}_m/\text{s}$  ( $52.2 \text{ kg/s}$ ), 5.5 inches (14.0 cm) and 7.0 inches (17.8 cm), respectively, the chamber length was varied from 10 to 20 in 0.5 inch increments. Figure

44 plots the various results. Errors did occur in this study and are represented as empty spaces in the plots. As chamber length increases, the chamber pressure and throat area increase leading to improved performance (including vacuum thrust); shown on the vacuum specific impulse plot, for a total 2.3% increase. The  $T/W$  is decreasing for two reasons: first, more material is added to the chamber and to the aerospike internal to the chamber with increasing chamber length; second, similar to the aerospike radius trade study, the coolant is picking up more heat leading to increased structural jacket thickness and mass. As observed in Figure 44, the chamber and aerospike wall temperature as a percentage of the material melting point is increasing leading to higher wall temperatures and more heat transfer to the coolant.

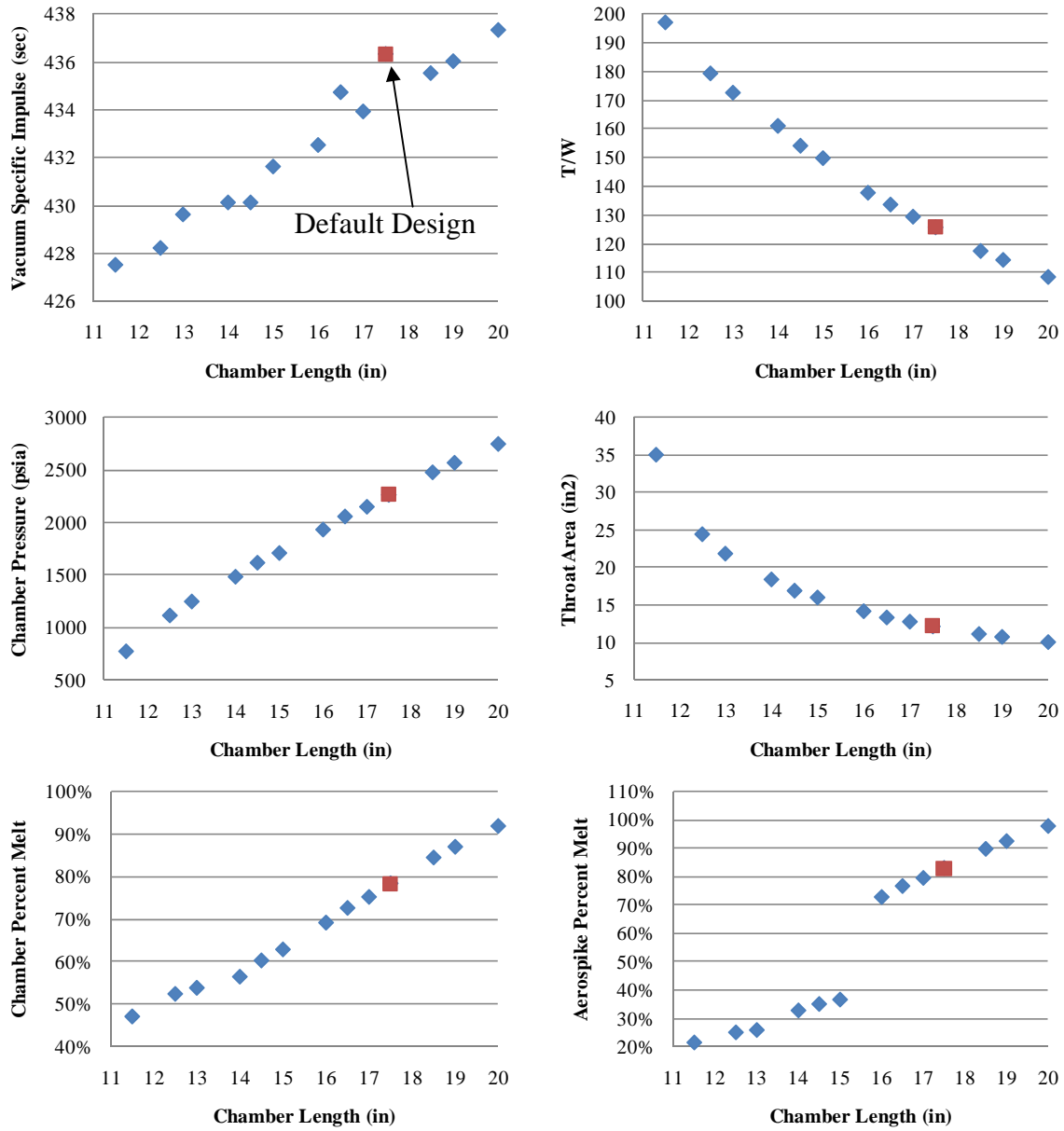


**Figure 44. Various Plots for Chamber Length Study**

Setting chamber length, aerospike radius and chamber radius to a constant 17.5 inches (44.5 cm), 5.5 inches (14.0 cm) and 7.0 inches (17.78 cm), respectively, the engine mass flow rate was varied from 85 to 130 in 1 lb<sub>m</sub>/s (1 lb<sub>m</sub>/s = 0.45 kg/s) increments. Figure 45 contains the various results.

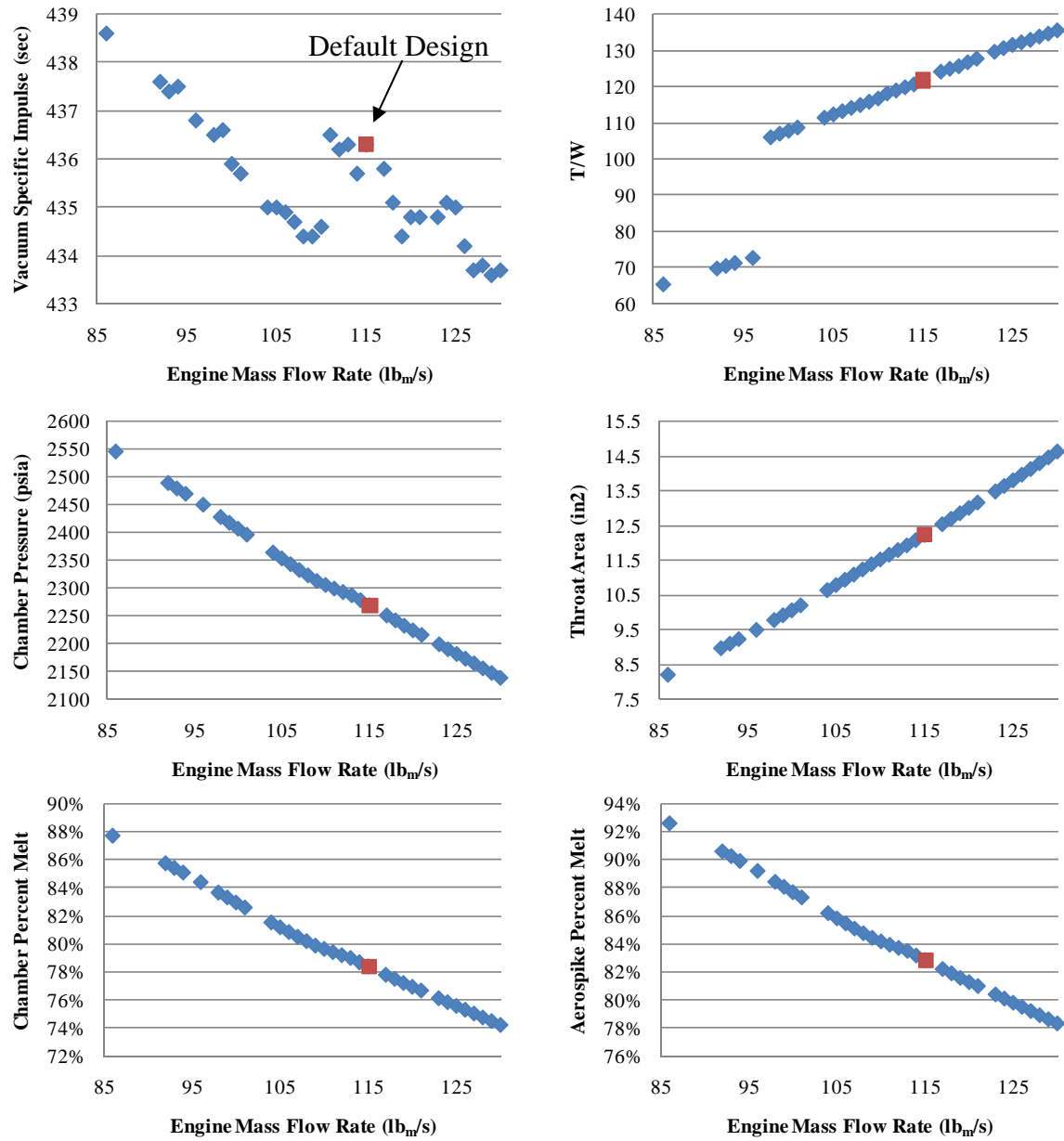


**Figure 45. Various Plots for Engine Mass Flow Trade Study**

With a constant chamber length and increased engine mass flow, the heat transfer to the coolant in the cooling channels will decrease due to the fluid moving faster through the cooling channels and having less time to gain energy. The decrease in coolant temperature into the turbine means a decrease in turbine power (or pump available power). The increase in engine mass flow leads to an increase in pump available power.

Consequently, the overall pump available power is increasing for increased engine mass flow; however, the power is not increasing enough to raise the pressure of the propellant to where it could be with increased coolant temperature. Through a series of pressure drops through the system to the injectors, the resulting chamber pressure is lower leading to a larger throat area for increased engine mass flow. The performance impact is decreased vacuum specific impulse as shown in Figure 45 and increased vacuum thrust (similar to the plot shape in Figure 39). The decrease in specific impulse is approximately 1.1%; the plot is noisy due to how  $F_{nondesign}$  is calculated.

Due to the lower coolant temperature for increased engine mass flow, there is a decrease in the chamber and aerospike maximum wall temperature and in the chamber and aerospike percent melt values. The lower coolant temperatures also result in higher strength for the structural jacket materials. The higher strength results in a smaller structural jacket thickness and less structural jacket mass. At the same time, the turbopump mass increases with increased mass flow. With the current material selection, the turbopump adds more to the total engine weight than the structural jackets. Therefore, for the current material selection, the total engine mass increases for increased mass flow. Since there is a greater increase in vacuum thrust than in total engine mass, the  $T/W$  increases, as shown in Figure 45.

Another observation from the aerospike radius, chamber length and engine mass flow trade studies is a difference in trend in the maximum Mach number in the hydrogen expander cycle. As mass flow increases, the hydrogen maximum Mach number increases. As chamber length increases, the hydrogen maximum Mach number decreases. Both variable influences of engine mass flow and chamber length on

hydrogen maximum Mach number are reasonable. As aerospike radius approaches the chamber radius, the hydrogen fluid maximum Mach number drastically increases; especially from 6 to 6.5 inches (15.2 to 16.5 cm). At an aerospike radius of 6.0 inches (15.2 cm) and below, the hydrogen maximum Mach number decreases, in a similar trend to the chamber length trade study, proving a Mach number outlier exists at 6.5 inches (16.5 cm). Looking closely at the 6.5 inch (16.5 cm) aerospike radius, the maximum hydrogen fluid temperature is approximately equal to 921 R (511.7 K). The maximum temperature for the hydrogen Mach number third order polynomial from Simmons [6] is 640 R (355.6 K). For hydrogen temperatures above 640 R (355.6 K), the output from the polynomial cannot be trusted; for example, the outlier at the 6.5 inch (16.5 cm) aerospike radius.

Evaluating other high pressure options by increasing the chamber and increasing the aerospike radius close to the chamber radius, strange maximum Mach numbers on the hydrogen side were identified. For example, some geometry designs led to negative Mach numbers even though the velocity, temperature, and pressure profiles from NPSS were positive. The oxygen fluid maximum Mach number seemed satisfactory; however, the maximum temperature for the third order polynomial is 900 R (500 K) [6]. To remedy the Mach calculations, the individual third order polynomials need to be updated to evaluate higher fluid temperatures; however, it may not be the best answer. Higher fluid temperatures may lead to spontaneous reactions of the propellant with wall surface materials, especially for the oxidizer. The fluid temperature limits to both hydrogen and oxygen are unknown, leaving the Mach number calculation currently in the DEAN model with this known limitation. As long as the fluid temperatures remain below 640 R and

900 R (355.6 and 500 K) for the hydrogen and oxygen, respectively, the Mach numbers can be trusted.

Clearly seen from Figures 43, 44, and 45, are the influence of aerospike radius, chamber length, and engine mass flow rate on the performance and *T/W* of the DEAN. Without changing the chamber radius, the designer can improve the vacuum specific impulse of the DEAN. Because of the design approach, best vacuum specific impulse is achieved for an aerospike radius close to the chamber radius with a long chamber length and low mass flow rate. However, an engine design with an aerospike radius close to the chamber radius with a long chamber length and low mass flow rate may not be physically possible due to high wall temperatures. A design tradeoff is recognized; high wall temperatures are associated with higher chamber pressures leading to increased vacuum performance.

Performance is directly linked to expansion ratio. Increasing expansion ratio leads to improved performance. To increase the expansion ratio, the chamber exit lip radius must increase and/or the throat area decrease. Chamber exit lip radius is a function of the design variable *ChamberRadius* (the chamber radius at the injector face). By increasing the length of the chamber and setting the aerospike radius close to the chamber radius, the throat area decreases leading to the performance improvements observed in Figures 43 and 44. A large design of experiments (DOE) was performed using the built-in ModelCenter tool to evaluate larger chamber radii.

To perform the DOE, the mass flow rate was set to a constant 130 lb<sub>m</sub>/s (59.0 kg/s) in an attempt to maximize NPSS convergence. The chamber length, aerospike radius, and chamber radius had variable ranges from 14 to 26 inches and 5 to 20 inches (1

in = 2.54 cm), respectively. The material selection in Table 19 was used for the DOE, except silicon carbide was used for the structural jackets instead of aluminum 7075 T6 due to the high strength at high temperatures and low density of silicon carbide. The DOE utilized the Full Factorial option at 15 levels for a total of 3,375 runs. The Full Factorial DOE calculates samples of the design variables at their upper and lower values and determines what samples to run in-between by the user defined number of levels [42]. A physical constraint is the aerospike radius must be less than the chamber radius. The DOE does not recognize the engine radial constraint when creating samples; therefore, samples violating this limit were manually deleted. The number of runs decreased from 3,375 to 1,784. Only 442 out of 1,784 runs were successful, showing the brittleness of the NPSS DEAN model. Figure 46 plots vacuum specific impulse as a function of chamber radius for the successful runs.

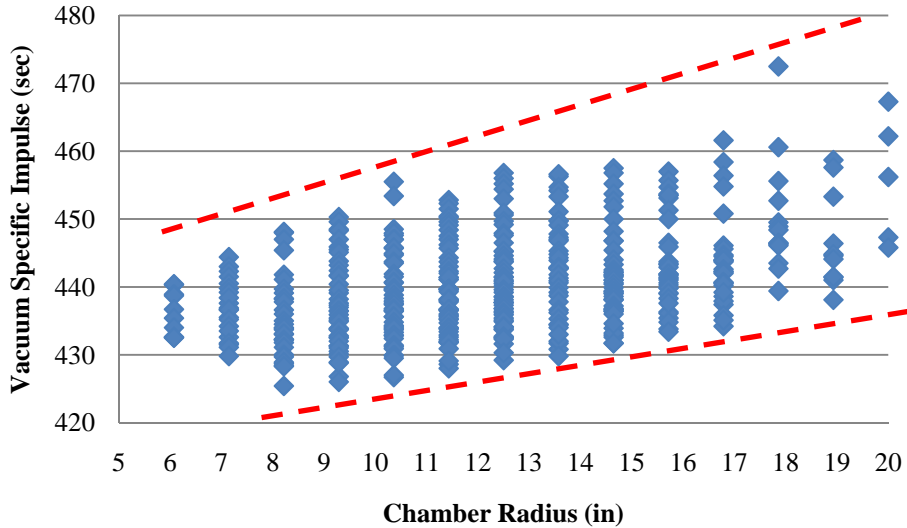


**Figure 46. Influence of Chamber Radius on Vacuum Specific Impulse**

The result is quite interesting; increasing the chamber radius does not automatically equate to a higher vacuum specific impulse. The influence of increasing

chamber radius is most clearly recognized at the data points close to the lower red line. As chamber radius increases, there is an increase in expansion ratio leading to an increase in vacuum specific impulse. The data points close to the lower red dotted line in Figure 46 represent engine designs with shorter chamber lengths and smaller aerospike radii resulting in lower chamber pressures, higher throat areas, lower expansion ratios, and lower vacuum specific impulse. In contrast, the data points close to the upper red dotted line represent engines with long chamber lengths and aerospike radii close to the chamber radii. The result is higher chamber pressures, small throat areas, higher expansion ratios, and improved vacuum specific impulse. Clearly seen in Figure 46 is the difference in vacuum specific impulse between the upper and lower red dotted lines is not due to an increase in chamber radius alone.

To understand the influence of chamber radius, aerospike radius, and chamber length on vacuum specific impulse better, Figure 47 plots the successful runs with chamber radius on the x-axis, chamber length on the y-axis, and aerospike radius on the z-axis. The color and size of the boxes in the glyph plot relate to vacuum specific impulse. The small blue boxes are lower vacuum specific impulse, while the large red boxes are higher vacuum specific impulse.

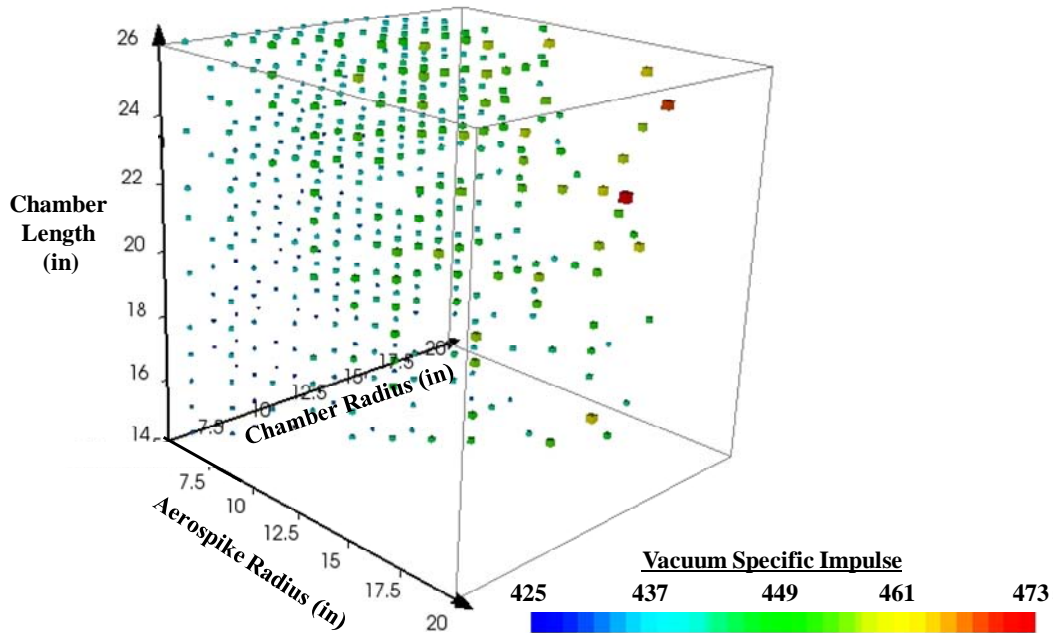


**Figure 47. Influence of Design Variables on Vacuum Specific Impulse**

The conclusion is to obtain high vacuum specific impulse, increased chamber radius combined with a long chamber length and an aerospike radius close to the chamber radius is required. The expansion ratio will be larger with increased chamber exit lip radius and a smaller throat area. Again, the high specific impulse values have high wall temperatures leading to low  $T/W$ , making the designs not as desirable. Figure 48 plots the successful runs with vacuum specific impulse on the x-axis and  $T/W$  on the y-axis. The vacuum thrust range for the successful runs is 55,000 to 62,000 lb<sub>f</sub> (224.7 to 275.8 kN). The vacuum specific impulse design goal of 464 seconds and the  $T/W$  design goal of 106.5 are also shown. The red square boxes with an “X” in the center represent design points where the chamber and/or aerospike maximum wall temperature exceeded the material melting point. The orange circles represent design points with chamber and/or aerospike maximum wall temperatures above the 60% melting point reusability goal.

The blue diamonds represent design points with wall temperatures below the 60% melting point reusability goal.

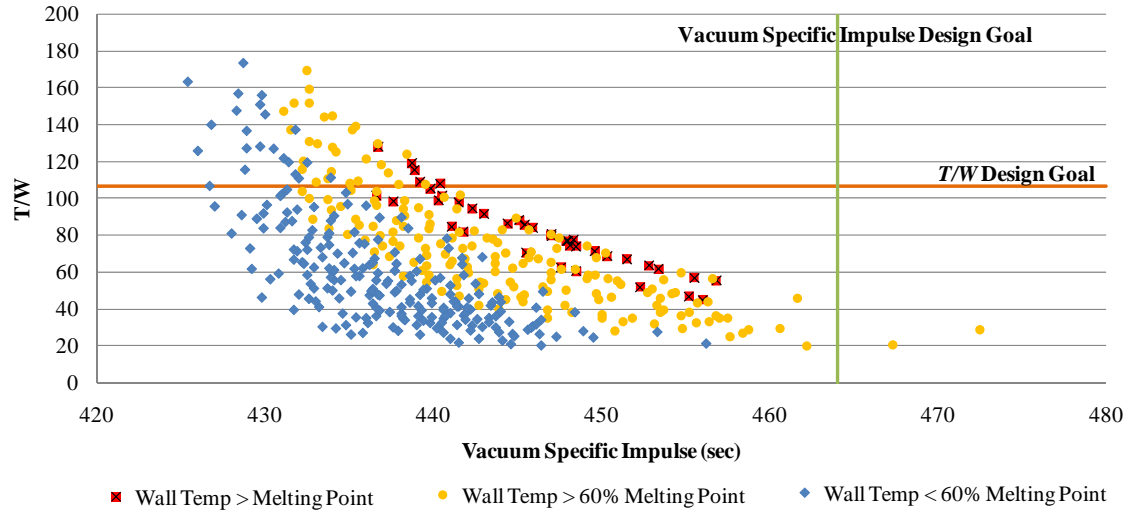


**Figure 48. T/W and Vacuum Specific Impulse of Potential DEAN Designs**

Surprisingly, acceptable designs both meeting the  $T/W$  design goal and below the wall temperature reusability goal congregate around 425 to 435 seconds vacuum specific impulse. To obtain high vacuum specific impulse, higher wall temperatures are expected with low  $T/W$ . The low  $T/W$  is due to lower material strength from the increased wall and coolant temperatures leading to increased structural jacket thicknesses. Furthermore, higher vacuum specific impulses occur for long chamber lengths and large chamber and aerospike radii leading to more material volume and high component weights.

For some of the designs the Mach numbers are trustworthy, for others, the Mach numbers are inaccurate. Figure 49 plots the oxygen and hydrogen maximum fluid temperatures for the successful DOE runs. The grayed areas show maximum fluid temperatures greater than the interpolated Mach number polynomial limits; the red and blue lines represent the hydrogen and oxygen limits, respectively. Mach numbers for the engine designs calculated in the grey areas are erroneous.

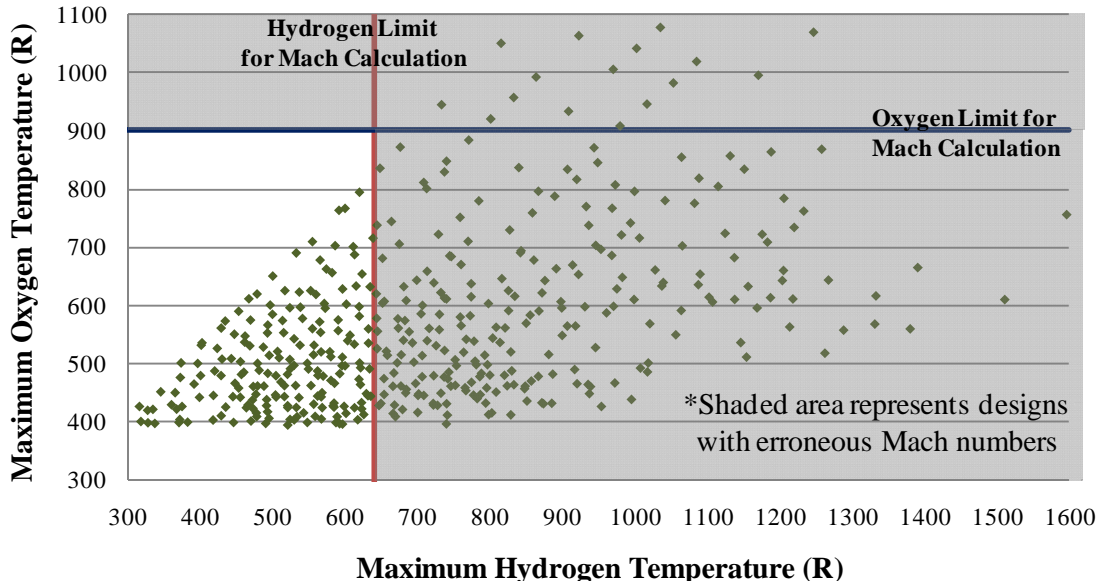


**Figure 49. Maximum Hydrogen and Oxygen Fluid Temperatures of Potential DEAN Designs**

Numerous DOE designs led to high hydrogen and oxygen fluid temperatures. Out of 442 runs, approximately 189 designs meet both the hydrogen and oxygen limits for Mach number accuracy. The designs meeting the fluid temperature limits tend to be the designs around the 430 second vacuum specific impulse range in Figure 48. Previous conclusions made about the accuracy of the calculated Mach numbers from the chamber length, aerospike radius, and engine mass flow trade studies also apply here.

The DOE represents a very small sample of the solution space and may not accurately represent the true solution space. The acceptable designs led to NPSS convergence with set NPSS inputs (i.e. cooling channel geometry and percentage of oxygen bypassing the turbine); however, there are many more potential designs. The potential designs require just the right combination of values of the NPSS inputs and the design variables. To optimize the DEAN system-level model accurately, the coupled relationship between the variables is required. With the current DOE results, the best

DEAN designs meeting the thrust and  $T/W$  design goals and meeting physical constraints (both wall temperature and Mach numbers) are the designs with a vacuum specific impulse around 430 seconds. To meet the other design goals (i.e.  $T/W$ ), the vacuum specific impulse design goal cannot currently be met.

From the DOE, designs meeting the vacuum specific impulse and vacuum thrust design goals are achievable; however, the reusability and  $T/W$  design goals cannot be met. Table 20 tabulates the design variables and selected outputs of a plausible design meeting the performance goals. The material selection is the same material selection used in the DOE study. To increase the engine  $T/W$  and lower the performance values closer to the design goals, the aerospike nozzle was truncated. Figure 50 shows an axial diagram of the engine design; the yellow ring around the aerospike nozzle visually shows the location where the end of the hydrogen cooling jacket is. The black arrows are one foot (30.48 cm) in length.

The chamber and aerospike wall percent melting point is extremely high and realistically too close to the melting point to be considered a desirable design. The oxygen maximum Mach number is accurate due to the oxygen maximum fluid temperature being below the polynomial limit. On the contrary, the hydrogen maximum Mach number cannot be trusted due to the maximum hydrogen fluid temperature being greater than the polynomial limit. Although the design in Table 20 does meet the vacuum specific impulse performance design goals, the high wall and fluid temperatures and low  $T/W$  make the design undesirable.

**Table 20. DEAN Design Meeting Performance Design Goals**

Design Variables		Response Variables	
<i>O/F</i>	6.0	<b>Vacuum Thrust</b>	51224 lb <sub>f</sub> (227.9 kN)
<b>Engine Mass Flow</b>	110 lb <sub>m</sub> /s (50.0 kg/s)	<b>Vacuum Specific Impulse</b>	465.7 s
<b>Chamber Length</b>	21.7 in (55.1 cm)	<b>T/W</b>	27.7
<b>Chamber Radius</b>	17.9 in (45.5 cm)	<b>Total Engine Weight</b>	1852.4 lb (840.2 kg)
<b>Aerospike Radius</b>	15.7 in (39.9 cm)	<b>Chamber Percent Melt</b>	93%
<b>Percent Nozzle Truncation</b>	84.5%	<b>Aerospike Percent Melt</b>	92%
		<b>Chamber Pressure</b>	2884 psia (19.9 MPa)
		<b>Throat Area</b>	9.34 in <sup>2</sup> (60.3 cm <sup>2</sup> )
		<b>Max Oxygen Fluid Temperature</b>	751 R (417.2 K)
		<b>Max Hydrogen Fluid Temperature</b>	931 R (517.2 K)
		<b>Max Oxygen Fluid Mach Number</b>	0.06
		<b>Max Hydrogen Fluid Mach Number</b>	0.13

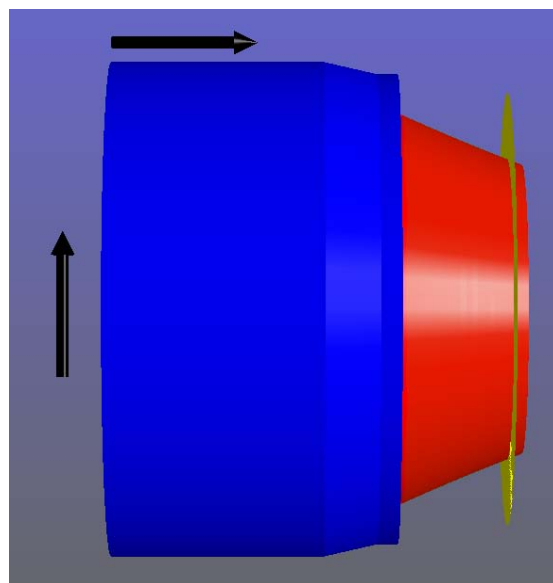


**Figure 50. Truncated DEAN Design Meeting Performance Design Goals**

Discussed in the verification and validation of the DEAN model, another portion of the model is the capability to compare the calculated aerospike performance to an equivalent expansion ratio bell nozzle by a percent difference calculation. NPSS calculates the bell nozzle performance internally. The variables *Per\_Diff\_Thrust* and *Per\_Diff\_Isp* are used to compare the bell nozzle and aerospike performance; a negative value means the aerospike has less performance than the bell nozzle. The calculated bell nozzle performance does not include any performance losses, while the aerospike performance values contain nozzle boundary layer losses. An interesting trend can be seen with the percent difference performance variables. As chamber length increases, the percent difference in performance decreases. As aerospike radius approaches the chamber radius, the percent difference decreases. As chamber radius increases, the percent difference decreases. The range of percent differences between the aerospike and bell nozzle is -5% to +10% based on DEAN geometry. Smaller geometry leads to positive performance differences. The percent difference is not drastically different from a bell nozzle. As previously stated in chapter II, above the design altitude of the aerospike nozzle, especially in vacuum conditions, the aerospike will behave more like a conventional bell nozzle [28]. The conclusion is with the current range of percent performance difference, the DEAN model shows similar performance to an equivalent bell nozzle, correlating well with literature.

For the current research effort, a final DEAN design decision was made for further *T/W* optimization studies. The design decision was based on the number of design goals that could be met. From Figure 48, a majority of design points meeting the thrust and *T/W* design goals within acceptable wall temperature and fluid Mach number

physical constraints occur around a vacuum specific impulse of 430 seconds. Although the vacuum specific impulse design goal cannot be met, Table 21 tabulates the selected full-length nozzle DEAN design for continued *T/W* optimization studies.

**Table 21. Final DEAN Design Variables**

<b>Design Variables</b>		<b>Response Variables</b>	
<b>O/F</b>	6	<b>Vacuum Thrust</b>	50,161 lb <sub>f</sub> (223.1 kN)
<b>Engine Mass Flow</b>	116.5 lb <sub>m</sub> /s (52.8 kg/s)	<b>Vacuum Specific Impulse</b>	430.6 s
<b>Chamber Length</b>	14.5 in (36.8 cm)	<b>Chamber Pressure</b>	1,548 psia (10.7 MPa)
<b>Chamber Radius</b>	6 in (15.2 cm)	<b>Throat Area</b>	18.0 in <sup>2</sup> (116.1 cm <sup>2</sup> )
<b>Aerospike Radius</b>	4.5 in (11.4 cm)	<b>Max Oxygen Fluid Temperature</b>	507 R (281.7 K)
		<b>Max Hydrogen Fluid Temperature</b>	364 R (202.2 R)
		<b>Max Oxygen Fluid Mach Number</b>	0.26
		<b>Max Hydrogen Fluid Mach Number</b>	0.38
		<b>Total Engine Length</b>	26.7 in (67.8 cm)

#### *IV.2.c. Influence of Material Selection on Thrust-to-Weight Ratio*

Using the new DEAN design point (Table 21) with a cooling channel cover and structural jacket, a trade study for each engine component was performed to determine the influence material selection of an individual component has on the *T/W* of the total engine. Turbopump weight was neglected for this study since it is a function of engine mass flow and not influenced by material selection. Maximum wall temperature as a function of the material melting point was also neglected for the study. To start, all seven engine components requiring material selection are set to pure copper giving an engine

$T/W$  of 69.2. The corresponding  $T/W$  for various materials of a single engine component is shown in Figure 51; the process is performed for all seven engine components.

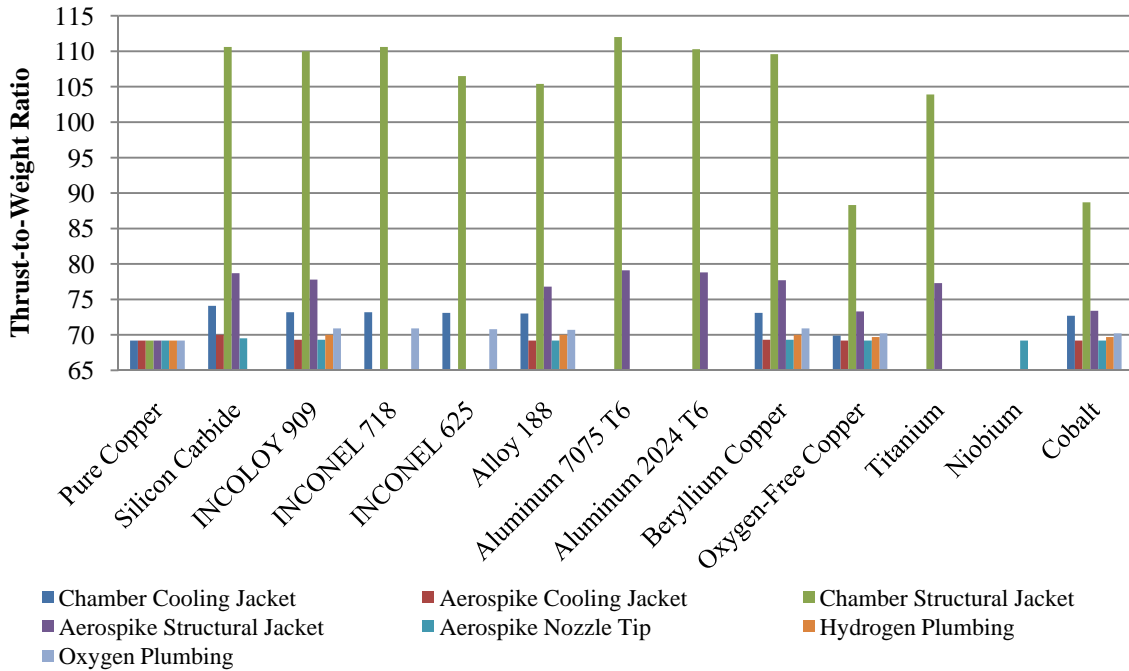


**Figure 51. Influence of Material Selection on  $T/W$  for DEAN Engine Components**

Clearly seen in Figure 51, as material selection changes for just the chamber cooling jacket, the  $T/W$  varies from 69.2 as a minimum up to 112.0 as a maximum; a far bigger range than any other engine component. Therefore, the conclusion is the chamber structural jacket has the most influence on  $T/W$  for any engine component requiring material selection. The next most influential engine component is the aerospike structural jacket followed by the chamber cooling jacket.

The material selection maximizing and minimizing  $T/W$  will be referred to as the “best material selection” and “worst material selection”, respectively. The best and worst material selections bound potential  $T/W$  values for the new DEAN design. Table 22 tabulates the best and worst material selection using the ultimate tensile strength option, nozzle viscous performance losses, and a 5% hardware weight estimate.

**Table 22. Material Selection for Maximum and Minimum T/W**

<b>Engine Component</b>	<b>Best Material Selection (T/W = 176.5)</b>	<b>Worst Material Selection (T/W = 69.2)</b>
Chamber Cooling Jacket	Silicon Carbide	Copper
Aerospike Cooling Jacket	Silicon Carbide	Alloy 188
Chamber Structural Jacket	Aluminum 7075 T6	Copper
Aerospike Structural Jacket	Aluminum 7075 T6	Copper
Aerospike Nozzle Tip	Silicon Carbide	Alloy 188
Hydrogen Plumbing	INCOLOY 909	Copper
Oxygen Plumbing	INCONEL 718	Copper

The results in Figure 51 neglect turbopump mass; however, it is desirable to understand the influence of turbopump mass on the total engine mass. Table 23 tabulates all engine components' mass for the worst and best material selection, along with the percent component weight. The bar graph shown in Figure 52 graphically shows the weight of the major engine components (aerospike, chamber, plumbing, turbopumps, and hardware).

The chamber and, more specifically, the chamber structural jacket account for the highest percentage of total engine weight for the worst material selection. Conversely, for the best material selection, the engine component with the highest percentage of total engine weight is the oxidizer turbopump. For different material selections, the engine components with the most influence on total engine weight will be the structural jackets and turbopumps. The influence of the structural jackets is reasonable since the structural jackets have the most volume out of any engine component. As high strength, low density, good conductivity materials are utilized, the combined fuel and oxidizer turbopump weight will remain constant while other components will decrease in weight causing the ratio of turbopump weight to total engine weight to increase; shown in Table 23 where total turbopump weight accounts for 75% of the total engine weight using the

best material selection. Which turbopump has greater influence on overall engine weight is highly coupled to the *O/F* ratio.

**Table 23. Component Weight and Percent Component Weight to Total Engine Weight for Different Material Selections**

Engine Component	Worst Material Selection		Best Material Selection	
	Component Weight	Percent Component Weight	Component Weight	Percent Component Weight
<b>Chamber</b>	332.2 lb (150.7 kg)	45.8%	34.0 lb (15.4 kg)	12.0%
<b>Structural Jacket</b>	293.5 lb (133.1 kg)	40.5%	28.7 lb (13.0 kg)	10.1%
<b>Cooling Jacket</b>	38.8 lb (17.6 kg)	5.3%	5.3 lb (2.4 kg)	1.9%
<b>Aerospike</b>	117.1 lb (53.1 kg)	16.2%	20.1 lb (9.1 kg)	7.1%
<b>Structural Jacket</b>	99.9 lb (45.3 kg)	13.8%	14.0 lb (6.4 kg)	4.9%
<b>Cooling Jacket</b>	12.1 lb (5.5 kg)	1.7%	4.3 lb (2.0 kg)	1.5%
<b>Uncooled Nozzle Tip</b>	5.0 lb (2.3 kg)	0.7%	1.8 lb (0.82 kg)	0.6%
<b>Plumbing</b>	27.9 lb (12.7 kg)	3.8%	3.5 lb (1.6 kg)	1.2%
<b>Fuel</b>	9.5 lb (4.3 kg)	1.3%	1.3 lb (0.6 kg)	0.5%
<b>Oxidizer</b>	18.4 lb (8.3 kg)	2.5%	2.2 lb (1.0 kg)	0.8%
<b>Turbopump</b>	213.1 lb (96.7 kg)	29.4%	213.1 lb (96.7 kg)	75.0%
<b>Fuel</b>	86.8 lb (39.4 kg)	12.0%	86.8 lb (39.4 kg)	30.6%
<b>Oxidizer</b>	126.3 lb (57.3 kg)	17.4%	126.3 lb (57.3 kg)	44.4%
<b>Hardware</b>	34.5 lb (15.6 kg)	5.0%	13.5 lb (6.1 kg)	5.0%
<b>Total Engine Weight</b>	724.7 lb (328.7 kg)		284.2 lb (128.9 kg)	

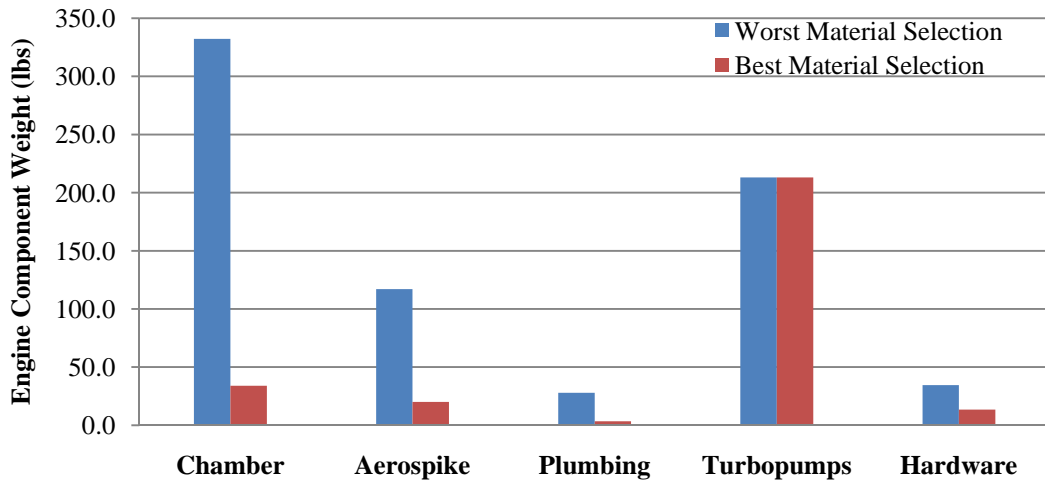


**Figure 52. Engine Component Most Influencing T/W**

The cooling jacket material selection has very little influence on the engine T/W; however, the material selection has a large influence on whether the chamber and aerospike cooling jacket walls will melt. A bar plot is shown in Figure 53 showing the influence of material selection on the maximum wall temperature as a function of material melting point (percent material melting point). As a result of NPSS calculating a constant convection heat transfer coefficient on the hot and cold side of the cooling jacket wall, the calculated maximum wall temperature for each material is different. The maximum wall temperature is a function of the constant convection heat transfer coefficient and the thermal conductivity and strength of the material. The strength of the material determines the thickness of the cooling jacket required to prevent failure. The thicker the cooling jacket, the higher the maximum wall temperature due to the coolant being further away. Therefore, the bars representing different materials in Figure 53 correspond to different maximum wall temperatures and cooling jacket thicknesses.

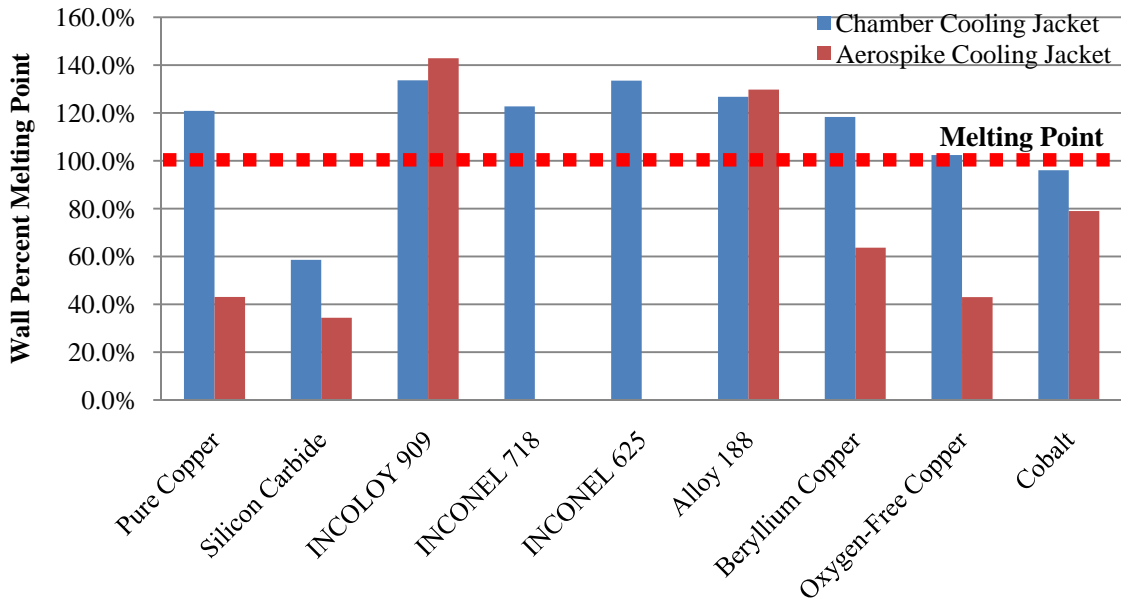


**Figure 53. Influence of Material Selection on Cooling Jacket Wall Temperature**

For the current DEAN design, there is only one material choice for the chamber and five material choices for the aerospike where the maximum wall temperature is less than the material melting point. The material of choice for the aerospike is the material providing the lowest melting point percentage. The cooling jacket material choice for further studies will be silicon carbide for both the chamber and aerospike. Since the plumbing and aerospike nozzle tip have very little influence over the engine  $T/W$ , a material can be selected for those components and kept constant. For the plumbing and aerospike nozzle tip, the material choice selected for further studies is the best material selection in Table 22.

The best material selection exceeds the  $T/W$  design goal. Since the structural jackets most influence the engine  $T/W$ , the material selections for only the chamber and aerospike structural jackets were allowed to vary while keeping the remaining materials constant (i.e. cooling jackets, plumbing, and aerospike nozzle tip). The goal is to find

multiple material selections for the structural jackets meeting or exceeding the engine  $T/W$  requirement. There are a total of 10 and 12 material selections for the aerospike and chamber structural jackets, respectively, for 120 total material combinations. All material combinations and the resulting  $T/W$  could not be tabulated or plotted; however, Figure 54 shows a surface plot of  $T/W$  values for various chamber and aerospike structural jacket materials; the  $T/W$  range is 78 to 176.5. A red color means low  $T/W$  while a blue color means high  $T/W$ .

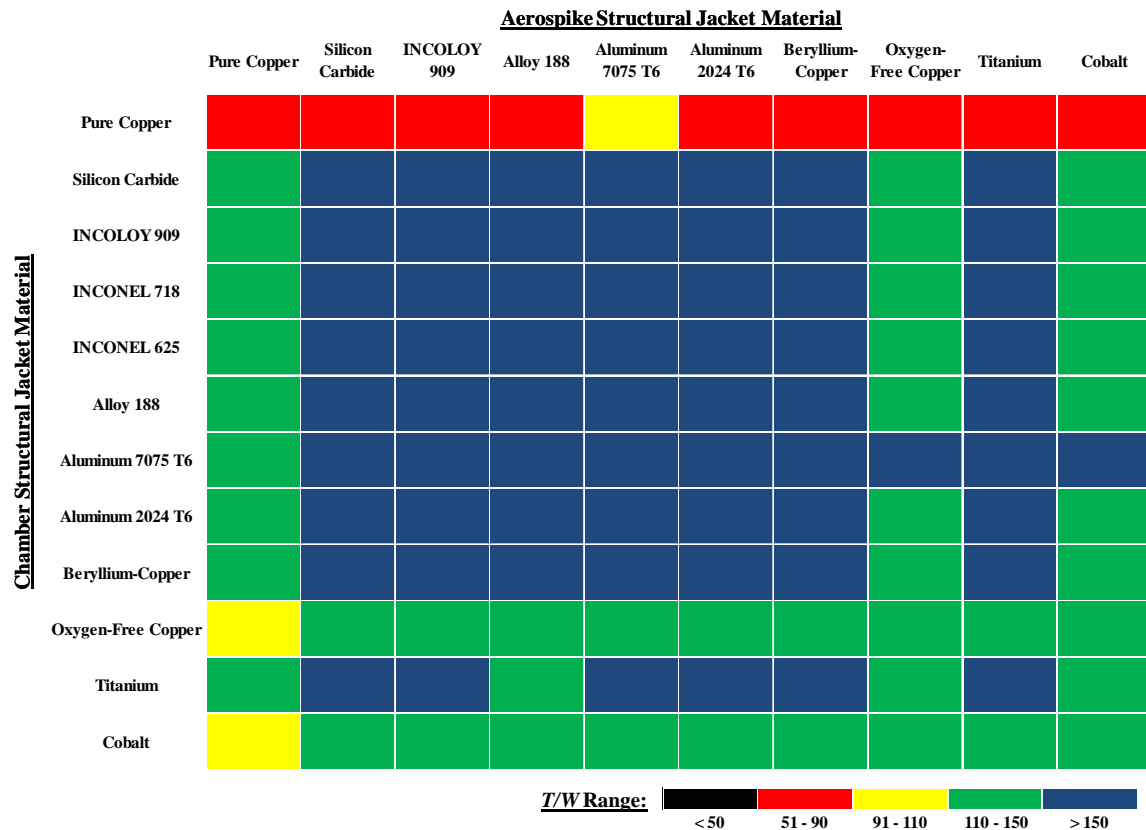


**Figure 54. Influence of Structural Jacket Material on  $T/W$  Using Material Ultimate Tensile Strength**

There are numerous material selections meeting or exceeding the  $T/W$  design goal of 106.5 using the ultimate tensile strength option. Any material combination for the aerospike structural jacket used with a pure copper chamber structural jacket results in

low  $T/W$ . On the other hand, using aluminum 7075 T6 or silicon carbide for both structural jackets result in high  $T/W$ .

The conclusion is the structural jackets are the most influential engine component requiring material selection on the total weight and  $T/W$  of the engine. With the current DEAN design, there are multiple material selections meeting or exceeding the  $T/W$  design goal while ensuring the cooling jackets will not melt.

#### ***IV.2.d. DEAN Reusability***

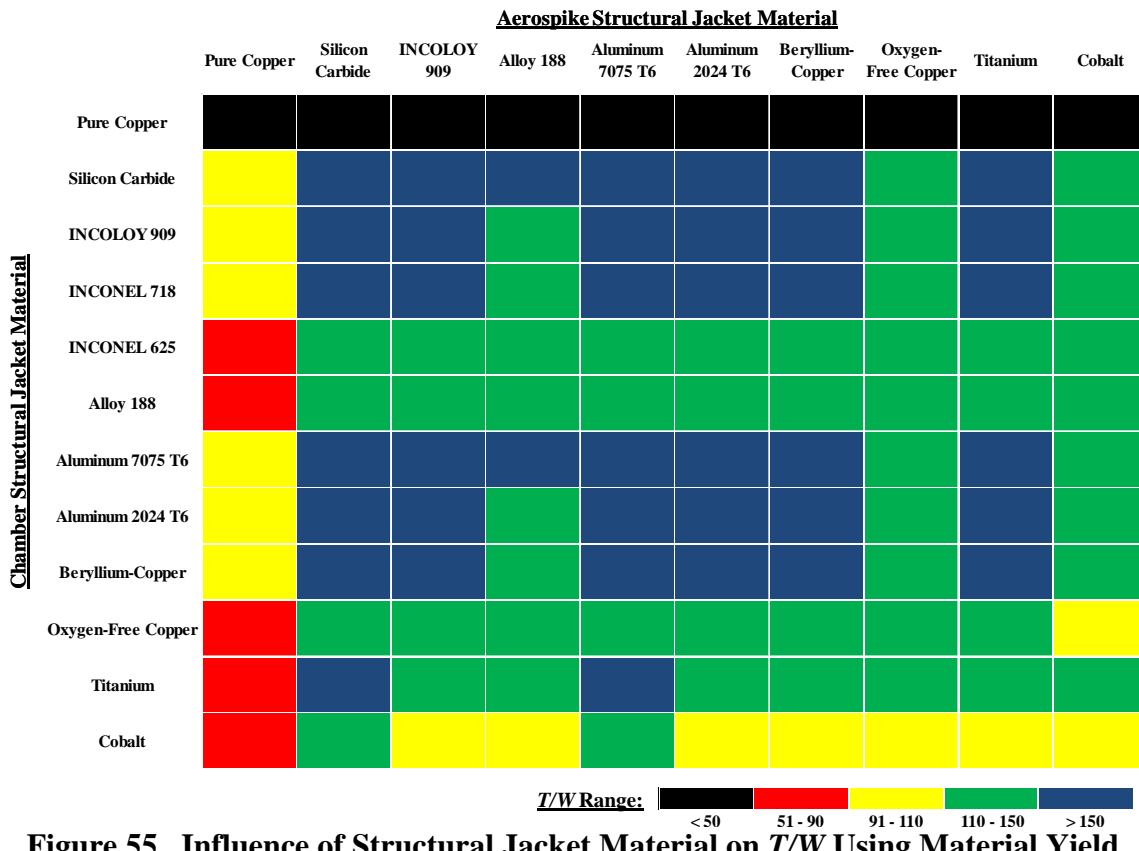
In order for the DEAN to be considered reusable, the maximum wall temperature compared to the material melting point must be less than or equal to 60%. When a material is stressed beyond the yield strength and less than the ultimate tensile strength, permanent deformation occurs. For reusability, permanent deformation is unacceptable and the material strength option should be set to yield strength with a conservative factor of safety of 1.5. The goal of this study is to determine if the current DEAN design can meet the reusability requirements.

Table 24 shows the best and worst material selections and their corresponding total weight and  $T/W$  for the two different material strength options. As expected, using material yield strength to determine structural jacket and plumbing wall thicknesses, the total engine weight is greater and the  $T/W$  less compared with using ultimate tensile material strength. The influence is much more profound at the worst material selection. The worse material selection does not meet the maximum cooling jacket wall temperature reusability design goal; however, the best material selection does.

**Table 24. Impact of Material Strength on  $T/W$**

	Worst Material Selection		Best Material Selection	
	Yield Strength	Ultimate Strength	Yield Strength	Ultimate Strength
<b>Total Weight</b>	4030.6 lbs (1828.2 kg)	724.7 lbs (328.7 kg)	291.2 lbs (132.1 kg)	284.2 lbs (128.9 kg)
<b><math>T/W</math></b>	12.4	69.2	172.3	176.5

From Figure 53, there is only one material option for the chamber where the chamber will meet the 60% melting point reusability goal: silicon carbide. For the aerospike, there are three options: pure copper, silicon carbide, and oxygen-free copper. The structural jacket can be any of the material selections. Redoing Figure 54 with the yield strength option (Figure 55) results in a much larger range  $T/W$  range (the range is 14 to 171).



**Figure 55. Influence of Structural Jacket Material on  $T/W$  Using Material Yield Strength**

A similar surface plot is noticeable between Figures 54 and 55; however, the range of  $T/W$  values is drastically different. For the yield strength option, there are not as many options for material selection meeting the  $T/W$  design goal. For low density, high strength materials, such as aluminum 7075 T6, the difference in  $T/W$  between ultimate and yield strength is minimal (~3% decrease). However, for highly conductive, high density materials, such as pure copper, there is approximately an 82% decrease in  $T/W$  from changing the material strength option from ultimate tensile to yield strength; note the pure copper is annealed leading to the low  $T/W$  for pure copper, compared to oxygen-free copper and beryllium-copper.

With the current DEAN design using the yield strength option, the conclusion is that there are multiple material selections meeting or exceeding the  $T/W$  design goal while meeting the reusability design goals.

#### ***IV.2.e. Best Manufacturing DEAN Design***

To improve aerospike manufacturability for a reusable engine, the same material will be utilized for the aerospike cooling jacket and structural jacket. The best material selection is challenging for fabrication. For the aerospike, it would be difficult to fabricate the axisymmetric cooling jacket first with silicon carbide and then place an axisymmetric structural jacket made of aluminum inside the cooling jacket. Using the same material simplifies the process by allowing the manufacturer to fabricate both the structural jacket and cooling jacket at the same time with one piece of material.

Due to the complex geometry of the aerospike, silicon carbide is not recommended for the aerospike structural and cooling jackets. Therefore, only oxygen-

free copper and pure copper remain as potential aerospike materials from Figure 53; the cooling jacket material is the limiting factor for aerospike material selection. Using pure copper and oxygen-free copper on the aerospike nozzle tip, cooling jacket, and structural jacket, Table 25 compares the differences in weight and  $T/W$  for both material strength options. The material selections for the chamber components and plumbing remain the best material selection option in Table 22.

**Table 25. Impact of Material Strength on  $T/W$**

	Ultimate Tensile Strength		Yield Strength	
	Pure Copper	Oxygen-Free Copper	Pure Copper	Oxygen-Free Copper
<b>Total Weight</b>	391.3 lbs (177.5 kg)	351.2 lbs (159.3 kg)	548.3 lbs (248.7 kg)	352.7 lbs (160.0 kg)
<b><math>T/W</math></b>	128.2	142.8	91.5	142.2

Surprisingly, the oxygen-free copper has less total engine weight compared to pure copper. Oxygen-free copper is 99% pure copper and has similar density to pure copper; the expectation is the weight should be similar. The material properties for both materials came from different sources. The oxygen-free copper has only one thermal conductivity value compared to pure copper that has ten values as a function of maximum wall temperature. As a consequence, the calculated wall temperatures can lead to the use of lower thermal conductivity values for the pure copper; whereas, oxygen-free copper uses only one value. For this DEAN design, the calculated wall temperatures and maximum fluid temperatures for both material selections were coincidentally approximately equal.

The ultimate tensile and yield strengths for the two copper types are significantly different. The oxygen-free copper has higher strength leading to a smaller structural

jacket wall thickness compared to pure copper. A smaller structural jacket wall thickness equates to a lighter aerospike structural jacket and overall lighter engine. At the current DEAN design, the difference in material strength alone accounts for the difference in total engine weight and  $T/W$  for the two material selections. The composition of both materials are approximately equal; however, the difference in strength is due to the pure copper being annealed and the oxygen-free copper being heat treated for improved strength. The annealed pure copper is more ductile than the oxygen-free copper with lower ultimate tensile and yield strength.

Using the ultimate tensile strength option, both materials exceed the  $T/W$  design goal. On the other hand, using the yield strength option, only oxygen-free copper exceeds the  $T/W$  design goal; pure copper falls short by approximately 14%. Therefore, for a reusable engine using the best manufacturing design, the oxygen-free copper will be used for all aerospike components along with the best material selection for the chamber and plumbing in Table 22.

#### ***IV.2.f. Aerospike Nozzle Truncation Study***

Truncation studies evaluated 0 to 100% nozzle truncation in 1% increments using the best manufacturing DEAN design and the yield strength option. Percent nozzle truncation refers to the percentage of nozzle length removed from the full-length nozzle tip. The goal of the study is to determine if nozzle truncation leads to  $T/W$  improvements with minimal performance losses.

For truncation studies between 0 and 50% of the full-length aerospike nozzle, the engine expander cycles will not change. However, for truncation studies equal to or

greater than 50%, the engine expander cycles will change. As observed in Figures 56 and 57, the output chamber pressure, throat area, and the ability of NPSS to converge will change.

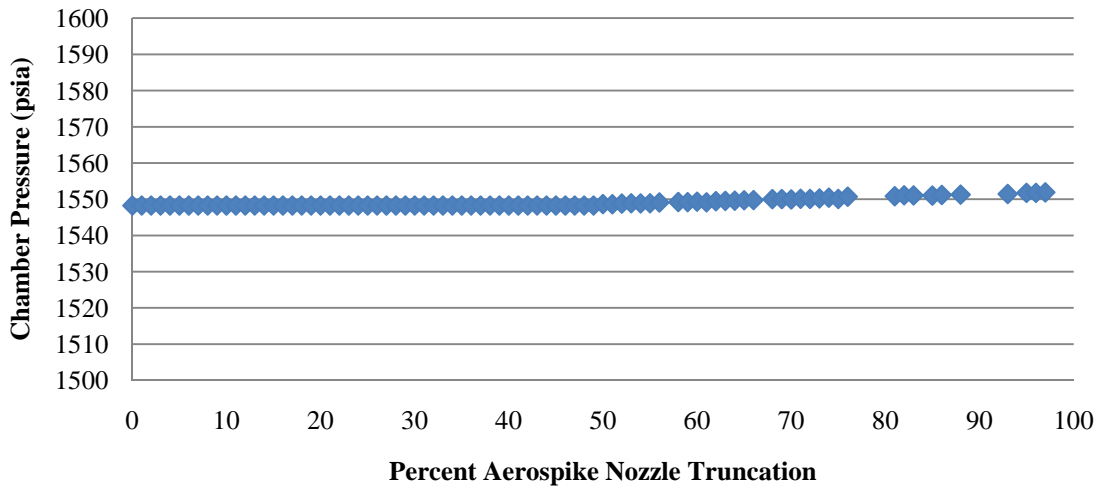


**Figure 56. Influence of Aerospike Nozzle Truncation on Chamber Pressure**

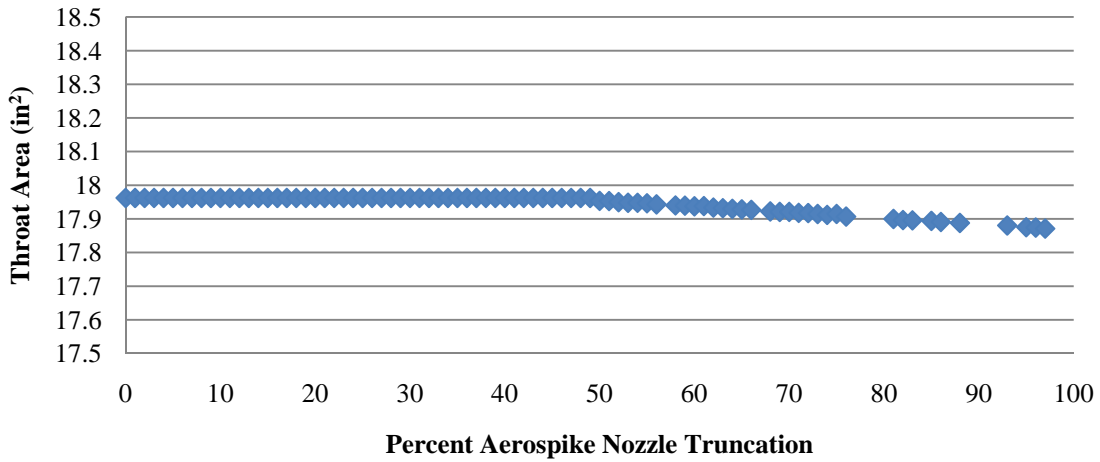


**Figure 57. Influence of Aerospike Nozzle Truncation on Throat Area**

There are NPSS failures, denoted by empty space on the plot curve, for nozzle truncation greater than 50%; maximum successful nozzle truncation was 97%. For the error runs, NPSS was unable to converge to a solution and common NPSS errors, such as the inability to conserve mass through the engine, were noted. The error runs occur due

to brittleness in the NPSS model and can be neglected. The chamber pressure and throat area plots are almost linear with very little change in magnitude for nozzle truncation greater than 50%. Due to the very small changes in NPSS outputs, the performance calculated for nozzle truncation greater than 50% can be compared to nozzle truncation less than 50%. Figures 58 and 59 plot the influence of nozzle truncation on vacuum performance (thrust and specific impulse).

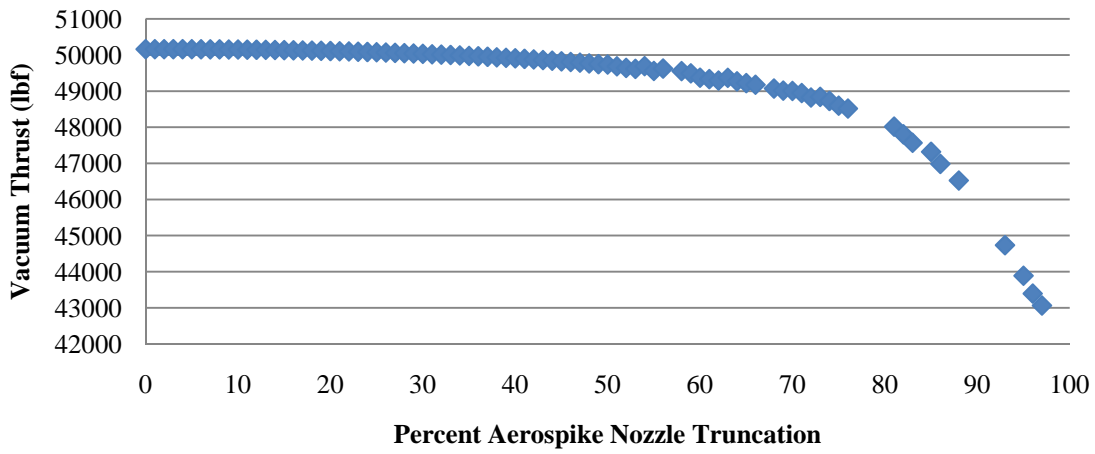


**Figure 58. Influence of Aerospike Nozzle Truncation on Vacuum Thrust**

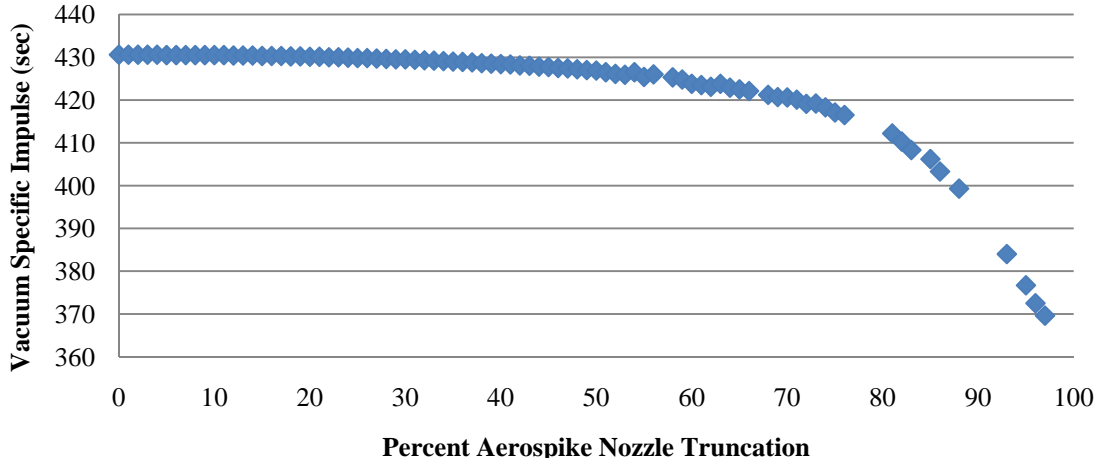


**Figure 59. Influence of Aerospike Nozzle Truncation on Vacuum Specific Impulse**

The noise observed in the figures for nozzle truncation greater than 50% is due to variations in the calculated NPSS expander cycles. Between 0 and 49% nozzle truncation, there is approximately a 0.83% loss in vacuum performance. Between 0% and 97% truncation, there is approximately a 14.2% loss in vacuum performance. The greatest decrease in performance occurs for percent truncation greater than 80%; even from 0 to 75% nozzle truncation there is only approximately a 3.1% decrease in vacuum performance. As a reminder, the performance values include aerospike nozzle viscous losses. Figures 60 and 61 plot aerospike mass and total engine weight as a function of nozzle truncation.

Clearly seen in Figures 60 and 61, from 0 to 49% nozzle truncation, the aerospike mass and total engine weight decrease steadily. At 50% nozzle truncation, there is a jump in aerospike mass and engine weight and then an eventual decrease at 97% truncation. In general, for truncation studies above 50% with changes to the expander cycles, turbopump mass increases, while chamber, hardware, and plumbing masses slightly decrease for increased nozzle truncation. Chamber and hardware mass decrease from 0 to 97% nozzle truncation by approximately 0.2 and 0.4 lbs (0.09 and 0.18 kg), respectively. The hydrogen plumbing decreases by approximately 1.5 lbs (0.68 kg), while the turbopump masses increases by approximately 3.75 lbs (1.7 kg). The changes in mass may seem insignificant for nozzle truncation studies greater than or equal to 50%; however, these mass changes lead to the plot shape in Figure 61.

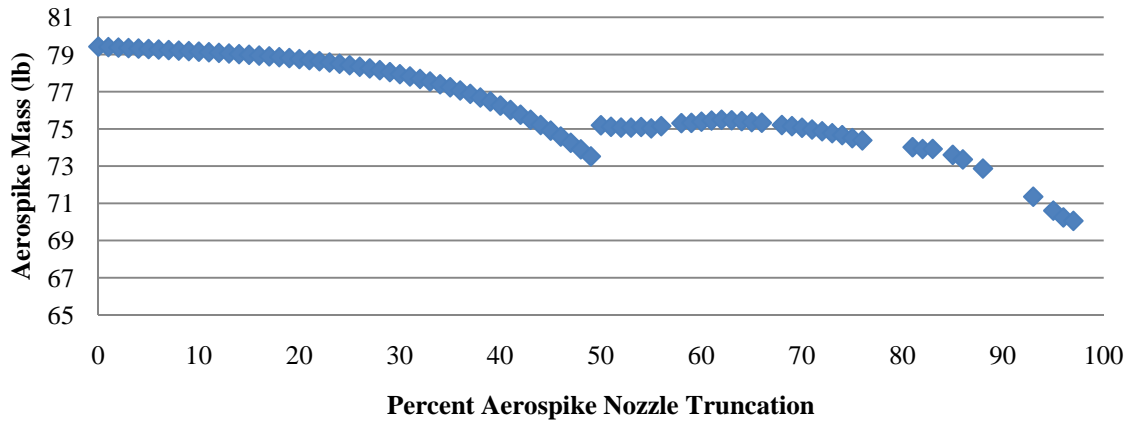


**Figure 60. Influence of Aerospike Nozzle Truncation on Aerospike Mass**

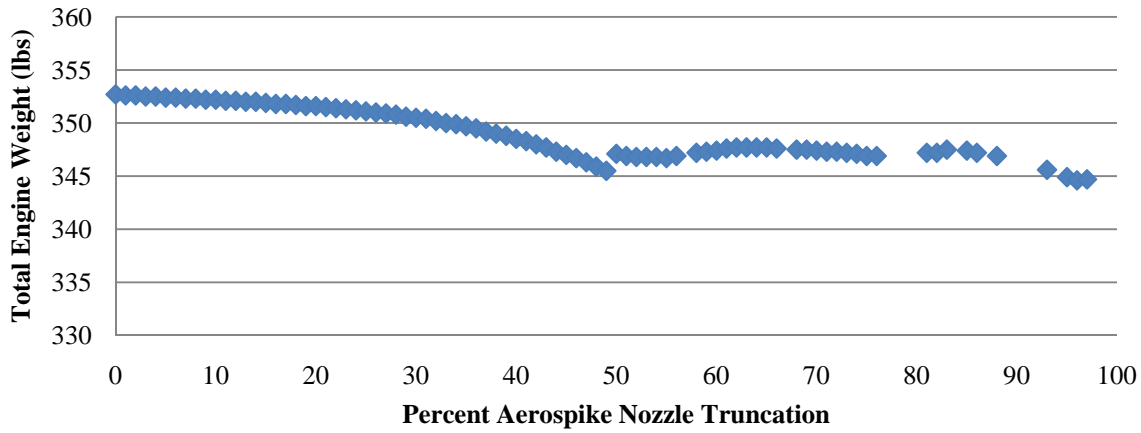
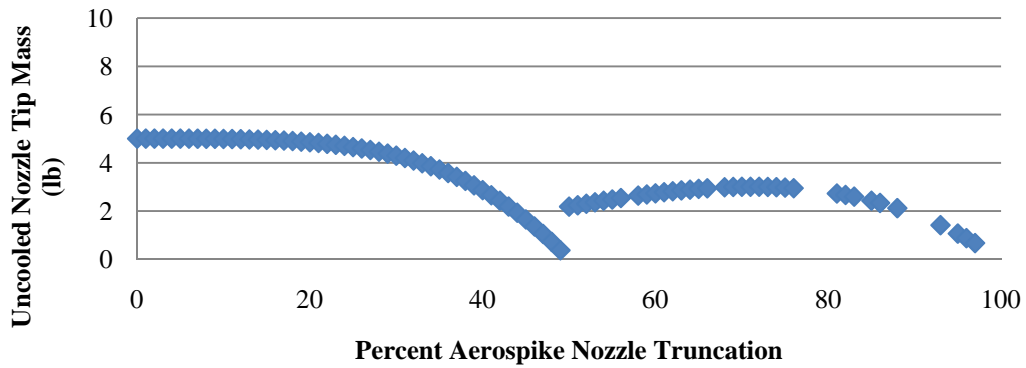


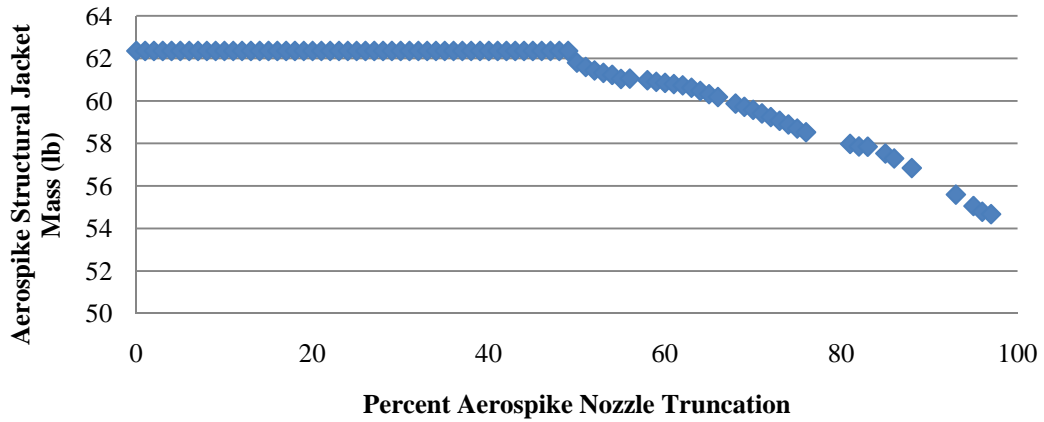
**Figure 61. Influence of Aerospike Nozzle Truncation on Total Engine Weight**

In Figure 60, the difference in aerospike mass for nozzle truncation above 50% is not only due to the difference in the expander cycles, but also due to differences in how the uncooled aerospike nozzle tip is calculated. For nozzle truncation above 50%, the uncooled aerospike nozzle tip is set to 10% the truncated nozzle length by the design variable *Per\_Uncooled\_Spike*; the nozzle tip mass is a function of both *Per\_Uncooled\_Spike* and percent nozzle truncation. Below 50% truncation, the nozzle tip mass is a function of percent nozzle truncation alone. Figure 62 plots the individual aerospike components as a function of percent nozzle truncation. The aerospike cooling

jacket is not plotted due to almost linear mass with changes noted due to changes in the expander cycle. The interesting plot shape in Figure 62a for the nozzle tip mass above 50% nozzle truncation is due to the nozzle tip mass being a function of two variables.



a) Uncooled Nozzle Tip



b) Structural Jacket

**Figure 62. Influence of Nozzle Truncation on Aerospike Components' Mass**

The aerospike structural jacket decreases for increased nozzle truncation greater than 50% due to expander cycle changes and due to a decrease in the maximum fluid temperature through the aerospike cooling jacket. As nozzle truncation approaches 100%, the aerospike cooling jacket has similar surface area for heat exchange to the chamber. With less surface area for heat exchange, the hydrogen does not gain as much heat from heat transfer thus causing a lower maximum fluid temperature. The maximum

fluid temperature is used to calculate the structural jacket thickness; therefore, with lower fluid temperature, the structural jacket thickness decreases causing the plot trend in Figure 62b. Also with less heat transfer from the combusted gases to the coolant, the maximum fluid Mach number through the aerospike cooling jacket decreases leading to increased maximum wall temperature. With the increase in maximum wall temperature for truncation studies, the designer needs to verify the wall temperature does not surpass the material melting point or the reusability wall temperature point. For the current DEAN design, the aerospike nozzle never exceeds the material melting point for increased truncation; however, the nozzle surpasses the reusability design goal at 85% nozzle truncation.

Figure 63 plots engine  $T/W$  as a function of nozzle truncation. Below 50% nozzle truncation, the engine  $T/W$  increases due to a low loss in vacuum thrust and a larger loss in aerospike nozzle tip mass. There is a 0.83% loss in vacuum thrust and a 2.0% reduction in total engine weight leading to a 1.3% increase in engine  $T/W$  at 49% truncation. For nozzle truncation studies greater than 50%, there is a much larger decrease in performance compared to the decrease in engine mass accounting for the decrease in the engine  $T/W$ . From 50 to 97% nozzle truncation, there is a 13.42% loss in vacuum thrust and a 0.69% reduction in total engine weight. From 0 to 97% nozzle truncation, there is a total vacuum thrust loss of 14.2%, a total engine weight reduction of 2.3%, a  $T/W$  reduction of 12.2%, and a total engine length reduction of 44.3%. Even at 97% truncation, the  $T/W$  design goal of 106.5 is met.

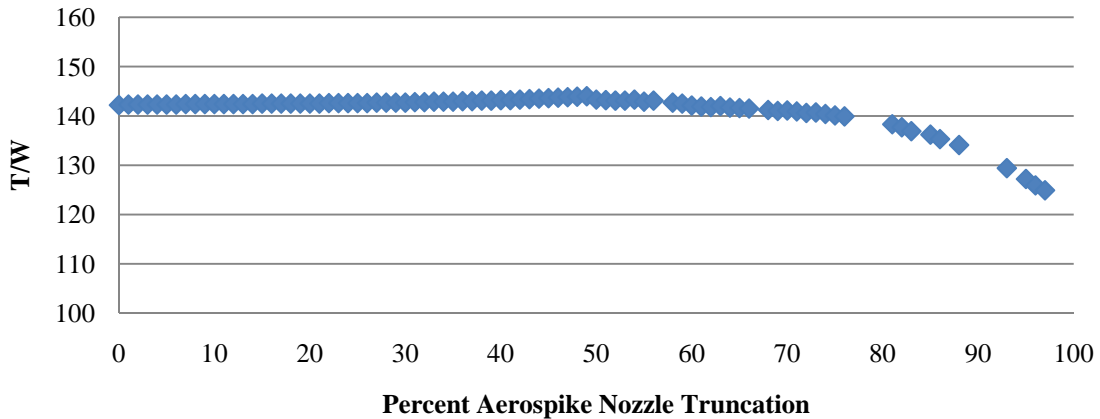


**Figure 63. Influence of Aerospike Nozzle Truncation on  $T/W$**

There is a design tradeoff in truncation studies. A great deal of the total engine length can be truncated with minimal performance losses. For example, using the current design at 75% nozzle truncation, the vacuum performance (includes both thrust and specific impulse),  $T/W$ , and engine length losses compared to the full-length nozzle are 3.1%, 1.5%, and 34%, respectively. At 75% truncation, the vacuum thrust, vacuum specific impulse,  $T/W$ , and total engine length equal 48,595 lb<sub>f</sub> (216.2 kg), 417.1 sec, 140.1, and 17.56 inches (44.6 cm). The performance design goals are not met; however, changes in the design variables can lead to improved performance. The true benefit is in the engine length. By decreasing the engine length, less space is required in the launch vehicle adding indirect benefits to the total launch vehicle. For example, a shorter engine leads to a shorter, lighter interstage. From the decrease in interstage weight, the extra weight can be used for a heavier payload or more propellant. The design tradeoff is does the launch vehicle mission require a shorter, lighter engine with slightly less performance or a heavier, longer engine with better performance. Both engine types (full-length nozzle compared to truncated nozzle) have advantages and disadvantages.

Since the current DEAN design does not meet the specific impulse goals, the final DEAN design will utilize the full-length aerospike nozzle for maximum performance.

### IV.3 Final DEAN Design

Due to the complexity of the DEAN system level ModelCenter model, many interesting outputs are obtainable for any variation of the design variables. The final DEAN design utilizes the full-length aerospike nozzle using the design variables in Table 21 and using the best manufacturing material selection from section IV.2.e. This section summarizes the outputs of interest for the final DEAN design.

The performance values for the final design, also tabulated in Table 21, meet the vacuum thrust and *T/W* design goals; the performance values are 50,161 lb<sub>f</sub> (223.1 kN) vacuum thrust, 430.6 seconds vacuum specific impulse, and a *T/W* of 142.2. The design also meets the DEAN reusability design goals with a percent melting point of 58.6% and 43.0% for the chamber and aerospike, respectively, and with passing the structural analyses using yield strength with a factor of safety of 1.5 for the cooling jacket walls and structural jackets. The characteristic length,  $L^*$ , for the final design is 37.8 inches (96.0 cm); within the recommended range for O<sub>2</sub>/H<sub>2</sub> engines from Huzel and Huang [8]. The throat area is equal to 18.0 in<sup>2</sup> (116.1 cm<sup>2</sup>), equating to a radius difference of 0.61 inches (1.6 cm) between the chamber and aerospike throat radii. The engine expansion ratio is equal to 4.37 and the exit Mach number is equal to 2.63.

Table 26 summarizes the fuel and oxidizer turbopump parameters for the final DEAN design; the turbopump efficiency values are in Table 5. Five percent of the oxidizer flow bypasses the turbine leading to the lower turbine mass flow rate.

**Table 26. DEAN Turbopump Parameters**

	<b>Oxidizer</b>	<b>Fuel</b>
Pump #1 Pressure Ratio	95.90	8.46
Pump #1 Power	-1945.06 HP (-1.45 MW)	-419.28 HP (-0.31 MW)
Pump #2 Pressure Ratio	--	8.46
Pump #2 Power	--	-3163.83 (-2.36 MW)
Pump #1 and #2 Mass Flow Rate	99.86 lb <sub>m</sub> /s (45.30 kg/s)	16.64 lb <sub>m</sub> /s (7.55 kg/s)
Turbine Pressure Ratio	1.84	1.56
Turbine Power	1945.07 HP (1.45 MW)	3583.11 HP (2.67 MW)
Turbine Mass Flow Rate	94.86 lb <sub>m</sub> /s (43.03 kg/s)	16.64 lb <sub>m</sub> /s (7.55 kg/s)
Turbopump Shaft Speed (RPM)	32,000	110,000

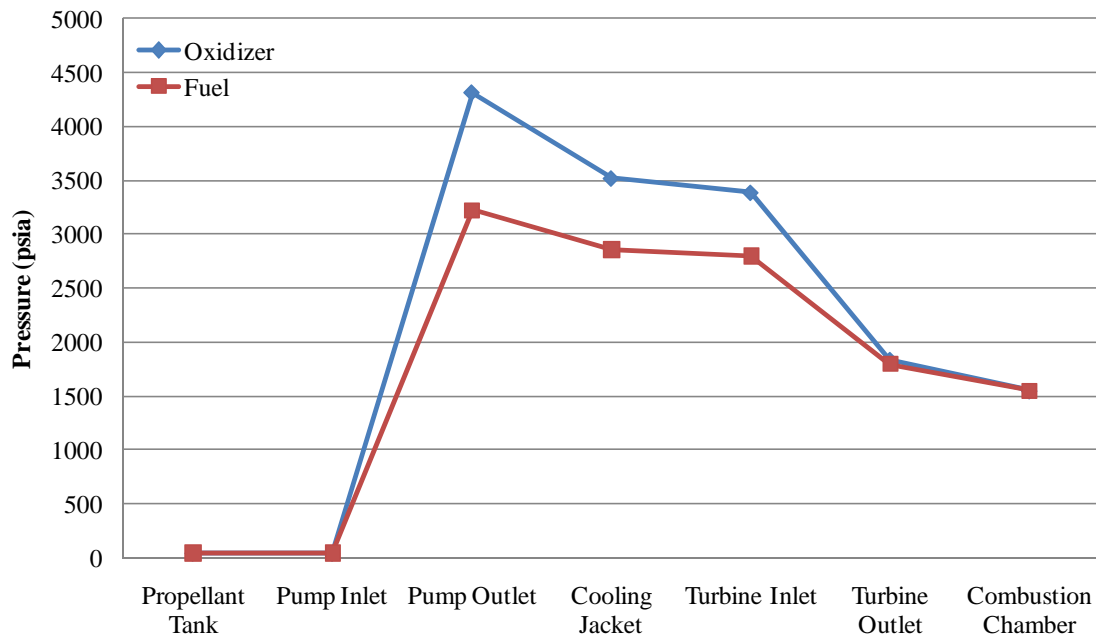
Table 27 summarizes the final engine component mass for the DEAN design.

The total thickness of the chamber and aerospike at the injector face, including the cooling jacket wall thickness, cooling channel height, cooling channel cover thickness, and structural jacket thickness, are 0.64 and 0.55 inches (1.6 and 1.4 cm), respectively. The minimum required structural thickness for the oxidizer and fuel plumbing are 0.02 and 0.03 inches (0.05 and 0.08 cm), respectively.

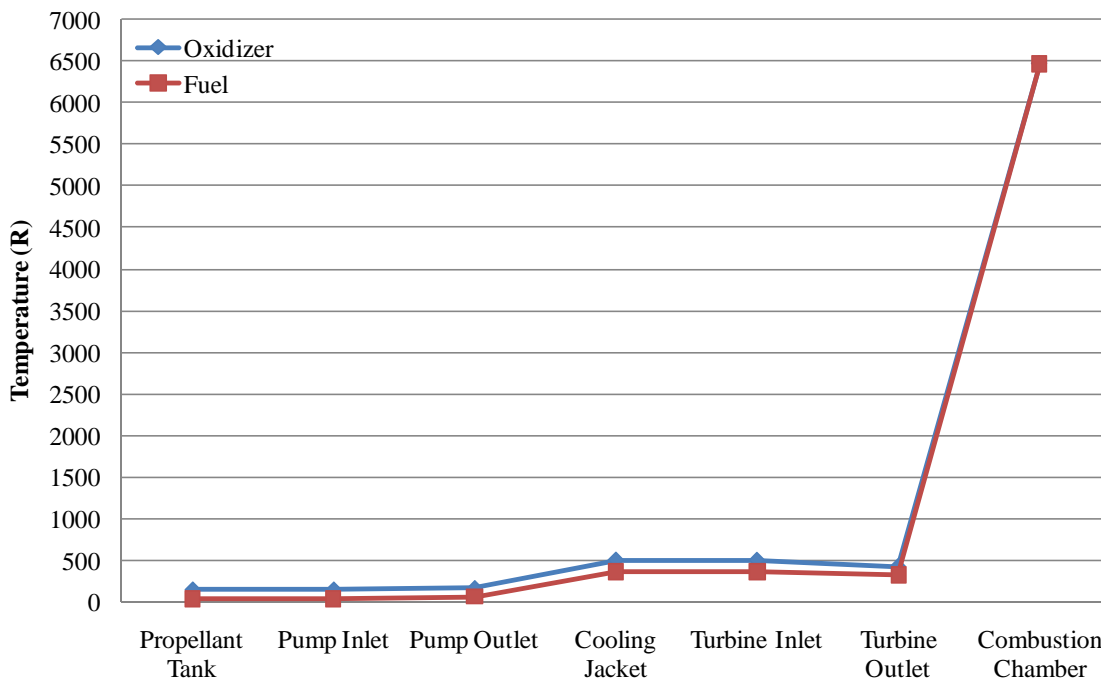
**Table 27. Engine Component Mass**

<b>Engine Component</b>	<b>Mass</b>
Chamber	39.1 lb (17.7 kg)
Aerospike	79.4 lb (36.0 kg)
Plumbing	4.3 lb (1.95 kg)
Turbopumps	213.1 lb (96.7 kg)
Hardware	16.8 lb (7.6 kg)
<b>TOTAL ENGINE MASS</b>	<b>352.7 lb (160.0 kg)</b>

Figure 64 plots the final DEAN design fluid pressure and fluid temperature profiles through the engine. The pressure profile clearly shows the initial propellant tank pressure is low, the pump increases the pressure and then designed pressure drops through the cooling jacket, turbine, and injectors occur until both the oxidizer and fuel have the same combustion chamber pressure. The temperature profile shows minor fluid temperature increase until the fluid enters the cooling jacket. Temperature increases in the cooling jacket due to the heat transfer between the combusted gases and coolant. Upon exiting the cooling jacket, the fluid loses some temperature before drastically increasing to the combustion temperature. Based on the pressure and temperatures, the oxygen becomes supercritical at cooling jacket station 4 and remains supercritical to the injectors. The hydrogen becomes supercritical at the second pump outlet and remains supercritical to the injectors.



a) Engine Pressure Profile



b) Engine Temperature Profile

Figure 64. Final DEAN Design Fluid Profiles

The cooling jacket is an integral portion of the chamber and aerospike. Figure 65 plots the hot and cold wall temperature profiles for both the chamber and aerospike. The

hot wall corresponds to the cooling jacket wall exposed to the combusted products. The cold wall corresponds to the cooling jacket wall exposed to the coolant. Stations 7 and 8 correspond to the two aerospike nozzle stations. In the cooling jackets, the coolant flows from the pump to the last cooling jacket station and then back towards the injector. Station 1 states “to injectors,” meaning the fluid after station 1 will exit the cooling jacket at the injector face, travel to the turbine, and then to the injectors for injection into the combustion chamber.

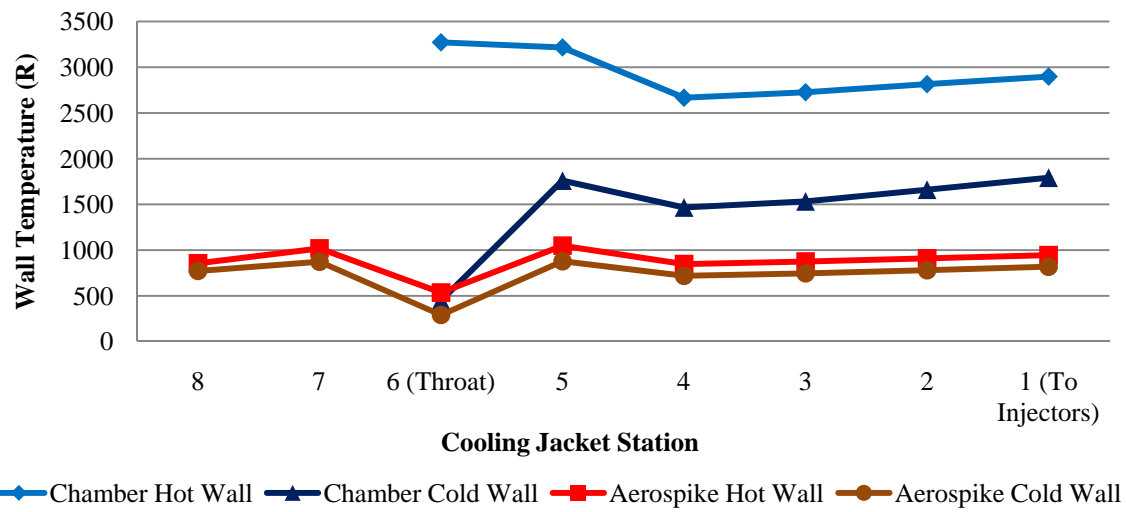


**Figure 65. Chamber and Aerospike Hot and Cold Wall Temperature Profile**

The difference between the aerospike hot and cold wall is negligible due to the high thermal conductivity of oxygen-free copper. In contrast, the chamber hot and cold wall difference is quite large. The chamber is made of silicon carbide with high thermal conductivity at low temperatures and very low thermal conductivity at higher temperatures. With increased wall temperatures on the chamber, the thermal conductivity is low, leading to a large difference between the chamber hot and cold wall temperatures.

Figure 66 plots the fluid Mach numbers in the cooling channels. Maximum Mach number is expected at Station 1, the last cooling jacket station before the fluid enters the turbine. A minimum is observed at the last cooling jacket station. As the fluid travels from the last cooling jacket station towards the first cooling station, the fluid gains velocity through heat transfer along the cooling jacket wall accounting for the increased Mach number. The maximum fluid temperatures, Table 21, are below the Mach polynomial limits; therefore, the Mach numbers are trustworthy.

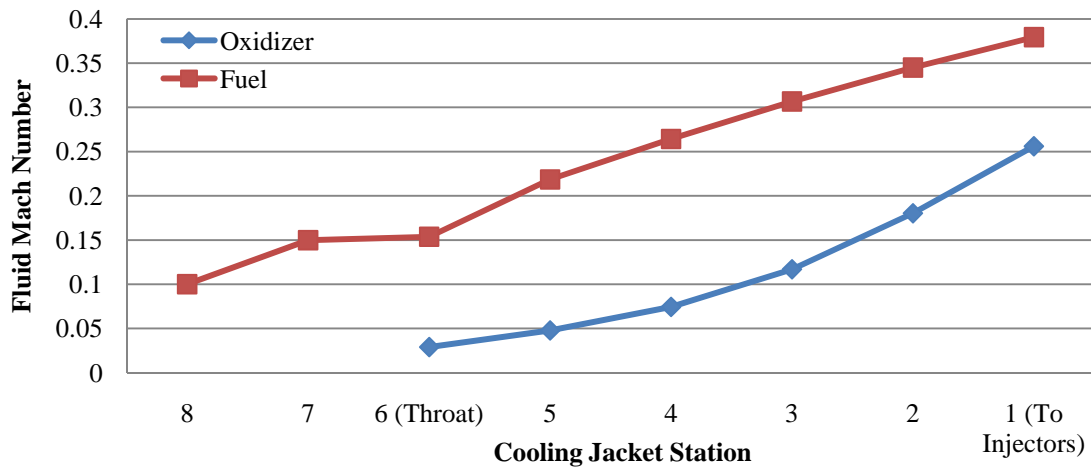


**Figure 66. Cooling Jacket Fluid Mach Number**

Table 28 tabulates the individual thrust components. The aerospike nozzle exit pressure is equal to 97.7 psia (0.7 MPa) relating to a design altitude of approximately 220 feet (67 m) under ocean water. Due to the small radial geometry of the final DEAN design, the exit pressure is much higher than sea level ambient pressure. The high exit pressure leads to a high  $F_{nondesign}$  value for DEAN operation in vacuum conditions. The total percent boundary layers loss on the aerospike nozzle is 4.4% included in the nozzle pressure thrust value. There are no other performance losses accounted for.

**Table 28. Individual Thrust Components**

Thrust Component	Thrust
Aerospike Nozzle Pressure Thrust	8,216 lb <sub>f</sub> (36.5 kN)
Momentum Thrust	34,314 lb <sub>f</sub> (152.6 kN)
Thrust due to Operation at Altitude other than Design Altitude ( $F_{nondesign}$ )	7,677 lb <sub>f</sub> (34.1 kN)
Chamber Exit Lip Pressure Thrust	-46 lb <sub>f</sub> (-0.2 kN)
Total DEAN Vacuum Thrust	50,161 lb <sub>f</sub> (223.1 kN)

The difference is engine mass flow rate between the TDK calculated value and the user design variable is -4.4 lb<sub>m</sub>/s (-2.0 kg/s). The lower TDK engine mass flow leads to a lower nozzle exit pressure, leading to a lower value for  $F_{nondesign}$ . The calculated performance is underestimated, but by how much? Varying the Mach number used to correct the throat pressure that equates to a choked throat, the mass flow difference can be minimized. Getting the mass flow rate difference to within 0.17%, the resulting nozzle exit pressure is 101.4 psia (0.7 MPa). The difference between the larger and smaller engine mass flow difference is an exit pressure of 3.7 psia (0.026 MPa). The difference in exit pressure equates to underestimation of the final DEAN performance values by 291 lb<sub>f</sub> (1.29 kN) or 0.58% and 2.5 seconds or 0.58% for vacuum thrust and vacuum specific impulse, respectively. This little correction factor would need to be performed for each DEAN design and would add complexity to the model. Therefore, the current correction factor process used to link NPSS and TDK together, is valid providing a good performance estimate, although it slightly underestimates performance.

Table 29 compares the final DEAN design to a conventional bell nozzle with equivalent expansion ratio. The bell nozzle performance does not include any performance losses. With DEAN operation above its design altitude, the aerospike

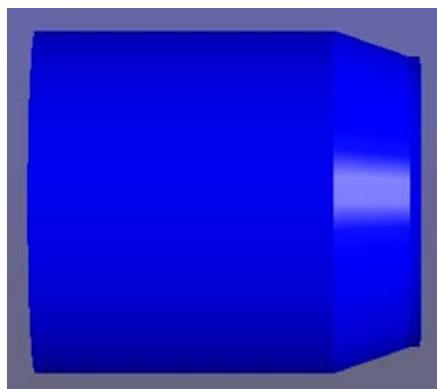
behaves more like a conventional bell nozzle; with the percent difference around +10%, there is similarity between the two engine designs.

**Table 29. Aerospike and Bell Nozzle Comparison**

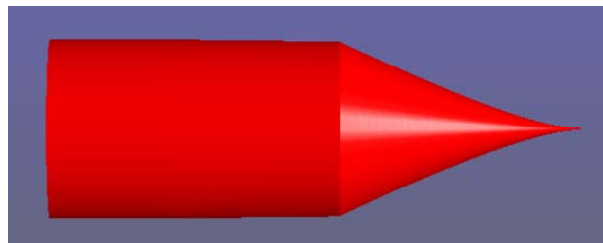
	Aerospike	Bell	Percent Difference
<b>Vacuum Thrust</b>	50,161 lbf (223.1 kN)	45,652 lbf (203.1 kN)	9.88%
<b>Vacuum Specific Impulse (sec)</b>	430.6	391.9	9.87%

Figure 67 shows the rendered chamber, aerospike, and final DEAN engine designs. In Figure 67b, due to the chosen aerospike radius design variable, the aerospike portion internal to the chamber is almost linear in nature with a slightly negative slope to the throat. From the orthogonal views, the total thickness of the chamber and aerospike is visible. The total engine length from the injector face to the end of the aerospike tip is 26.7 inches (67.8 cm) with a maximum diameter at the injector face of 12 inches (30.5 cm). The ModelCenter model contains the axial and radial arrays used to render the geometry.

Other outputs of interest depend on the engine designer. Actual dimensions of every engine component are also available including, but not limited to, cooling channels, cooling jackets, structural jackets, and plumbing. More thermo chemistry outputs from NPSS are available if needed. If NPSS converges for specific design variables, reliable system-level estimates for engine performance, weight, and geometry parameters can be obtained from the ModelCenter DEAN model.



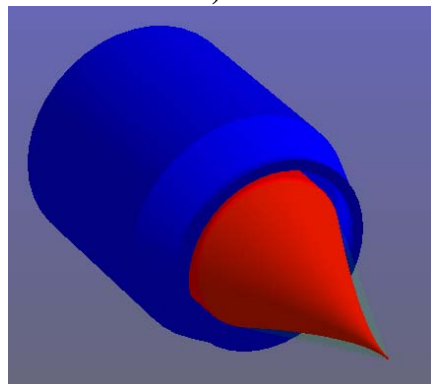
a) Chamber



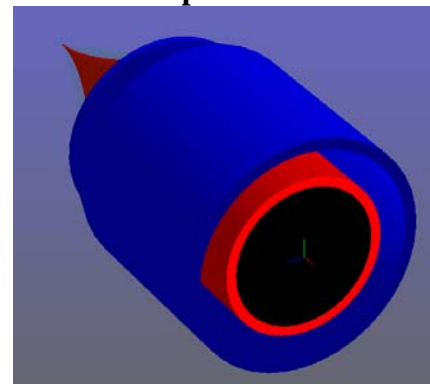
b) Aerospike



c) Bored Hole in Center of Aerospike



d) Orthogonal Front View



e) Orthogonal Back View

Figure 67. Rendered Final DEAN Geometry

## V. Conclusions and Recommendations

Chapter V discusses the conclusions of the current research effort, along with the significance of the research, followed by recommendations for future work.

### V.1 Research Conclusions

The use of high-fidelity rocket engine design programs, such as NPSS and TDK'04, combined with the integration of ModelCenter led to the creation of a system level DEAN model that could reliably estimate engine performance, weight, and geometry. Previous DEAN research at AFIT provided a good foundation for the current research effort.

Various variable sensitivity analyses and trade studies in Appendix C and D showed the final ModelCenter model to be more complex computationally than need be. The linear NPSS model alone could provide a reliable rough estimate of DEAN performance (reference Appendix C.5). Even though the linear NPSS model calculates performance using bell nozzle relationships, the calculated performance value will be anywhere from -5% to +10% off from actual aerospike calculations based on geometry inputs. Assuming a 5% performance loss for improved accuracy, the linear NPSS model could provide a quick snapshot of the DEAN solution space through ModelCenter DOEs. Moreover, the linear DEAN model used for the 2011 AIAA Aerospace Sciences Meeting [7] would not only provide a rough estimate for performance but also a rough estimate for engine weight and  $T/W$ . One iteration of the linear DEAN model is only a fraction of the computational load of the final nonlinear ModelCenter model. A large ModelCenter DOE of the design variables using the linear DEAN model would lead to reasonable

performance and weight estimates much faster. Once potential designs are found, the designs can be evaluated in the nonlinear ModelCenter model for improved accuracy in estimating engine performance and weight.

The nonlinear DEAN model (final ModelCenter model) can also be simplified. When convergence occurs, the linear NPSS model will provide accurate thermo chemistry outputs for the DEAN. In addition, only one execution of TDK'04 with boundary layer approximations is required to provide a realistic method of characteristics aerospike nozzle contour with a useable nozzle pressure profile for estimating performance. Moreover, the cooling jacket structural analysis can be simplified from using curved beam theory to simple beam theory with an insignificant difference in results. The computation time for the nonlinear model can drastically be reduced with these small changes without affecting output accuracy.

The conclusion from the DEAN model is linear approximations provide reasonable estimates for performance and weight estimates when the expansion ratio as a function of radial chamber geometry is used.

There is an unknown coupled relationship between the NPSS inputs and the ModelCenter design variables. Educated guesses to the coupled relationship were made to find a variety of potential design points; however, not knowing the coupled relationship limited the search for the optimal DEAN geometry. The optimal design is an engine meeting the performance and *T/W* design goals without violating physical constraints for reusability.

The final DEAN design meets the vacuum thrust and *T/W* design goals without violating the physical constraints for reusability. Unfortunately, the final design fails to

meet the vacuum specific impulse design goal. Higher vacuum specific impulse designs are possible but undesirable due to higher wall temperatures and lower  $T/W$  values.

The research effort was able to meet the research objectives. The final DEAN ModelCenter model is the tool to optimize weight of the DEAN engine and its components and allow exploration of the solution space. Through literature review and various variable sensitivity and trade studies, critical technologies/limits were recognized for the DEAN model.

Some, but not all, of the IHPRPT Phase III goals were met; the ‘improve specific impulse’ IHPRPT goal was not met. The 50,000 lb<sub>f</sub> (222.4 kN) vacuum thrust design goal was set based on the decision to approximately double current operational upper stage engine performance (reference Table 1). Although a thrust requirement is not directly called out by the IHPRPT Phase III goals, the thought was doubling thrust and maintaining engine weight would indirectly meet the IHPRPT  $T/W$  goal. Since lower engine weight is possible using lightweight materials, the vacuum thrust design goal can be removed for future DEAN research. A new design focus solely on meeting the vacuum specific impulse design goal may lead to improved calculated vacuum specific impulse for the DEAN design, especially since the engine mass flow rate can be decreased. The vacuum thrust design goal could be set to the average thrust value of current operational upper stage engines. Bear in mind a DEAN design meeting the vacuum specific impulse design goal may lead to a design not meeting the  $T/W$  design goal.

## V.2 Research Significance

The current research effort developed a reliable system level modeling tool to estimate performance, engine weight, and geometry for the DEAN concept. The tool contains capability for evaluating the solution space and performing optimization studies. From the tool, a new DEAN design point was found. Although the design point falls short of the vacuum specific impulse design goal by 7.3%, the design far surpasses the average of current operational upper stage engines in vacuum thrust and  $T/W$ . The new DEAN design provides a 138% increase in vacuum thrust and a 195% increase in  $T/W$ . Common metals, alloys, and ceramics compatible with the propellants were used to improve near-term manufacturability of the DEAN, while meeting reusability constraints.

Furthermore, the new DEAN design is only 27 inches (68.6 cm) long, far shorter than any current operational upper stage engine. The shorter DEAN engine provides an indirect benefit to a shorter interstage for the launch vehicle. The shorter interstage combined with the lighter DEAN engine equates to less total launch vehicle mass. The subtraction of mass could be used for improved overall vehicle performance leading to cost savings. More realistically, the mass savings would be used for more fuel or, more importantly, for more payload mass increasing spacecraft capability.

## V.3 Recommendations for Future Research

### *V.3.a. Recommended Changes to DEAN Model*

First and foremost, more detailed verification and validation studies of the DEAN model are required.

Next, the coupled relationship between the design variables and NPSS inputs needs to be uncovered. Uncovering the coupled relationship would open the door to more comprehensive optimization studies to find an engine meeting the design goals without violating physical or reusability constraints.

Recommend simplifying the final DEAN model by executing only one linear NPSS model and one TDK PFG model with boundary layer. The results will be acceptable as shown from the sensitivity analyses in the current research effort.

A recommended test to see if the NPSS model becomes less brittle is to add a fuel bypass in the same location as the oxidizer bypass. The oxidizer bypass serves to balance the expander cycle; the same may be true on the fuel side. Martin originally had a fuel bypass located at the first pump outlet [4]. The pump bypass location had unwanted consequences as discussed by Simmons [5, 6]. A fuel bypass at the turbine may release new designs in the DEAN solution space.

The NPSS input pump and turbine efficiencies and turbopump shaft rotation speeds used in the DEAN model were assumed and were based on research at a specific design point from Martin [4]. The assumed turbopump inputs need to be parametric to model the turbopumps accurately at other than the design point used by Martin. Recommend integrating the “Potential\_Future\_Code” discussed in Section III.4.c into the DEAN model.

NPSS calculates the convection heat transfer coefficients for the hot exhaust gases and coolants assuming the cooling jacket wall temperatures on the hot side are the same on the cold side. The assumption is valid for materials with high thermal conductivity (i.e. copper). Recommend creating a table of the material properties as a function of

temperature (i.e. thermal conductivity, density, and material heat capacity at constant pressure) for use in NPSS; NPSS refers to the table as a “socket”. The use of the socket in the NPSS *Wall2* element will improve the accuracy of the calculated convection heat transfer coefficients for low thermal conductivity materials.

The NPSS model utilizes the *RocketComb1* element to model the combustion chamber. The element does not include the capability to evaluate combustion efficiency. An option for the future is to use the *ThrustChamber* NPSS element which calculates combustion using a user input efficiency value ( $\eta_{c*}$ ).

Recent efforts found CEA is not required for the TDK PFG model. CEA was originally used to test TDK outside the DEAN model. Since the NPSS model performs all necessary chemistry calculations such as the ratio of specific heats ( $\gamma$ ) and molecular weight, the NPSS outputs can be used as inputs into TDK. The pressure and temperature at the throat can be calculated from isentropic relationships and the speed of sound at the throat can be calculated. The change would improve the accuracy of the TDK inputs and may lead to better convergence between the TDK calculated mass flow rate and the user input mass flow rate. With the current use of CEA in the final DEAN model, the NPSS and CEA  $\gamma$  values are slightly different.

Research showed limitations in the Mach number polynomials. Future research should first find the maximum physical fluid temperature limits to the propellants to avoid spontaneous ignition in the engine plumbing. Second, the Mach polynomials need to be updated to meet those temperature limits.

The assumed variable length of the combustion chamber exit lip extending from the throat (reference Appendix C.1 and D.1) may result in higher than realistic

convection heat transfer coefficients in NPSS. At large chamber radii, the surface area of the NPSS throat station will be large influencing the value of the convection heat transfer coefficient. The chamber exit lip is required to straighten the flow out the throat to maximize thrust. In addition, a chamber exit lip with finite length is required for TDK and NPSS to execute. Future research should investigate making the chamber exit lip a constant length, regardless of chamber radius, and evaluate the effect on the convection heat transfer coefficient, coolant propellant temperature, and maximum wall temperature.

The results of trade and optimization studies of the final DEAN model showed the best specific impulse occurred for long chamber lengths, large chamber radii, and aerospike radii close to the chamber radii. The consequence was high wall temperatures. Two options to improve DEAN design with higher vacuum specific impulse while meeting physical constraints are as follows: first, add more materials to the model including some exotics; second, perform a model design variable change. The addition of materials is the easiest solution. Materials with high melting point and high strength at high temperatures are required. Furthermore, the thermal conductivity must be low enough to keep the maximum coolant temperature below fluid temperature limits, but high enough to keep the cooling jacket walls within thermal limits and limit thermal stress. Another way to decrease heat transfer to the coolant is to increase cooling jacket wall thickness; however, increased wall thickness results in higher wall temperatures. The second and preferred option is a model design variable change. The recommended change is to remove the chamber length design variable and add a new design variable in its place. The chamber length design variable has a large influence over the calculated throat area and corresponding performance. The influence has drastic consequences on

$T/W$  and chamber and aerospike cooling jacket wall temperatures. The linkage of chamber length to throat area is not necessary. Chamber length should be a model output instead of an input.

There are multiple ways to eliminate or work around the chamber length variable to gain more user control over the throat area. The first option is to use the  $O_2/H_2$  characteristic length as an input. The characteristic length can be used to calculate a chamber volume based on a guessed throat area. Another separate chamber volume calculation can be performed with a guessed chamber length. Using a ModelCenter optimizer, such as the gradient optimization tool, the chamber length can be varied until the calculated chamber volume equals the characteristic chamber length volume. As NPSS converges throat area, chamber length will change as an output instead of an input. Although the characteristic length is a guideline for engine design, for the system level model, it is acceptable to set the characteristic length and keep it constant. The second option is to create a new design variable that is the difference between the chamber and aerospike radii at the throat. This new design variable causes a major architecture change to the model. Instead of calculating chamber and aerospike geometry from the injector face to the throat, the model will calculate chamber and aerospike geometry in reverse from the throat to the injector face. The chamber and aerospike radii at the injector face design variables are no longer required; however, two new design variables are needed for the chamber and internal aerospike slopes. As NPSS converges throat area, the throat distance variable will be constant, causing the chamber and aerospike throat radii to change for each iteration. The user has indirect control over the throat area using the throat distance variable. The downside to the option is chamber length still needs to be

input. The best option is the combination of the two options making chamber length an output with two new design variables: characteristic length and the difference in throat radii. This best option leads to the smallest combustion chamber design possible without negatively influencing combustion. Also, the user has more control over throat area to improve the performance of the engine through increased expansion ratio. Lastly, the best option allows for improved performance without increased chamber length improving future DEAN *T/W* optimization studies. Be aware pursuing this best option may raise unknown issues with NPSS convergence.

The interaction of the exhaust flow with the ambient conditions is unknown resulting in an underestimated calculation of vacuum performance. Future research should create a computational fluid dynamics model to improve the quality of the performance estimation and better understand the engine exhaust flow field at other than design altitudes.

The final DEAN model is a ModelCenter data model and the execution sequence of the model depends on what variables need to be calculated and input in other model components. To improve the DEAN model, a ModelCenter process model should be utilized. With the process model, the user has the ability to control and track the execution sequence of the model; especially important for loops in the model.

Wolverine Ventures, Inc. released NPSS version 2.2.1 on 31 January 2011. The new release includes more functionality; however, the element names are different. If the new NPSS version were utilized, the NPSS DEAN model would need to be completely revamped. Although revamping the NPSS DEAN model will be challenging, it is highly recommended. The current NPSS model is very brittle and if the coupled relationship

between the variables cannot be uncovered, creating a new model in the more functional NPSS version may be an answer.

### ***V.3.b. Recommended Research Objectives***

The performance and weight saving advantages of the aerospike nozzle support continued research. Furthermore, the DEAN concept is a viable alternative to current operational upper stage engines. Continued research should first improve the system level model and then find an optimal engine design meeting the design goals without violating physical constraints. With an optimized system-level design, individual detailed component-level design and design optimization should occur. Strain and Arguello [40, 41] have already completed the component-level oxidizer and hydrogen turbopump designs. Their design processes can be reaccomplished for the new optimum engine. Furthermore, research into engine startup, throttability, and controllability (including thrust vectoring) needs to be accomplished. With complete detailed and optimized component designs, prototype development and testing can occur.

Other design options for the DEAN concept include alternative propellants, such as methane/oxygen, or modification of the chamber and aerospike from a basic cylinder shape to a concave shape. With the concave chamber and aerospike, the plumbing and turbopumps could be placed inside the concave aerospike shape. Furthermore, the chamber length could be decreased improving engine  $T/W$ .

Once the DEAN engine and its components are completely designed, a complete stage design should be performed. The stage design includes design of the propellant

tanks and plumbing, along with engine and launch vehicle attachment hardware. A detailed mission is required to accurately calculate the amount of propellant needed.

Lastly, recommend modifying the DEAN concept to use a full flow (boost) cycle instead of the expander cycle. The modification would change the mission of the DEAN from upper stage (orbit transfer) to boost, fully exploiting the altitude compensation capability of the aerospike nozzle.

#### **V.4 Research Summary**

In conclusion, with a solid foundation from past AFIT DEAN research, the current research effort was able to create a reliable computational tool to estimate the performance, weight, and geometry of the DEAN engine. From the tool, optimization and trade studies were performed to better understand the solution space. Furthermore, literature review and trade studies showed the existence of both model and physical limitations. A new DEAN design point was found meeting the vacuum thrust and thrust-to-weight ratio design goals without violating physical and reusability constraints. The pathway is set for further research to find the optimum DEAN design point meeting all the design goals including vacuum specific impulse.

## Appendix A: Lessons Learned

Several lessons were learned from the current research effort. First, resources are available for NPSS. The NPSS user guide is helpful, along with the individual element source codes. The NPSS Consortium recently started a website at [www.npssconsortium.org](http://www.npssconsortium.org). The website has technical tips along with forums for users to ask questions. The sole distributor of NPSS is Wolverine Ventures, Inc (web address is [www.wolverine-ventures.com](http://www.wolverine-ventures.com)). Wolverine Ventures is a good starting point for NPSS specific questions, including obtaining the most recent software release.

Second, in some instances the TDK PFG with boundary layer model will output values from the master document instead of the using the current document made in the temporary folder. When this occurs, the DEAN model will calculate an unreasonably high thrust and specific impulse value. To fix the issue, invalidate all the model variables by changing a design variable. Change the design variable back to the desired value and rerun the model. The model should use the correct values from the TDK temporary file.

For every execution of TDK, ModelCenter will create a new temporary folder. The temporary folders allow ModelCenter to read the numerous output files for a specific design. The temporary folders take up a lot of hard drive space. For example, 100 temporary folders equal 334 megabytes. With the current DEAN model, TDK will execute up to 11 times, creating 11 temporary folders. When trade or optimization studies occur, the folders add up very quickly. It is recommended to delete the temporary files immediately in the C:/DEAN/TKDEAN directory after running a trade or optimization study and when ModelCenter is exited out.

## Appendix B: Material Properties

Appendix B contains the material properties in the units used by the DEAN model. Equivalent SI units have been added. Some properties obtained from the references were converted.

### B.1. Material Selection

Material	Reference*
Pure Copper (Annealed)	Reference 55, 61
Silicon Carbide (Highly-Pure)	Reference 33, 56
INCOLOY® 909 (Age Hardened)	Reference 57
HAYNES® 188 alloy (Bright Annealed)	Reference 60
Beryllium Copper (C17000 TH04)	Reference 61
Oxygen-Free Copper (C10100 1180 Temper)	Reference 61
Cobalt (Forged Electrolytic)	Reference 55
INCONEL® 718 (Annealed & Aged)	Reference 58
INCONEL® 625 (Annealed)	Reference 59
Aluminum 7075 T6	Reference 61
Aluminum 2024 T6	Reference 61
Titanium (ASTM Grade 3, 99.1% Ti)	Reference 55, 61, 62
Pure Niobium	Reference 55, 61

\*Material Properties from stated reference(s)

### B.2. Material Density

Material	Density (lb <sub>m</sub> /in <sup>3</sup> )	Density (kg/m <sup>3</sup> )
Pure Copper	0.3237	8960
Silicon Carbide	0.1142	3161
INCOLOY 909	0.296	8193
INCONEL 625	0.305	8442
INCONEL 718	0.297	8221
Haynes 188	0.324	8968
Aluminum 7075 T6	0.101	2796
Aluminum 2024 T6	0.100	2768
Beryllium Copper	0.298	8249
Oxygen-Free Copper	0.323	8941
Pure Titanium	0.1629	4509
Pure Niobium	0.3107	8600
Pure Cobalt	0.3197	8849

### B.3. Material Melting Point

Material	Melting Point (R)	Melting Point (K)
Pure Copper	2442.87	1357
Silicon Carbide	5580.00	3100
INCOLOY 909	3002.67	1668
INCONEL 625	2813.67	1563
INCONEL 718	2759.67	1533
Haynes 188	2858.67	1588
Aluminum 7075 T6	1450.67	806
Aluminum 2024 T6	1395.67	775
Beryllium Copper	2050.67	1139
Oxygen-Free Copper	2441.67	1356
Pure Titanium	3492.27	1940
Pure Niobium	4932.27	2740
Pure Cobalt	3182.67	1768

### B.4. Material Thermal Conductivity

Wall Temperature (R)	Wall Temperature (K)	$k$ (BTU/in-R-s)	$k$ (W/m-K)
<b>Pure Copper</b>			
180	100	0.00646	483
360	200	0.00552	413
540	300	0.00532	398
720	400	0.00524	392
1080	600	0.00512	383
1440	800	0.00496	371
1800	1000	0.00478	357
2160	1200	0.00457	342
2520	1400	0.00223	167
2880	1600	0.00233	174

Wall Temperature (R)	Wall Temperature (K)	<i>k</i> (BTU/in-R-s)	<i>k</i> (W/m-K)
<b>Silicon Carbide</b>			
540	300	0.00655	490
1800	1000	0.00116	87
2160	1200	0.00078	58
2700	1500	0.00040	30

<b>INCOLOY 909</b>			
513.47	285	0.00020	14.8
593.47	330	0.00022	16.3
693.47	385	0.00024	17.8
793.47	441	0.00025	18.9
893.47	496	0.00027	19.8
993.47	552	0.00028	20.8
1093.47	607	0.00029	21.8
1193.47	663	0.00030	22.5
1293.47	719	0.00031	23.3

<b>INCONEL 625</b>			
530.67	295	0.00013	9.7
560.67	311	0.00014	10.5
660.67	367	0.00015	11.2
860.67	478	0.00017	12.7
1060.67	589	0.00019	14.2
1260.67	700	0.00021	15.7
1460.67	811	0.00023	17.2
1660.67	923	0.00026	19.4
1860.67	1034	0.00028	20.9
2060.67	1145	0.00031	23.2
2260.67	1256	0.00034	25.4

Wall Temperature (R)	Wall Temperature (K)	<i>k</i> (BTU/in-R-s)	<i>k</i> (W/m-K)
<b>INCONEL 718</b>			
530.67	295	0.00015	11.2
660.67	367	0.00017	12.7
860.67	478	0.00019	14.2
1060.67	589	0.00022	16.4
1260.67	700	0.00024	17.9
1460.67	811	0.00026	19.4
1660.67	923	0.00029	21.7
1860.67	1034	0.00031	23.2
2060.67	1145	0.00033	24.7
2460.67	1367	0.00038	28.4

<b>Haynes 188</b>			
1260.67	700	0.00024	17.9
1460.67	811	0.00027	20.2
1660.67	923	0.00029	21.7
1860.67	1034	0.00032	23.9
2060.67	1145	0.00034	25.4
2260.67	1256	0.00037	27.7

<b>Aluminum 7075 T6</b>			
536.67	298	0.00174	130

<b>Aluminum 2024 T6</b>			
536.67	298	0.00202	151

<b>Beryllium Copper</b>			
527.67	293	0.00158	118
851.67	473	0.00194	145

<b>Oxygen-Free Copper</b>			
527.67	293	0.00523	391

Wall Temperature (R)	Wall Temperature (K)	<i>k</i> (BTU/in-R-s)	<i>k</i> (W/m-K)
<b>Pure Titanium</b>			
540	300	0.00022	16.5
720	400	0.00019	14.5
900	500	0.00018	13.5
1080	600	0.00017	13.0
1260	700	0.00018	13.7
1440	800	0.00019	14.5
1620	900	0.00021	15.5
1800	1000	0.00021	16.0
2160	1200	0.00022	16.7
2520	1400	0.00023	17.1

<b>Pure Niobium</b>			
491.67	273	0.00070	52.3
671.67	373	0.00073	54.4
851.67	473	0.00076	56.5
1031.67	573	0.00078	58.6
1211.67	673	0.00081	60.7
1391.67	773	0.00085	63.2
1571.67	873	0.00087	65.3

<b>Pure Cobalt</b>			
540	300	0.00116	87.0
720	400	0.00106	79.0
900	500	0.00094	70.0
1080	600	0.00084	63.0
1260	700	0.00075	56.0
1440	800	0.00075	56.0
1620	900	0.00071	53.0
1800	1000	0.00068	51.0
2160	1200	0.00066	49.0
2520	1400	0.00056	42.0
2880	1600	0.00062	46.0

### B.5. Material Ultimate Tensile and Yield Strength

Wall Temperature (R)	Wall Temperature (K)	Ultimate Tensile Strength ( $10^3$ psi)	Ultimate Tensile Strength (MPa)	Yield Strength ( $10^3$ psi)	Yield Strength (MPa)
<b>Pure Copper</b>					
529.47	294	31.4	220	8.7	60
781.47	434	26.3	184	6.5	45
1033.47	574	18.8	132	5	34
1231.47	684	12.1	85	3.5	24
1492.47	829	6.9	48.5	3	21
1663.47	924	4.3	33	2.8	19
1915.47	1064	2.7	19	2.7	19
2239.47	1244	1.1	8	1.1	8
<b>Silicon Carbide</b>					
540	300	80	552	80	552
1080	600	75	517	75	517
<b>INCOLOY 909</b>					
660.67	367	185	1276	148	1020
860.67	478	178	178	144	144
1060.67	589	175	175	141	141
1260.67	700	173	173	139	139
1460.67	811	168	168	137	137
1660.67	923	148	148	125	125
1860.67	1034	88	88	78	78
<b>INCONEL 625</b>					
530.67	295	140	965	69.5	479
1660.67	923	146.5	146.5	106.5	106.5
1860.67	1034	84.8	84.8	79	79
2060.67	1145	41.2	41.2	40	40

Wall Temperature (R)	Wall Temperature (K)	Ultimate Tensile Strength ( $10^3$ psi)	Ultimate Tensile Strength (MPa)	Yield Strength ( $10^3$ psi)	Yield Strength (MPa)
<b>INCONEL 718</b>					
530.67	295	198	1365	163	1124
1060.67	589	183.5	1265	156	1076
1460.67	811	173	1193	148	1020
1660.67	923	160	1103	140	965
1760.67	978	146	1007	135	931
1860.67	1034	123.5	852	116	800
1960.67	1089	105	724	100	689

<b>Haynes 188</b>					
530.67	295	137.2	946	67.3	464
1460.67	811	108.5	748	42	290
1660.67	923	103.3	712	39.7	274
1860.67	1034	89.9	620	38.9	268
2060.67	1145	60	414	35.9	248
2260.67	1256	35.2	243	19	131
2460.67	1367	18.7	129	9.3	64

<b>Aluminum 7075 T6</b>					
140.67	78	102	703	92	634
348.67	194	90	621	79	545
442.67	246	86	593	75	517
535.67	298	83	572	73	503
672.67	374	70	483	65	448
760.67	423	31	214	27	186
860.67	478	16	110	13	90
960.67	534	11	76	9	62
1060.67	589	8	55	6.5	45
1160.67	645	6	41	4.6	32

Wall Temperature (R)	Wall Temperature (K)	Ultimate Tensile Strength ( $10^3$ psi)	Ultimate Tensile Strength (MPa)	Yield Strength ( $10^3$ psi)	Yield Strength (MPa)
<b>Aluminum 2024 T6</b>					
140.67	78	84	579	68	469
348.67	194	72	496	59	407
442.67	246	70	483	58	400
535.67	298	69	476	57	393
672.67	374	65	448	54	372
760.67	423	45	310	36	248
860.67	478	26	179	19	131
960.67	534	11	76	9	62
1060.67	589	7.5	52	6	41
1160.67	645	5	34	4	28
<b>Beryllium Copper</b>					
527.67	293	180	1245	155	1070
<b>Oxygen-Free Copper</b>					
671.67	373	57.3	395	56.6	390
851.67	473	47.9	330	46.4	320
1031.67	573	37.7	260	36.3	250
1211.67	673	21.8	150	17.4	120
1391.67	773	10.2	70	10.9	20
1571.67	873	5.1	35	1.5	10
1751.67	973	2.9	20	0.29	2
1931.67	1073	1.5	10	0.15	1
<b>Pure Titanium</b>					
671.67	373	62.27	429	55.11	380
851.67	473	49.31	340	39.16	270
1031.67	573	39.16	270	29.01	200
1211.67	673	31.91	220	21.76	150
1391.67	773	26.11	180	15.95	110
1571.67	873	20.31	140	10.15	70

Wall Temperature (R)	Wall Temperature (K)	Ultimate Tensile Strength ( $10^3$ psi)	Ultimate Tensile Strength (MPa)	Yield Strength ( $10^3$ psi)	Yield Strength (MPa)
<b>Pure Niobium</b>					
527.67	293	50.33	347	42.21	291
851.67	473	54.39	375	35.24	243
1031.67	573	45.54	314	29.88	206
1211.67	673	49.75	343	32.49	224
1391.37	773	45.54	314	28.57	197
1571.67	873	47.28	326	18.13	125
1679.67	933	47.28	326	16.1	111
1931.67	1073	45.83	316	14.94	103
2237.67	1243	27.99	193	11.89	82
2381.67	1323	18.56	128	10.01	69

## Appendix C: NPSS Model

Appendix C serves to document the enhancements made to the NPSS DEAN model and the different analyses performed to create the linear and nonlinear NPSS models used in the final DEAN ModelCenter model.

### C.1. NPSS DEAN Model Enhancements

The architecture of the NPSS model for the current research effort is similar to Simmons' architecture [5]. The number of cooling jacket stations on the chamber and aerospike are the same, as are the NPSS elements making up the DEAN model. Furthermore, the NPSS model as enhanced by Simmons continues to iterate until the input guessed throat area and the output throat area converge [5, 6]. Differences include additional further parameterization of NPSS element inputs and the creation of a separate linear and nonlinear NPSS DEAN model.

Required NPSS input geometry values at the throat (Figure 19, station 6 on the chamber and aerospike), such as area of heat exchange and volume, were finite values. To parameterize these values, a finite throat length of 0.1 multiplied by the aerospike throat radius was assumed. The assumed length is required for other portions of the final ModelCenter DEAN model. Realistically, the throat station has no length; however, a length was required for NPSS to execute. The parametric equations used for the other stations now apply to the throat. For the *RocketComb1* element, the propellant area of heat exchange at station 6 for the chamber and aerospike is equal to the surface area of a cylinder. For the chamber and aerospike cooling jacket stations representing the throat

(station 6), both the volume of the flow and the area of heat exchange utilize the finite throat length.

The *CoolingVolume02* elements not corresponding to the cooling jackets, such as the cooling volumes included in the plumbing from the tank to the pump or from the turbine to the injectors, have flow cross-sectional area and volume inputs. The volume was originally hardcoded to 10 in<sup>3</sup> by Martin [4]. Performing a simple test and changing the volume to 0.1, 1, 100, 1000, 10000 in<sup>3</sup> (1 in<sup>3</sup> = 16.4 cm<sup>3</sup>) resulted in no change to the NPSS outputs; however, when the volume was set to zero, NPSS would fail to execute. The conclusion was the volume variable for *CoolingVolume02* elements not representing cooling jacket stations was required to execute but the value of the variable was trivial. The volume was edited to equal the physical cross-sectional area of the channel multiplied by an assumed length of one inch.

The physical cross-sectional area of the *CoolingVolume02* elements not corresponding to the cooling jackets was also tested. Previously hardcoded values were deleted and replaced by a new variable called *pipe\_area*. The variable assumes all cross-sectional pipe areas for *CoolingVolume02* elements not associated with the cooling jacket are one value. Changing the value of *pipe\_area* from a range of 1 to 10 in 0.5 in<sup>2</sup> (1 in<sup>2</sup> = 6.45 cm<sup>2</sup>) increments resulted in no changes to NPSS output chamber temperature, chamber pressure, and throat area. Chamber temperature, chamber pressure, and throat area directly influence the output thrust and specific impulse. A *pipe\_area* value of 100 and 1000 in<sup>2</sup> had the same results. The same conclusion as previously stated for volume can be made about the pipe cross-sectional area; NPSS requires a nonzero *pipe\_area*

value but the actual value is trivial. The *pipe\_area* value was set to 2.0 in<sup>2</sup> (12.9 cm<sup>2</sup>); however, the variable remains user configurable.

The physical reason the *CoolingVolume02* volume and area NPSS variables are trivial is because no heat loss (adiabatic) is assumed in those elements. The elements are not performing any heat transfer and, therefore, are not serving the primary purpose of the element. However, the elements are required to link plumbing elements (i.e. *Valve04*) to properly flow mass through the engine.

Further parameterization of the NPSS model occurred in the *Valve04* elements. The DEAN model utilizes the *Valve04* elements to represent pressure drops in engine plumbing/valves. There are five pipe elements built into NPSS. Martin chose to use *Valve04* elements in the DEAN model instead of the pipe elements since the pipe elements either are for water flow, require a user specified resistance value, calculate incompressible flow, and/or are unique for jet engine designs [4, 43, 44]. The *Valve04* element acts as a good connector between the *CoolingVolume02* elements while providing adequate pressure drop calculations. A user input for *Valve04* is a pressure loss coefficient, also known as the K-factor (K). Huzel and Huang state the pressure loss coefficient, K, “accounts for pressure losses in contractions, expansions, and bends in the flow path” [8]. A technical document by Crane Co. state it is impossible to obtain accurate pressure loss test data for every size and type of valve, pipe, and fitting; therefore, a pressure loss coefficient, also known as the resistance coefficient, is a way to extrapolate information from published test data [65]. The resistance coefficient is “considered as being independent of friction factor or Reynolds number, and may be

treated as a constant for any given obstruction in a piping system under all conditions of flow, including laminar flow" [65]. Equation 60 calculates the value of K [8].

$$K = \frac{2g_o \rho \Delta P}{12^2 w^2} A^2 \quad (60)$$

where

$K$	=	Pressure Loss Coefficient
$g_o$	=	Gravitational Constant (ft/s <sup>2</sup> )
$\rho$	=	Density (lb <sub>f</sub> /ft <sup>3</sup> )
$\Delta P$	=	Pressure Drop (psia)
$w$	=	Weight Flow Rate (lb <sub>f</sub> /s)
$A$	=	Flow Area Normal to Flow Direction (in <sup>2</sup> )

The density in equation 60 is in units of lb<sub>f</sub>/ft<sup>3</sup> instead of the typical unit of lb<sub>m</sub>/ft<sup>3</sup>.

The previously hardcoded K values are now parametric in the NPSS model. NPSS uses the K value to determine a pressure drop based on an output pressure guess, calculate a friction coefficient value, determine the weight flow rate, and then iterate the output pressure until the weight flow in equals the weight flow out. By using equation 60 in the NPSS model, new inputs to the NPSS model are required. An assumed pressure profile guess is required to start the NPSS iteration loop; the pressure profile guess leads to the  $\Delta P$  used in equation 60. The flow area is equal to the area from the previous *CoolingVolume02* elements that are linked to the *Valve04* elements. The density values are new model inputs, which are outputs from the original Martin/Simmons NPSS model [4-6]. The mass flow rate, from which weight flow can be calculated, is a model design variable (input). In the final ModelCenter DEAN model, NPSS executes three separate times in an attempt to converge the input density and pressure guesses for an accurate K

value. By parameterizing the K value, the pressure drop across the plumbing will be more accurate, especially when designs different from Martin’s original design point are explored.

A simple change to the original NPSS model was to rename a variable from *O\_split* to *Ox\_Bypass*. The *O\_split* variable was used to state how much of the oxidizer flow went to the turbine instead of the bypass. For example, if 0.9 were used, 90% of the oxidizer flow would go straight to the turbine, while 10% bypassed the turbine and went to the injectors. To clarify the purpose of the variable, the variable was renamed *Ox\_Bypass* and the value changed to declare what percentage of the oxidizer flow went through the bypass. Therefore, if the user set *Ox\_Bypass* to 0.1, 10% of the oxidizer flow would bypass the turbine. The name change avoids confusion.

The NPSS model is now fully parameterized and enhanced for the final DEAN ModelCenter model.

## C.2. NPSS Linear and Nonlinear Model

Two variations of the enhanced NPSS model were developed: a linear model and a nonlinear model. Both the linear and nonlinear code were assembled in one master NPSS DEAN model. The code excerpts pertaining to linear and nonlinear assumptions are distinguished by the non-active model being commented so that particular code will not execute. Both models execute in the final ModelCenter DEAN model and their applications in the final model are discussed in section III.4.

The nonlinear code uses actual method of characteristic aerospike geometry in its calculations. One of the required inputs to the NPSS model is the area of heat exchange

for the hot combusted gases at each station in the chamber and along the aerospike. For the aerospike nozzle, stations 7 and 8 shown in Figure 19, integration of the surface area due to the nonlinear geometry is required; equations 34 and 35. A ModelCenter script component was used to perform the integration and calculate other nonlinear NPSS model inputs; a similar script component was also used for the linear NPSS model to calculate specific inputs such as expansion ratio and chamber volume.

The linear approximation code was entered to verify the integration code using equations 34 and 35 was working correctly. The difference between the linear and nonlinear area of heat exchange was 0.56% at station 7 and 3.0% at station 8. The difference is reasonable since the center of station 7 and 8 is located a factor 1/8 and 3/8 the total spike length away from the throat and the linear geometry mostly mirrors the nonlinear geometry near the throat.

Inputs into both the nonlinear and linear model include: total engine mass flow rate, a guessed chamber pressure and temperature, an oxidizer-to-fuel ratio, a guessed throat area, expansion ratio, percent oxidizer bypass, guessed hot wall temperature for the chamber and aerospike, pipe area for non-cooling channel plumbing/valves, the aerospike and chamber radii at the injector face, chamber length, chamber volume, radius of the aerospike at the throat, ambient pressure, aerospike nozzle length, flow angle out the throat, axial and radii coordinates for the two aerospike nozzle stations, and the area of heat exchange for the two aerospike stations. Chamber volume calculations are similar for the linear and nonlinear model; both use linear approximation equations, detailed by Simmons [5, 6]. Other NPSS inputs include guessed enthalpy, pressure, and density values at certain *CoolingVolume02* element stations; these inputs are based on values

from outputs from Martin’s/Simmons’ NPSS DEAN model [4-6]. The propellant tank temperature and pressure are also required; currently these values are set to keep the propellants in the tank in liquid phase. Turbopump parameters are also input, such as pump and turbine efficiency, pump gear ratio, guessed pump pressure ratio, and guessed turbopump shaft rotational speed. Currently the original hardcoded values by Martin are used for turbopump inputs (Table 5) [4]. Lastly, the cooling jacket geometry is input. Inputs include the half-width of the cooling channel flow at the first fluid station, the half-width between cooling channels, and the cooling channel fluid flow aspect ratio.

An interesting variable in the NPSS code is the exhaust flow area along the aerospike nozzle at stations 7 and 8. The actual flow area is unknown and a complex computational model is required to evaluate the interaction of the exhaust flow with the freestream flow. However, the exhaust flow area is precisely known at the nozzle design altitude. At the nozzle design altitude, the flow will follow a parallel path to the centerline from the chamber exit lip to the nozzle exit plane. Above the design altitude, the flow will expand radially outward and vice versa for nozzle operation below the design altitude. Unfortunately, NPSS fails to converge using the design altitude flow area giving a “station is choked” error. Therefore, to close NPSS, the exhaust flow area along the nozzle is assumed underexpanded (outward radial expansion of the flow) by a guessed constant times the throat area; constant is two and four for stations 7 and 8, respectively.

### C.3. NPSS Variable Sensitivity Analyses

The linear NPSS model with the required input script was added to ModelCenter to enable parametric trade studies of input variables. The goal of the trade studies was to determine the sensitivity of select NPSS model inputs. The guessed chamber pressure, chamber temperature, chamber and aerospike wall temperatures, and the percent oxygen bypassing the turbine were tested. After testing the variables in the linear model, the same tests were performed in the nonlinear NPSS model to verify the conclusions in the linear model were the same for the nonlinear model. Table 13 tabulates the default design variables used for the trade studies.

Two trade studies were run to determine the sensitivity of the NPSS user-specified chamber pressure input. NPSS used the default design variables as inputs.

The first chamber pressure trade study evaluates the influence of converging and not converging the chamber pressure on selected NPSS outputs for an oxidizer-to-fuel ratio (*O/F*) range of 5.5 to 8.0 in 0.5 increments. To execute NPSS, a chamber pressure guess input is required. After NPSS execution, the calculated output chamber pressure may differ from the input guessed chamber pressure. The “not converged” test compares NPSS performance outputs without converging the input and output chamber pressure. To converge chamber pressure, a ModelCenter converger tool was added to the model. The converger began with the initial chamber pressure guess from Table 13 and the calculated NPSS output chamber pressure. The output chamber pressure was then entered as the NPSS input and a new output chamber pressure calculated. The input and output values were converged until they were within a specified tolerance. The tolerance was set to 0.001, an absolute difference between the variables. Table 30 tabulates the

percent difference between the “converged” and “not converged” tests. The throat area converger was still in place and executed for this test.

**Table 30. O/F Study Evaluating NPSS Chamber Pressure Input Sensitivity**

<b>O/F</b>	5.5	6	6.5	7	7.5	8
<b>% Difference <math>P_c</math></b>	0.0057	0.0031	0.0025	0.0106	0.0028	0.0010
<b>% Difference Throat Area</b>	0	0.0053	0	0.0096	0	0
<b>% Difference Vacuum Thrust</b>	0.0025	0.0005	0.0005	0.0013	0	0.0003
<b>% Difference Vacuum <math>I_{sp}</math></b>	0	0	0	0	0	0

The percent difference for both trades was calculated taking the difference between the converged and not converged chamber pressure outputs and dividing by the converged chamber pressure NPSS output. The percent difference for the entire *O/F* trade is negligible thus concluding the NPSS chamber pressure input guess is insignificant.

The second chamber pressure trade study evaluates the influence of converging and not converging the chamber pressure on selected NPSS outputs for an engine mass flow rate range of 90 to 120 lb<sub>m</sub>/s in 5 lb<sub>m</sub>/s increments. Table 31 tabulates the results.

**Table 31. Engine Mass Flow Rate Study Evaluating NPSS Chamber Pressure Input Influence**

<b>Engine Mass Flow Rate</b>	90 lb <sub>m</sub> /s (40.8 kg/s)	95 lb <sub>m</sub> /s (43.1 kg/s)	100 lb <sub>m</sub> /s (45.4 kg/s)	105 lb <sub>m</sub> /s (47.6 kg/s)	115 lb <sub>m</sub> /s (52.2 kg/s)	120 lb <sub>m</sub> /s (54.4 kg/s)
<b>% Difference <math>P_c</math></b>	0.0003	0.0008	0.0023	0.0012	0.0007	0.0013
<b>% Difference Throat Area</b>	0	0	0	0	0	0
<b>% Difference Vacuum Thrust</b>	0.0015	0.0022	0.0068	0.0046	0.0024	0.0033
<b>% Difference Vacuum Specific Impulse</b>	0.0008	0.0002	0.0036	0.0017	0.0002	0.0002

The percent difference for the entire engine mass flow rate trade study is negligible; the same conclusion from Table 30 can be made here. However, one run failed for the converged chamber pressure trade study; 110 lb<sub>m</sub>/s (49.9 kg/s) values are not included in Table 31. The second trade study was run again for an initial chamber pressure guess of 1500 psia (10.3 MPa) and 2000 psia (13.8 MPa); similar results were noted with some runs ending in failure.

Both trades were repeated for the nonlinear model with very similar results. As long as NPSS closes, the difference in output values between the “converged” and “not converged chamber pressure” outputs is negligible. However, the value of the initial guess for chamber pressure is vital in first getting NPSS to close. Note chamber pressure converges within 2 to 3 iterations.

The final conclusion from the chamber pressure trade studies is NPSS requires an assumed chamber pressure input value and, as long as NPSS converges, the outputs are acceptable without converging chamber pressure. However, if NPSS fails to converge, the chamber pressure input value needs to be evaluated, along with the other NPSS inputs, to find a combination of input values that close the design. Therefore, the guessed chamber pressure NPSS input is a design variable and is set to 1740 psia (12 MPa) in the final ModelCenter model.

The trade study performed on the NPSS guessed chamber temperature input varied from 1000 to 10000 R in 1000 R (1 R = 0.56 K) increments. The semi-log plot, in Figure 68, shows the sensitivity of the guessed temperature value on specific NPSS outputs.

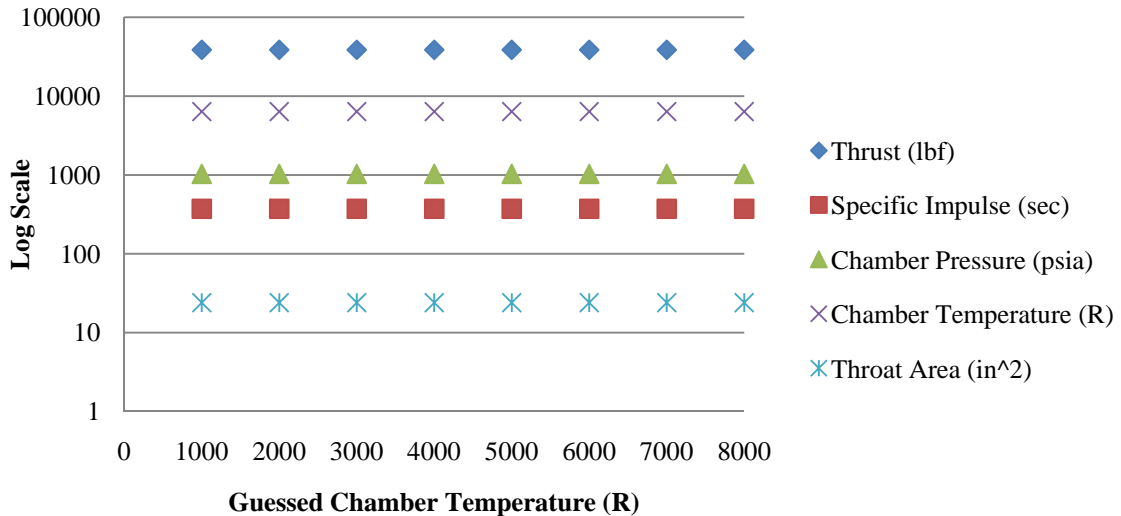


**Figure 68. NPSS Chamber Temperature Input Sensitivity**

The sensitivity of the chamber temperature input is negligible, shown in Figure 68 as relatively straight lines for the outputs. The percent difference between the maximum and minimum values calculated for the NPSS outputs is less than 0.01% for each output variable. Even the guessed chamber temperature does not significantly influence the value of the NPSS calculated output chamber temperature. However, NPSS failed to execute when the chamber temperature guess was 9000 and 10000 R (5000 and 5555.6 K). A similar conclusion about chamber pressure can be made here. A guessed input chamber temperature value is required, and if NPSS converges, the outputs are acceptable. However, if NPSS fails to execute, the chamber temperature input, along with other NPSS inputs, need to be evaluated and varied until NPSS closes.

Three unique trade studies were run to determine the sensitivity of the NPSS user-specified maximum wall temperature for the aerospike and chamber cooling jackets. Each study assumes the guessed wall temperature is constant across the entire cooling

jacket wall. Calculated wall temperatures are a function of material selection, and more specifically, the material thermal conductivity.

The default design variables and the best material selection in Table 19 were used as inputs into NPSS for the three trade studies. The linear NPSS model was used due to its simplicity and since it only has one convergence loop for throat area. The nonlinear NPSS model is more complex, although to verify conclusions from the linear model, the same trades were run for the nonlinear model. For this trade study, the reference to the nonlinear model means the complete ModelCenter model including a linear NPSS model run and two nonlinear NPSS model runs. The wall temperatures are calculated in an external script component called “Cooling\_Jacket”. The goal is to show the sensitivity of the NPSS input chamber and aerospike wall temperatures.

NPSS requires a guessed wall temperature to execute. “Cooling\_Jacket” outputs relating to the actual aerospike and chamber maximum wall temperatures are compared in each trade study to the user-specified NPSS input values. It is possible for the NPSS input value to differ from the material properties guessed value.

The first trade study, using the linear NPSS model, evaluated a single NPSS maximum wall temperature guess of 900 R (500 K) for the chamber and aerospike. NPSS was executed and the resulting outputs of interest are tabulated in Table 32 under the ‘user input maximum wall temperature’ column. Next, the NPSS input value for the chamber and aerospike were linked to the cooling jacket and material properties code allowing for converged guessed and calculated maximum wall temperatures to be used as inputs into NPSS. NPSS outputs of interest for this calculation are also tabulated in Table 32 under the ‘actual maximum wall temperature’ column. The percent difference

for all trades was calculated taking the difference between the outputs and dividing by the ‘actual maximum wall temperature’ outputs.

**Table 32. NPSS Output Comparison of Maximum Wall Temperature Inputs**

	User Input Maximum Wall Temperature	Actual Maximum Wall Temperature	% Difference
Chamber Maximum Wall Temperature	900 R (500 K)	3297.99 R (1832.2 K)	--
Aerospike Maximum Wall Temperature	900 R (500 K)	1989.01 R (1105 K)	--
Vacuum Thrust	40397.9 lbf (179.7 kN)	40395.4 lbf (179.7 kN)	0.0062
Vacuum Specific Impulse (sec)	388.4	388.4	0
Chamber Pressure	1310.15 psia (9.0 MPa)	1309.97 psia (9.0 MPa)	0.0137
Chamber Temperature	6412.93 R (3562.7 K)	6412.73 R (3562.6 K)	0.0031
Throat Area	18.891 in <sup>2</sup> (121.9 cm <sup>2</sup> )	18.893 in <sup>2</sup> (121.9 cm <sup>2</sup> )	0.0106
Maximum LOX Mach Number	0.36643	0.36641	0.0055
Maximum LH <sub>2</sub> Mach Number	0.95637	0.95634	0.0031
% Chamber Melting Point	59.11	59.1	0.0169
% Spike Melting Point	35.65	35.64	0.0281
Calculated Chamber Maximum Wall Temperature	3298.35 R (1832.4 K)	3297.78 R (1832.1 K)	0.0173
Calculated Aerospike Maximum Wall Temperature	1989.33 R (1105.2 K)	1988.65 R (1104.8 K)	0.0342
Computation Time (sec)	44	184	76.0870

The percent difference in Table 32 is negligible, except for the computation time. The conclusion is the improvement in NPSS outputs for using the ‘actual maximum wall temperatures’ method does not justify the 76% increase in computation time.

The second trade study, using the linear NPSS model, compares the ‘actual maximum wall temperature’ NPSS outputs to a range of ‘user input NPSS maximum wall temperatures’. Table 33 tabulates the results. The ‘user input NPSS maximum wall

temperature' range was from 500 to 3000 R in 100 R (1 R = 0.56 K) increments. The chamber and aerospike 'user input maximum wall temperatures' were equal. The 'user input wall temperature' NPSS outputs tabulated show the maximum and minimum output values for the entire temperature range.

**Table 33. NPSS Output Comparison of Range of Maximum Wall Temperature Inputs**

	Actual Maximum Wall Temperature	Maximum User Input Wall Temperature Output	Minimum User Input Wall Temperature Output	% Difference Max	% Difference Min
Vacuum Thrust	40395.4 lb <sub>f</sub> (179.7 kN)	40396.8 lb <sub>f</sub> (179.7 kN)	40395.0 lb <sub>f</sub> (179.7 kN)	0.0035	0.0010
Vacuum Specific Impulse (sec)	388.4	388.4	388.4	0	0
Chamber Pressure	1309.97 psia (9.0 MPa)	1310.24 psia (9.0 MPa)	1309.97 psia (9.0 MPa)	0.0206	0
Chamber Temperature	6412.73 R (3562.6 K)	6413.01 R (3562.7 K)	6412.66 R (3562.6 K)	0.0044	0.0011
Throat Area	18.893 in <sup>2</sup> (121.9 cm <sup>2</sup> )	18.893 in <sup>2</sup> (121.9 cm <sup>2</sup> )	18.89 in <sup>2</sup> (121.9 cm <sup>2</sup> )	0.0000	0.0159
Maximum LOX Mach Number	0.36641	0.36644	0.36632	0.0088	0.0250
Maximum LH <sub>2</sub> Mach Number	0.95634	0.95642	0.95620	0.0086	0.0142
% Chamber Melting Point	59.1	59.1	59.1	0	0
% Spike Melting Point	35.64	35.64	35.64	0	0
Calculated Chamber Maximum Wall Temperature	3297.78 R (1832.1 K)	3298.04 R (1832.4 K)	3297.75 R (1832.2 K)	0.0080	0.0009
Calculated Aerospike Maximum Wall Temperature	1988.65 R (1104.8 K)	1989.07 R (1105.0 K)	1988.84 R (1104.9 K)	0.0210	0.0093
Computation Time (sec)	184	44	44	76.0870	76.0870

The percent difference shown in Table 33 is negligible between the maximum and minimum outputs from the user input NPSS values over an entire range of temperatures and the actual NPSS outputs relating to the true maximum wall temperatures. The same conclusion from Table 32 can be made here. Furthermore, one can conclude using equal chamber and aerospike user input wall temperature values are insignificant.

A third trade study, using the linear NPSS model, was run to finalize the conclusion of the sensitivity of the wall temperature NPSS input. Using the design of experiments (DOE) tool in ModelCenter, the aerospike and chamber maximum wall temperatures each varied from 500 to 1900 R in 200 R increments leading to 64 runs. The DOE performed a parameter scan evaluating 8 levels for each of the two NPSS wall temperature inputs. The DOE tool allows the two NPSS input values to vary throughout the specified range. For example, the DOE will execute the model for a chamber wall temperature input of 500 to 1900 R in 200 R increments at a constant aerospike wall temperature input of 900 R; this equals 8 runs. The next 8 runs will keep the chamber wall temperature input constant at 500 R and the aerospike will vary from 500 to 1900 R accounting for 8 more runs. The process will continue until all 64 runs are completed. For this trade study, the chamber and aerospike temperature inputs were allowed to differ, as opposed to the second trade study where the input values were equal. Table 34 tabulates the results. Similar to the second trade study, only the results equating to the maximum and minimum NPSS outputs of interest were tabulated for the ‘user input wall temperature’ columns.

**Table 34. NPSS Output Comparison of Various Maximum Wall Temperature Inputs**

	Actual Maximum Wall Temperature	Maximum User Input Wall Temperature Output	Minimum User Input Wall Temperature Output	% Difference Max	% Difference Min
Vacuum Thrust	40395.4 lb <sub>f</sub> (179.7 kN)	40397.2 lb <sub>f</sub> (179.7 kN)	40394.6 lb <sub>f</sub> (179.7 kN)	0.0045	0.0020
Vacuum Specific Impulse (sec)	388.4	388.4	388.4	0	0
Chamber Pressure	1309.97 psia (9.0 MPa)	1310.24 psia (9.0 MPa)	1309.98 psia (9.0 MPa)	0.0206	0.0008
Chamber Temperature	6412.73 R (3562.6 K)	6413.01 R (3562.8 K)	6412.54 R (3562.5 K)	0.0044	0.0030
Throat Area	18.893 in <sup>2</sup> (121.9 cm <sup>2</sup> )	18.893 in <sup>2</sup> (121.9 cm <sup>2</sup> )	18.890 in <sup>2</sup> (121.9 cm <sup>2</sup> )	0	0.0159
Maximum LOX Mach Number	0.36641	0.366458	0.366318	0.0131	0.0250
Maximum LH <sub>2</sub> Mach Number	0.95634	0.956423	0.956204	0.0086	0.0142
% Chamber Melting Point	59.10	59.11	59.10	0.0169	0
% Spike Melting Point	35.64	35.65	35.64	0.0281	0
Calculated Chamber Maximum Wall Temperature	3297.78 R (1832.1 K)	3298.201 R (1832.3 K)	3297.69 R (1832.1 K)	0.0128	0.0029
Calculated Aerospike Maximum Wall Temperature	1988.65 R (1104.8 K)	1989.19 R (1105.1 K)	1988.81 R (1104.9 K)	0.0271	0.0079
Computation Time (sec)	184	44	44	76.0870	76.0870

Similar conclusions to the previous tables can be made here in Table 34 with the percent difference in output values being negligible. However, during this trade study 3 of 64 NPSS runs failed. The first failed run resulted due to the enthalpy of a specific hydrogen cooling channel station not affecting one of the error terms. The next two

failed runs were due to the NPSS model not converging in the allowable number of iterations. The fact there were failures shows the wall temperature guesses do influence model convergence

Similar trade studies were run for the nonlinear model (complete ModelCenter model with one linear and two nonlinear NPSS model executions) with very similar results including errors at certain wall temperature guesses. All percent differences were well under 1%. Linking the nonlinear NPSS wall temperature inputs to the guessed wall temperature in the material properties script component resulted in a computation time of 404 sec (~7 min) as opposed to 128 sec (~2 min) if not linked.

Errors in NPSS execution with only chamber and aerospike wall temperature guesses changing show the two variables add brittleness to the NPSS model. Even in converging wall temperatures, there still has to be an initial guess to start the process (2000 R (1111.1 K) for the aerospike and 3000 R (1666.7 K) for the chamber wall). There is no way to guarantee initial guesses in wall temperature will always lead NPSS to convergence. Therefore, the wall temperature inputs are potential sources for any NPSS related error, along with other NPSS inputs.

Ideally, computation time should be minimized without affecting model validity. Understanding the wall temperature guesses affect NPSS convergence, the trade studies absolutely show when NPSS does converge, the percent difference in actual versus guessed wall temperature outputs is negligible. The final conclusion is a single chamber and aerospike wall temperature can be assumed minimizing computation time, as long as the model converges. If the model fails to converge, then wall temperature inputs need to be evaluated along with the other NPSS inputs to find a combination of input values

closing the design. The guessed aerospike and chamber wall temperature inputs are both set to the original value of 900 R (500 K) used by Martin [4] for the final ModelCenter DEAN model.

A trade study on the user specified *Ox\_Bypass* NPSS input (the percentage of oxygen flow bypassing the turbine), was performed from 0% to 50%. Default design variables were utilized and all were kept constant. Table 35 tabulates the trade study results.

**Table 35. Influence of Percent Oxygen Bypassing Turbine on Specific NPSS Outputs**

% Oxygen Bypassing Turbine	10%	15%	20%	25%
<b>Vacuum Thrust</b>	40396.1 lb <sub>f</sub> (179.7 kN)	41471.4 lb <sub>f</sub> (184.5 kN)	41931.7 lb <sub>f</sub> (186.5 kN)	41825.3 lb <sub>f</sub> (186.1 kN)
<b>Vacuum Specific Impulse (sec)</b>	388.4	398.8	403.2	402.2
<b>Chamber Pressure</b>	1310.1 psia (9 MPa)	1629.4 psia (11.2 MPa)	1790.2 psia (12.3 MPa)	1754.0 psia (12.1 MPa)
<b>Chamber Temperature</b>	6412.91 R (3562.7 K)	6464.97 R (3591.7 K)	6492.6 R (3607.0 K)	6485.64 R (3603.1 K)
<b>Throat Area</b>	18.892 in <sup>2</sup> (121.9 cm <sup>2</sup> )	15.225 in <sup>2</sup> (98.2 cm <sup>2</sup> )	13.877 in <sup>2</sup> (89.5 cm <sup>2</sup> )	14.158 in <sup>2</sup> (91.3 cm <sup>2</sup> )

Table 35 only shows successful test runs. 0 - 5% and 30 – 50% oxygen bypass led to NPSS errors such as a specific internal combustion chamber station being choked or the enthalpy of a cooling channel station not affecting one of the error terms. From the values that did work, the chamber pressure decreases for increase in bypass resulting in a larger throat area. As the percentage of bypass increases, less propellant is traveling through the turbine leading to a lower turbine pressure ratio. The lower turbine pressure ratio directly influences the amount of power supplied to the pump resulting in a lower pump pressure rise and lower chamber pressure. In order to keep engine mass flow constant, the throat area of the engine must increase to support the lower chamber

pressure. The trend noticed in Table 35 is physically acceptable. The conclusion of this sensitivity analysis is the amount of oxygen bypassing the turbine directly influences NPSS convergence. However, if NPSS does converge, a low bypass value is preferred to maximize engine performance.

All the sensitivity analyses showed certain input variable values affect NPSS convergence. In addition, if NPSS did converge, the guessed input would lead to acceptable outputs. The same conclusion about NPSS convergence applies to other NPSS inputs as well, including input pressure and enthalpy profile guesses. When NPSS does converge, the NPSS DEAN model is reliable and will be used for further research in a complete ModelCenter model.

#### **C.4. Troubleshooting NPSS**

The DEAN NPSS models are extremely brittle. There is an unknown coupled relationship between the design variables and the NPSS inputs. Chamber length, chamber and aerospike radii at the injector face, engine mass flow rate, percentage oxidizer bypassing the turbine, and oxygen and hydrogen cooling channel geometry, such as aspect ratio and initial half-width, all need to be the right combination to prevent NPSS errors. This section discusses the different troubleshooting steps performed to improve NPSS flexibility.

Common NPSS errors are as follows:

- “HCV3.ind\_ht did not affect any of the error terms”; error applies to any cooling volume station

- “SecantSolver ‘OV.F1\_O.FL\_O.htSolver\_for\_setTotalTP’: Slope between two points went off to infinity”
- “RocetUnReactedFlowStation Nozz.HxFlow: Flow Station is Choked”
- “Failed to converge in 5000 iterations”
- “Error for H2PumpsPR is not affected by any of the independent perturbations”
- “Error for Dependent, CVH1.integ\_U, is not affected by any of the independent perturbations”; error applies to any cooling volume station

The errors occur due to the inability of the NPSS solver to conserve mass, energy, or both through the engine. Cooling volume geometry is a critical parameter in NPSS solver convergence.

Troubleshooting began with changing the cooling channel geometry. The original NPSS model by Martin assumed constant aspect ratio for the cooling channel geometry. As chamber or aerospike radius increases, the width of the cooling channels will increase and a lower channel height will result to maintain a constant aspect ratio. Troubleshooting evaluated constant channel height, constant channel width, variable aspect ratio, constant channel cross-sectional area, and a combination of each. All except one resulted in the aforementioned errors with no noticeable improvement in model flexibility.

Constant channel cross-sectional area did provide model flexibility to the aerospike radius at the injector face. Instead of being able to evaluate only one or two aerospike radii with constant chamber radius, now multiple aerospike radii points could be evaluated. The increase in NPSS flexibility, although only on the aerospike side, is an

improvement. From the increased flexibility, new design solutions could be evaluated. For example, as the aerospike radius approaches the chamber radius, the chamber pressure increases leading to a smaller throat area and improved thrust and specific impulse. Constant channel cross-sectional area is utilized in the final ModelCenter DEAN model.

Other troubleshooting evaluated the chamber length design variable. The value of chamber length influences how much heat transfer occurs between the hot exhaust gases and the coolant. Higher coolant temperatures lead to higher flow velocities. If the chamber was too long, too much heat transfer may occur and the solver may lead to supersonic cooling channel velocities choking a particular station. Instead of making chamber length a design variable, troubleshooting evaluated making chamber length a function of the characteristic length. As previously mentioned for H<sub>2</sub>/O<sub>2</sub> engines, the characteristic length range is 22 – 40 inches (55.9 – 101.6 cm) [8]. Characteristic length is a function of volume and throat area; therefore, as NPSS converges throat area, volume is known and the actual chamber length would vary while keeping the characteristic length constant. This troubleshooting attempt had no influence on NPSS errors nor did it unlock any flexibility. However, troubleshooting concluded NPSS could still converge with supersonic Mach numbers. The “station is choked” errors do not relate to the cooling channel stations; rather, the errors relate to the chamber and nozzle fluid flow stations. There were instances where characteristic length as an input provided less NPSS flexibility; therefore, the option to use chamber length as a function of characteristic length was avoided for the final model.

NPSS requires pressure profile guesses and turbopump parameters to function. In an attempt to further parameterize the NPSS model and increase flexibility, the pressure profile and turbopump processes by Humble *et al.* were coded in ModelCenter and linked to NPSS [20]. For instance, the pump efficiency, pressure ratio, turbine efficiency, and turbopump shaft mechanical speed would all be parametric for a system level study. The hypothesis was the pressure profile would provide better input guesses and improve NPSS flexibility. Unfortunately both processes did not work. The NPSS model did not work with pressure profile values different from the values assumed by Martin [4]. NPSS also requires an input enthalpy profile. The enthalpy profile was maintained at the output values from the NPSS model by Martin [4] and did not vary with the pressure profile; maintaining the value of the enthalpy profile is a hypothesized reason why the pressure profile did not work. In addition, the NPSS model did not work for changes to the turbopump shaft mechanical speed. However, the model did close for various pump and turbine efficiency values. At any rate, the code was removed from the execution sequence of the final ModelCenter model and left as potential code for future research. The final decision was to keep the turbopump and pressure profile values from Martin in the final NPSS model as tabulated in Table 5.

Troubleshooting only found one option to provide added flexibility to the NPSS models. The option was included in the final ModelCenter DEAN model. To unlock NPSS for automated performance optimization studies in the future, the coupled relationship between the design variables and NPSS inputs must be found.

### C.5. Simplification to the Execution of the NPSS DEAN Models

The DEAN ModelCenter model utilizes one linear and two nonlinear NPSS model runs. The purpose is to increase the validity of the “guess” inputs. The throat area convergence loops for the two nonlinear NPSS models in the final DEAN ModelCenter model are linked to the throat area in the Angelino Code allowing the aerospike nozzle geometry to be recalculated for each iteration of NPSS throat area convergence. However, after performing some tests, the outputs of each model were close in value. An experiment using the design variables in Table 13 was run taking out the throat area converger of the first NPSS model. The results between the first and second nonlinear NPSS models were acceptable except when larger chamber and aerospike radii were tested. The next experiment evaluated deleting the throat area converger link to Angelino and replacing the link to the NPSS input script component. The new link allowed the throat area in NPSS to still converge while not executing CEA, Angelino, and TDK for each converger iteration, thus decreasing computation time. The improvement in computation time did not drastically influence the results from the linear and two nonlinear NPSS models as shown in Table 36. Table 36 also shows the percent difference between the outputs of the linear and the second nonlinear NPSS models.

**Table 36. Comparison of Linear and Nonlinear NPSS Model Outputs**

<b>VARIABLES</b>	<b>Linear NPSS Model</b>	<b>Nonlinear NPSS Model #1</b>	<b>Nonlinear NPSS Model #2</b>	<b>% Difference between Linear and Nonlinear #2</b>
<b>Chamber Pressure</b>	1367.81 psia (9.4 MPa)	1366.37 psia (9.4 MPa)	1368.13 psia (9.4 MPa)	0.0234
<b>Chamber Temperature</b>	6427.24 R (3570.7 K)	6424.46 R (3569.1 K)	6424.71 R (3569.3 K)	0.0394
<b>Throat Area</b>	18.11 in <sup>2</sup> (116.8 cm <sup>2</sup> )	18.13 in <sup>2</sup> (117.0 cm <sup>2</sup> )	18.10 in <sup>2</sup> (116.8 cm <sup>2</sup> )	0.0552
<b>Bell Nozzle Thrust</b>	40632.70 lb <sub>f</sub> (180.7 kN)	40621.30 lb <sub>f</sub> (180.7 kN)	40622.50 lb <sub>f</sub> (180.7 kN)	0.0251
<b>Bell Nozzle Specific Impulse (sec)</b>	390.70	390.60	390.60	0.0256

The difference between the linear and nonlinear NPSS model outputs is, at most, less than 0.06%. The results of the study provide rationale to continue use of the edited throat converger in the first nonlinear NPSS model. Furthermore, the results show the difference between the linear and nonlinear NPSS models is insignificant. Similar conclusions to the previous NPSS sensitivity analyses can be made here. When NPSS successfully executes, the outputs are acceptable and there is no need for input variable convergence except for throat area. Furthermore, an accurate system level design for the DEAN can be made with the linear NPSS model only, leading to improved model computation time without invalidating the results. Since the DEAN ModelCenter model is complete with a linear and two nonlinear NPSS model executions, the model will remain as is for the current research effort.

## Appendix D: TDK Model

Appendix D serves to document the decision process used to choose the TDK PFG model for the final ModelCenter DEAN model. In addition, this appendix documents the TDK PFG sensitivity analyses used to simplify the TDK model and its execution.

### D.1. TDK Model Comparison

Two unique TDK models were created and tested: a kinetic model using the TDK problem type and a PFG model using the PFG problem type. Both models are compared for differences in output nozzle geometry and pressure profiles with a final boundary layer calculation comparison. The goal is to determine which TDK model is best suited for the final DEAN ModelCenter model.

Before discussing the tests performed to compare the models, it is important to note TDK requires more user inputs than previously mentioned. Most of the inputs are geometry related and are required to execute the code. For example, TDK requires a nozzle attachment angle (*THETA*), a nozzle exit angle (*THE*), a lower wall (also known as the cowl or chamber exit lip) nozzle attachment angle (*THALW*), an axial cowl length normalized by the throat radius (*XCOWL*), a downstream normalized wall throat radius of curvature ratio (*RWTD*), and a normalized radius at the nozzle exit plane (*RMAX*). These geometric inputs are user configurable; however, the TDK user manual recommends certain values to improve software efficiency. *THETA* declares the initial turning angle of the aerospike at the throat; it is set to 25° for each of the tests. *THE* is set to 0° so the flow is straightened leaving the nozzle and optimizing thrust. *THALW* is the exit angle of

the cowl and influences the exit angle of the flow; for the following tests, the value is set to Martin's original design value of  $2.5^\circ$  [4]. *XCOWL* means the chamber exit lip extends a specified distance past the throat; the variable is normalized to the throat radius. *XCOWL* is set to 0.1, linking the variable to the assumed NPSS chamber throat length of 0.1 multiplied by the aerospike throat radius. *RWTD* is set to 0.05 as recommended by the TDK user manual to model a corner expansion (i.e. Prandtl-Meyer expansion fan) [48]. The last geometric input, *RMAX*, must be a nonzero negative number. The negative is required by TDK to flag use of scramjet nozzle MOC code. The current value is set to a normalized value of -0.01. The geometric variables mentioned remain constant for the kinetic and PFG model comparison tests.

One specific user required flow variable has a huge impact on TDK calculated performance, *VSJ* or *MSJ*. *VSJ* is the velocity at the scramjet nozzle inlet, or in the case of the DEAN aerospike, the velocity at the throat of the nozzle. *MSJ* is a similar variable, except it is the Mach number of the flow at the nozzle throat. *MSJ* or *VSJ* must be input into the TDK model. Since TDK models the aerospike as a scramjet, both *VSJ* and *MSJ* variables must have supersonic values. The supersonic values cause inflation in TDK performance calculations and is addressed in section III.3.e. For now, note the value of *VSJ* will influence model comparison tests.

For the TDK MOC module, the number of points on the initial line (*MP*) can effect TDK execution. The user can define the number of points on the starting line from 0 to 275 points. The more points on the initial line, the more characteristics will be calculated. However, due to the complexity of the aerospike nozzle, the number of points on the initial line is limited. Characteristic lines are not allowed to cross one another;

however, when they do, TDK automatically deletes the characteristic intersecting another characteristic. After TDK deletes ten characteristics (value is user configurable using TDK *NTMAX* variable), the program will fail. To avoid the issue, the value of *MP* can be lowered. *MP* is set to 100 points for the following studies.

The first test between the kinetic and PFG model was to determine if either model resulted in differences in geometry. The same design variables as stated for the Angelino and TDK comparison were used. The kinetic model is linked to Angelino and the PFG model is linked to both CEA and Angelino. As can be seen in Figure 69, the PFG and kinetic models are very similar in terms of nozzle geometry.

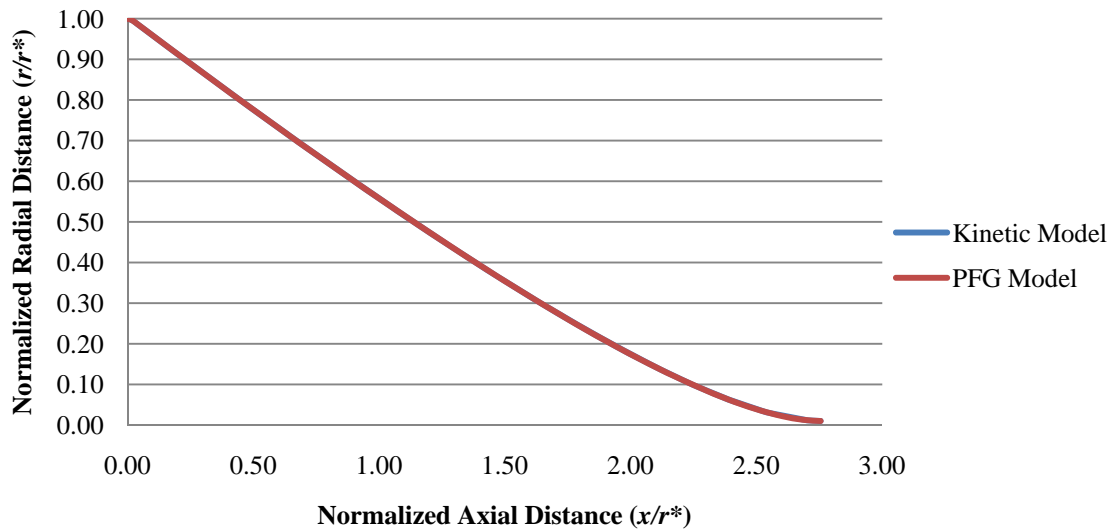
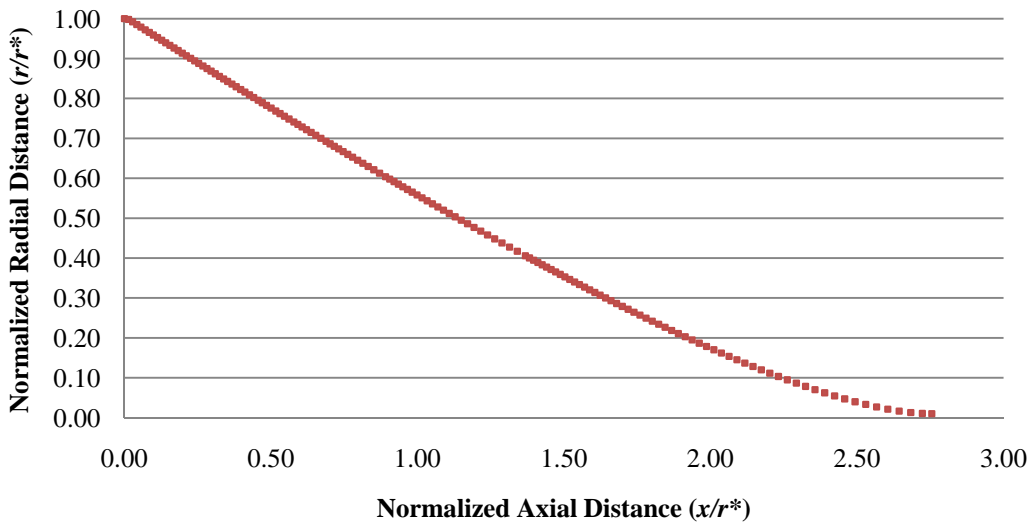
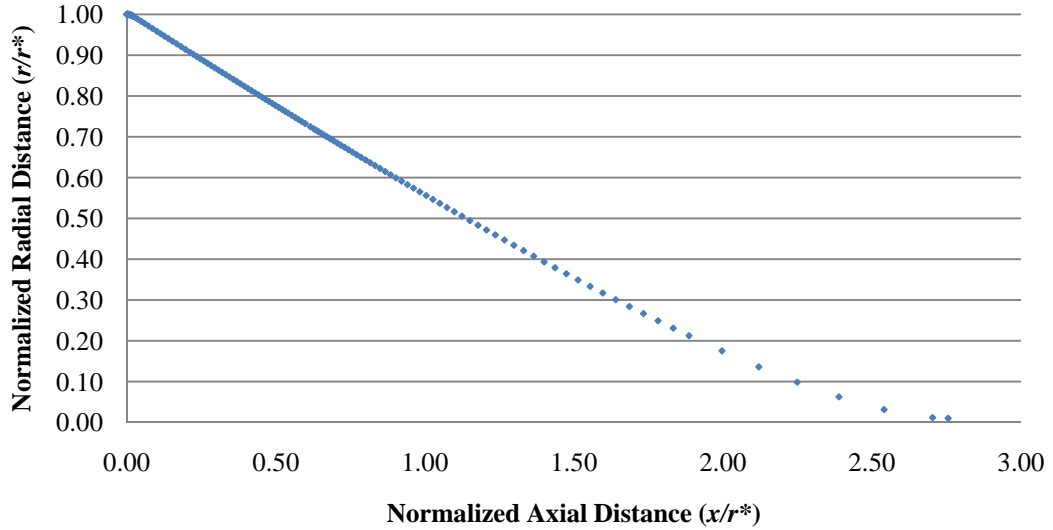


**Figure 69. TDK Model Comparison of Nozzle Geometry**

Figure 69 represents the data as straight line segments connecting the data points. Plotting just the data points for both the kinetic and PFG model (Figure 70), what is observed is the kinetic model (Figure 70b) has the most concentration of data points towards the throat while the PFG model (Figure 70a) has data points more equally spaced along the spike.



**a) PFG Model**



**b) Kinetic Model**

**Figure 70. Aerospike Nozzle Geometry for a) PFG and b) Kinetic TDK Models**

Drawing a straight line to each point, the PFG model will appear more curved compared to the kinetic model. When Figure 69 is magnified at the spike tip with a straight line attached to each data point as shown in Figure 71, the kinetic model appears more linear from point to point compared to the PFG model. This difference is only an artifact of the kinetic model having fewer points near the nozzle tip. The difference in

the spike geometry between the kinetic and PFG TDK models is insignificant and, therefore, either model is useable to define the spike geometry.

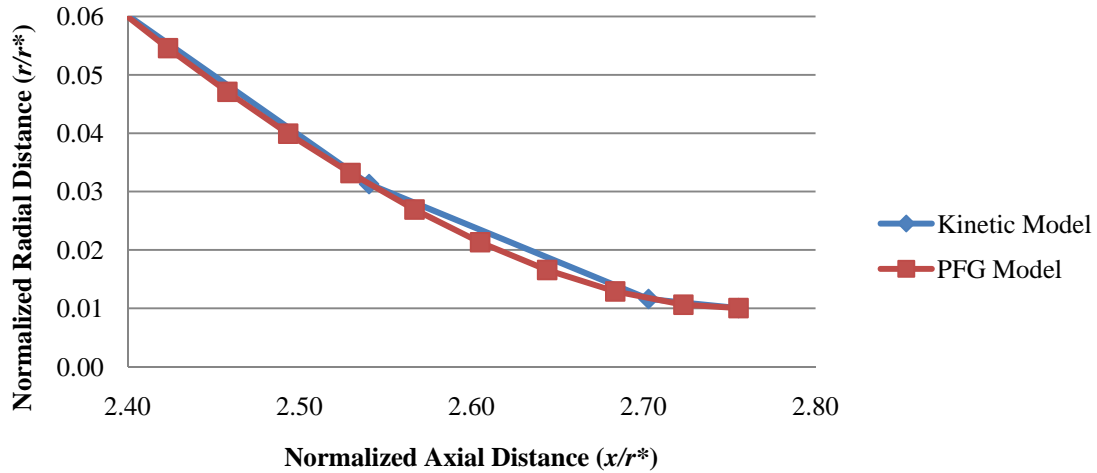


**Figure 71. Magnified Aerospike Nozzle Geometry Comparison at Spike Tip**

The next comparison test was the difference in the models' pressure profile. Figure 72 compares the pressure profiles.

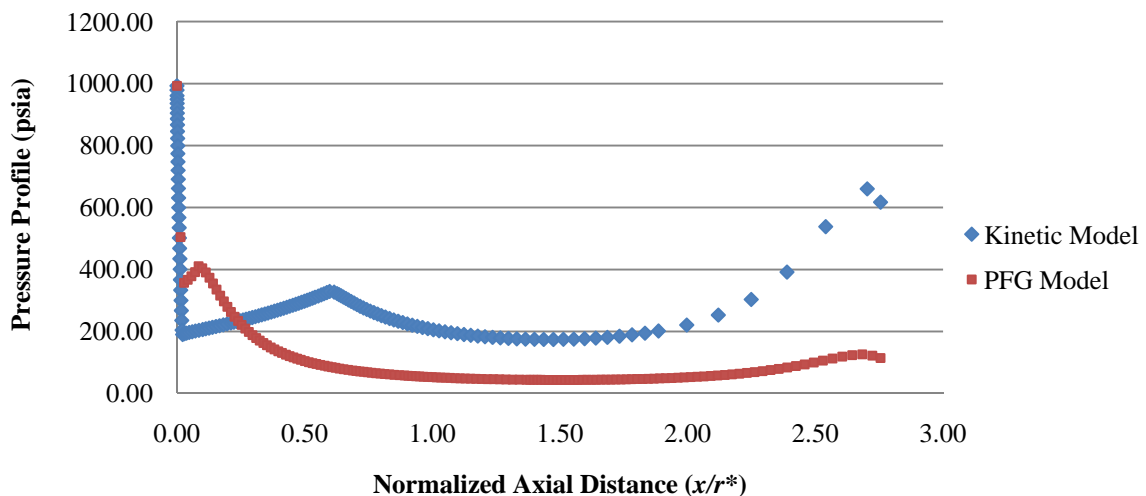


**Figure 72. Aerospike Nozzle Pressure Profile Comparison Run #1**

A large difference in the pressure profiles is observed; however, the difference in pressure profiles is due to the difference in the  $VSJ$  value only. The PFG model sets  $VSJ$  so the throat Mach number is equal to 1.1. The kinetic model does not allow as much

flexibility in lowering the  $VSJ$  value to an equivalent throat Mach number equal to 1.1. Therefore, the test was re-performed setting the  $VSJ$  value in the PFG model to 14,000 ft/sec (4,267.2 m/s). Figure 73 plots the results.

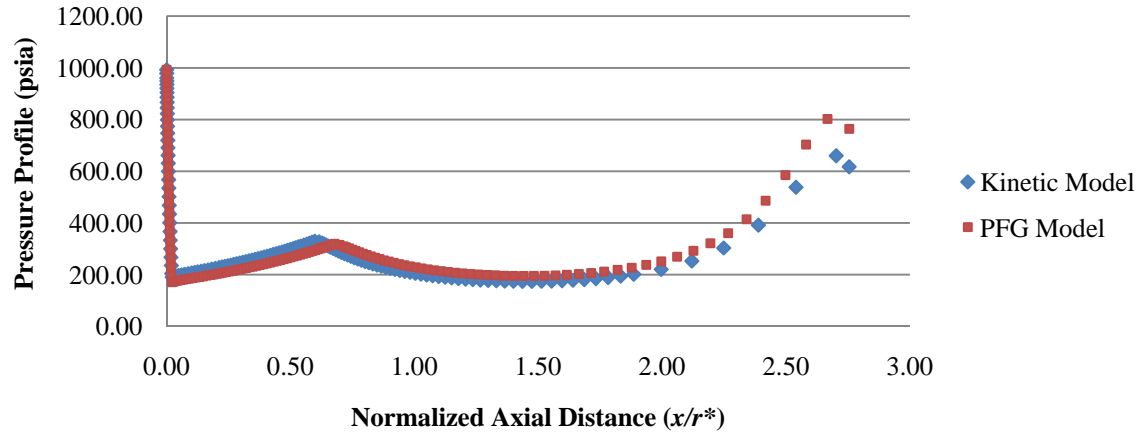


**Figure 73. Aerospike Nozzle Pressure Profile Comparison Run #2**

Figure 73 shows the pressure profiles are similar in shape when the equivalent  $VSJ$  values are used, with a higher exit pressure observed for the PFG model. The increase in exit pressure for the PFG model would equate to a higher pressure thrust. The difference between the kinetic and PFG pressure profiles is due to a difference in the calculated mass flow rate. Even though the velocity through the throat is equal, the PFG mass flow rate is approximately 25% greater than the kinetic value. When the PFG  $VSJ$  value is changed so the mass flow rate equals the kinetic  $VSJ$  value of 14,000 ft/sec (4,267.2 m/s), the resulting pressure profile is shown in Figure 74.

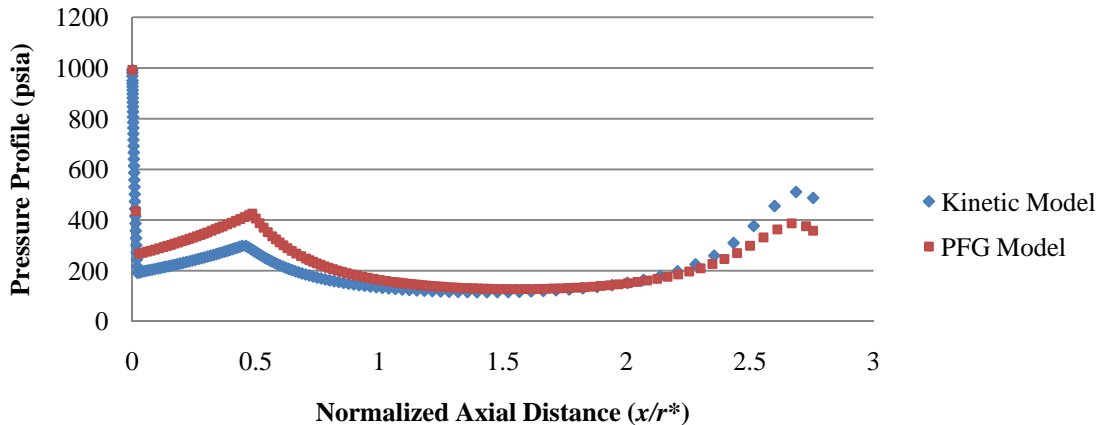


**Figure 74. Aerospike Nozzle Pressure Profile Comparison Run #3**

The percent difference in the  $VSJ$  value of the models is approximately 25% to get the calculated mass flow rates equal. The PFG model is observed to have lower exit pressure than the kinetic model; however, the PFG model results in a higher calculated pressure thrust value. Therefore, the pressure thrust calculated for the DEAN using the PFG model will be inflated compared to using the kinetic model. However, when the performance of the DEAN is evaluated in vacuum conditions, the kinetic model will overall have greater thrust. The individual thrust components are discussed in detail in section III.4.k. An additional thrust component is produced from DEAN engine operation in vacuum conditions; the magnitude of the thrust is a function of the nozzle exit pressure. Interestingly, the kinetic model has 15% greater nozzle thrust compared to the PFG model when the nozzle thrust is only equal to the pressure thrust plus the thrust produced from engine operation in a vacuum.

The last comparison test evaluated the differences in the boundary layer loss approximations. The TDK MABL module was added to both the PFG and kinetic models. The kinetic  $VSJ$  was set to 14,000 ft/s (4,267.2 m/s) and the PFG  $VSJ$  was set to

a value where the calculated engine mass flow rates between the models are approximately equal. The percentage of pressure thrust loss on the aerospike due to boundary layer effects is equal to 6.1% and 10.3% for the PFG and kinetic model, respectively. Percent pressure thrust loss due to boundary layer effects was calculated by taking the difference between the calculated pressure thrust and pressure thrust with boundary layer values and dividing the difference by the pressure thrust without boundary layer. The percent thrust loss due to boundary layer effects is directly proportional to the mass flow through the throat. Since the mass flow between the models is approximately equivalent, the kinetic model shows more thrust loss than the PFG model. When boundary layer effects are evaluated in the total thrust (pressure thrust plus thrust produced from engine operation in a vacuum), the PFG model still underestimates performance compared to the more accurate kinetic model performance estimate.

The comparison between the kinetic and PFG models' pressure profiles and boundary layer losses are not exact due to the difference in each models approach and assumptions in solving the problem. Realistically, the kinetic model is a more accurate thrust estimate; however, the kinetic model is limited in lowering the throat Mach number or flow velocity to within a reasonable range of choked flow at the throat. TDK variables *NTMAX* and *VERTIL* can improve the kinetic model in lowering the *VSJ* value; however, even with these improvements, the kinetic model is still not as flexible as the PFG model. The PFG model can successfully execute with a minimum throat Mach number equal to 1.1, while the kinetic model sometimes runs for Mach numbers equal to 1.5 to 2.0 and always runs for Mach numbers greater than 2.5. Although the PFG model overestimates

pressure thrust, overall the calculated thrust will be underestimated compared to the kinetic model including boundary layer losses. Therefore, taking a conservative approach, the PFG model will be used for the final ModelCenter DEAN model for both nozzle geometry and the pressure profile.

## D.2. TDK Perfect Gas (PFG) Model Sensitivity Analyses

Choosing the TDK PFG model for the final DEAN ModelCenter model, sensitivity analyses of specific TDK inputs were accomplished. The overall goal was to determine if not converging specific NPSS variables would influence TDK results. Ambient pressure ( $P_{amb}=PINF$ ), the freestream Mach number ( $MINF$ ),  $THETA$ , velocity of the flow at the throat ( $VSJ$ ), and chamber pressure ( $P_c$ ) inputs were analyzed. For these studies, the following variables were kept constant:  $THALW= 2.5^\circ$ ,  $MP = 100$  points,  $THETA = 25^\circ$ , and  $THE = 0^\circ$ . In addition, CEA and Angelino are linked to TDK for these analyses. The design variables in Table 37 were used for the sensitivity analyses unless otherwise noted. The operational ambient pressure of the DEAN is vacuum conditions; however, TDK requires a non-zero value so an ambient pressure of 1 Pa or 0.000145 psia was used.

**Table 37. VSJ Sensitivity Analysis Design Variables**

Variable	Value
$O/F$	6
Chamber Pressure	1740 psia (12.0 MPa)
Chamber Radius at Throat	6 in (15.24 cm)
Throat Area	18.9 in <sup>2</sup> (121.9 cm <sup>2</sup> )
Engine Mass Flow Rate	104 lb <sub>m</sub> /s (47.2 kg/s)
$P_{inf}$ – Operational	0.000145 psia (1 Pa)

The first TDK sensitivity analysis is ambient pressure (TDK variable  $PINF$ ). Ambient pressure was varied from 0 to 500 in 10 psia (1 psia = 6894.8 Pa) increments. The results of the study were constant TDK outputs. No changes in calculated thrust, specific impulse, throat area, engine mass flow rate, pressure profile, or nozzle geometry were noticed. TDK typically calculates performance and the exhaust flow field at the nozzle design altitude. SEA, Inc. recommends changing both  $PINF$  and  $MINF$  (the freestream Mach number) to calculate off-design performance and the exhaust flow field for the nozzle.  $MINF$  was kept constant for the study (equal to zero) and, most likely, led to the reason there were no changes to the TDK outputs.

$MINF$  is a function of mission profile and, more specifically, ambient conditions. The final DEAN model will estimate vacuum thrust where ambient pressure is realistically zero, but mathematically 0.000145 psia (1 Pa) for TDK to function. When  $MINF$  is varied from 0 to 50 in 5 unit increments at  $PINF = \sim 0$  psia, the TDK outputs are constant. However, if  $PINF$  was equal to the design altitude pressure and  $MINF$  is varied, the pressure thrust increases for increased  $MINF$ . The pressure profile plot is similar in shape to the PFG model in Figure 72. As  $MINF$  increases at design altitude ambient pressure, the pressure profile shape remains constant with a slight increase in magnitude. More importantly, the nozzle exit pressure increases for increased  $MINF$ .

If  $MINF$  and  $PINF$  were known for a specific mission profile, the performance could be calculated at varying altitudes. However, the DEAN is being designed to reach vacuum performance design goals and  $MINF$  is not a contributor when  $PINF$  equals or is close to zero. The conclusion is  $PINF$  and  $MINF$  do not influence the shape and/or

pressure profile for the variable space where the DEAN model will calculate performance/geometry.

The nozzle attachment angle,  $THETA$ , input variable was evaluated next from set values of 0 to 90 in 5 degree increments. Figure 75 shows the influence of  $THETA$  on nozzle geometry. As  $THETA$  increases, the slope of the aerospike at the throat increases leading to a more concave nozzle and also the length of the aerospike decreases. With a more concave shorter nozzle, the weight of the aerospike will decrease. Note TDK failed for  $THETA$  from 0 to 20 degrees.

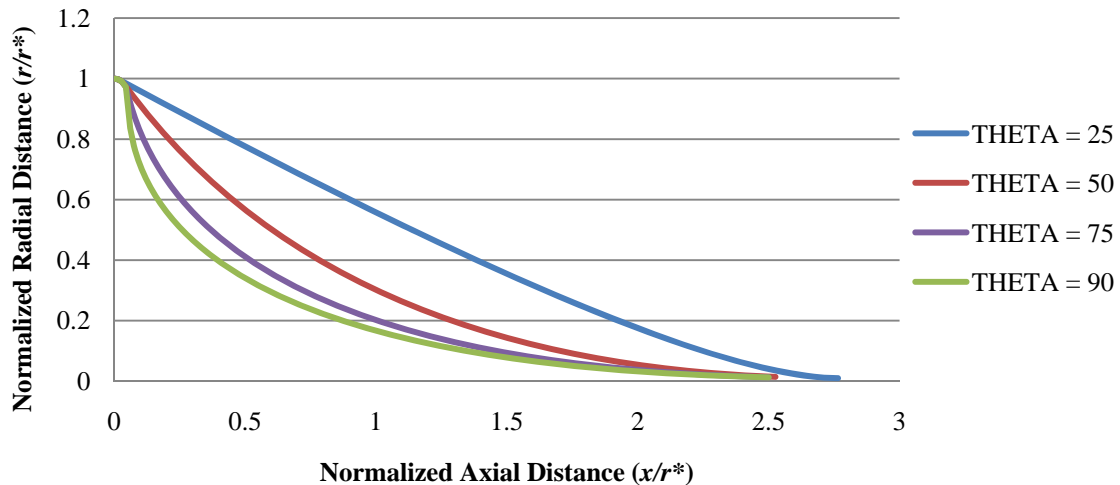


**Figure 75. Influence of  $THETA$  on Aerospike Nozzle Geometry**

Figure 76 shows the influence of  $THETA$  on the nozzle pressure profile. As  $THETA$  increases, the shape and magnitude of the pressure profile changes. More importantly, the exit pressure decreases. Figure 77 plots the resulting pressure thrust along the full-length aerospike nozzle for multiple  $THETA$  points.

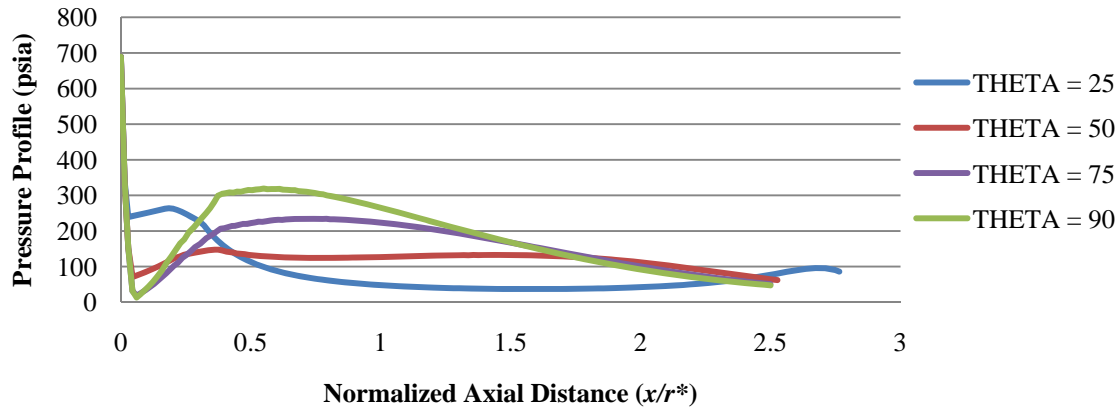


**Figure 76. Influence of *THETA* on the Nozzle Pressure Profile**

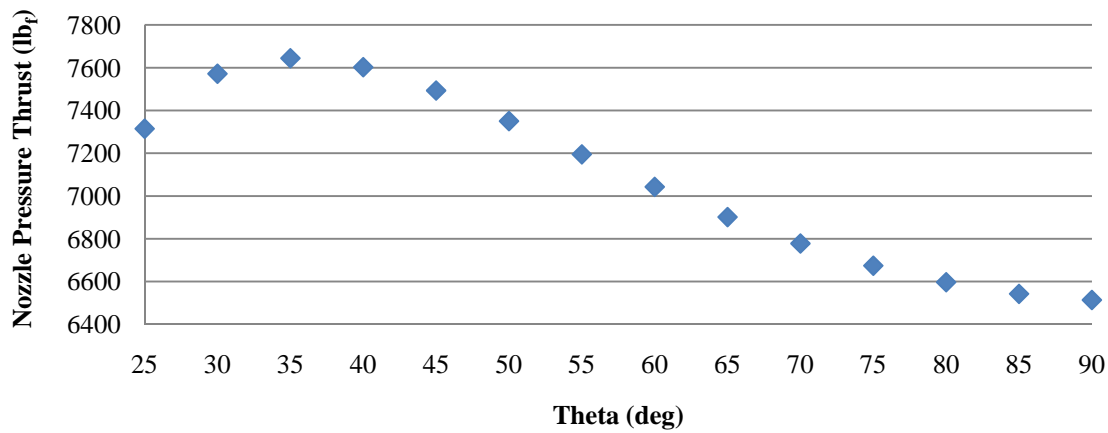


**Figure 77. Influence of *THETA* on Nozzle Pressure Thrust**

A peak in pressure thrust is observed at *THETA* equal to 35 degrees. The conclusion is *THETA* should equal 35 degrees for this specific design point and *THETA* should be optimized to provide maximum pressure thrust in the final DEAN model for various design points. However, with increased *THETA* comes decreased exit pressure. Individual thrust components will be discussed in detail in section III.4.k. For now recognize when the DEAN operates at an altitude other than its design altitude, a new thrust component will be introduced (known as  $F_{nondesign}$ ).  $F_{nondesign}$  is a function of nozzle exit pressure and ambient pressure. For vacuum thrust, ambient pressure is

mathematically close to zero. Figure 78 shows the influence of  $THETA$  on the summation of  $F_{nondesign}$  and the nozzle pressure thrust; momentum thrust out the throat is constant. The performance peak is no longer observed at  $THETA = 35$  degrees but now at 25 degrees. TDK fails to execute for  $THETA$  less than 25 degrees.

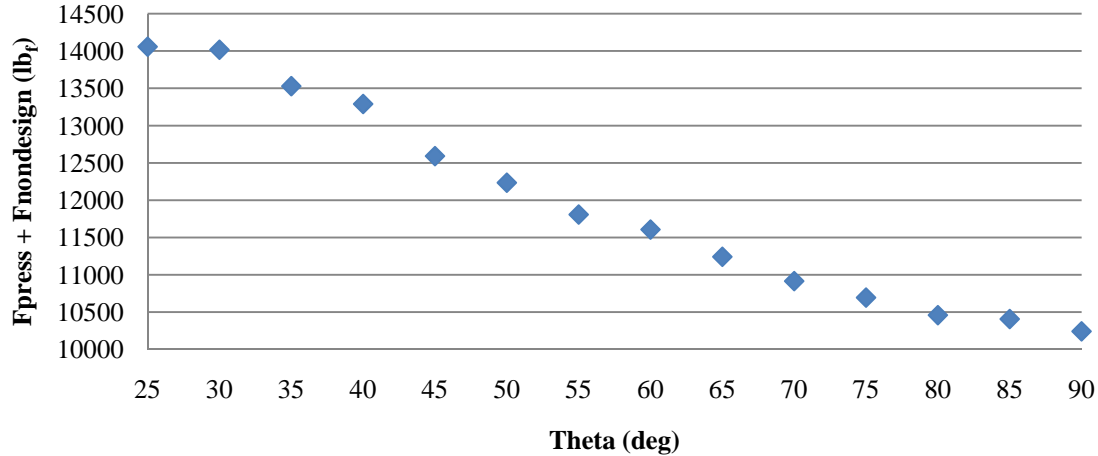


**Figure 78. Influence of  $THETA$  on Nozzle Performance**

A method by Anderson for a calorically perfect gas, two dimensional minimum-length nozzle includes a calculation for the maximum expansion angle [47]. The expansion angle extends from the horizontal plane of the throat to the nozzle wall. Using equation 30 and the nozzle exit Mach number, calculated in Angelino for the TDK PFG model, the Prandtl-Meyer function can be calculated. The expansion angle is equal to one-half the Prandtl-Meyer function [47]. An experiment was performed setting the TDK variable  $THETA$  equal to the expansion angle and seeing if maximum performance (pressure thrust plus  $F_{nondesign}$ ) could be achieved. Surprisingly the answer is no.  $THETA$  equal to 25 degrees provides the best overall performance. Therefore, for the final DEAN model,  $THETA$  was set to 25 degrees.

One of the design goals for the DEAN is to maximize  $T/W$ . Currently the DEAN design is having trouble meeting the thrust and specific impulse design goals leading to the decision of  $THETA$  equal to 25 degrees. Once a valid design point is found meeting the performance design goals, a trade study on  $THETA$  should be performed to find a value maximizing  $T/W$  while still meeting the performance design goals.

The next sensitivity analysis performed is with the *VSJ* TDK input evaluating a range of 6,000 to 20,000 in 1,000 ft/sec (1 ft/s = 0.305 m/s) increments. As previously stated, since TDK uses a scramjet to model the aerospike nozzle, *VSJ* must equate to a Mach value at the throat (*MSJ*) greater than 1.0. Either the *VSJ* or *MSJ* variable must be input in the TDK PFG model. *VSJ* or *MSJ* is an important parameter in determining the calculated pressure thrust and corresponding pressure profile along the spike since it directly influences the value of the mass flow rate calculated through the throat. Testing the flexibility of *MSJ* and *VSJ*, *VSJ* has more flexibility and influence on the output mass flow rate than *MSJ*. The number of significant figures that can be input limit the use of *MSJ*. Therefore, *VSJ* was chosen as the desired input for the PFG model.

The result of increasing *VSJ* on the geometry of the nozzle, shown in Figure 79, clearly shows the value of *VSJ* has no influence on the calculated aerospike nozzle geometry.

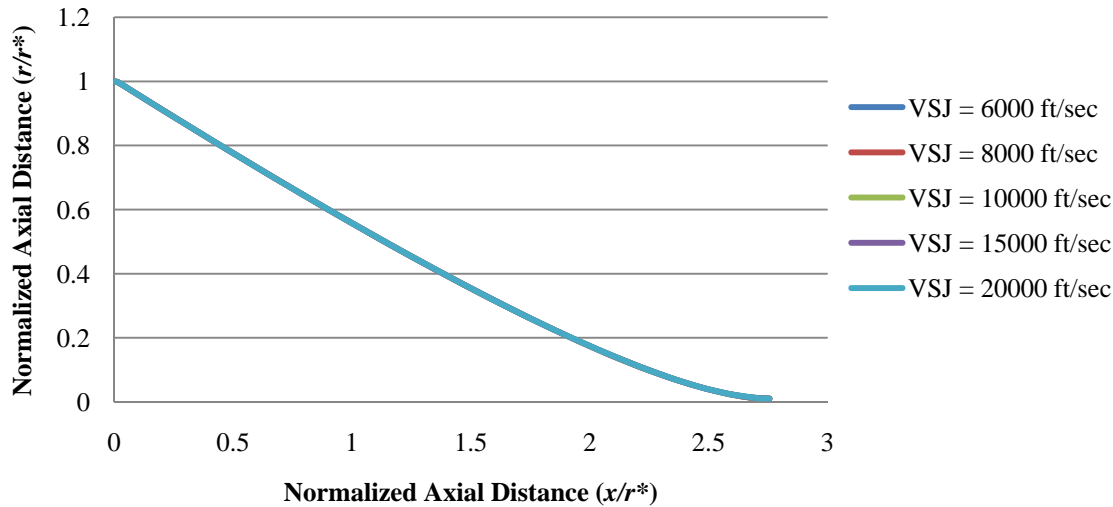


**Figure 79. Influence of TDK VSJ Input on Nozzle Geometry**

Next, the influence of VSJ on the nozzle pressure profile was evaluated and is shown in Figure 80. The figure clearly shows the input value of VSJ is vital in getting a correct pressure profile along the aerospike for the DEAN.

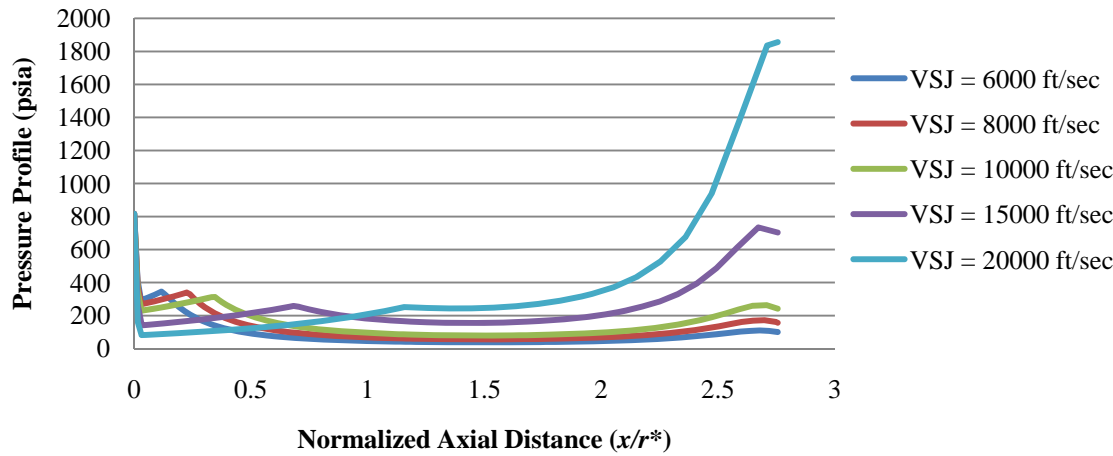


**Figure 80. Influence of TDK VSJ Input on the Nozzle Pressure Profile**

The integration of the pressure profile with respect to nozzle cross-sectional area leads to the value of pressure thrust. TDK outputs the pressure thrust value for the full-length aerospike nozzle. Figure 81 shows the result of increased VSJ on aerospike

pressure thrust. Again, the conclusion is the input value of  $VSJ$  is vital in getting the correct TDK outputs for the DEAN design.

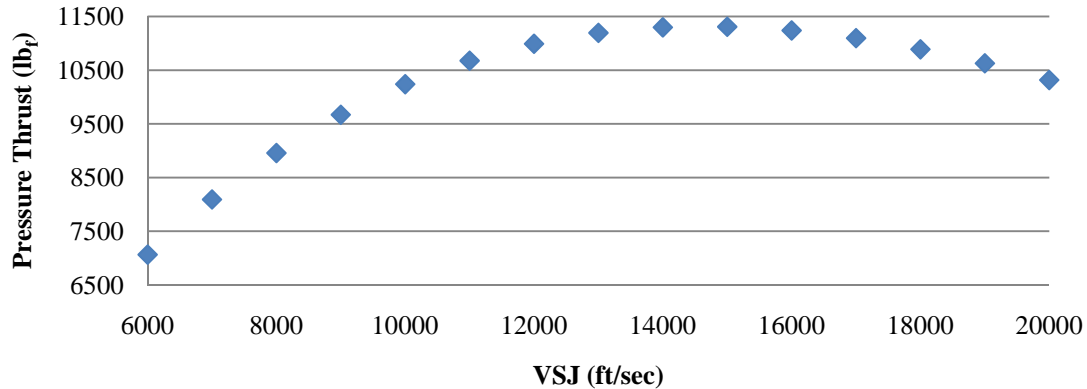


**Figure 81. Influence of TDK VSJ Input on Nozzle Pressure Thrust**

Figure 82 shows the influence of  $VSJ$  on the calculated engine mass flow rate. As  $VSJ$  increases, the engine mass flow rate increases. Increased engine mass flow makes sense since  $VSJ$  is the velocity of the flow through the scramjet throat.

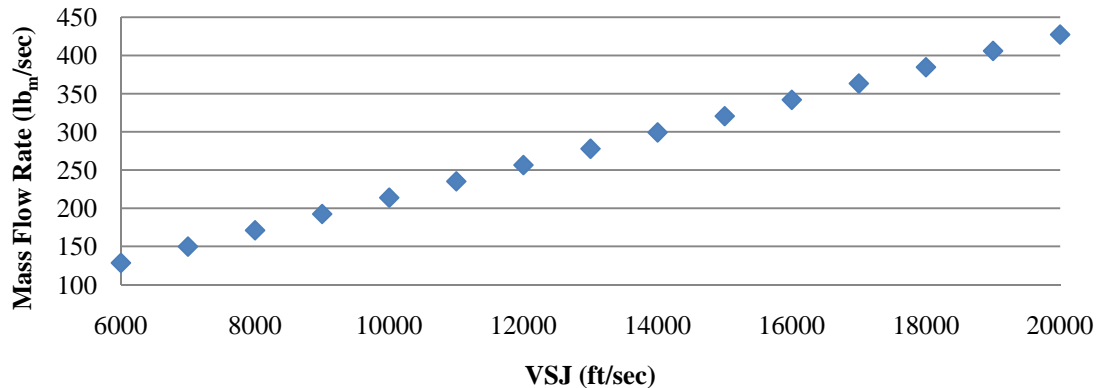


**Figure 82. Influence of TDK VSJ Input on Engine Mass Flow Rate**

The value of  $VSJ$  does not affect nozzle geometry; however, clearly from these tests, the value of  $VSJ$  must be carefully selected to calculate the correct DEAN pressure profile and pressure thrust. Although the value of  $VSJ$  is a user input into TDK, the value does not need to be a “guess” but rather it can be calculated. Since the TDK PFG model

is linked to CEA, the user can get the speed of sound at the throat from CEA. Assuming a supersonic Mach number at the throat the velocity of the flow through the throat can be calculated using equation 61.

$$VSJ = aM^* \quad (61)$$

where

$VSJ$	=	Velocity of Flow through Throat (ft/s)
$a$	=	Speed of Sound at the Throat (ft/s)
$M^*$	=	Mach Number at the Throat

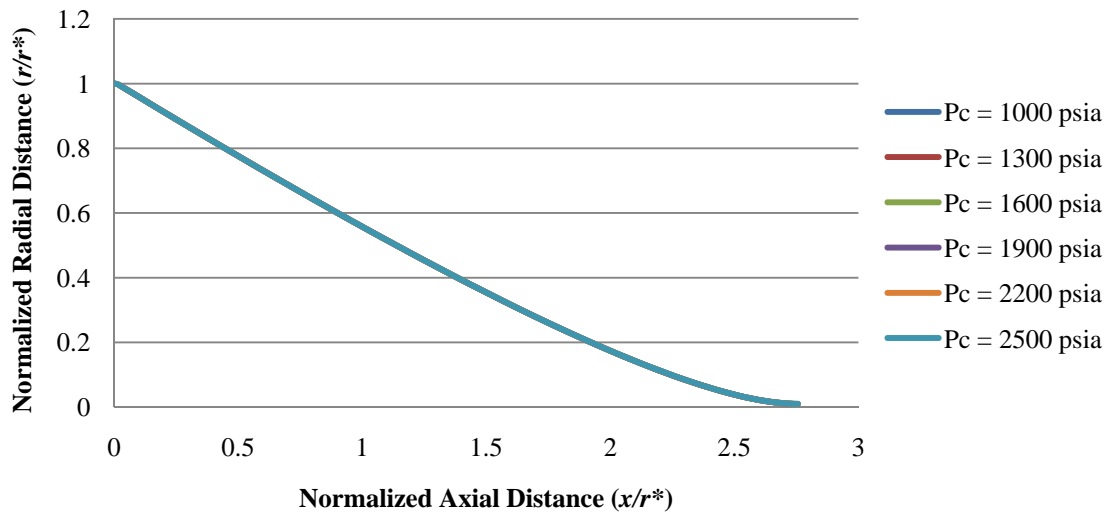
In testing different values for  $M^*$  close to 1.0 for a choked throat, the minimum  $M^*$  successfully used in TDK was 1.1. The result is an acceptable slightly inflated pressure thrust and pressure profile with no influence to geometry.

The next TDK input sensitivity analysis was chamber pressure. TDK requires the pressure at the throat to be input ( $PSJ$ ); however, with the TDK link to CEA, the throat pressure is known from CEA. A parametric  $VSJ$  from equation 61 was used for this analysis. The goal is to determine if chamber pressure has an effect on nozzle shape and nozzle pressure profile. Table 38 tabulates the design variables for the analysis.

**Table 38. Chamber Pressure Sensitivity Analysis Design Variables.**

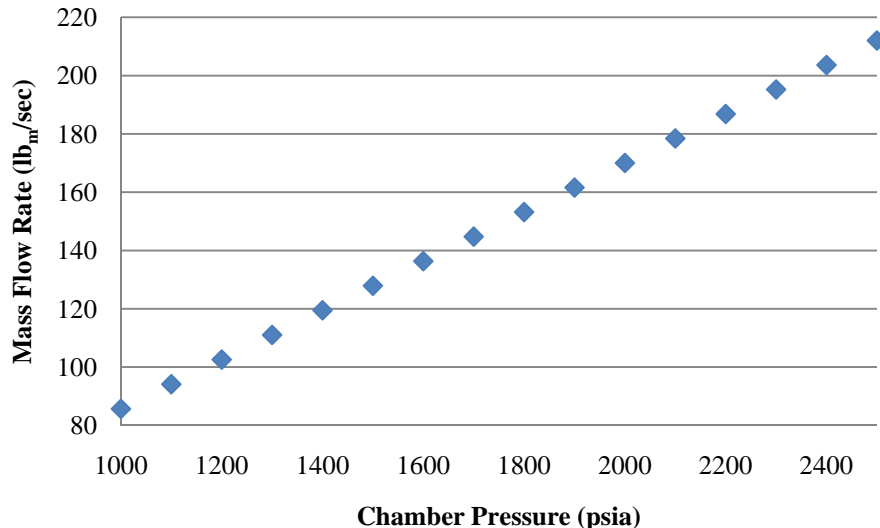
Variable	Value
$O/F$	6
Chamber Pressure	1000 – 2500 psia (6.9 – 17.2 MPa)
Chamber Radius at Throat	6 in (15.2 cm)
Throat Area	18.899 in <sup>2</sup> (121.9 cm <sup>2</sup> )
Engine Mass Flow Rate	104 lb <sub>m</sub> /s (47.2 kg/s)
$P_{inf}$ – Operational	0.000145 psia (1 Pa)

Figure 83 shows the influence of chamber pressure ( $P_c$ ) on nozzle geometry. The result is the chamber pressure value has little influence on nozzle geometry. Looking at the actual values, there is a slight increase in normalized nozzle length at the 1/1000 decimal place; the influence is negligible. The reason chamber pressure has little influence on nozzle geometry is due to the assumption of constant throat area for the study.



**Figure 83. Influence of Chamber Pressure TDK Input on Nozzle Geometry**

To maintain constant throat area, as chamber pressure increases, the engine mass flow rate must also increase. Figure 84 plots engine mass flow rate as a function of chamber pressure with expected results.



**Figure 84. Influence of Chamber Pressure TDK Input on Engine Mass Flow Rate**

Next, the influence of chamber pressure on the nozzle pressure profile was analyzed and plotted in Figure 85. As chamber pressure increases, there is an increase in the pressure profile magnitude along the length of the nozzle. This is as expected with increased chamber pressure, increased mass flow, and constant throat area.

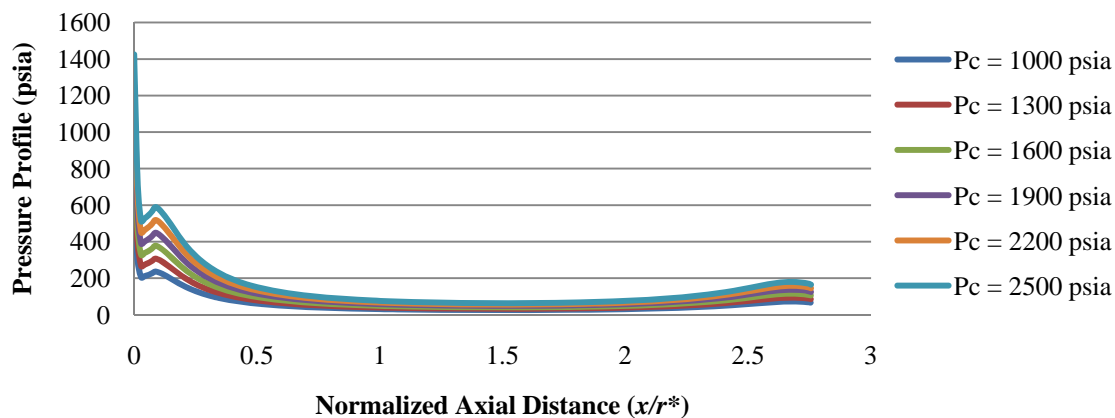


**Figure 85. Influence of Chamber Pressure TDK Input on Nozzle Pressure Profile**

With *VSJ* now a variable instead of a user guess, the pressure profile looks more like the profile documented in literature. The pressure ratio is defined as chamber pressure divided by ambient pressure; or more precisely, chamber pressure divided by the

nozzle exit pressure at design altitude. When the pressure ratio is small, decreases and increases in the pressure profile are noted along the length of the nozzle. The pressure profile would look like multiple triangles along the length of the nozzle. On the contrary, when the pressure ratio is large, the pressure profile flattens out and becomes asymptotic to the nozzle exit pressure. For the DEAN design shown in Figure 85, the pressure ratio is neither small nor large and the profile shows a relatively small pressure increase and decrease near the throat and a pressure increase at the exit plane. The profile matches very closely with Hagemann *et al.* for a linear aerospike and with Connors *et al.* for an annular aerospike [26-28].

The conclusion from the chamber pressure sensitivity analysis is chamber pressure does not influence geometry yet it does influence the pressure profile when throat area is constant. When TDK is linked to NPSS properly, the throat area will vary for different chamber pressures, and the chamber pressure TDK input should provide a valid pressure profile.

The TDK sensitivity analyses for *PINF*, *MINF*, *THETA*, *VSJ*, and chamber pressure were vital in determining the variables' proper use in the TDK PFG model and ultimately in the final ModelCenter DEAN model.

## **Appendix E: DEAN Model Code**

The AFIT Department of Aeronautics and Astronautics archived all code pertaining to the DEAN ModelCenter model. For access to the code, please contact the AFIT/ENY front office at (937) 255 – 3069.

## References

- [1] Donely, M. and Schwartz, N. *Mission Statement and Priorities*. Excerpt from 15 September 2008 senior leader letter to airmen. <http://www.af.mil/information/viewpoints/jvp.asp?id=401>. 16 April 2010. Page 1.
- [2] DeGeorge, D. and Fletcher, S. *The Integrated High Payoff Rocket Propulsion Technology Program and Tactical Missile Propulsion Status*. AFRL-PR-EN-TP-2002-214. Pages 1-3.
- [3] DeGeorge, D. Subject: Thesis Question. Electronic Message. 133400 EST, 8 April 2010.
- [4] Martin, D. *Computational Design of Upperstage Chamber, Aerospike, and Cooling Jacket for Dual-Expander Rocket Engine*. MS thesis, AFIT/GAE/ENY/08-M20. Graduate School of Engineering and Management, Air Force Institute of Technology (AU), Wright-Patterson AFB, OH. March 2008.
- [5] Simmons, J. *Parametric Study of Dual-Expander Aerospike Nozzle Upper Stage Rocket Engine*. JANNAF Conference. May 2010.
- [6] Simmons, J. and Branam, R. *Parametric Study of Dual-Expander Aerospike Nozzle Upper Stage Rocket Engine*. AIAA Journal of Spacecraft and Rockets, Volume 48, Number 2, March – April 2011.
- [7] Hall, J., Hartsfield, C., Simmons, J. and Branam, R. *Optimized Dual-Expander Aerospike Nozzle Upper Stage Rocket Engine*. 49th AIAA Aerospace Sciences Meeting and Exhibit. Orlando, FL. 4-7 January 2011.
- [8] Huzel, D. and Huang, D. *Modern Engineering for Design of Liquid-Propellant Rocket Engines*. Progress in Astronautics and Aeronautics, Volume 147, AIAA, 1992.
- [9] Edited by Baker, D. *Jane's Space Directory 2006 – 2007*. Jane's Information Group Limited, United Kingdom, 2006. Pages 257, 320, 322, 330, 360, and 361.
- [10] Wade, M. Encyclopedia Astronautica. Summary of engine performance specifications. <http://www.astronautix.com/engines/vinci.htm> and <http://www.astronautix.com/engines/rd0146.htm>. 18 April 2010.
- [11] Alliot, P. *et al.* *Overview of the Development Progress of the Ariane 5 Upper Stage VINCI Engine*. 53<sup>rd</sup> International Astronautical Congress, Houston, Texas, 10-19 October 2002. IAC-02-S.1.03. Page 3.
- [12] Sackheim, R. *Overview of United States Space Propulsion Technology and Associated Space Transportation Systems*. Journal of Propulsion and Power, Volume 22, Number 6, November – December 2006. Page 1314, 1325, and 1327.
- [13] Wade, M. Encyclopedia Astronautica. Summary of J-2 performance specifications. <http://www.astronautix.com/engines/j2.htm>. 3 May 2010.
- [14] O'Leary, R. and Beck, J. *Nozzle Design*. Threshold: Pratt & Whitney Rocketdyne's engineering journal of power technology. Spring 1992. <http://www.pwreengineering.com/articles/nozzledesign.htm>.
- [15] Bui, T. *et al.* *Flight Research of an Aerospike Nozzle Using High Power Solid Rockets*. 41<sup>st</sup> AIAA/ASME/SAE/ASEE Joint Propulsion Conference & Exhibit. 10 – 13 July, 2005. Tucson, AZ. AIAA 2005-3797.

[16] Johnson, R. and Leary, B. *An Aerospike Nozzle Design for Solid Aluminized Composite Rocket Propellant*. 20<sup>th</sup> JANNAF Rocket Nozzle Technology Subcommittee Meeting. CPIA Publication 694, CPIA, Columbia, MD. November 1999.

[17] Besnard, E. and Garvey, J. *Aerospike Engines for Nanosat and Small Launch Vehicles (NLV/SLV)*. AIAA 2004-6005. Space 2004 Conference and Exhibit. 28-30 September 2004, San Diego, CA.

[18] Wertz, J. *Mission Geometry; Orbit and Constellation Design and Management*. Microcosm Press, CA, 2001. Page 58.

[19] Sellers, J. *Understanding Space: An Introduction to Astronautics*. Revised Second Edition. McGraw-Hill, 2004. Page 164.

[20] Humble R., Henry, G., and Larson, W. *Space Propulsion Analysis and Design*. McGraw-Hill, 1995, NY.

[21] Manski, D. *et al.* *Cycles for Earth-to-Orbit Propulsion*. Journal of Propulsion and Power, Volume 14, Number 5, September – October 1998. Pages 588-590 and 594.

[22] Krach, A. and Sutton, A. *Another Look at the Practical and Theoretical Limits of an Expander Cycle, LOX/H<sub>2</sub> Engine*. 35<sup>th</sup> AIAA/ASME/SAE/ASEE Joint Propulsion Conference and Exhibit. 20-24 June, 1999. Los Angeles, CA. AIAA.

[23] Sutton, G. and Biblarz, O. *Rocket Propulsion Elements*. Seventh Edition. John Wiley & Sons. 2001.

[24] Turns, S. *An Introduction to Combustion: Concepts and Applications*. Second Edition. McGraw-Hill, 2000. Page 18-19 and 149-150.

[25] Dressler, G. and Bauer, J. *TRW Pintle Engine Heritage and Performance Characteristics*. AIAA Paper 2000-3871. 36<sup>th</sup> AIAA/ASME/SAE/ASEE Joint Propulsion Conference and Exhibit. 16-19 July 2000. Huntsville, AL. Page 1-2.

[26] Hagemann, G., Immich, H., Nguyen, T., Dumnov, G. *Advanced Rocket Nozzles*. Journal of Propulsion and Power, Volume 14, Number 5, September – October 1998. Page 627.

[27] Connor, J., Cubbison, R., and Mitchell, G. *Annular Internal-External-Expansion Rocket Nozzles for Large Booster Applications*. NASA Technical Note D-1049. September 1961. Page 31.

[28] Hagemann, G., Immich, H., and Terhardt, M. *Flow Phenomena in Advance Rocket Nozzles – The Plug Nozzle*. DLR-74239/D-81663, Published with permission by AIAA, 1998.

[29] Coats, D. Subject: TDK Code Questions. Electronic Message. 142100 EST, 18 August 2010.

[30] Ito, T., Fujii, K., and Hayashi, A. *Computations of the Axisymmetric Plug Nozzle Flow Fields – Flow Structures and Thrust Performance*. AIAA Paper 99-3211. 1999.

[31] Ito, T. and Fujii, K. *Flow Field Analysis of the Base Region of Axisymmetric Aerospike Nozzles*. AIAA 2001-1051. 39<sup>th</sup> AIAA Aerospace Sciences Meeting and Exhibit. 8-11 January 2001. Reno, NV. Page 10.

[32] Ito, T. and Fujii, K. *Numerical Analysis of the Base Bleed Effect on the Aerospike Nozzles*. AIAA 2002-0512. 40<sup>th</sup> AIAA Aerospace Sciences Meeting and Exhibit. 14-17 January 2002. Reno, NV. Page 8.

[33] Incropera, F and DeWitt, D. *Fundamentals of Heat and Mass Transfer*. Fifth Edition. John Wiley & Sons, 2002. Pages 3-11 and 492.

[34] Hill, P. and Peterson, C. *Mechanics and Thermodynamics of Propulsion*. Second Edition. Addison-Wesley Publishing Company, 1992. Page 541 – 545.

[35] Brown, W. *Enhanced Heat Transfer Rocket Combustor Technology Component Hot-Fire Test Results*. AIAA 90-2182. 26<sup>th</sup> AIAA/ASME/SAE/ASEE Joint Propulsion Conference. 16-18 July 1990. Orlando, FL.

[36] Schmidt, G., Popp, M., and Frohlich, T. *Design Studies for a 10 Ton Class High Performance Expander Cycle Engine*. AIAA Paper 1998-3673. 1998.

[37] Carlile, J. *An Experimental Investigation of High-Aspect-Ratio Cooling Passages*. AIAA Paper 92-3154. 28<sup>th</sup> AIAA/ASME/SAE/ASEE Joint Propulsion Conference and Exhibit. 6-8 July 1992. Nashville, TN.

[38] Wadel, M. and Meyer, M. *Validation of high aspect ratio cooling in a 89 kN (20,000 lb<sub>f</sub>) thrust combustion chamber*. AIAA 96-2584. 32<sup>nd</sup> AIAA/ASME/SAE/ASEE Joint Propulsion Conference and Exhibit. 1-3 July 1996. Lake Buena Vista, FL.

[39] Schuff, R. *et al. Integrated Modeling and Analysis for a LOX/Methane Expander Cycle Engine: Focusing on Regenerative Cooling Jacket Design*. AIAA 2006-4534. 42<sup>nd</sup> AIAA/ASME/SAE/ASEE Joint Propulsion Conference and Exhibit. 9-12 July 2006. Sacramento, CA.

[40] Arguello, M. *The Concept Design of a Split Flow Liquid Hydrogen Turbopump*. MS thesis, AFIT/GAE/ENY/08-M01. Graduate School of Engineering and Management, Air Force Institute of Technology (AU), Wright-Patterson AFB, OH. March 2008.

[41] Strain, M. *Design of an Oxygen Turbopump for a Dual Expander Cycle Rocket Engine*. AFIT/GAE/ENY/08-M26. Graduate School of Engineering and Management, Air Force Institute of Technology (AU), Wright-Patterson AFB OH. March 2008.

[42] ModelCenter 8.0 User Manual. Phoenix Integration. Blacksburg, VA, 2009.

[43] NASA Glenn Research Center. *NPSS User Guide*. Tech Report NPSS v1.6.4, 2006.

[44] NASA Glenn Research Center. *NPSS Rockets Supplement*. Tech Report NPSS v1.6.5, 12 March 2008.

[45] Steward, J. *Calculus: Concepts and Contexts*. 2<sup>nd</sup> Edition. Wadsworth Group, Brooks/Cole, Thomas Learning<sup>TM</sup>. 2001. Page 418, 881.

[46] Gordon, S. and McBride, B. *Complex Chemical Equilibrium Compositions and Applications, I. Analysis*. NASA Reference Publication 1311, 1994. Page 1 and 25-31.

[47] Anderson, J. *Modern Compressible Flow with Historical Perspective*. Third Edition. McGraw-Hill. 2003. Pages 186-187, 403-407.

[48] Dunn, S. and Coats, D. *TDK'04<sup>TM</sup> Two-Dimensional Kinetics (TDK) Nozzle Performance Computer Program User's Manual*. Software & Engineering Associates, Inc. 2005.

[49] Dunn, S. and Coats, D. *Nozzle Performance Predictions Using the TDK 97 Code*. 33rd AIAA / ASME / SAE / ASEE Joint Propulsion Conference and Exhibit, Seattle, WA, AIAA 1997-2807. 1997.

[50] Dunn, S. and Coats, D. *Optimum Nozzle Contours for Aerospike Nozzles Using the TDK99<sup>TM</sup> Computer Code*. 36th JANNAF Combustion Subcommittee, Cocoa Beach, FL, 1999.

[51] Angelino, G. *Approximate Method for Plug Nozzle Design*. AIAA Journal, Vol. 2, No. 10, October 1964, page 1834 – 1835.

[52] *Thermophysical Properties of Fluid Systems*. National Institute of Standards and Technology (NIST). <http://webbook.nist.gov/chemistry/fluid/>. 13 January 2011.

[53] Shoeman, L. *Final Report Oxygen Materials Compatibility Testing*. NASACR-182195. January 1989. Page 184.

[54] Buch, A. "Pure Metals Properties: A Scientific-Technical Handbook". ASM International. 1999.

[55] ASM International. "Engineered Materials Handbook". Desk Edition. 2001. CD-ROM.

[56] Special Metals. INCOLOY(R) alloy 909. Publication Number SMC-077. Special Metals Corporation, 2004.

[57] Special Metals. INCONEL(R) alloy 718. Publication Number SMC-045. Special Metals Corporation, 2007.

[58] Special Metals. INCONEL(R) alloy 625. Publication Number SMC-063. Special Metals Corporation, 2006.

[59] Haynes International. "Heat-Resistant Alloy at a Glance: Haynes(R) 188 Alloy". Haynes International. 2008.

[60] Metals Handbook, Vol.2 - Properties and Selection: Nonferrous Alloys and Special-Purpose Materials, ASM International 10th Ed. 1990.

[61] Ross, Robert B. "Metallic Materials Specification Handbook". 4th Edition. Chapman & Hall. 1992.

[62] Shigley, J. and Mischke, C. *Mechanical Engineering Design*. Fifth Edition. McGraw-Hill. 1989.

[63] Raymer, D. *Aircraft Design: A Conceptual Approach*. Fourth Edition. AIAA, 2006.

[64] *Delta IV Payload Planners Guide*. ULA Document 06H0233. United Launch Alliance. September 2007. Page 1-4.

[65] Crane Engineering Department. *Flow of Fluids through Valves, Fittings, and Pipe*. Technical Paper No. 410. Crane Co. 1988, page 2-8.

## **VI. Vita**

Captain Joshua N. Hall commissioned as an officer in the United States Air Force in 2005 through the Reserve Officer Training Corps program at Wilkes University, Wilkes-Barre, Pennsylvania earning a Bachelor of Science degree in Mechanical Engineering. His first assignment was to Cape Canaveral Air Force Station, Florida providing mission assurance and serving as the mechanical systems expert for the Delta II launch vehicle program.

In 2009, Captain Hall began working towards a Master's of Science degree in Aeronautical Engineering at the Air Force Institute of Technology, Dayton, OH with a focus in aeronautics and rocket propulsion technology. Upon graduation, he will work at the Air Force Research Laboratory Propulsion Directorate at Edwards Air Force Base, California.

<b>REPORT DOCUMENTATION PAGE</b>					Form Approved OMB No. 074-0188
<p>The public reporting burden for this collection of information is estimated to average 1 hour per response, including the time for reviewing instructions, searching existing data sources, gathering and maintaining the data needed, and completing and reviewing the collection of information. Send comments regarding this burden estimate or any other aspect of the collection of information, including suggestions for reducing this burden to Department of Defense, Washington Headquarters Services, Directorate for Information Operations and Reports (0704-0188), 1215 Jefferson Davis Highway, Suite 1204, Arlington, VA 22202-4302. Respondents should be aware that notwithstanding any other provision of law, no person shall be subject to an penalty for failing to comply with a collection of information if it does not display a currently valid OMB control number.</p> <p><b>PLEASE DO NOT RETURN YOUR FORM TO THE ABOVE ADDRESS.</b></p>					
<b>1. REPORT DATE (DD-MM-YYYY)</b> 24-03-2011		<b>2. REPORT TYPE</b> Master's Thesis		<b>3. DATES COVERED (From – To)</b> October 2009 – March 2011	
<b>4. TITLE AND SUBTITLE</b>  Optimized Dual Expander Aerospike Rocket			<b>5a. CONTRACT NUMBER</b>		
			<b>5b. GRANT NUMBER</b>		
			<b>5c. PROGRAM ELEMENT NUMBER</b>		
<b>6. AUTHOR(S)</b>  Hall, Joshua N., Capt, USAF			<b>5d. PROJECT NUMBER</b>		
			<b>5e. TASK NUMBER</b>		
			<b>5f. WORK UNIT NUMBER</b>		
<b>7. PERFORMING ORGANIZATION NAMES(S) AND ADDRESS(S)</b>  Air Force Institute of Technology Graduate School of Engineering and Management (AFIT/EN) 2950 Hobson Way, Building 640 WPAFB OH 45433-8865				<b>8. PERFORMING ORGANIZATION REPORT NUMBER</b>  AFIT/GAE/ENY/11-M10	
<b>9. SPONSORING/MONITORING AGENCY NAME(S) AND ADDRESS(ES)</b>  Mr. Michael Huggins / Air Force Research Laboratory Propulsion Directorate Building: 8353 Room: 216B 5 Pollux Drive, Edwards AFB, CA 93524 michael.huggins@edwards.af.mil / (661) 275 - 5230				<b>10. SPONSOR/MONITOR's ACRONYM(S)</b> AFRL/RZS	
				<b>11. SPONSOR/MONITOR's REPORT NUMBER(S)</b>	
<b>12. DISTRIBUTION/AVAILABILITY STATEMENT</b> APPROVED FOR PUBLIC RELEASE; DISTRIBUTION UNLIMITED.					
<b>13. SUPPLEMENTARY NOTES</b> The views expressed in this thesis are those of the author and do not reflect the official policy or position of the United States Air Force, Department of Defense, or the United States Government. This material is declared a work of the U.S. Government and is not subject to copyright protection in the United States.					
<b>14. ABSTRACT</b> Research at the Air Force Institute of Technology (AFIT) focused on designing a cryogenic dual-expander aerospike nozzle (DEAN) upper stage rocket engine to produce 50,000 pounds-force (222.4 kilo-Newton) vacuum thrust, 464 seconds of vacuum specific impulse and a thrust-to-weight ratio of 106.5. The use of dual expander cycles improves engine reliability, maximizes efficiency, and eliminates some catastrophic failure modes. An upper stage engine with an aerospike nozzle is shorter and lighter than an equivalent performing conventional bell nozzle upper stage engine. Previous research focused on first developing a feasible closed DEAN design model and secondly expanding the model to support parametric trade and optimization studies. The current research effort used previous research as a foundation to create a reliable system level modeling tool to estimate performance, engine weight, and geometry for the DEAN concept. The model incorporated the Numerical Propulsion System Simulation (NPSS <sup>TM</sup> ) software by NASA, Two-Dimensional Kinetics '04 (TDK'04 <sup>TM</sup> ) by Software and Engineering Associates, Inc, and ModelCenter <sup>TM</sup> by Phoenix Integration. Research obtained a new DEAN design point meeting physical and reusability design constraints from model trade and optimization studies. The new design has a vacuum thrust and a thrust-to-weight ratio of 50,161 lb <sub>f</sub> (223.1 kN) and 142.2, respectively. Furthermore, the new design has a vacuum specific impulse of 430.6 seconds, failing to meet the vacuum specific impulse design goal by 33.4 seconds or 7.3%. The model used common metals, alloys, and ceramics to improve near-term manufacturability of the DEAN. Current research laid a pathway for further research to find the optimum DEAN design point meeting all the design goals including vacuum specific impulse.					
<b>15. SUBJECT TERMS</b> Upperstage, Aerospike, Plug Nozzle, Regenerative Cooling, Expander Cycle, ModelCenter, NPSS, TDK, Hydrogen, Oxygen					
<b>16. SECURITY CLASSIFICATION OF:</b>		<b>17. LIMITATION OF ABSTRACT</b>  UU	<b>18. NUMBER OF PAGES</b>  303	<b>19a. NAME OF RESPONSIBLE PERSON</b> Carl R. Hartsfield, Lt Col, USAF	
a. REPORT U	b. ABSTRACT U			c. THIS PAGE U	<b>19b. TELEPHONE NUMBER (Include area code)</b> (937) 255-3636 ext. 7472 (carl.hartsfield@afit.edu)